TU/e EINDHOVEN UNIVERSITY OF TECHNOLOGY

Eindhoven University of Technology

MASTER

Optimization of a snap-fit connection

a steel connection for the built environment

Moriche Quesada, S.

Award date:
2016

Link to publication

Optimization of a Snap-Fit Connection

A steel connection for the built environment

Sergio Moriche Quesada

Student No.0885681

Graduation No. A-2016.153.

Supervisors:

dr.ir. H. Hofmeyer
prof.ir. H.H. Snijder
prof.dr.ir. A.S.J. Suiker

Thesis Submitted in Partial Fulfilment of the
Requirements for the Degree of
Master of Science

in the
Unit of Structural Design
Department of the Built Environment

Eindhoven, August 2016

Summary

Steel structures are widely used to build the skeleton of constructions in the built environment. They are generally formed by standardized profiles acting as columns or beams, which are commonly connected by means of fasteners or welds. Those connections require long assembly times, which is directly translated into economic expenses.

A new typology of steel connection for the built environment is proposed by A. Verbossen. Considering that this connection would substantially reduce the assembly time between elements and therefore the complete erection of buildings, there is need to study the behaviour, reliability and possible optimization of its performance, which are the main goals of the thesis.

Two typologies of experimental test are performed: (1) cantilever tests (in which the connection is loaded by a M-V combination while its rotation is measured) motivated to validate a numerical model and (2) tensile tests (in which a steel sheet specimen from the connection is tested under an uni-axial tensile force while the elongation is measured) used to determine the mechanical properties of the material of the connection.

Numerical models are validated by simulating the cantilever tests and comparing the results with the experimental data. The mathematical solutions of the models are verified by refining the mesh of the simulations and comparing its relative error. The validated finite element models are used to gain insight on the behaviour of the connection by performing sensitivity and parametric analysis, based on the knowledge gathered a design with an optimized performance is proposed.

The results of the simulations consider the behaviour of the connection disregarding the stiffness and resistance of adjacent members. The results provided by the finite element method are used as input into a mechanical component model that accounts for the interaction between all components and allows to compare the behaviour of the complete connection in terms of bending capacity and ductility.

Keywords: *Snap-Fit connection, Steel Dovetail, FEM, Component method, Parametric study, Sensitivity analysis, Optimization.*

Contents

List of Figures

List of Scripts

Chapter 1

Introduction

Steel profiles are a popular and efficient solution for the structural skeleton of building constructions. The material distribution of steel profiles (e.g. HE) provides great effectiveness for acting bending moments. However the connection between the profiles, splices or beam-to-column connections, has remained a critical issue over time.

Two of the most currently used solutions in the building environment are either welded or fastened connections (see Fig. 1.1).

- Welded connections are considered those where all members are joined by means of welds. The assemblage of steel profiles joined with welds is carried out on the building site, which requires long working times of high skilled workers, thus increasing the total cost of the construction. Moreover the quality of welds is decreased because of the uncontrolled environment. As a result of those two drawbacks the use of fastened connections is commonly preferred.

- Fastened connections are prepared in the workshop and assembled on the building site. Their assemblage difficulty and assemblage time depends on the connection configuration. Additionally the load transfer of this typology of connection is localized on the fasteners. To obtain greater resistances, the fasteners used are of higher steel grades thus exhibiting rather brittle behaviours and reducing the rotation capacity of the connection.

(a) Welded connection   (b) Fastened connection

Figure 1.1: General connection typologies [1]

Oppositely, a snap fit connection is a joint that connects two elements without neither fasteners nor welds with the main characteristic of ease of assemblage. This typology of connection is frequently used with materials such as, plastics or aluminium, where the flexibility of the material allow the parts to slightly deflect until its interlock mechanism is activated (see Fig. 1.2)

Adrianus and Sebastiaan Verbossen, head of "A.F.M Verbossen constructeur" have developed a prototype of snap-fit connection made out of steel (see Fig. 1.3) from here on referred as *"Snap-Fit connection"*. In this case the interlock mechanism is split. The first function is given by a tapered

---
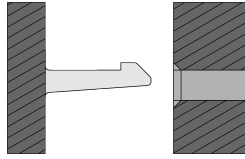
Figure 1.2: Cantilever snap fit connection [2]

dovetail that provides resistance and the second function, the snap fit action, is provided by two position pins that are retractable by means of springs. When one of the parts of the connection slides into the other the pins go back, the final position is reached and the pins snap into the provided pin holes locking the connection completely.
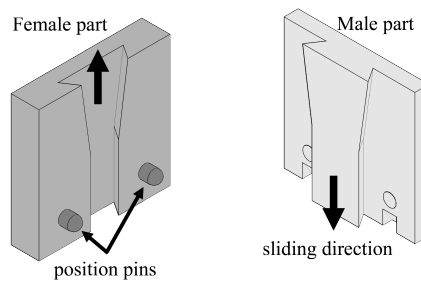
Figure 1.3: *Snap-Fit connection*

This prototype may have the characteristics to overcome assembly weakness shown in common current connections. Still its reliability and effectiveness needs to be studied.

1.1 Research goal and thesis outline

The main aim of this project is to optimize the *Snap-Fit connection* prototype subjected to bending action in terms of bending capacity. Additionally two secondary aims are defined; investigate the behaviour and reliability of the *Snap-Fit connection*.

The flow chart of Fig. 1.4 presents an overview of the tasks carried out on the course of this master thesis. The gray blocks represent the main chapters of the report. The white blocks show the main tasks of every chapter and the superscripts refer to which of the research goals those tasks contribute.

The Master thesis starts introducing the motivation of the research, the characteristics of the connection and the research goals. Experimental tests are performed to provide information to validate a numerical model. The set-ups of the tests are described and the results are presented and discussed.

Thereafter the numerical model its described, its verified and validated. Additionally the sensitivity of some factors is investigated to determine the degree of reliability of the connection. Parametric and configuration changes are simulated with help of the numerical model to optimize the performance of the connection.

The results provided by the finite element model are introduced into a mechanical component method to evaluate the influence on the overall behaviour of the joint. Finally the overall conclusions and recommendations of this project are presented.

```
┌─────────────────────────────────────────────────────────┐
│  Introduction                                            │
└─────────────────────────────────────────────────────────┘
                        ↓
┌─────────────────────────────────────────────────────────┐
│                    ┌──────────────────────────────────┐  │
│                    │ Cantilever test [2]              │  │
│  Experimental test └──────────────────────────────────┘  │
│                    ┌──────────────────────────────────┐  │
│                    │ Tensile test [2]                 │  │
│                    └──────────────────────────────────┘  │
└─────────────────────────────────────────────────────────┘
                        ↓
┌─────────────────────────────────────────────────────────┐
│                    ┌──────────────────────────────────┐  │
│                    │ Modelling of the connection [1,2,3]│ │
│                    └──────────────────────────────────┘  │
│  Numerical model   ┌──────────────────────────────────┐  │
│                    │ Validation of the model [1,2,3]  │  │
│                    └──────────────────────────────────┘  │
│                    ┌──────────────────────────────────┐  │
│                    │ Verification of the model [1,2,3]│  │
│                    └──────────────────────────────────┘  │
└─────────────────────────────────────────────────────────┘
                        ↓
┌─────────────────────────────────────────────────────────┐
│  Sensitivities [2,3]                                     │
└─────────────────────────────────────────────────────────┘
                        ↓
┌─────────────────────────────────────────────────────────┐
│  Comparison with connections [2]                         │
└─────────────────────────────────────────────────────────┘
                        ↓
┌─────────────────────────────────────────────────────────┐
│  Parametric study [1,2]                                  │
└─────────────────────────────────────────────────────────┘
                        ↓
┌─────────────────────────────────────────────────────────┐
│  Alternative configuration [3]                           │
└─────────────────────────────────────────────────────────┘
                        ↓
┌─────────────────────────────────────────────────────────┐
│  Conclusions                                             │
└─────────────────────────────────────────────────────────┘
```
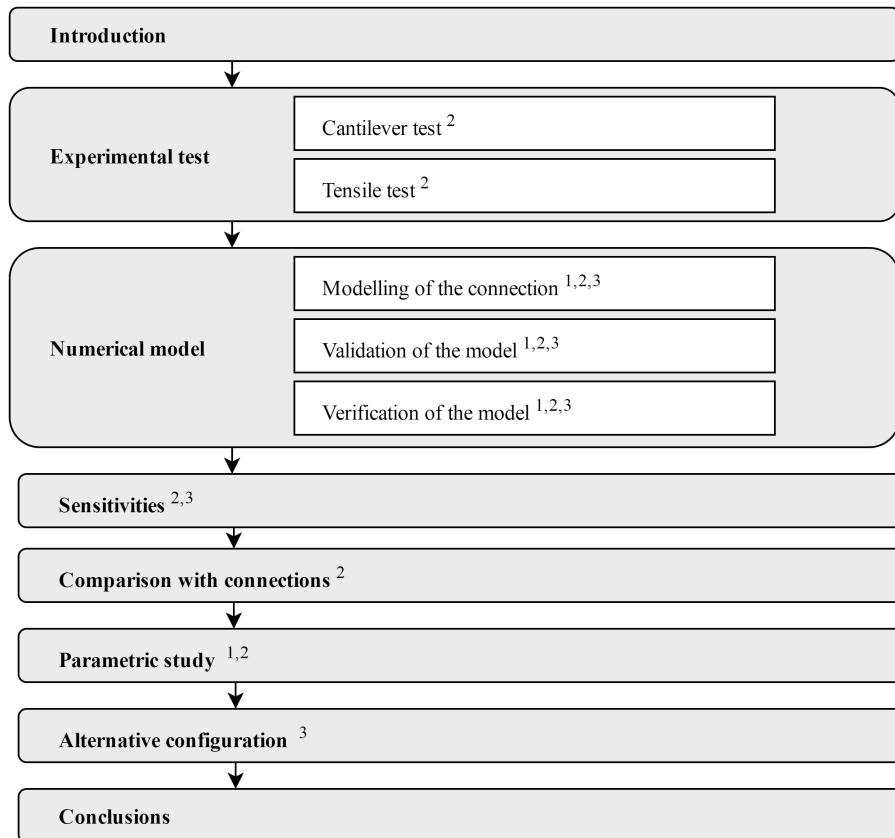
Figure 1.4: Flow chart of the tasks of the project

---

[1]Main goal: Optimize the *Snap-Fit connection*
[2]Sub-goal: Understand the behaviour of the connection
[3]Sub-goal: Study the reliability of the connection

Chapter 2

Experimental tests

This chapter presents experimental tests carried out on the course of this thesis, it describes the tests set-ups and its results are presented and discussed.

Two typologies of test are differentiated, those which study the behaviour of the connection such as cantilever tests and the tensile test, which studies the mechanical properties of the material used.

2.1 Cantilever test A

The cantilever test aims to study the behaviour of the connection by studying its stiffness (K). The stiffness of the connection relates the applied bending moment with the rotation such as $K = \frac{M}{\theta}$. In Fig. 2.1 a schematic representation of the test is presented. The rotational spring depicts the *Snap-Fit connection* which is connected on the left to a rigid support and on the right to a cantilever beam (displayed in gray).
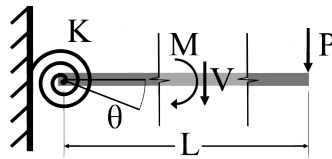
Figure 2.1: Cantilever test scheme

Test set-up

The structure of the test set-up is formed by two profiles HEB-140, each of those profiles is welded to one of the parts of the *Snap-Fit connection*.

The profile on the left (attached to the female part of the connection) regards to the rigid support of the mechanical model in Fig. 2.1. The profile on the right hand side relates to the cantilever beam, see Fig. 2.2. It may be pointed out, that the profile on the left does not completely represent a rigid support, however this is solved by measuring the rotation of the connection locally.

The *Snap-Fit connection* specimen is measured with a digital caliper and Fig. 2.3 shows a sketch of its geometry.
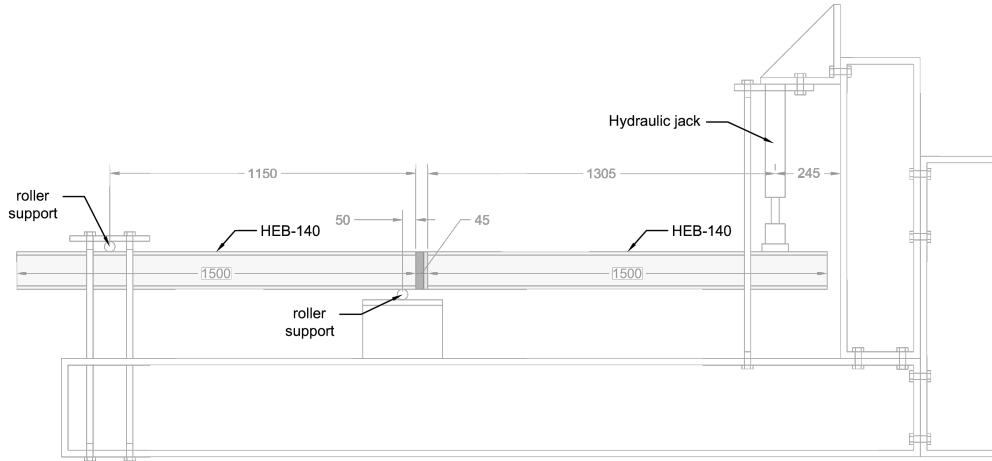
Figure 2.2: Cantilever test set-up
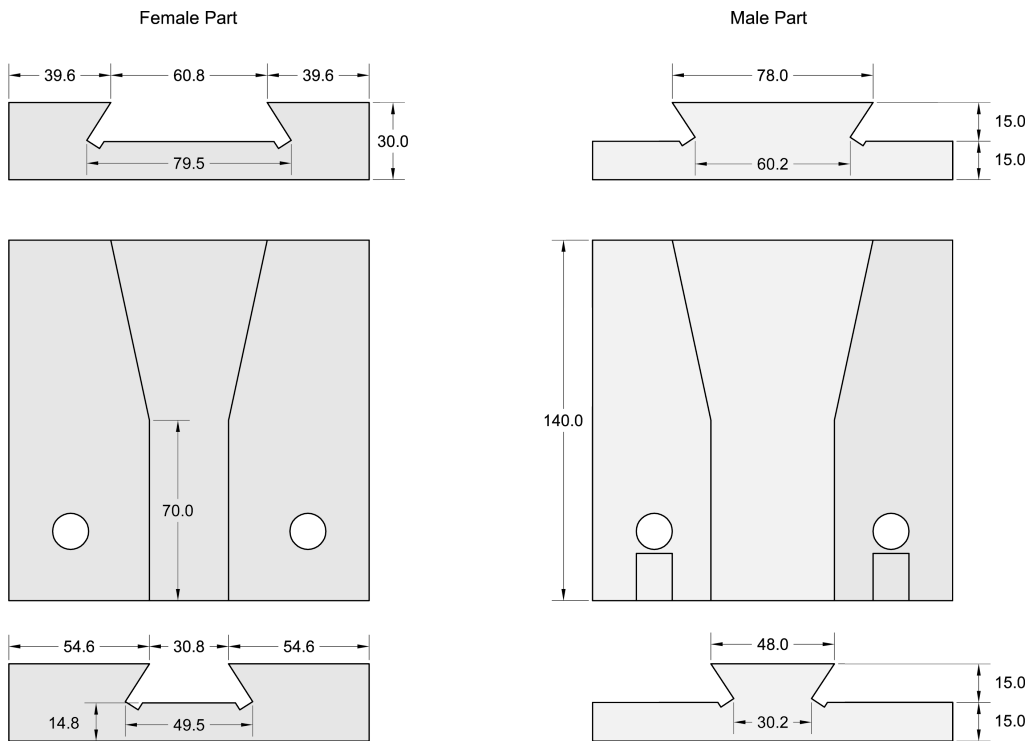
Figure 2.3: Geometry of the *Snap-Fit connection* specimen

The welds between the profiles and the connection parts are conservatively designed to avoid failure in those parts. The profile is welded to the connection along all its perimeter; the two outer welds on the flange are considered the main welds, the edges are prepared with an angle of 45 degrees to have a better penetration, the rest of the welds are smaller fillet welds.

During assembling of the two parts of the connection, the interfaces are lubricated to ensure an easy assemblage. The lubricant used here is a copper paste on a bentone base, produced by Rolith Chemicals. Additionally the position pins are removed due to their non-structural nature and to avoid any interferences or interactions between them.

The load is introduced at the tip of the cantilever by a hydraulic jack, this produces a shear force and a bending moment in the connection causing a deflection of the cantilever and a rotation on the connection.

Five measurement devices are placed to record the behaviour during the test, two sensors are located at the tip of the cantilever, a load cell under the hydraulic jack provides the applied force and an indicator gives the deflection of the cantilever tip (see Fig. 2.4). Other three sensors are placed locally at the connection, a LDTV provides the displacement between the two parts of the connection and two inclinometers at each side of the connection parts provide information about the local rotation of the each of the members (see Fig. 2.5).
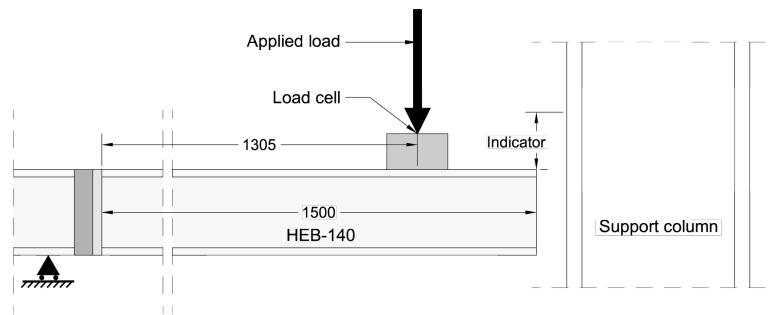
Figure 2.4: Measurements at the tip of the cantilever

(a) Upper view

(b) Side view
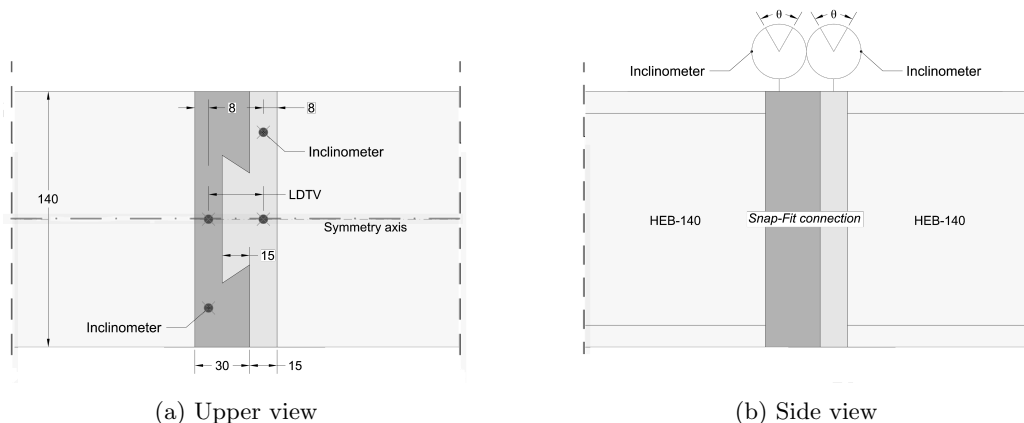
Figure 2.5: Local measurements on the *Snap-Fit connection*

The rotation of each of the members is measured locally to obtain the rotation of the connection without the contribution of the flexibility of the profiles, thus fulfilling the assumption made on the mechanical model where only the stiffness of the connection is considered.

Test results

The original data correspond to the test performed on the structural design laboratory of the Eindhoven University of Technology on the 16th of December of 2015 with the set-up described in section 2.1. The results presented here have been compiled, post-processed and resumed, this section describes those results in order to explain the behaviour of the connection during the test.

The graph in Fig. 2.6 represents the relation between the moment and the relative rotation between the two parts of the connection measured with the inclinometers.
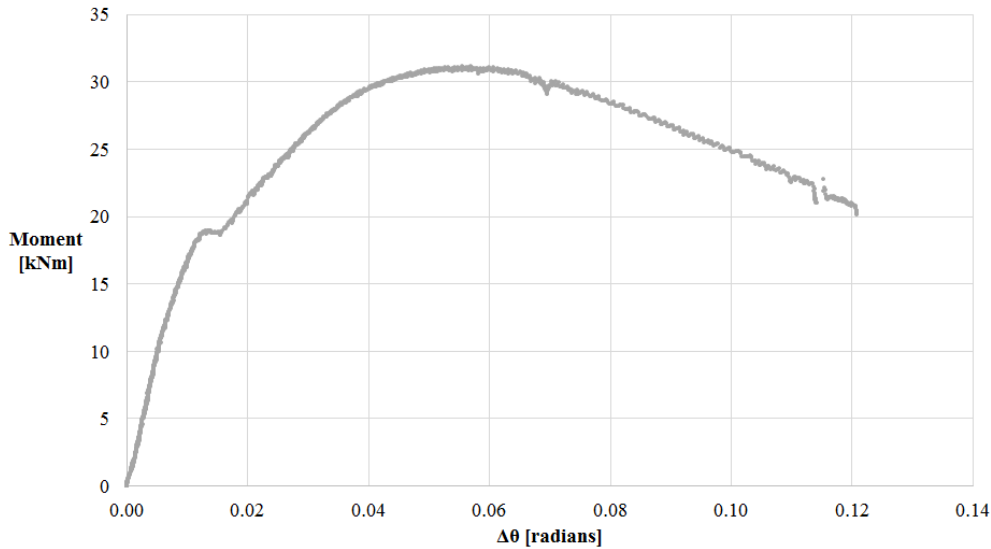
Figure 2.6: M-$\Delta\theta$ of the *Snap-Fit connection*

It can be seen from Fig. 2.7 that the behaviour of the connection it is approximately linear up to a bending moment of about 18kNm. At that load level a sudden increase of relative rotation occurs. At this point a partial uplift or slide out of the male part of the connection is observed. Thereafter the capacity of the connection increases with a significant different stiffness. After the M_{max} is reached at about 30.0kNm the rotation of the connection is increased even for lower loads.

In order to verify the measurements given by the inclinometers, the data recorded is compared with the output recorded by the indicator and the LDTV.

The indicator is located at the bottom of the tip of the cantilever, and records the vertical deflection of the cantilever beam. The data of the inclinometers is converted by means of trigonometry in order to compare the results. Fig. 2.7 shows a comparison of the $F - \delta$ at the tip of the cantilever provided by the two different sensors. Both measurements show qualitatively same results, however quantitatively some differences are observed. The first part of the graph, before the slide out of the connection occurs, is fairly similar, the slight differences on this part are attributed to the accuracy of the indicator. Thereafter a divergence of results can be seen, in this case this may be explained by the uplift of one of the parts of the connection. Thus invalidating the trigonometrical assumptions used for the data conversion.

A second verification of the data recorded by the inclinometers is done by comparing it to the LDTV measurements. This sensor measures the horizontal gap opening between the two parts of the connection. Again the data recorded by the inclinometers is converted by means of trigonometry to an effective gap opening. The center of rotation of the connection is assumed to be located at the bottom of the connection.
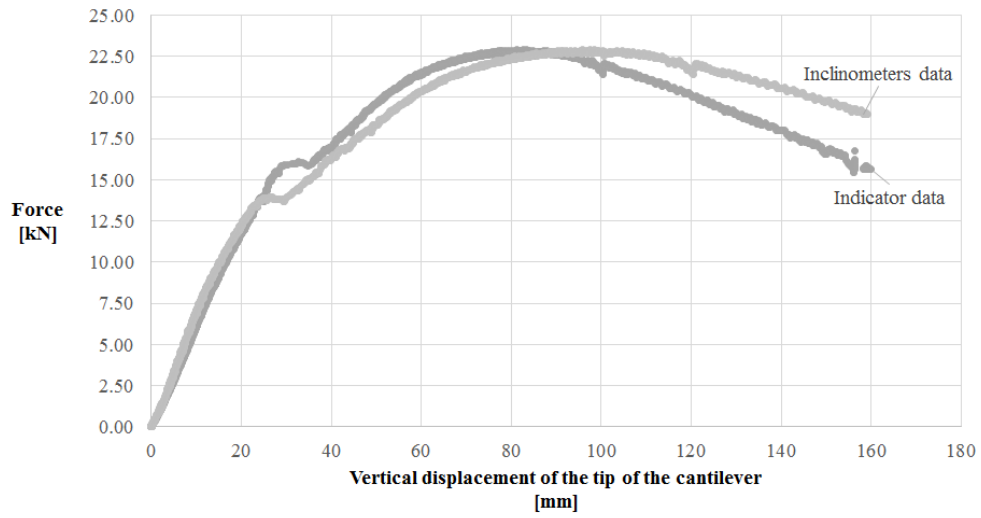
Figure 2.7: $F - \delta$ of the tip of the cantilever
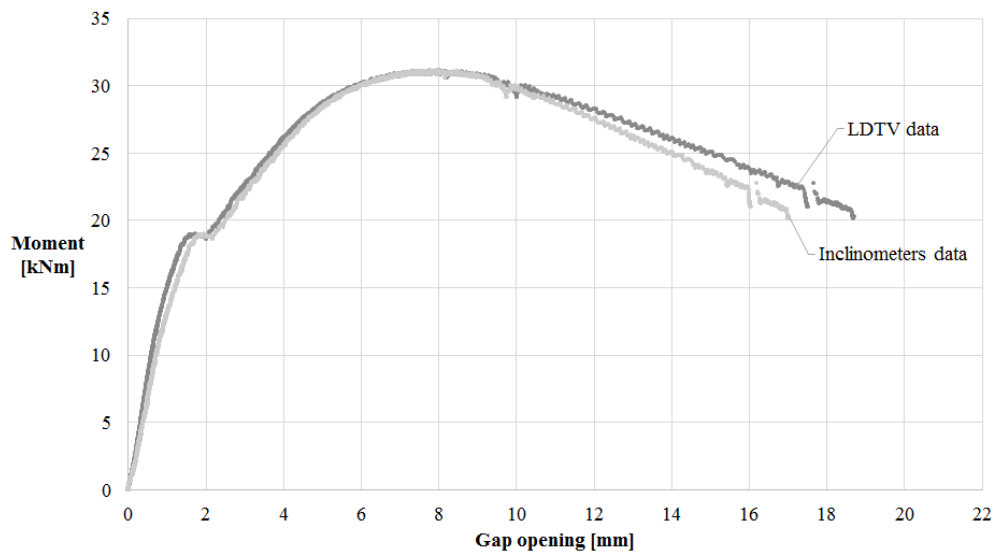
Figure 2.8: M-Gap opening of the *Snap-Fit connection*

It is shown in Fig. 2.8 that both sensors show qualitative and quantitative the same results. It is only after a gap opening of about 10mm that some diffrence is visible. This again is attributed to the disturbance due to the uplift of the connection.

No specific sensors where provided to record the amount of uplift, nevertheless graphical data taken at specific time frames has helped to show the uplift at few points.

(a) Image uplift data 1

(b) Image uplift data 2

(c) Image uplift data 3

(d) Imageuplift data 4
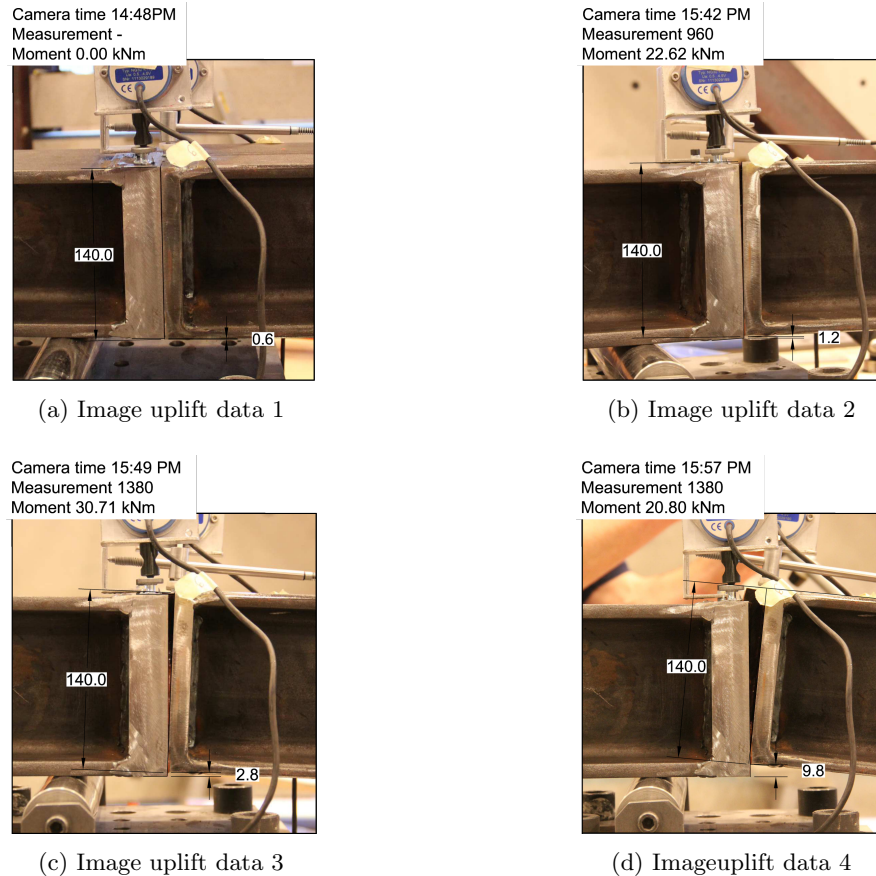
Figure 2.9: Graphic data measurements of the uplift

It may be seen from Fig. 2.9, that the difference shown between the data recorded with the LDTV and the inclinometers can be attributed to the assumption of considering the center of rotation at the bottom of the connection, which is invalidated when the uplift occurs.

The graph in Fig. 2.10 shows 4 measurements relating the bending moment with the uplift of the connection. It can be seen that due to the absence of any vertical restraint, the vertical frictional forces are not sufficiently high to prevent the male part to uplift.
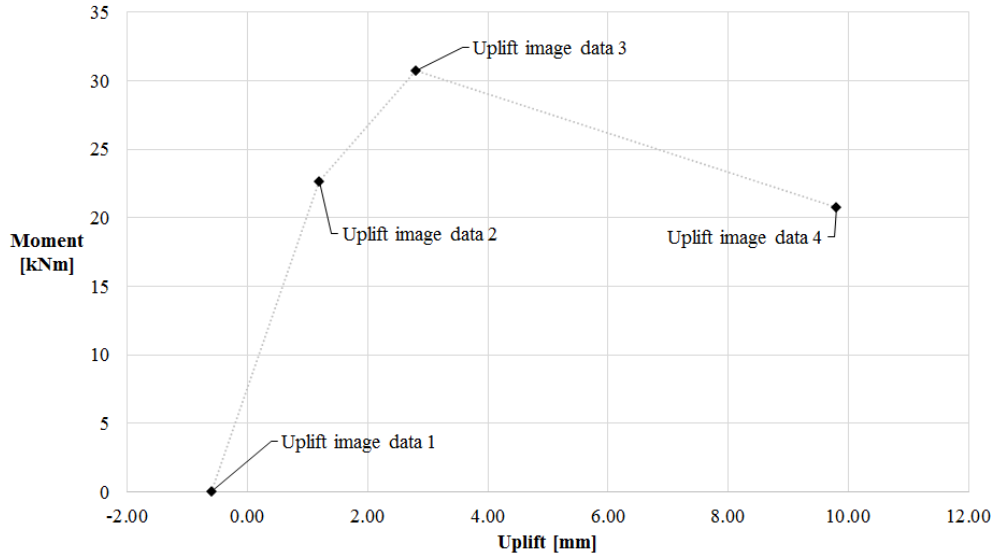
Figure 2.10: Uplift of the male part of the *Snap-Fit connection*

2.2 Cantilever test B

This test very similarly to the "Cantilever test A" on section 2.1 aims to study the behaviour of the *Snap-Fit connection*, particularly when the uplift of the connection is prevented by introducing position pins. As earlier, a cantilever test scheme is used (see Fig. 2.11), where the parameter of interest is the rotational stiffness K, representing the *Snap-Fit connection*.
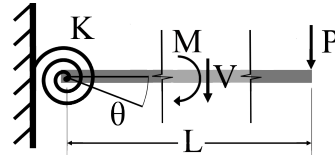
Figure 2.11: Cantilever test scheme

Test set-up

As seen on the sketch of Fig. 2.12 the cantilever structure is formed by two HEB-300 profiles. The profile on the left is supported by two rollers, the profile on the right hand side is cantilevering from the *Snap-Fit connection*. The load is introduced with a hydraulic jack at the tip of the cantilever.

Both profiles are joined to steel plates for practical reasons, the *Snap-Fit connection* is welded to each of the steel plates as shown in Fig. 2.13. The connection is welded on its perimeter on the front side and an additional perimeter weld is provided on a hole of 70x70mm on the back part of the plate to avoid premature failure of the welds.

The male part of the connection is on the left and the female part of the connection is welded to the cantilevering profile on the right hand side.
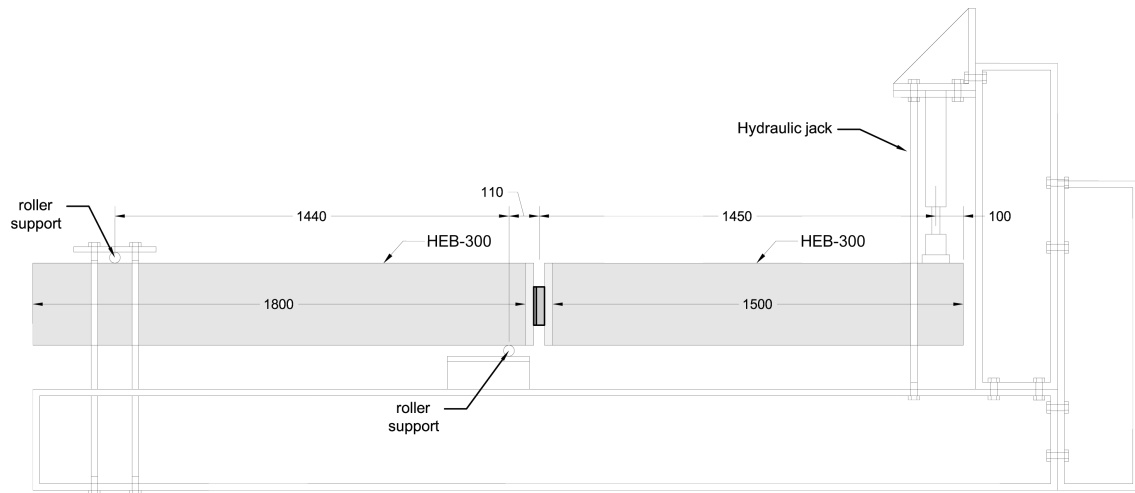
Figure 2.12: Cantilever test set-up

(a) Front view of the plate

(b) Back view of the plate
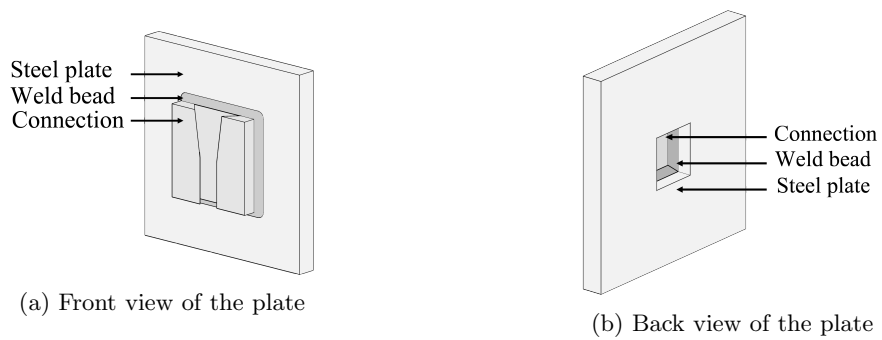
Figure 2.13: Weld connection between the *Snap-Fit connection* and the plate

It is remarkable that the profiles that form the cantilever structure and the welds connecting the members are of bigger dimensions than on the previous cantilever test. This is motivated by a modified geometry of the *Snap-Fit connection* from which a higher capacity is expected.

The *Snap-Fit connection* specimen of reference is measured with a digital caliper and Fig. 2.14 shows a sketch of its geometry.
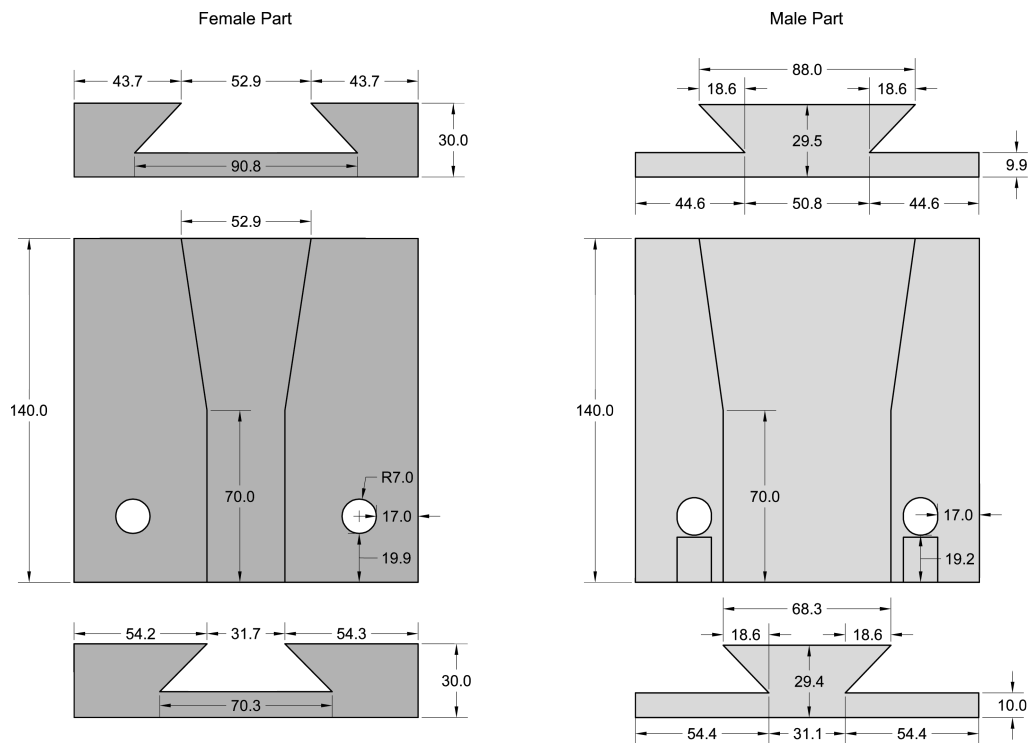
Figure 2.14: Geometry of the *Snap-Fit connection* specimen

The positions pins used during the experimental test have a diameter of 13.9mm, the pin holes on the female part have a diameter of 14.1mm, and the pin holes on the male part are slightly slotted (see Fig. 2.14). The position pins are made out of brass, a metal alloy of copper and zinc. Its specific composition is unknown.

The assemblage of the connection is done with cleaned and non lubricated surfaces. Due to the great amount of heat input introduced to the connection while welding, together with a small tolerances between the fitting parts, made that a force of 250kN was required to position together the two parts of the connection.

Five measuring devices are placed on the test to record different variables during the test. Two sensors are placed at the tip of the cantilever; a load cell below the hydraulic jack to record the load applied, and a draw wire sensor glued to the bottom of the beam to measure the vertical displacement of the cantilever (see Fig. 2.15).

The other three sensors are placed on the surroundings of the connection. Two inclinometers are placed on the welded steel plates just next to the connection, which will record the relative rotation between the plates and therefore between the parts of the *Snap-Fit conneciton*. A LDTV sensor measures the horizontal distance between the tops of the two steel plates (see Fig. 2.16).
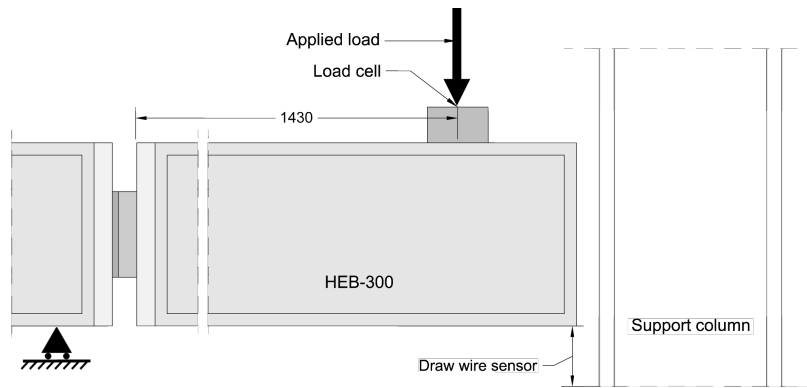
Figure 2.15: Measurements at the tip of the cantilever
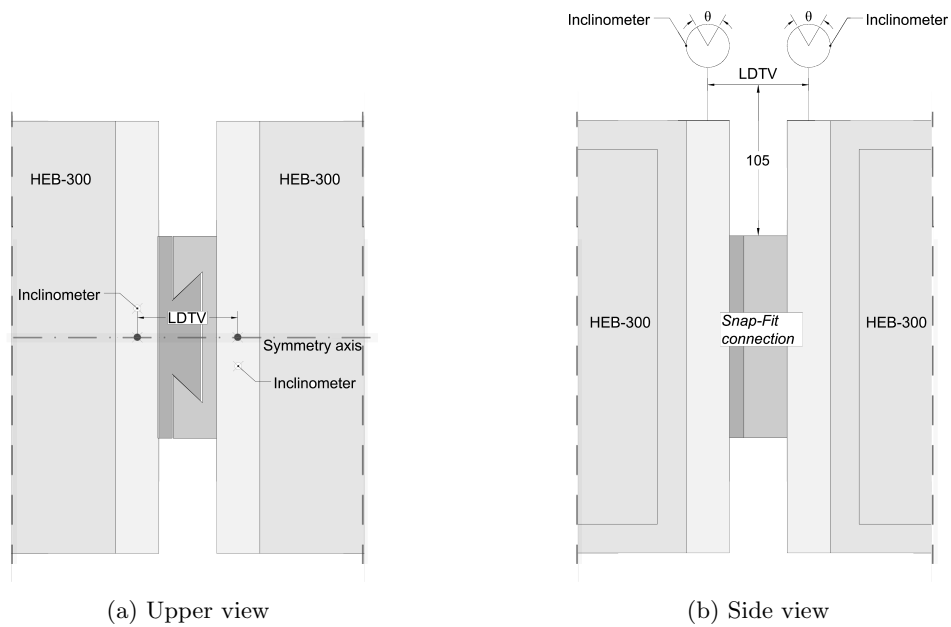
(a) Upper view

(b) Side view

Figure 2.16: Local measurements on the *Snap-Fit connection*

Test results

The original data correspond to the test performed on the structural design laboratory of the Eindhoven University of Technology on the 20th of June of 2016 with the set-up described in section 2.2. The results presented here have been compiled, post-processed and resumed, this section describes those results in order to explain the behaviour of the connection during the test.

The graph of Fig. 2.17 shows the relation between the applied moment and the relative rotation measured on the *Snap-Fit connection* with the inclinometers.
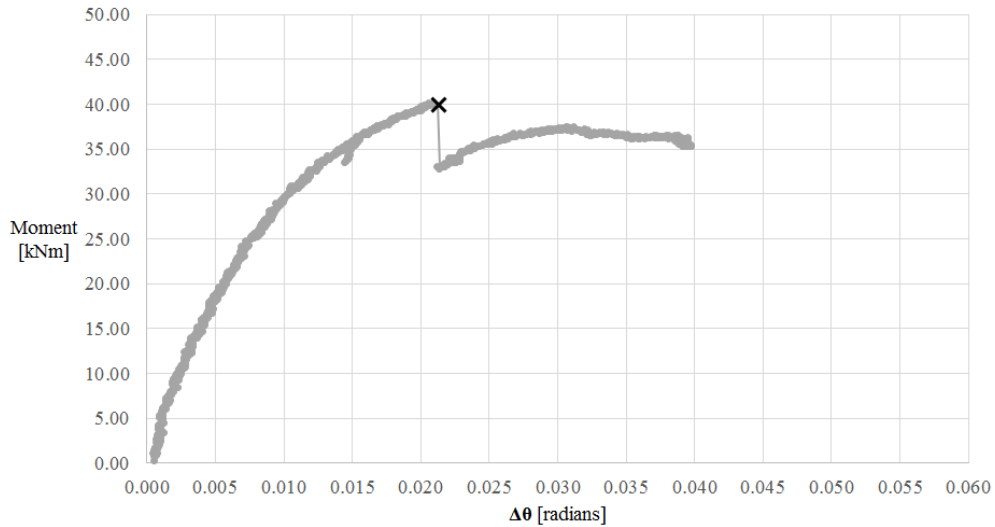
Figure 2.17: $M - \Delta\theta$ of the *Snap-Fit connection*

It is noticeable that the stiffness of the connection is nonlinear from a very early stage. The connection showed a maximum capacity of about 40kNm, where a sudden loud noise occurred. At this same stage the load capacity drops drastically. A crack is observed at one of the roots of the shoulders of the dovetail (see Fig. 2.18). Even thought the test kept running and recording the behaviour of the connection, the reliability of a fractured connection is questionable and depends on the specific mechanical properties of that part of the material and the speed of crack growth. Here for simplicity only the capacity of the connection prior to that event is considered.
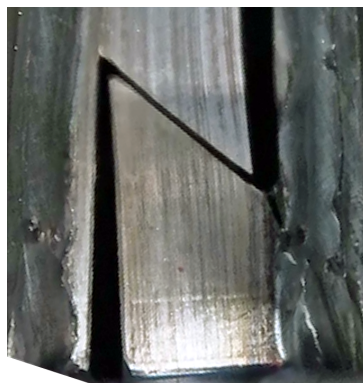
Figure 2.18: Crack at the root of the dovetail

In order to make sure that the measurements recorded by the inclinometers are correct, those measurements are compared to the data recorded by the the draw wire and LDTV sensors. The

draw wire sensor measures the vertical displacement of the tip of the cantilever; the data obtained from the inclinometers is converted by means of trigonometry to obtain the vertical displacement of the cantilever.
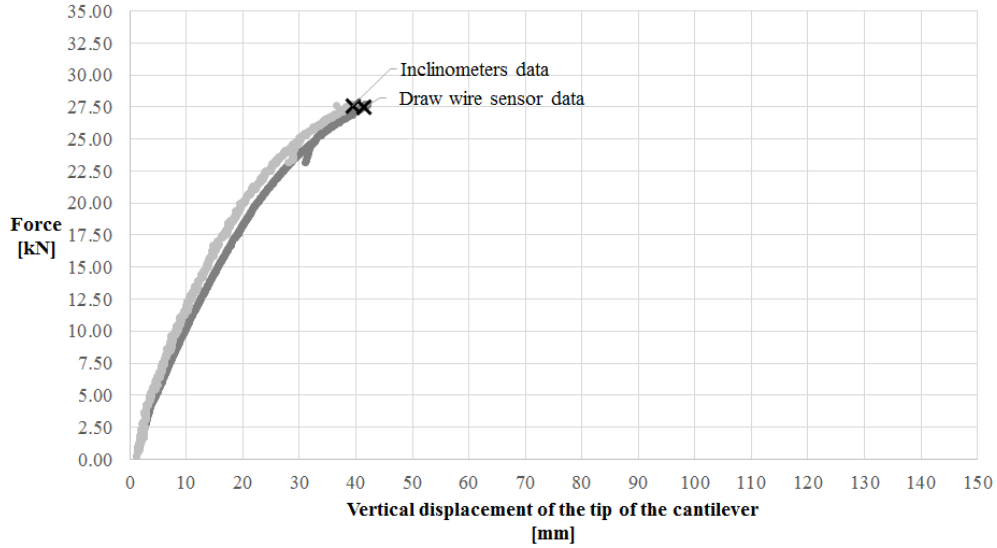
Figure 2.19: $F - \delta$ of the tip of the cantilever

Additionally also the data recorded by the LDTV are compared to the inclinometers. The relative rotation of the inclinometers are transformed to an effective gap opening at the top of the *Snap-Fit connection*, it is assumed that the center of rotation of the connection is located at the bottom of the connection. (see Fig. 2.20)
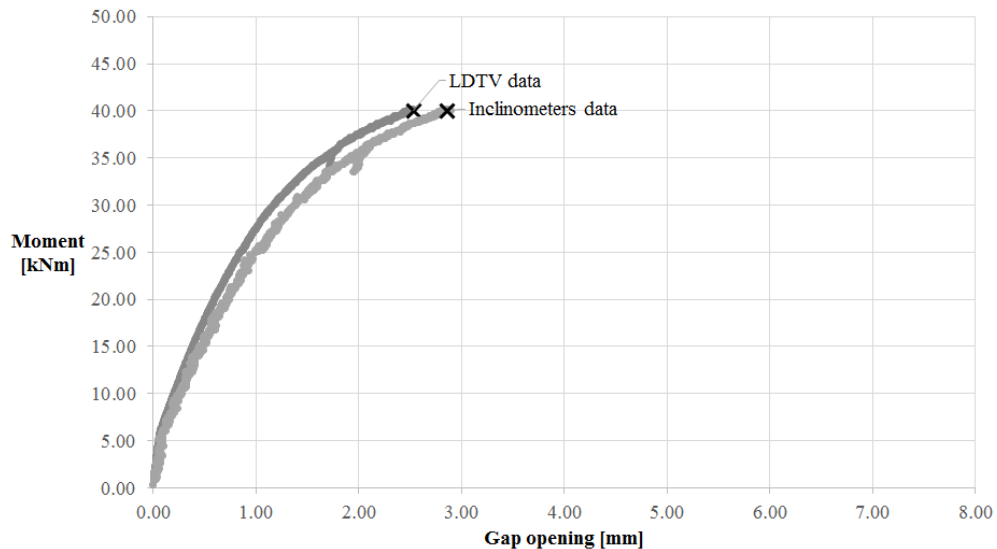
Figure 2.20: M-Gap opening of the *Snap-Fit connection*

It may be seen that both cases show agreement and consequently the recorded measurements from the inclinometers are considered valid.

2.3 Cantilever test C

This test similarly to the "Cantilever test A" on section 2.1 aims to study the behaviour of the *Snap-Fit connection*, particularly, when the design avoids or delays a fracture failure. The geometry of the *Snap-Fit connection* specimen is modified according to a study on section 4.5 to reduce the risk of fracture. As earlier, a cantilever test scheme is used (see Fig. 2.21), where the parameter of interest is the rotational stiffness K, representing the *Snap-Fit connection*.
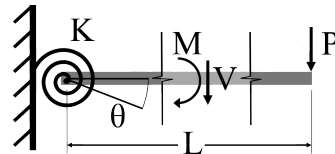
Figure 2.21: Cantilever test scheme

Test set-up

As seen on the sketch of Fig. 2.22 the cantilever structure is formed by two HEB-140 profiles (light shaded). The profile on the left is supported by two rollers, the profile on the right hand side is cantilevering from the *Snap-Fit connection* (Darked shaded). The load is introduced with a hydraulic jack at the tip of the cantilever.
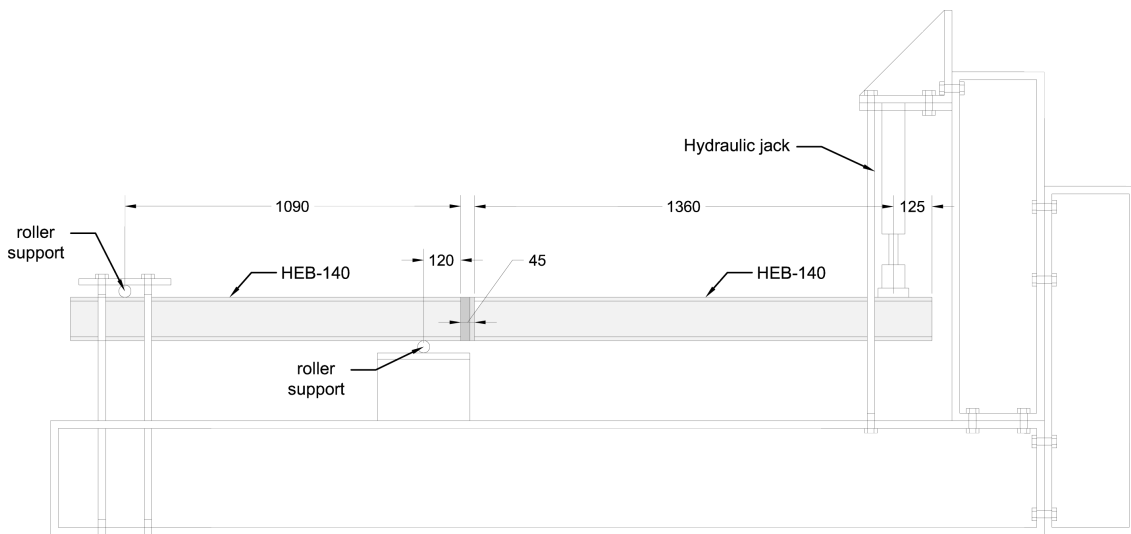
Figure 2.22: Cantilever test set-up

The beam profiles are welded to the *Snap-Fit connection* on its backplate perimeter with fillet welds, on the upper and bottom part of the flanges butt welds are provided. The welds are over-dimensioned to avoid failure on this part.

The *Snap-Fit connection* specimen of reference is measured with a digital caliper and Fig. 2.23 shows a sketch of its geometry.

The position pins used during the experimental test have a tight fit on the pin holes, no appreciable tolerance is measured. They are made out of steel, however its specific properties are unknown.

The assembly of the connection is done with cleaned and dry surfaces, the assembly is easy and no force is required to join the parts together.
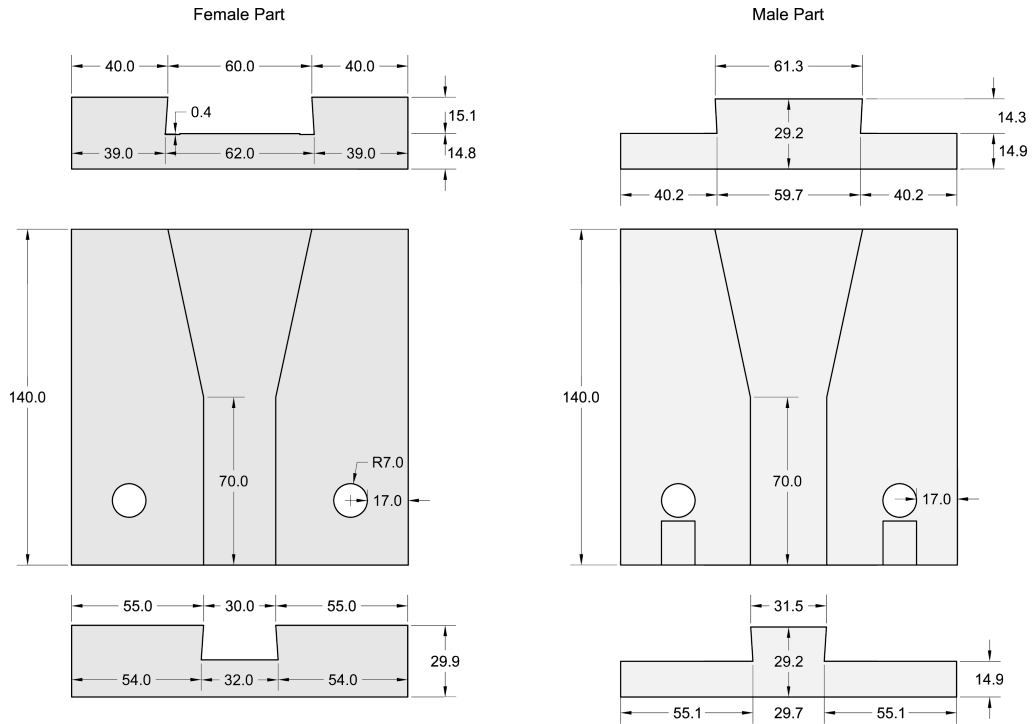
Figure 2.23: Geometry of the *Snap-Fit connection*

Five measuring devices are placed on the test to record different variables during the test. Two sensors are placed at the tip of the cantilever; a load cell below the hydraulic jack to record the load applied, and a draw wire sensor glued to the bottom of the beam to measure the vertical displacement of the cantilever (see Fig. 2.24).
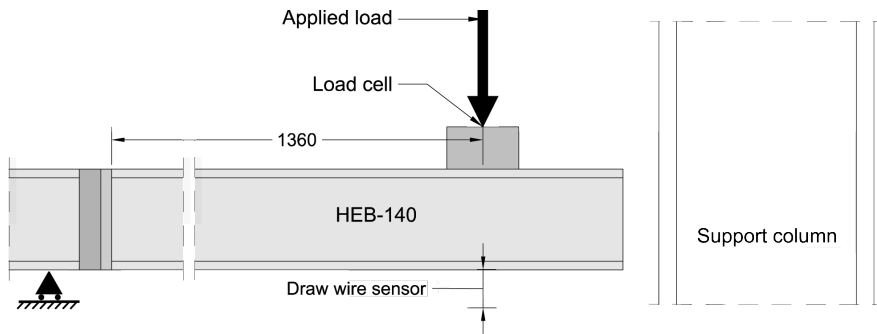
Figure 2.24: Measurements at the tip of the cantilever

The other three sensors are placed on the connection. Two inclinometers record the relative rotation between the two parts, and a LDTV sensor measures the horizontal distance between male and female when the connection rotates (see Fig. 2.25).

Test results

The original data correspond to the test performed on the structural design laboratory of the Eindhoven University of Technology on the 25th of July of 2016 with the set-up described in

(a) Upper view

(b) Side view
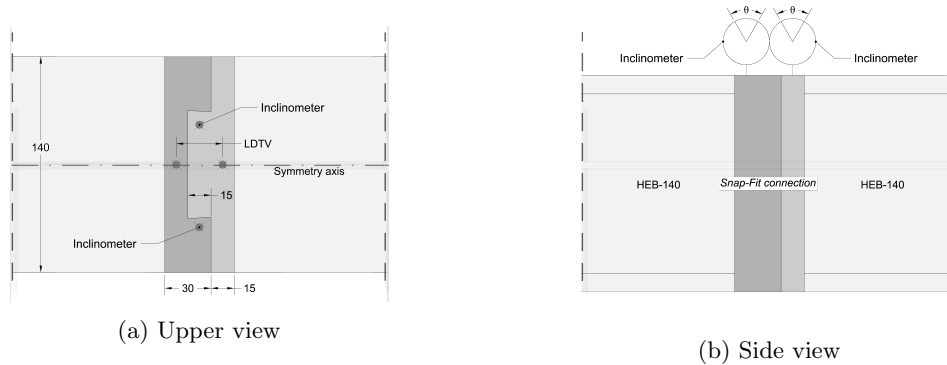
Figure 2.25: Local measurements on the *Snap-Fit connection*

section 2.3. The results presented here have been compiled, post-processed and resumed, this section describes those results in order to explain the behaviour of the connection during the test.

The graph of Fig. 2.26 shows the relation between the applied moment and the rotation measured on the *Snap-Fit connection* with the inclinometers.
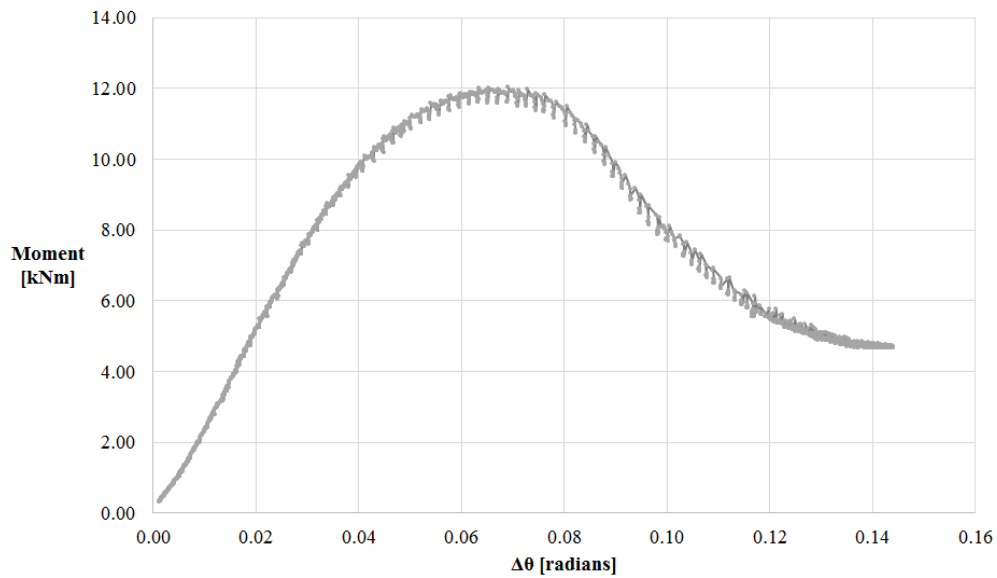
Figure 2.26: $M - \Delta\theta$ of the *Snap-Fit connection*

At first glance, it is remarkable that the connection has a lower capacity than the previous, but its behaviour is more ductile. A initial linear stiffness describes the $M - \theta$ behaviour up to a bending moment of about 10kNm. Thereafter the stiffness of the connection smoothly changes reaching a maximum bending moment of about 12kNm. From there on the rotation of the connection increases even for lower load levels. The maximum rotation measured corresponds to 0.14 radians, where the upper part of the male dovetail is out of the female dovetail, still due to the tapering of the dovetail a remaining bending capacity is shown. At this stage the experiment is stopped due to the set-up limitations.

In order to make sure that the measurements recorded by the inclinometers are correct, those measurements are compared to the data recorded by the the draw wire and LDTV sensors. The relation between the applied force and the tip displacement is used to check the data by comparing

it to the data recorded with the draw wire sensor. The draw wire sensor measures the vertical displacement of the tip of the cantilever; the data obtained from the inclinometers is converted by means of trigonometry to obtain the vertical displacement of the cantilever.
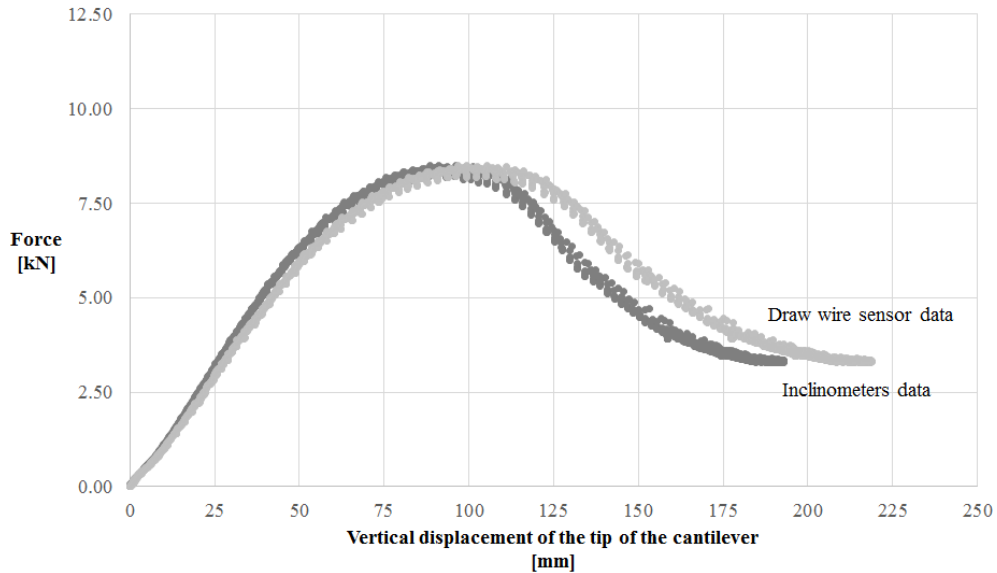
Figure 2.27: $F - \delta$ of the tip of the cantilever

Fig. 2.27 shows that both results agree up until the maximum bending capacity is reached, thereafter differences are appreciated, those differences are attributed to trigonometric assumptions that are invalidated when large rotations occur.

Additionally also the data recorded by the LDTV are compared to the inclinometers. The relative rotation of the inclinometers are transformed to an effective gap opening at the top of the *Snap-Fit connection.* (see Fig. 2.28)

From Fig. 2.28 may be seen again that the data corresponding to both sensors agree up until the maximum bending moment is reached. Again in this case the divergence of results is attributed to the same cause, and therefore it is concluded that if the inclinometers measure correctly small angles they are consequently able to record larger angles accurately too.
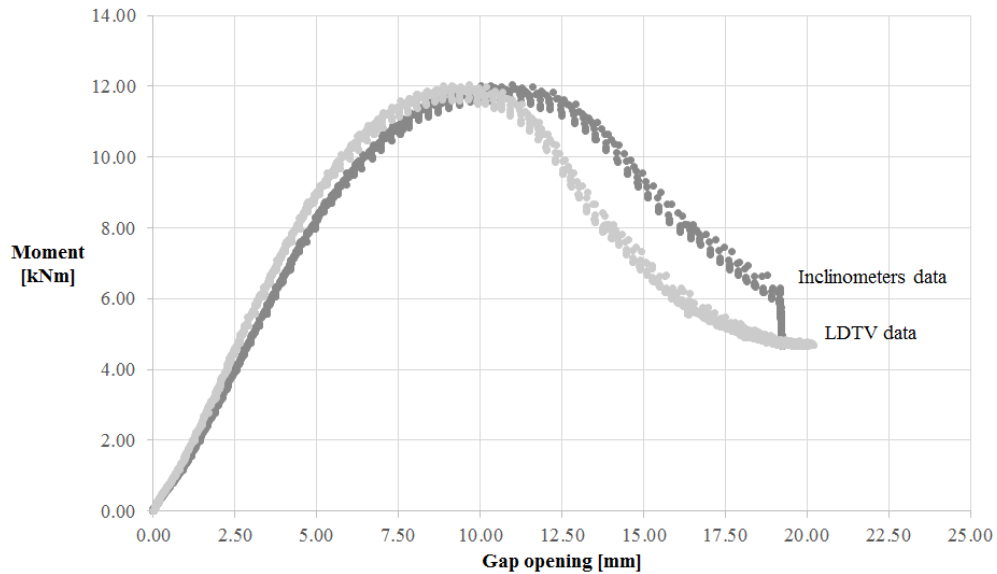
Figure 2.28: M-Gap opening of the *Snap-Fit connection*

2.4 Tensile test

This test aims to provide material related information to build the numerical model. It is a standard tensile test which is used to obtain information on the behaviour of a material piece under a uni-axial tensile force (see Fig. 2.29).

Figure 2.29: Tensile test scheme

Test set-up

The material pieces that are tested belong to the *Snap-Fit connection* which has been previously tested on the cantilever test A described in section 2.1. The specimens that are to be tested are cut from the outer edges of the connection see Fig. 2.30a, where the material is expected to have the least amount of internal stresses as a consequence of the previous test.

Four specimens are cut from the connection, each specimen belongs to one side of each part of the connection, specimens called A belong to the female part of the connection and specimens B to the male part. The pieces are shaped as a standard sheet specimens see Fig. 2.30b, the grip sections of the specimens are machined to prepare the surface for the serrated wedges of the tensile test machine.

(a) Original location of specimens

(b) Shape of the tensile specimens
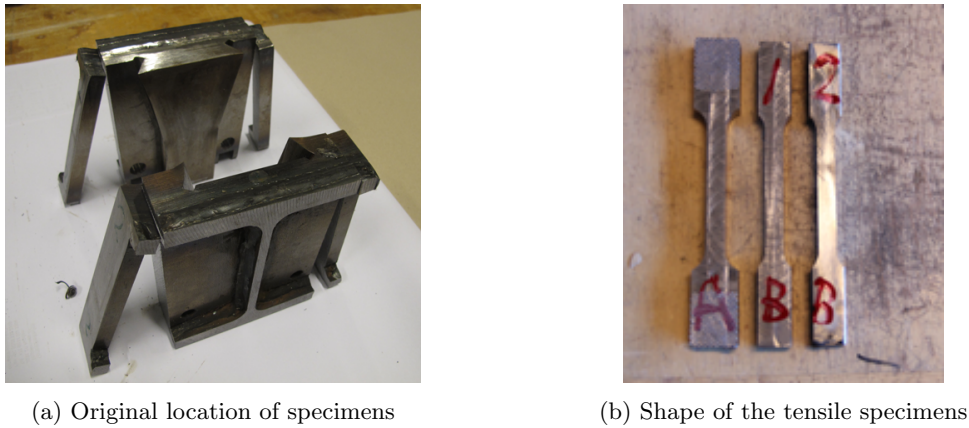
Figure 2.30: Tensile test specimens

The overall length of the specimens is 140mm which is determined by the dimension of the connection, the gauge length is in all cases 50mm, the width and thickness of the specimens has been measured at three different locations within the gauge length with a digital caliper (see Fig. 2.31).

Property	Location	Units	Specimens			
			A1	A2	B1	B2
Width	Bottom	[mm]	7.96	7.98	7.94	7.95
	Middle		7.94	7.98	7.96	7.96
	Top		7.94	7.97	7.94	7.97
Thickness	Bottom	[mm]	10.05	10.06	10.04	10.03
	Middle		10.04	10.04	10.03	10.01
	Top		10.01	10.04	10.04	10.01
Cross section	Bottom	[mm^2]	80	80.28	79.72	79.74
	Middle		79.72	80.12	79.84	79.68
	Top		79.48	80.02	79.72	79.78
	min		79.48	80.02	79.72	79.68

Figure 2.31: Dimensions of the test specimens

The equipment used is a tension testing machine (see Fig. 2.32) with two extensometers that measure the displacement while loading. The first extensometer has a maximum range of about 2mm and is the most accurate, the second extensometer can cover larger ranges of displacement however its accuracy is inferior. With the only purpose of verifying the measurements an external indicator is included, which can cover the complete range of displacement but its accuracy is lower than the two previous ones.

Test results

The original results correspond to the tests performed on the structural design laboratory of the Eindhoven University of Technology on the 4th of January of 2016 with the set-up described in section 2.2.1. This section presents compiled and post-processed data in order to describe and interpret the results.
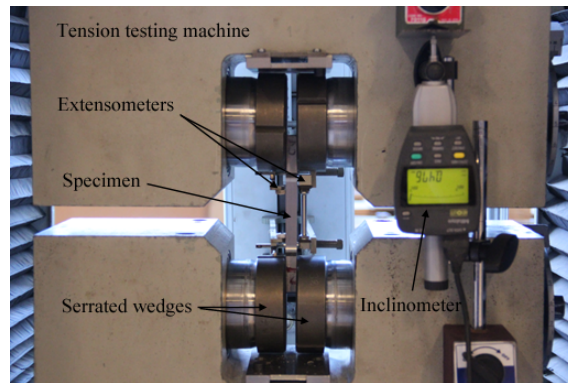
Figure 2.32: Tensile test set-up

The four specimens provide three force-displacement curves each corresponding to the three measuring devices (for the data related to the specimen A1 see Fig. 2.33), the compilation procedure consist on obtaining a representative behaviour out of those three measurements.
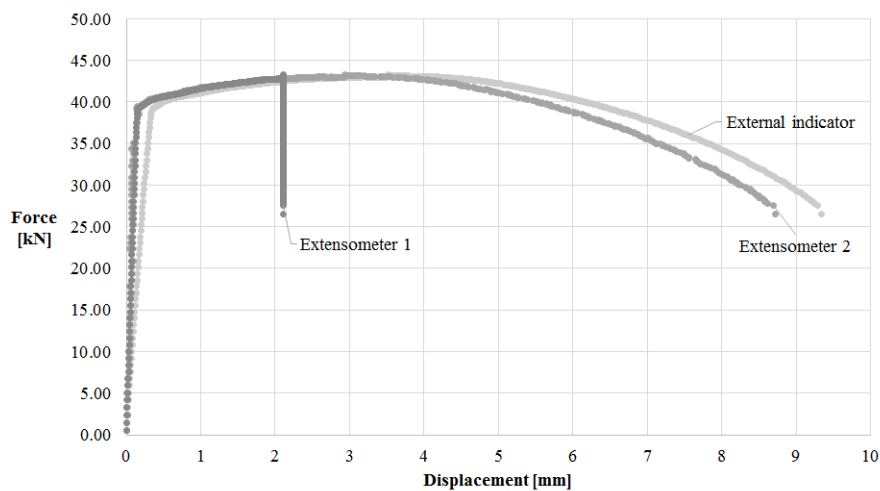
Figure 2.33: $F - \delta$ of the specimen A1

The graph in Fig. 2.33 correspond to the results of the specimen A1, it can be seen that all three measurements are consistent, some slight differences occur however they are attributed to the accuracy of each of the devices.

The extensometer 1 is considered the most accurate device, its range is limited on 2mm, as seen in the graph above, thereafter the device cannot cover the greater range of displacements. The compilation is built hierarchically corresponding with the degree of accuracy of each of the devices. The first part of the curve is built with the data provided from extensometer 1, when this device cannot provide any more information, the data from extensometer 2 continues (see Fig. 2.34). The measurements of the external indicator are not used on those compilations due to its lower accuracy, however is used as a source to verify that the data from other measurements devices is of the same order of magnitude.

In order to compare the results of the four tests the compiled force-displacement curves are generalized to a true stress- true strain curve, to do so the gauge length and the minimum of the cross sections in Table 1 for each of the specimens is used.
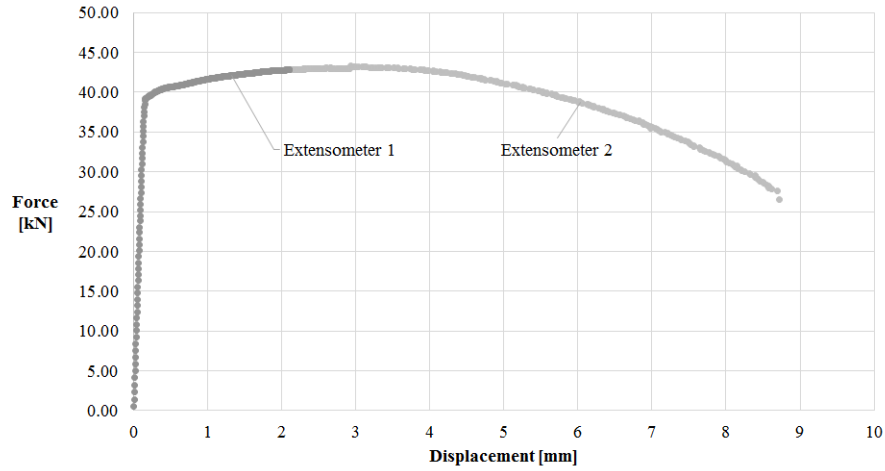
Figure 2.34: $F - \delta$ compiled results of the specimen A1

In Fig. 2.35 the four behaviours are presented, some differences appear due to either alterations at material level or differences of residual internal stresses introduced either during production or during the performance of the cantilever test.
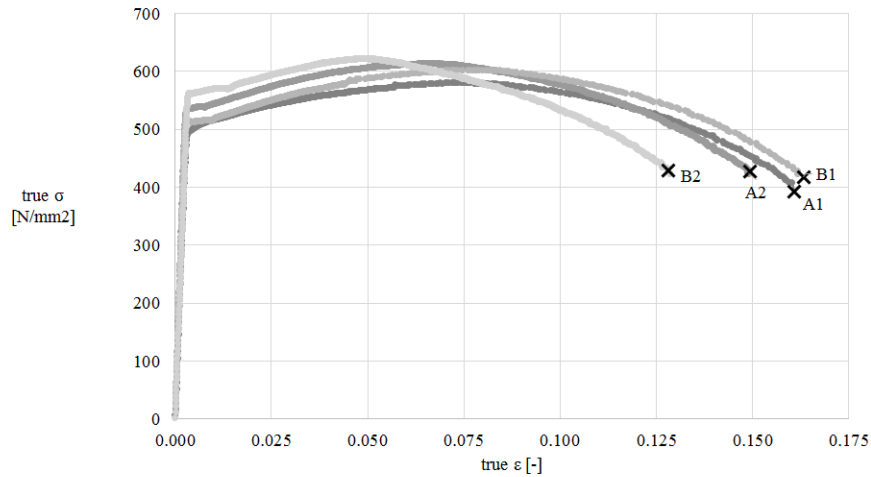
Figure 2.35: Comparison of the $\sigma_t - \epsilon_t$ of the four specimens

From the curves in Fig. 2.35 it is visible that the material used refers to a high-strength steel which has been hardened. Thus the material behaves linear elastically up to about 500MPa, where the material starts to yield, no hardening is observed and the material elongates up to a strain of about 13-15% where fracture occurs.

The elastic and plastic behaviours can be differentiated. The elastic part is considered where the material behaves in a linear fashion, the rest of the behaviour is here considered as plastic. The elastic behaviour can be described through a single value with the modulus of elasticity. In order to get a representative value, the average elastic modulus of every specimen is computed from every stress-strain data and then the arithmetic mean of the four specimens is computed, lying the elastic modulus approximately at 195000MPa and the yield stressof 500MPa (see Fig. 2.36).
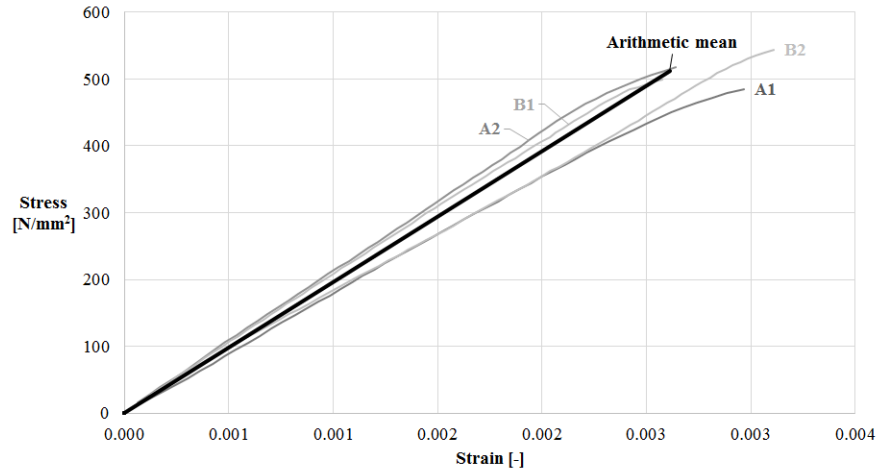
Figure 2.36: Elastic behaviour comparison of the four specimens and the mean

The plastic behaviour is captured by many points with measurement devices, it is practical to represent this behaviour with a few representative points which can be used as input on a numerical model. The least square method is used to curve fitting the four behaviours with a polynomial.(see Fig. 2.37) Then the plastic strain is discritized on a determined number of points and the related true stress is computed from the polynomials representing each of the behaviours.

$$Polynomial\ A1 : \sigma_t = -19170\epsilon_t^2 + 2656\epsilon_t + 487.54$$

$$Polynomial\ A2 : \sigma_t = -24090\epsilon_t^2 + 3033.9\epsilon_t + 515.62$$

$$Polynomial\ B1 : \sigma_t = -20276\epsilon_t^2 + 2958.2\epsilon_t + 491.24$$

$$Polynomial\ B2 : \sigma_t = -29200\epsilon_t^2 + 2829.7\epsilon_t + 545.06$$
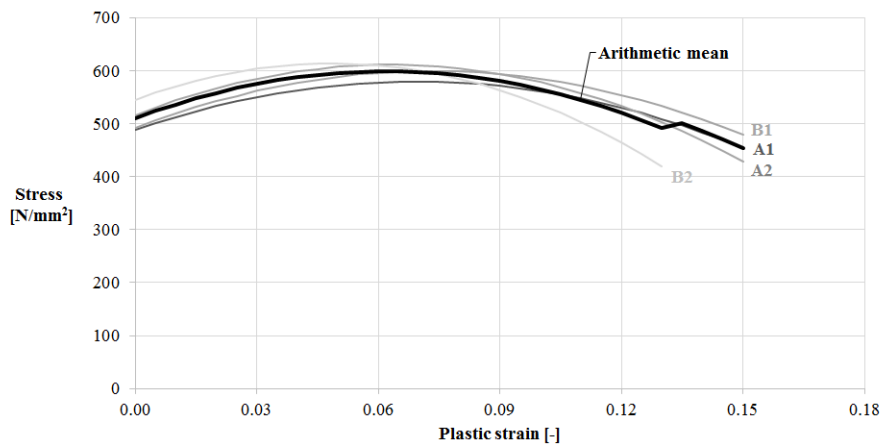
Figure 2.37: Plastic behaviour comparison of the four specimens and the mean

Chapter 3

Numerical model

Numerical methods such as finite element analysis represent a fast an efficient alternative to experimental tests in the laboratory when carrying parametric studies, however the model must be validated and verified to be reliable. In the following chapter the model built is described, the results of the numerical analysis are compared with a experimental tests to verify its behaviour and its validation is done by means of convergence studies.

3.1 Description of the model

The model used in this project is developed with a finite element software, ABAQUS v.6.14-1. It is composed of three parts, (1) female part of the connection, (2) male part of the connection and (3) a beam see Fig. 3.1. The stiffness of the adjacent members is considered infinite, as consequence the model represents only the connection (parts 1 and 2) and not the complete joint (parts 1 to 3). The beam is used to relate the applied bending moment with a shear force while the solver is displacement controlled. An imposed displacement at the tip of the beam introduces a bending moment and a shear force that are related through the length of the beam.
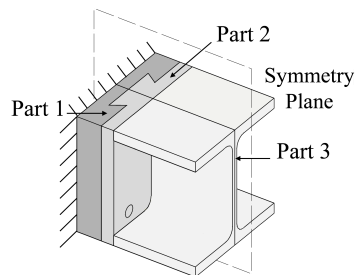
Figure 3.1: Parts of the model

Female and Male parts of the connection are modelled with 3D brick elements and 3D wedge elements for the shoulders of the connection. The dimension of the elements is as such to include the effects of the complex stress field distribution that is caused by the characteristic geometry of the connection. The element types are chosen to avoid excessive distortion of the elements in a latter parametric studies of the geometry. Brick elements fit well in the prismatic parts of the connection and the wedge elements adapt well to the wedge shape of the shoulders of the connection (see Fig. 3.2). The beam is modelled as rigid body element through a kinematic constraint.
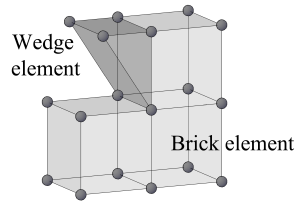
Figure 3.2: Brick and wedge elements

The connection contains one plane of symmetry, therefore only half connection is modelled thus reducing the cost of each analysis. The geometry of the model represents only half of the area and inertia of the connection, so the results of the analysis relate to half of the capacity of the complete connection, however the results included in this document are all post-processed and represent the complete connection.

The modelling of the geometry, loading and BC are described with help of the scripts that build the model.

Geometry modelling

The procedures to model the geometry of female and male part of the connection are very similar, to avoid repetition only the female tasks are briefly described. It starts creating a prism by extruding a rectangle (see line 13 of Listing 3.1). Note that the geometric relations are not built numerically but parametrically (see line 8 and 15 of Listing 3.1). This allows to geometrically control the connection trough parameters.

```
# Create female part of the connection

# sketch the gross cross section of the connection using rectangle tool
femaleProfileSketch=connectionModel \
         .ConstrainedSketch(name='Female Sketch', sheetSize=200)
femaleProfileSketch.rectangle(
           point1=(0.0,0.0),
           point2=(connection_half_width, female_thickness_total))

# Create a 3D deformable part named 'Female' by extruding the sketch
FemalePart=connectionModel.Part(
           name='Female', dimensionality=THREE_D, type=DEFORMABLE_BODY)
FemalePart.BaseSolidExtrude(
           sketch=femaleProfileSketch, depth=connection_length)
```

Script 3.1: Create female block

Once the prism is modelled the connection is formed by cutting parts out of the prism, first the straight part of the dovetail is removed and thereafter the inclined part see Fig. 3.3. The procedures to create those cuts are almost identical, therefore only the first cut (see Fig. 3.3b) is described in python language. Fig. 3.4 shows the parameters used on this part of the script.

The first cut of the prism is created through a cut extrusion (see line 54 of Listing 3.2). Before performing this task several actions need to be defined; a coordinated based on the geometry of the connection is placed on the front face of the prism (see line 12 of Listing 3.2). To orientate the sketch to be drawn on the front face, the right edge is selected (see line 20). Once the prism is orientated, the sketch is defined (see line 32). Only half of the connection is modelled, consequently the section to be cut refers to a half isosceles trapezoid, which is built with four segments (see

(a) Step 1   (b) Step 2   (c) Step 3   (d) Step 4
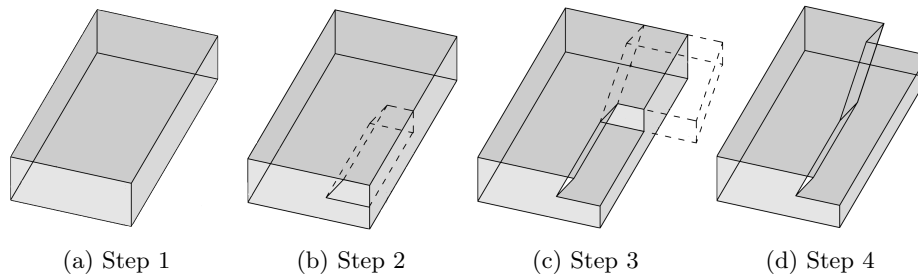
Figure 3.3: Female part modelling
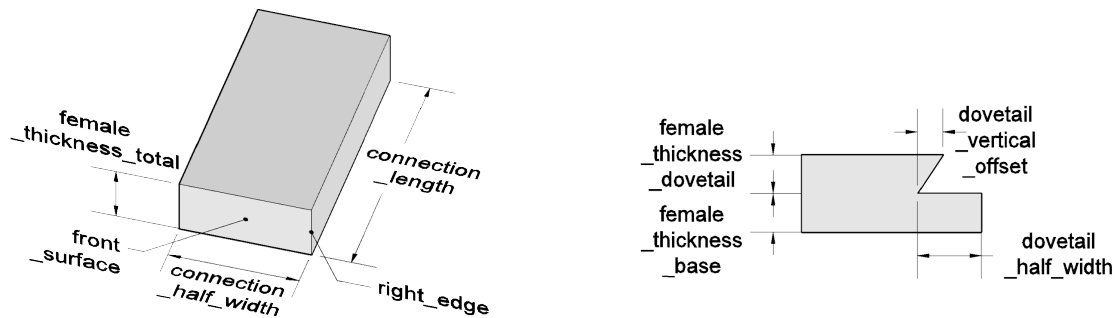
Figure 3.4: Parameters used for female modelling

lines 36,40,43 and 48). Thereafter only the depth of the cut extrusion remains to be specified to perform the cut action.

```
1   # Cut out the straight dovetail out of the female

    # The dovetail needs to be sketched onto the surface
    # In order to enter the sketcher, the surface and and axis need to be
5   # selected, they will appear vertical and right.

    # Select the front surface of the female
    sketch_dovetail_female_front_face_point=(
                    connection_half_width/2,
10                  female_thickness_total/4,
                    connection_length)
    sketch_dovetail_female_front_face=FemalePart.\
            faces.findAt(sketch_dovetail_female_front_face_point,)

15  # Select the right edge of front surface the female
    sketch_dovetail_female_right_edge_point=(
                    connection_half_width,
                    female_thickness_total/4,
                    connection_length)
20  sketch_dovetail_female_right_edge=FemalePart.\
            edges.findAt(sketch_dovetail_female_right_edge_point,)


    # The coord. from the sketch are transformed into the coord. of the part
    sketchFD1_transform=FemalePart.MakeSketchTransform(
25              sketchPlane=sketch_dovetail_female_front_face,
                sketchUpEdge=sketch_dovetail_female_right_edge,
                sketchPlaneSide=SIDE1,
                sketchOrientation=RIGHT,
                origin=(0.0,0.0,0.0))
```

```
30
    # Definition of the sketch of the straight dovetail in its own coord.
    dovetailfemaleCutoutSketch=connectionModel.ConstrainedSketch(
                    name='female dovetail cutout sketch',
                    sheetSize=200,
35                  transform=sketchFD1_transform)
    dovetailfemaleCutoutSketch.Line(point1=(connection_half_width,
                    female_thickness_base),
                    point2=(connection_half_width,
                    female_thickness_total))
40  dovetailfemaleCutoutSketch.Line(point1=(connection_half_width,
                    female_thickness_total),
                    point2=(connection_half_width-(dovetail_half_width-
                    dovetail_vertical_offset),
                    female_thickness_total))
    dovetailfemaleCutoutSketch.Line(point1=(connection_half_width-(dovetail_half_width-
        dovetail_vertical_offset),
45                  female_thickness_total),
                    point2=(connection_half_width-dovetail_half_width,
                    female_thickness_base))
    dovetailfemaleCutoutSketch.Line(point1=(connection_half_width-dovetail_half_width,
                    female_thickness_base),
50                  point2=(connection_half_width,
                    female_thickness_base))

    # Cut the dovetail out of the female part
    FemalePart.CutExtrude(depth=dovetail_straight_length,
55              flipExtrudeDirection=OFF,
                sketchPlane=sketch_dovetail_female_front_face,
                sketchPlaneSide=SIDE1,
                sketchUpEdge=sketch_dovetail_female_right_edge,
                sketchOrientation=RIGHT,
60              sketch=dovetailfemaleCutoutSketch)
```
Script 3.2: Create the straight cut in the female prism

The modelling of the beam and male part of the connection follow similar procedures, therefore no further description is included. With all three parts created, the assembly of the three parts represents the assemblage of the three individual element equations into a global system equation.

$$[\mathbf{F_i}] = [\mathbf{K_i}] \, [\mathbf{d_i}]$$

$$[\mathbf{F_{global}}] = [\mathbf{K_{global}}] \, [\mathbf{d_{global}}]$$

This procedure sets the final position and stiffness of the system. This is a systematic procedure with almost no user-interaction.

Material modelling and Interactions

The materials properties are obtained from post-processed data from the experimental "Tensile test" on section 2.4.

Contact between the parts is modelled with a contact pair algorithm with the penalty method.The pairs are explicitly defined as surfaces of the female and male part of the connection see lines 12-13 and 20-21 of Listing 3.3 and Fig. 3.5 where one of this pairs is shown for reference.

The tangent behaviour is modelled according to Coulombs' friction law, the friction coefficient is introduced as a parameter (see line 5 of Listing 3.3), to allow for a parametric study in a latter stage.

```
1   # Create contact interaction properties
    connectionModel.ContactProperty('Interaction property')
    connectionModel.interactionProperties['Interaction property'].TangentialBehavior(
```

```
5                                  formulation=PENALTY,
                                   table=((muS,),),
                                   maximumElasticSlip=FRACTION,
                                   fraction=0.005, )

     connectionModel.interactionProperties['Interaction property'].NormalBehavior(
10                                 allowSeparation=ON)

     # Definition of master and slave regions
     master_interior_region=connectionAssembly.surfaces['female interior']
     slave_interior_region=connectionAssembly.surfaces['male interior base']
15   [...]

     # Create the Interactions
     connectionModel.SurfaceToSurfaceContactExp(name='interior interaction',
                           createStepName='Apply force',
20                        master=master_interior_region,
                          slave=slave_interior_region,
                          sliding=FINITE,
                          mechanicalConstraint=PENALTY,
                          interactionProperty='Interaction property')
```

Script 3.3: Contact modelling
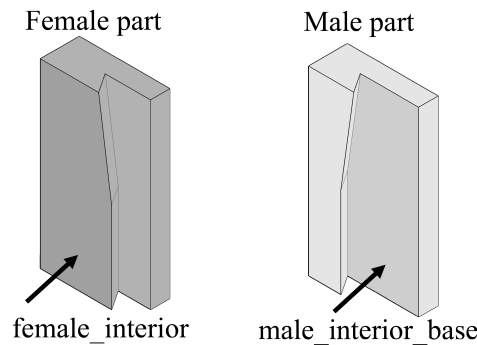
Figure 3.5: `female interior` and `male interior base` surface definition

Steps, Loadings and BC

The analysis of the connection is divided into two steps, the first pre-loads the connection with the self-weight of the beam, the second applies an imposed displacement at the tip of the beam. The introduction of a geometric tolerance gap produces a non-linearity, first a free body rotation exists and thereafter the contact between the two parts of the connection takes part. The first step applies the force corresponding to the mass of half cantilever beam (168.5N/m)(see line 11 of Listing 3.4), the load is increased with a smooth function (a 5th-order polynomial with $f'(x)$ and $f''(x)$ at the transitions being 0) to minimize the impact of the parts (see Listing 3.4), thereafter the load is kept constant to obtain a constant initial rotation (see Fig. 3.6).

```
1    # Create an amplitude for the selfweight-load
     connectionModel.SmoothStepAmplitude(name='Amp-load',
                       timeSpan=STEP,
                       data=(  (0.0,0.0),
5                            (1.0,1.0),
                             (10.0,1.0)))
     # Apply load
     connectionModel.LineLoad(name='Self-weight force',
                       createStepName='Apply force',
```

```
10              region=BeamInstance.sets['Beamset'],
                comp3=0.1685,
                amplitude='Amp-load')
```

<div align="center">Script 3.4: Create amplitude and self-weight load</div>
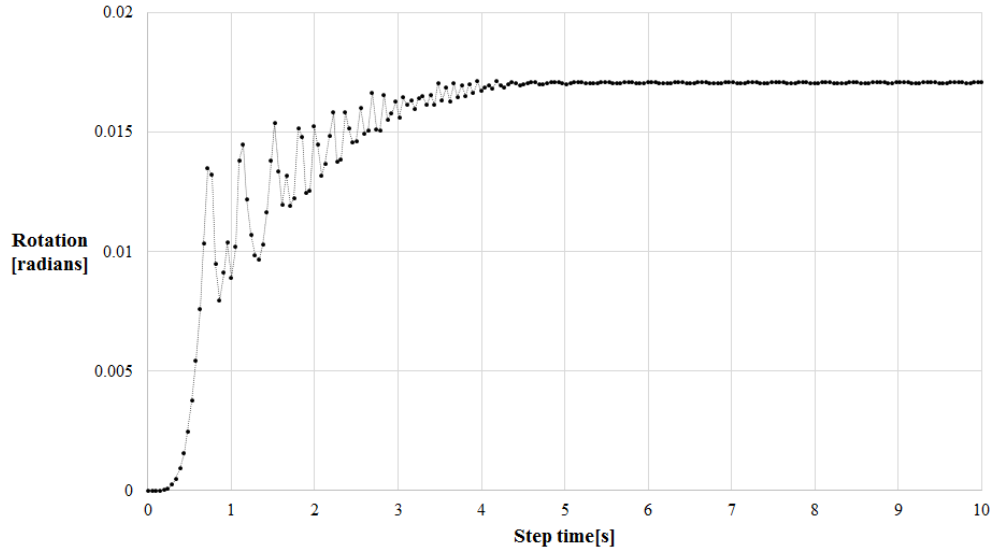
Figure 3.6: θ behaviour of the male part due to the self-weight of the beam

(a) Original state step 1   (b) Final state step 1
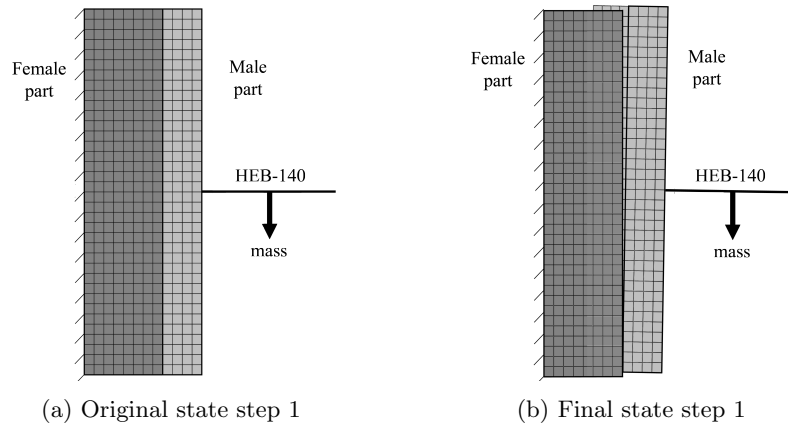
<div align="center">Figure 3.7: Practical effect of the first step</div>

The second step imports the initial state from the first step and starts with an initial rotation from the previous analysis (see Fig. 3.7).The import task between the two analysis transfers the coordinates and level of stress of the male part of the connection at the last increment of the first step into the second one (see Listing 3.5).

```
1  # Import the Initial state of the previous model
   connectionModelStatic.InitialState(
                updateReferenceConfiguration=ON,
                fileName='Snap{}'.format(templateName),
5               endStep=LAST_STEP,
                endIncrement=STEP_END,
                name='Predefined field male part',
                createStepName='Initial',
```

```
instances=(connectionModelStatic.rootAssembly.instances['Male
    Instance'],))
```
Script 3.5: Transfer of inital state between analysis

The boundary conditions applied to connection are four:

- Rigid restrain of the DOF contained within the welds

- Symmetry BC for the plane of symmetry for the Female part

- Symmetry BC for the plane of symmetry for the Male part

- Imposed displacement at the tip of the beam

The DOF contained within the welds are completely restrained. The 6 DOF of every node are either coupled or set to zero.

Symmetry BC for the planes of symmetry of the Female and Male parts restrain the DOF contained in the symmetry surface plane against displacements normal to this plane and rotations contained in the other two directions.

The loading of the system is applied by a displacement at the tip of the beam of $150\,mm$, thus forcing the solver algorithm to be displacement controlled.

Position pins

Shown the influence of the friction resistance on the behaviour of the connection, the introduction of position pins as structural element and a restraining mechanism is considered. Therefore this section studies the modelling possibilities of the position pins and its effect on the behaviour of the connection.

Modelling

This subsection studies whether the modelling of the position pins may be simplified, based on the influence of this simplification on the response of the connection. Two possibilities are considered; (1) tie nodes and (2) model of the position pins (see Fig. 3.8).

(a) Model with ties

(b) Model with position pins
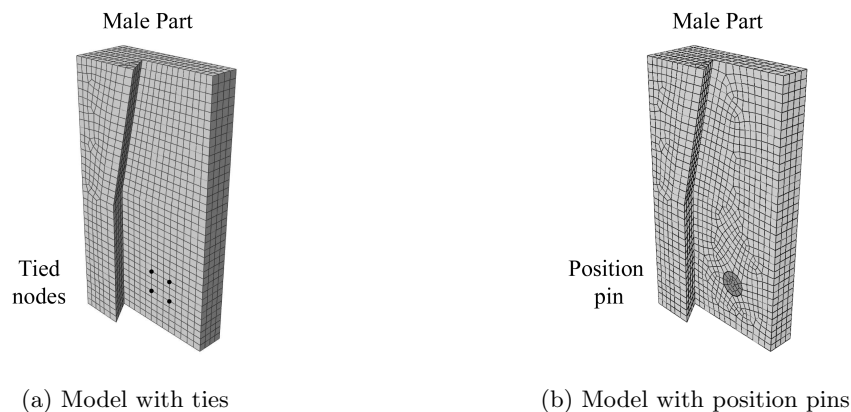
Figure 3.8: Restrain modelling options

The model with ties simplifies the computational model and the position pins are simply substituted by a kinematic coupling, four nodes of both female and male part at the height of the physical position pins are tied together.

The model with position pins, contains two extra features. (1) The male part has a pin hole of a radius of $7.00\,mm$, and (2) an extra 3D part representing the position pin is created. The position pin itself has a radius of $6.80\,mm$ thus providing a tolerance of $0.20\,mm$ between shaft of the pin and the pin hole. The position pin is modelled as cantilever from the female interface, the material properties are those of the connection and the contact interaction between the pin and the pin hole are the same as the ones between the interfaces of the connection parts.

Results of the simulations

The graph in Fig. 3.9 shows a comparison of the two simulations of the *Snap-Fit connection* with a friction coefficient equal to $\mu = 0.07$. The dark gray curve represents the model with ties. The simulation displayed in dotted light gray regards to the model built with position pins.
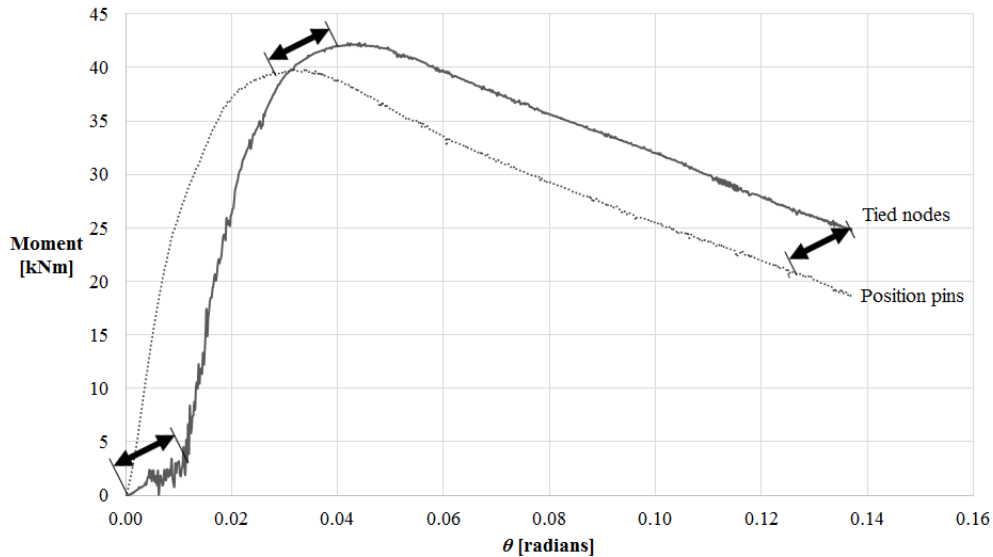
Figure 3.9: Comparison of modelling the restrain with ties or pins

Discussion of the results

It can be seen that the global behaviour of the connection is equivalent. However the model with ties shows a shift that alters the maximum bending capacity of the connection. This shift can be attributed to the instantaneous resistance that the interaction with ties produces. When applying the self-weight of the beam the male part of the connection does not rotate but is restrained by the ties, its when the ties have yield to a large extent that the connection develops its resistance.

Seen that the global performance of the connection is affected by the modelling procedure, the simplified approach is disregarded and the model including the position pins is taken for further study.

3.2 Validation model A

The validation process aims to ensure that the behaviour of the computational model is reliable and its behaviour represents the connection of study. This validation corresponds to the *Snap-Fit connection* with a configuration representing the "Cantilever test A".

The sample of the connection is measured with help of a digital caliper. The parameters that build the numerical model are adapted to represent the geometry of the physical specimen (see Fig. 3.10).

Female Part-bottom section   Male Part-bottom section
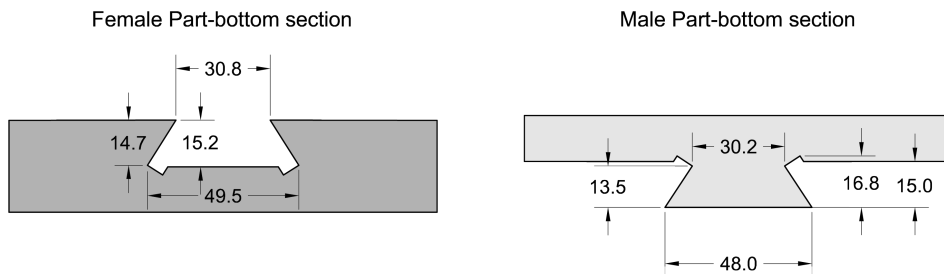
Figure 3.10: Tested *Snap-Fit connection*

Physical prototype   Model V20-H200
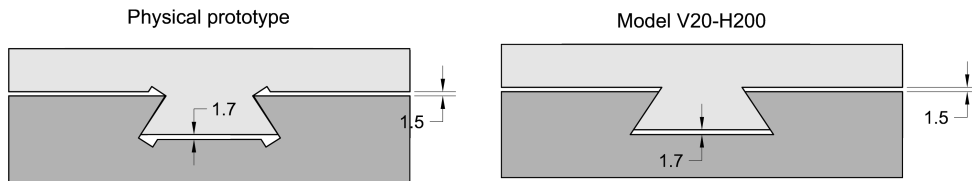
Figure 3.11: Numerical model tolerances simplification

The friction coefficient is considered a uncertain parameter dependent on the boundary lubrication. The lubricant used is a Copper paste with a bentone base from Rolith Chemicals. They do not provide friction information about its product, however Molykote has several pastes of similar characteristics which have been tested showing friction coefficients between 0.07 and 0.13 [7], thus reducing the range of uncertainty.

To confirm that the numerical model and the experimental test represent the same physical behaviour two checks are performed, the $M-\theta$ behaviour and the uplift of the connection are compared with the data collected from the experimental test. As the friction coefficient is considered uncertain, a series of simulations are analysed within the range of uncertainty range and are compared with the data of the experimental test.

Results of the simulations

The first graph in Fig. 3.12 displays in different shades of gray the results of 7 simulations of Model A with friction coefficients varying from 0.07 to 0.13. In black are displayed the results collected during the "Cantilever test A".

The second graph shows the relation between the uplift of the connection and the applied bending moment. The results of the simulations and the data of the experimental test are compared. The

---
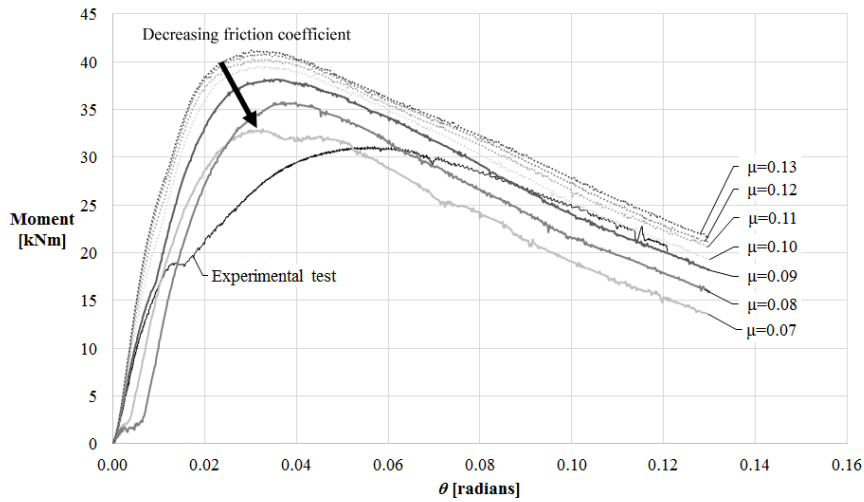
Figure 3.12: $M - \theta$ behaviour comparison

experimental data is displayed as black rhombus. The results from the simulations are displayed in different shades of gray.
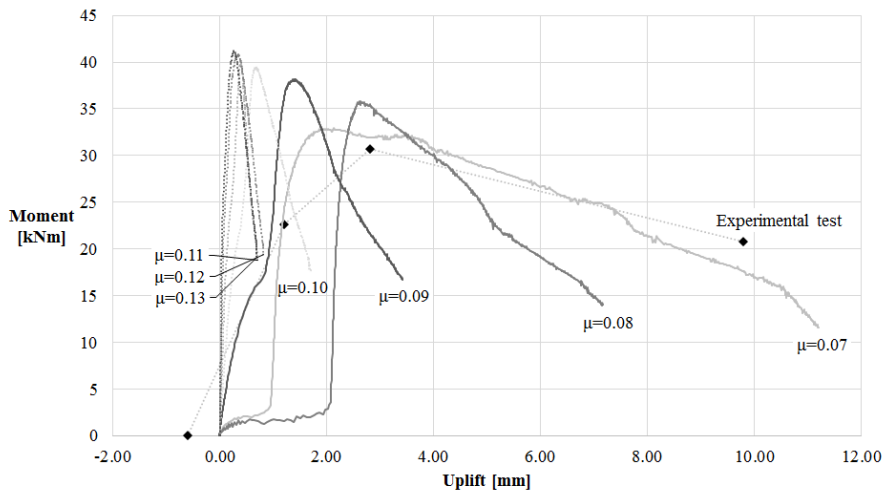
Figure 3.13: $M - uplift$ comparison

Discussion of the results

It can be seen from Fig. 3.12 that none of the simulations matches the experimental data accurately. It may be visible that the simulation with a $\mu = 0.09$ initially matches the linear $M - \theta$ behaviour as well as the uplift shown in Fig. 3.13. After the partial slide out of the male part of the connection, the stiffness of the connection according to the experimental data has a significant change that none of the simulations represent. However it is worth to note that the uplift and maximum bending capacity of the experimental test are equivalent to those shown by the simulation with a $\mu = 0.07$.

Despite those similarities, it cannot be said that the model is validated, the behaviours exhibited by the experimental test and the numerical model have considerable differences, which are attributed to the non-ideal conditions found on the experimental test in contrast with the ideal conditions of the numerical model.

As it is shown on Fig. 3.12 the behaviour is highly dependent on the frictional forces, thus a local imperfection between the boundary surface affects the local friction and consequently the complete behaviour of the connection.

3.3 Validation model B

This subsection similarly to the section 3.2 aims to validate the numerical model, it differs from the previous section on the test of reference. This validation corresponds to the *Snap-Fit connection* with a configuration representing the "Cantilever test B". The numerical model used is based on the model described in section 3.1, the modifications that have been performed to adapt the model to this particular case are the followings:

- Beam profile
  The cantilever structure used for this test is formed by profiles of bigger dimensions (HEB-300 with a lever arm of 1450mm), in correspondence with this fact the loading is changed. The cantilever beam which is modelled as rigid body elements has a line load of 0.585kN/m along its length to represent its own mass, and the length of the beam is modified to represent the proper M-V relation.

- BC
  As described on section 2.2 the *Snap-Fit connection* is first welded to steel plates and those are connected to the beams. As consequence, the welds on the *Snap-Fit connection* are not on its back plate but the weld bead runs on its perimeter (see Fig. 2.13). Therefore the BC representing those changes are modified accordingly (see Fig. 3.14).
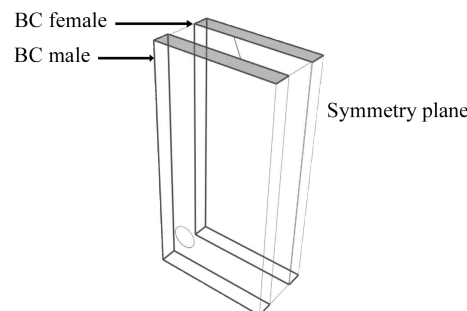
Figure 3.14: BC of the model representing the weld area

- Friction Coefficient
  In this case the surfaces in contact are clean and free of any lubricant, consequently a kinetic friction coefficient of 0.42 is taken according to [6].

  Due to the deformations experienced during the welding procedure a force of 250kN has been required to assemble together the parts of the connection. This introduces uncertainty on the state and properties of the contact boundaries between the parts.

- Geometry of the *Snap-Fit connection*
  The *Snap-Fit connection* sample used on the "Cantilever test B" is measured with help of a digital caliper. The model is parametrically adapted to to represent the physical connection (see Fig. 3.15).
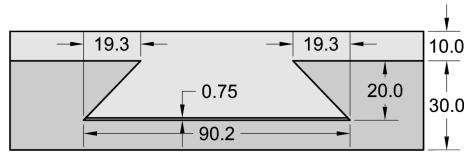
Figure 3.15: Top view of the geometry of the numerical model

- Material model for the position pins
  The position pins were initially design with a steel material and therefore on the original model description they have assigned steel properties. Thereafter the position pins to be used during the "Cantilever test B" are made out of brass, a metal alloy of copper and zinc. Its material properties are taken from literature (see Fig. 3.16). According to the Copper Development Association the production of pins is typically made out of one of those three alloys. For sake of completeness the numerical model uses the properties of the CuZn33 Alloy.

Alloy	Density [Kg/m3]	Elastic modulus [Mpa]	Stress 0.2% [Mpa]	Tensile strength [Mpa]	Strain [%]
CuZn30	8550	99000-117000	30*	40	35
CuZn33	8500	97000-114000	32*	41	32
CuZn37	8450	97000-111000	32*	41	28

Figure 3.16: Brass material and mechanical properties [3],[4],[5]

Results of the simulations

The graph in Fig. 3.17 shows a comparison of the $M-\theta$ relation between the experimental test data from "Cantilever test B" and the numerical model. Fracture or risk of fracture on the simulation is displayed with black cross when the principal maximum plastic strain reaches the value of 13%.
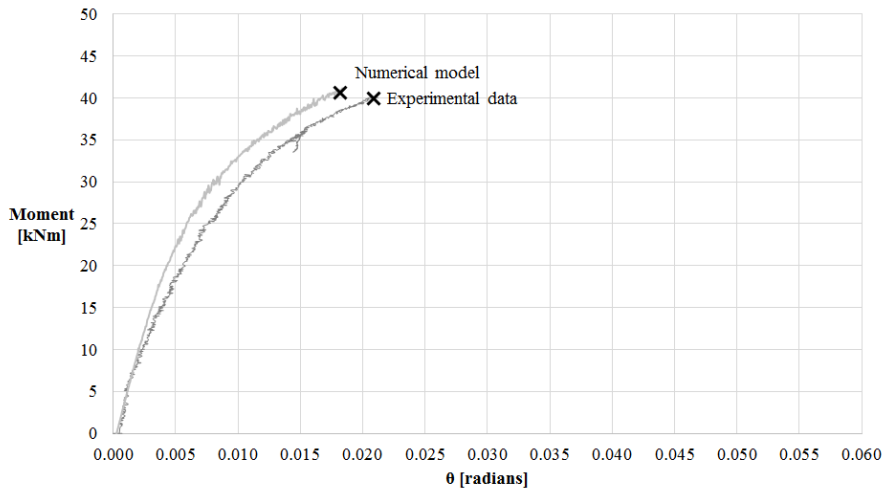
Figure 3.17: $M - \theta$ behaviour comparison

Fig. 3.18 shows the strain and stress fields of the top part of the connection at the load level where risk of fracture is detected.

PE, Max. Principal
(Avg: 0%)

0.125
0.100
0.075
0.050
0.025
0.000

(a) Plastic strain

(b) Tensile σ field
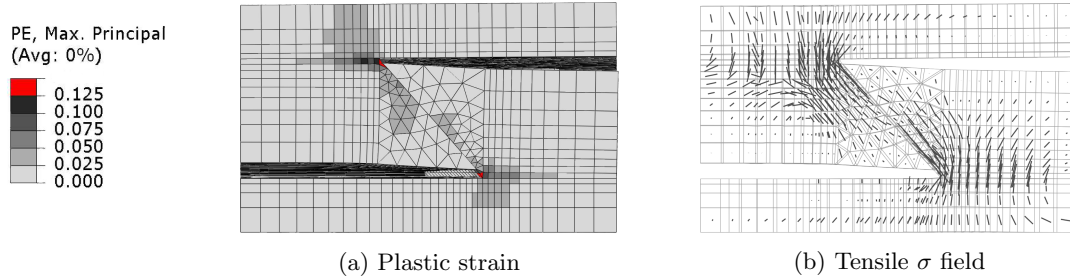
Figure 3.18: ϵ and σ fields at the top of the connection

Discussion of the results

It may be seen from Fig. 3.17 that the numerical model and the experimental data agree qualitatively and quantitatively, thus only slight stiffness differences are appreciated.

Slight differences on the stiffness of the connection are visible after the $M - \theta$ behaviour becomes non-linear. Those differences are attributed to imperfections introduced on the experimental test, for instance, deformations or softening due the welding procedure.

3.4 Validation model C

This subsection similarly to the section 3.2 aims to validate the numerical model, in this case the validation of the model corresponds to the *Snap-Fit connection* with a configuration representing the "Cantilever test C". The numerical model used is based on the model described in section 3.1, the modifications that are performed to adapt the model to this particular case are the followings:

- Element type
  On the original model the shoulders of the dovetail are built with *WEDGE* elements due to its geometrical similarity. In this case, due to the large inclination of the dovetail, those elements would be significantly distorted, therefore *BRICK* elements are used to model this part.

- Friction Coefficient
  In this case the surfaces in contact are clean and free of any lubricant, a kinetic friction coefficient of 0.42 is taken according to [6].

- Geometry of the *Snap-Fit connection*
  The physical sample used during the "Cantilever test C" is measured with help of a digital caliper, the parameters that build the numerical model are adapted to represent the connection (see Fig. 3.19)

- Lever arm
  The lever arm of "Cantilever test C" is $55\,mm$ larger than the original length of "Cantilever test A" (see Fig. 2.4 and Fig. 2.24). the model is adapted accordingly to represent the current M-V relationship.

The behaviour of this design it is expected to be very sensitive to frictional forces. Despite the efforts to measure accurately the geometry and tolerances of the connection, the dimensions are to
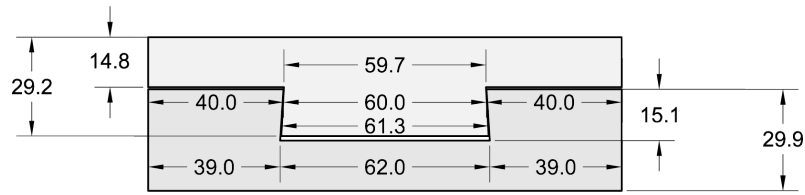
Figure 3.19: Top view of the geometry of the numerical model

some extent considered uncertain, due to the accuracy limitations and the human error introduced by measuring such a geometry.

In order to confirm that the experimental test and simulations represent the same behaviour, some simulations exploring those boundaries are performed.

Results of the simulations

The graph in Fig. 3.20 shows a comparison of the $M-\theta$ relation of three simulations with different geometries representing the degree of uncertainty of one of the measurements of the connection, namely; the width of the male dovetail at the top, which takes values of $[61.2, 61.3$ and $61.4\,mm]$. For comparison the behaviour of the experimental test is included.
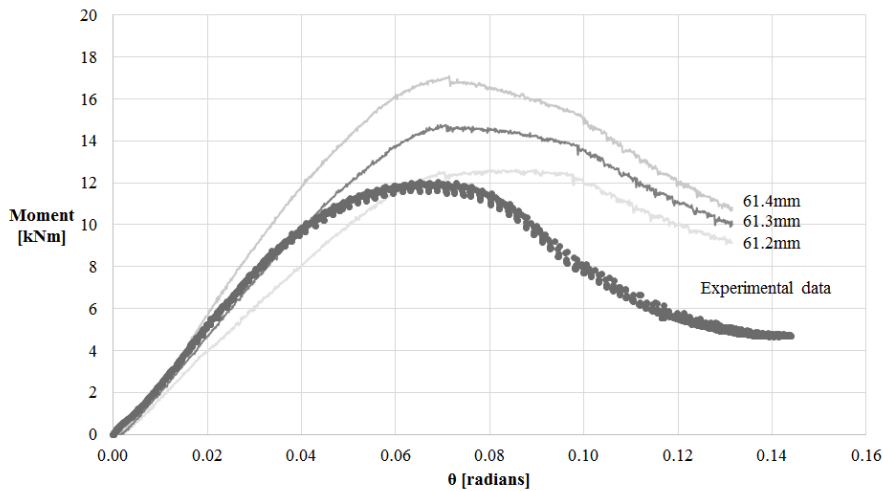
Figure 3.20: $M-\theta$ behaviour comparison

Discussion of the results

It can be seen from Fig. 3.20, that none of the three simulations agrees with the $M-\theta$ behaviour shown by the experimental test. This difference is attributed to the difficulties of accurately modelling a connection which behaviour is very sensitive to friction forces and therefore to tolerances or imperfections. It is shown for one of the taken measurements that the rounding up, has significant effects on the overall behaviour, thus confirming the sensitivity of the connection.

The simulations show behaviours qualitatively comparable to that shown by the experiment, however the model is not validated, thus is not able to predict accurately the maximum capacity or stiffness of the connection.

It is true that non of the simulations show risk of fracture, thus the rotation of the shoulders of the dovetail is very small due to the large inclination of the dovetails. However its use in practice should be avoided, thus the sensitivity of the connection to tolerances may lead to unexpected results.

3.5 Verification

The verification process aims to ensure that the error due to the mathematical approximation of the solution is sufficiently small.

This section studies the influence of the size of the mesh by means of convergence studies. It contains the verification of four models, (1) Model A: a numerical model with a configuration representing "Cantilever test A", (2) Model A-II: a numerical model with the same configuration as the previous but with the introduction of position pins, (3) Model B: a numerical model with a configuration representing "Cantilever test B" and (4) Model C: a numerical model with a configuration representing "Cantilever test C". After those convergence studies the detection of risk of fracture is analysed.

Model A

The geometry of the model represents the *Snap-Fit connection* of "Cantilever test A". The convergence study contains five simulations, they have different mesh densities with average mesh sizes of $[15, 7, 4, 2,$ and $1\,mm]$ (see Fig. 3.21) The simulation with an average mesh size of $1\,mm$ is refined only at the shoulders of the connection where the plastic resistance is developed.

(a) Mesh 15mm   (b) Mesh 7mm   (c) Mesh 4mm

(d) Mesh 2mm   (e) Mesh 1mm
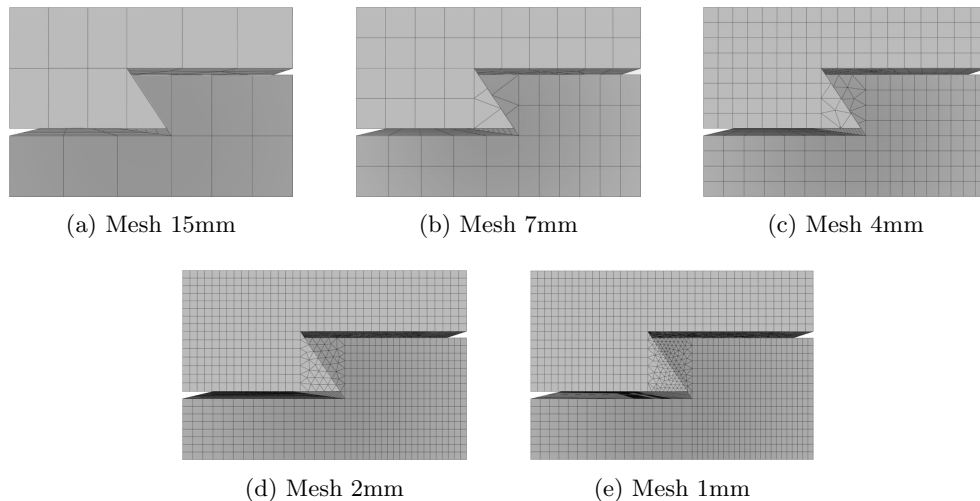
Figure 3.21: Mesh refinement of the convergence study

Results of the simulations

The results of the simulations are presented in Fig. 3.25, where the $M - \theta$ behaviours of the simulations are compared.

In Fig. 3.26 two graphs show a comparison of the M_{max} of the simulations, the graph on the left hand side compares the magnitudes of the resistances of the different refinements and the graph on
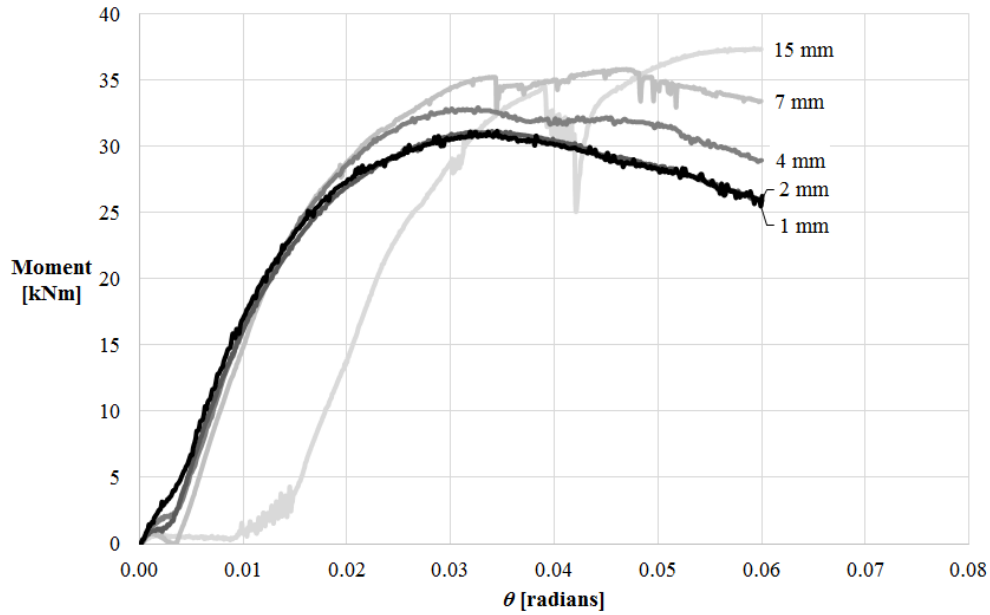
Figure 3.22: $M - \theta$ behaviour comparison of the convergence study

the right hand side shows the relative error related with the most accurate simulation performed. The simulation with a mesh size of 15mm is excluded because of its dissimilar behaviour.
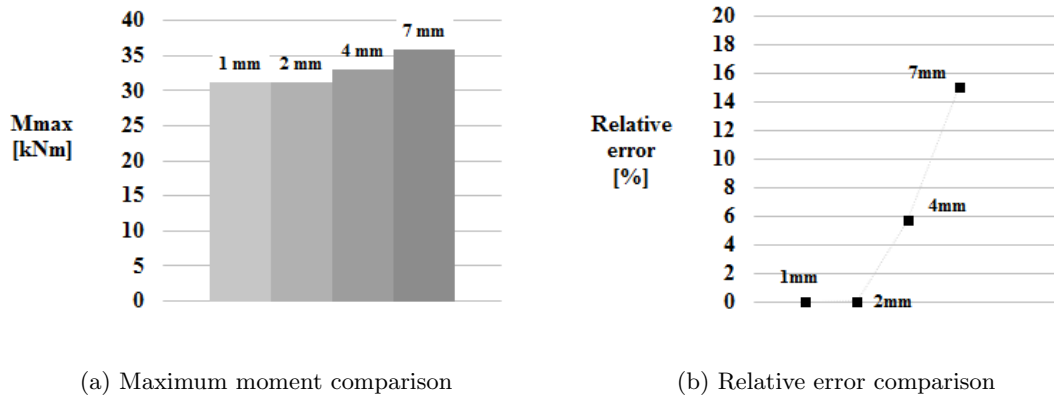
(a) Maximum moment comparison

(b) Relative error comparison

Figure 3.23: Convergence study

Discussion of the results

It can be seen from Fig. 3.25 that the $M - \theta$ behaviour of the simulations with smaller meshes (1 and 2mm) converge to the same solution. The simulation with a mesh of 4mm shows complete agreement up to a bending capacity of 25kNm, thereafter a small offset is observed. The simulation with a mesh of 7mm similarly to the simulation with a mesh of 4mm represents the behaviour well at first, but after a bending moment of 25kNm the behaviours significantly diverge. For last the simulation with a mesh size of 15mm represents a different physical behaviour.

Fig. 3.23 shows how the maximum moment captured by the simulations progressively converges as the mesh is refined, which indicates a sound mathematical solution.

Model A-II

The geometry of the Model A-II represents the *Snap-Fit connection* configuration of "Cantilever test A", in this case, steel position pins are introduced into the model to investigate its influence. The convergence study contains five simulations and similarly to the earlier section, it compares simulations with different mesh densities with an average mesh sizes of $[15, 7, 4, 2,$ and $1\,mm]$ (see Fig. 3.24).

(a) Mesh 15mm   (b) Mesh 7mm   (c) Mesh 4mm

(d) Mesh 2mm   (e) Mesh 1mm
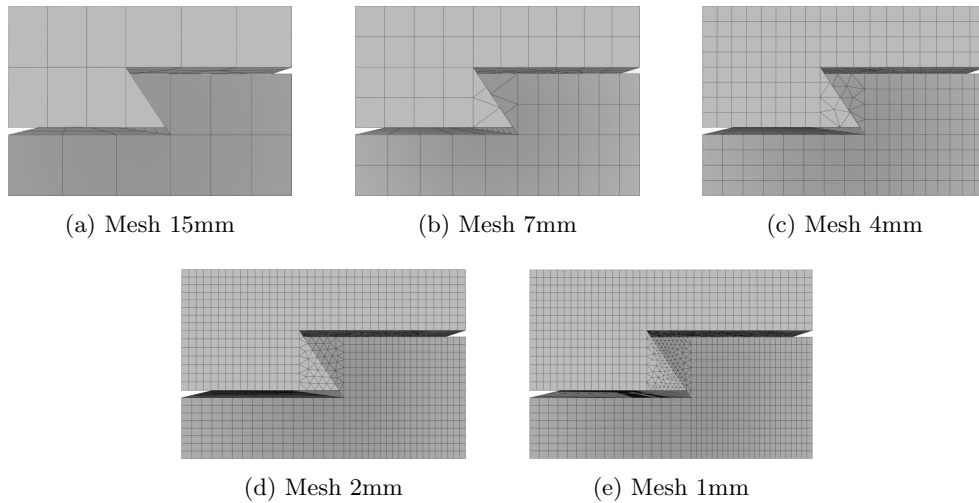
Figure 3.24: Mesh refinement of the convergence study

Results of the simulations

Fig. 3.25 shows the $M - \theta$ behaviour of the simulations with different mesh sizes in different shades of gray for comparison.

On Fig. 3.26 two graphs showing a comparison of the M_{max} of the simulations are presented, the graph on the left hand side compares the magnitudes of the resistances of the different refinements and the graph on the right hand side shows the error related with the most accurate simulation performed.

A comparison between the accuracy and the computational cost of the simulations is presented in Fig. 3.27. The computational cost, is the time in seconds of a single analysis with a single CPU.

Discussion of the results

It can be seen in Fig. 3.25 that the $M - \theta$ behaviour of the simulations with meshes of 1 and 2mm exhibit the same behaviour. Simulations with meshs of 4,7 and 15mm partially represent the same behaviour with slight differences depending on the level of refinement.

As shown on Fig. 3.26 the refinement of the mesh reduces the relative error between simulations, thus indicating the validity of the solution of the numerical model.
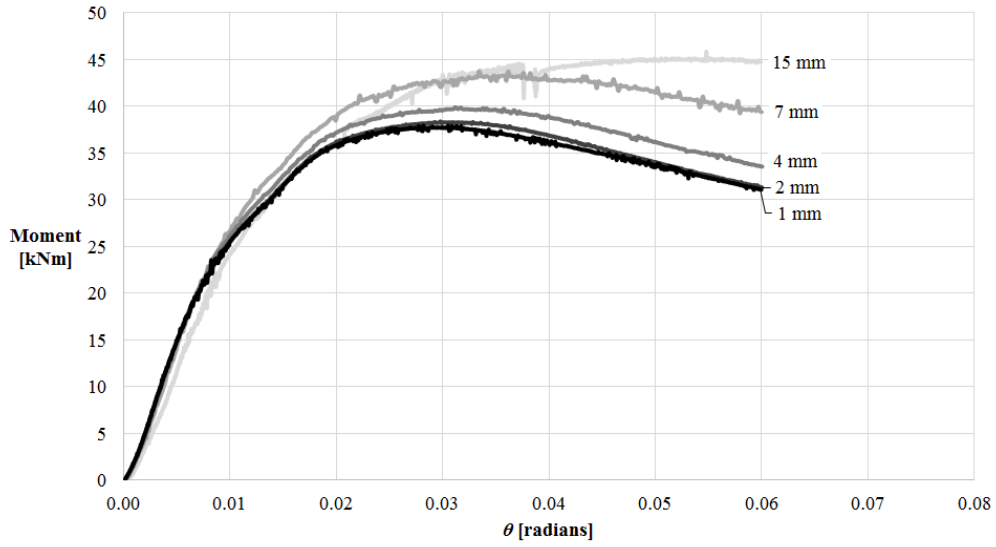
Figure 3.25: $M - \theta$ behaviour comparison of the convergence study
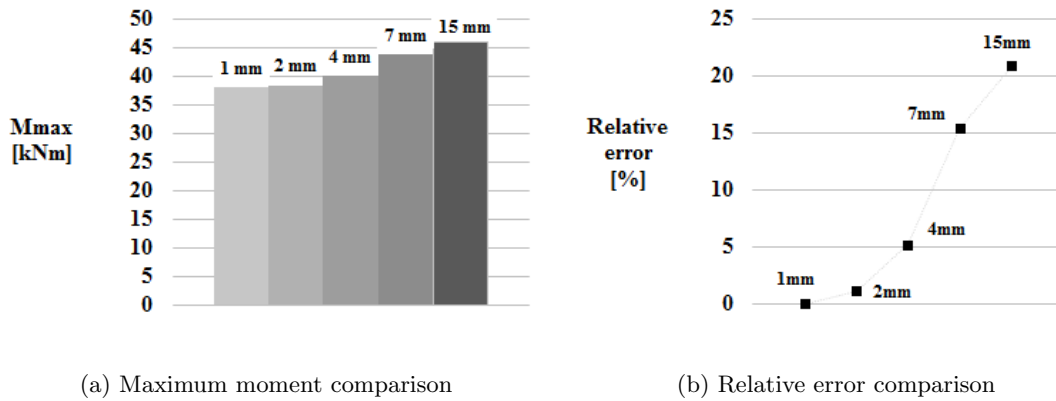
(a) Maximum moment comparison

(b) Relative error comparison

Figure 3.26: Convergence study
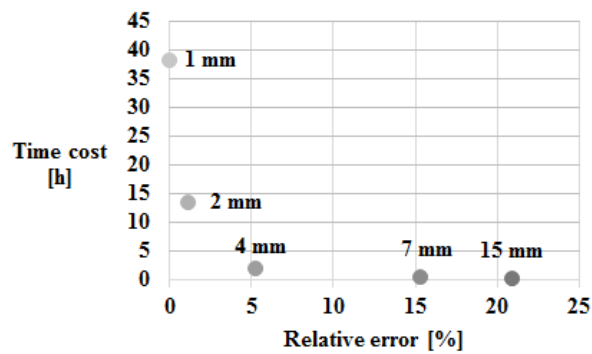
Figure 3.27: Comparison between accuracy and computational cost

Fig. 3.27 shows the rapid increase in computational cost for the simulations with smaller meshes. The simulation with a mesh of 4mm is the closest to the origin of coordinates, which represents the optimum balance between accuracy and computational cost.

Model B

The convergence study of this section relates to the numerical model B which represents the geometry and test set-up of "Cantilever test B". The convergence study contains five simulations with different average mesh densities of $[15\,,7\,,4\,,2\,,$ and $1\,mm]$ (see Fig. 3.28)

(a) Mesh 15mm   (b) Mesh 7mm   (c) Mesh 4mm

(d) Mesh 2mm   (e) Mesh 1mm
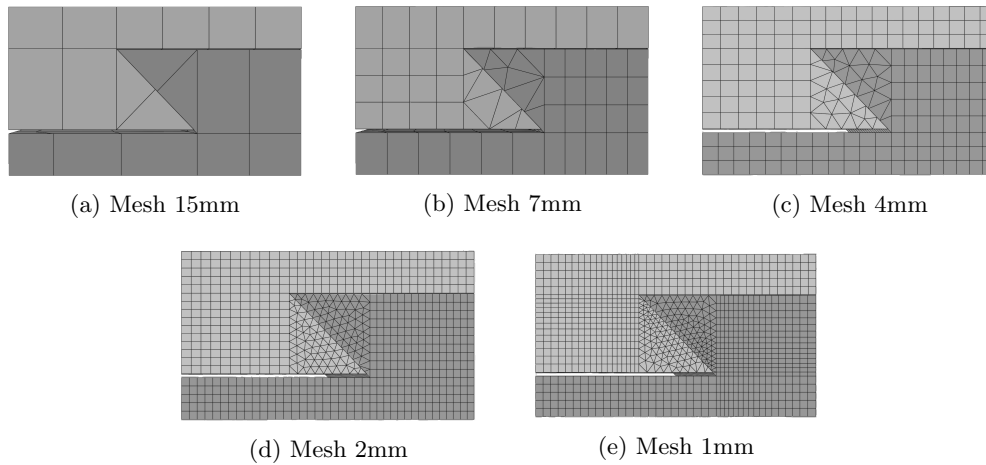
Figure 3.28: Mesh refinement of the convergence study

Results of the simulations

The results are presented in Fig. 3.29, where the $M - \theta$ behaviour of the simulations are compared in different shades of gray. Note that the simulations do not have the same extension in terms of rotation, the simulations with meshes of 2 and 1mm, are stopped earlier due to representation of unacceptable physical behaviours.

Fig. 3.30 shows two graphs to compare the M_{max} of the simulations with mesh densities of 4,2 and 1mm, the column chart shows the maximum moment captured by the simulations and the graph on the left hand side compares the relative error between the simulations. The simulations with meshes of 15 and 7mm are disregarded because their behaviour diverge significantly.

Discussion of the results

Fig. 3.29 shows that the $M - \theta$ behaviour of the simulations with meshes of 7 and 15mm are not able to represent the same behaviour as its refinements, thus from an early stage its stiffness is different. The simulations with average meshes of 4, 2 and 1mm have a complete agreement until a bending capacity of about 40kNm, thereafter the simulation with an average mesh of 4mm slightly diverges. Simulation of 1 and 2mm show the same behaviour until the simulations are manually stopped. The simulations with a mesh of 1 and 2mm show a sudden change of stiffness at rotations of 0.22 and 0.33 respectively which is attributed to the distortion of some elements due to excessive large strains.
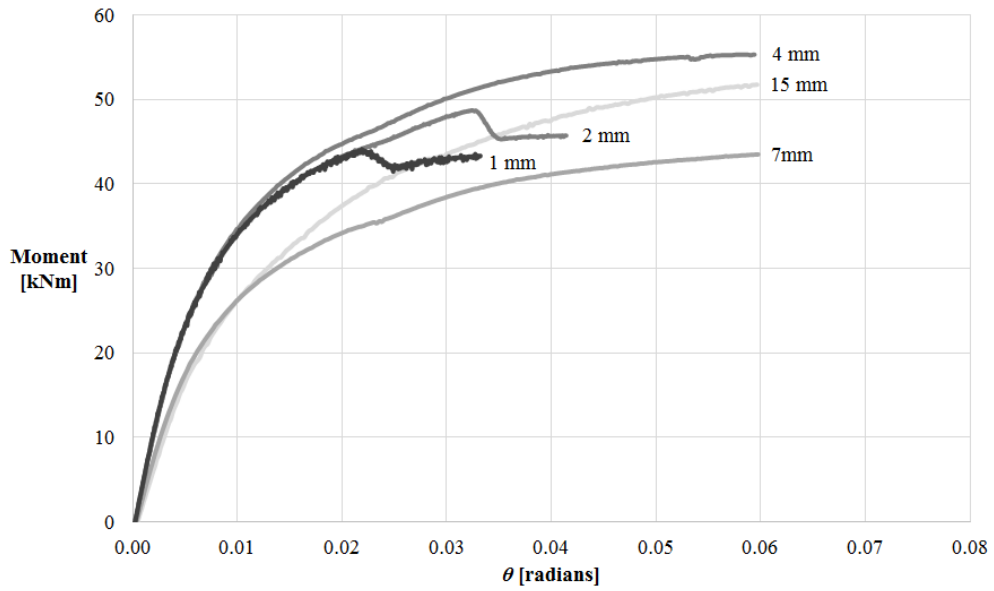
Figure 3.29: $M - \theta$ behaviour comparison of the convergence study
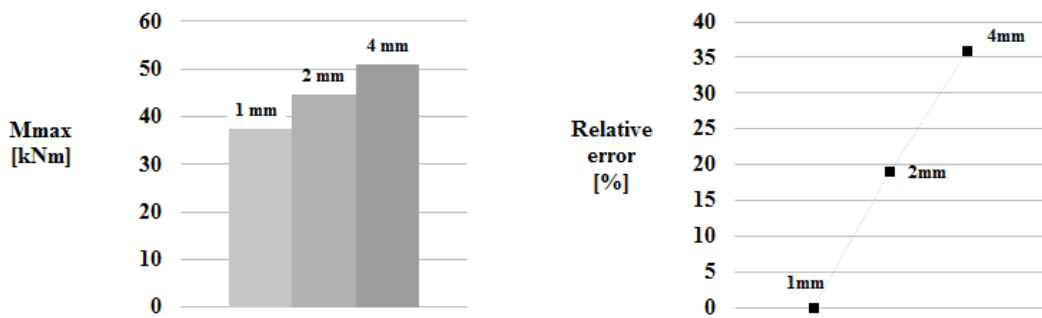
(a) Maximum moment comparison

(b) Relative error comparison

Figure 3.30: Convergence study

On the graph of Fig. 3.30 may be seen that not apparent convergence of a stable value is shown, thus the maximum moment is limited in this case by those distortions on the model. However it is shown how the behaviour represented before the extreme large strains are achieved converge to the same solution, thus indicating the validity of the numerical solutuion.

Model C

The convergence study of this section relates to the numerical model C which represents the geometry and test set-up of "Cantilever test C". The convergence study contains five simulations with different average mesh densities of $[15\,,7\,,4\,,2\,,$ and $1\,mm]$ (see Fig. 3.31)

(a) Mesh 15mm   (b) Mesh 7mm   (c) Mesh 4mm

(d) Mesh 2mm

(e) Mesh 1mm
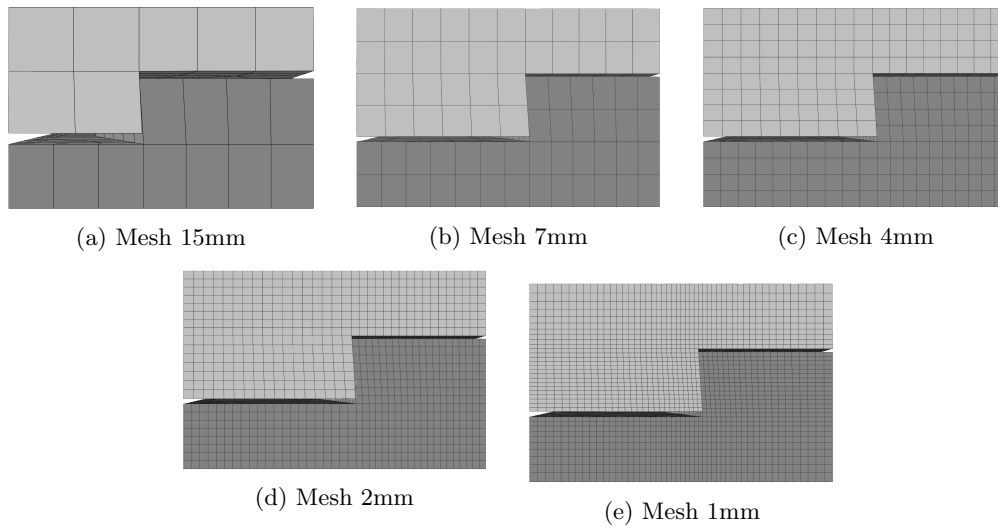
Figure 3.31: Mesh refinement of the convergence study

Results of the simulations

The results are presented in Fig. 3.32, where the $M - \theta$ behaviour of the simulations are compared in different shades of gray.

Fig. 3.30 shows two graphs in which the simulations with mesh densities of 4,2 and 1mm are compared. The column chart shows the maximum moment captured by the simulations and the graph on the left hand side compares the relative error between the simulations. The simulations with mesh densities of 15 and $7\,mm$ are not considered because their behaviour are not representative.

Discussion of the results

Fig. 3.32 shows that the $M - \theta$ behaviour of the simulations with meshes of 7 and 15mm are not able to represent the same behaviour as its refinements, thus from an early stage their stiffness are different. The simulations with average meshes of 4, 2 and 1mm show agreement almost until the maximum bending capacity,where the simulation with an average mesh of 4mm slightly diverges. Simulations of 1 and 2mm show the same behaviour over the complete path.

On the graph of Fig. 3.33 can be seen that the maximum bending capacity shown by the simulations converges to a stable value, indicating the validity of the solution.
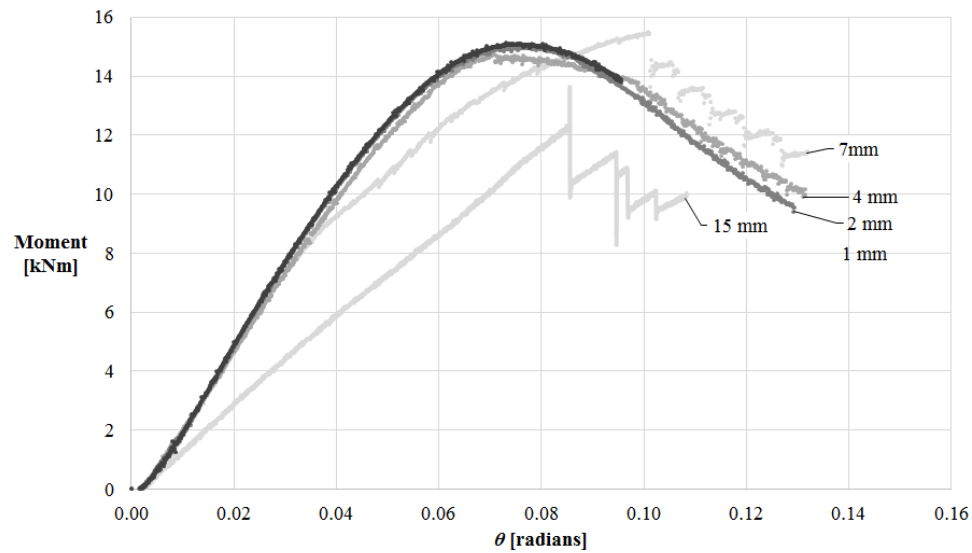
Figure 3.32: $M - \theta$ behaviour comparison of the convergence study
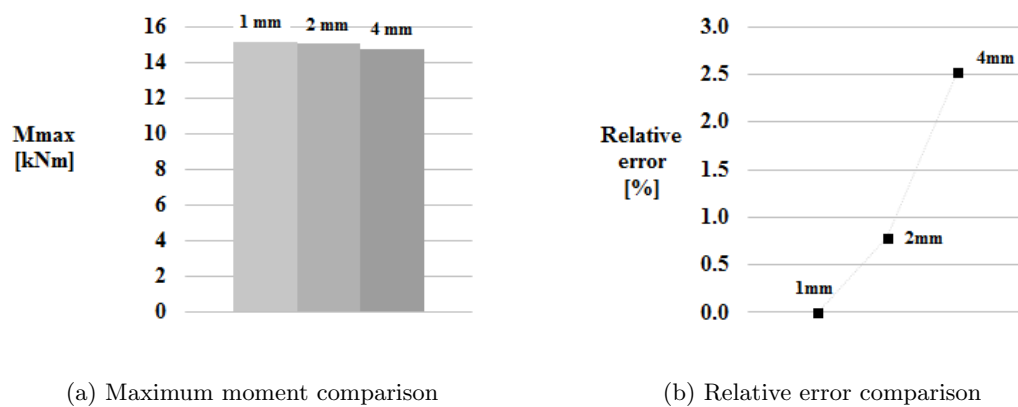
(a) Maximum moment comparison

(b) Relative error comparison

Figure 3.33: Convergence study

Risk of fracture

As shown during the experimental "Cantilever test B" fracture may appear and a brittle failure may occur. This section studies the prediction of fracture with the current numerical model by means of a simplified procedure.

The criteria established to consider whether risk of fracture is present, is to compare the maximum principal plastic strain of each element of the numerical model with the plastic strain which showed fracture during the experimental tensile test (see section 2.4). It is important to note, that this simplification neglects the effect of stress triaxility and therefore is a non-conservative approach. Despite of this, it provides an indication of the presence of risk of fracture.

The convergence study of Model A-II and Model B are used for this study, the simulations of both studies are compared. The simulations show with a black cross when the critical strain of 13% is reached, thus assuming that beyond this point the risk of fracture is present and the model is no longer able to represent the physical behaviour.

Results of the simulations

Fig. 3.34 shows a comparison of the $M - \theta$ behaviours of Model A-II and Model B with mesh densities of 4, 2 and 1mm, black crosses show a maximum principal tensile strain of 0.13.

(a) Model A-II   (b) Model B
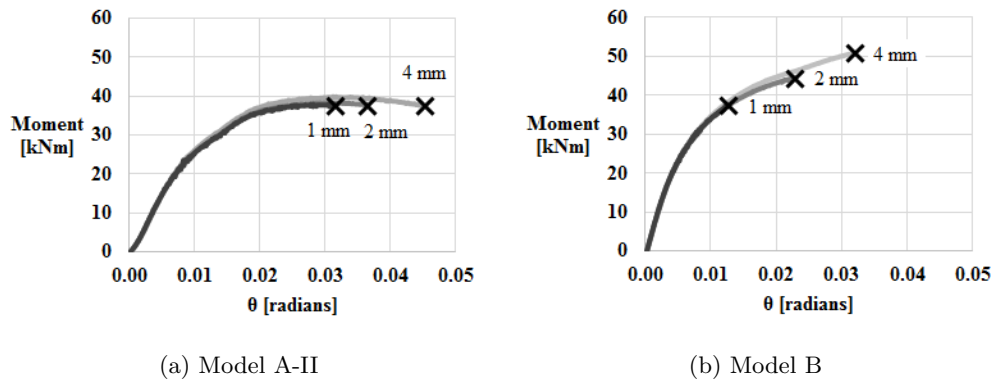
Figure 3.34: $M - \theta$ behaviour comparison

Fig. 3.35 presents two graphs to compare the maximum rotation capacity of the simulations at the stage when risk of fracture is detected for different mesh sizes.

(a) Model A-II   (b) Model B
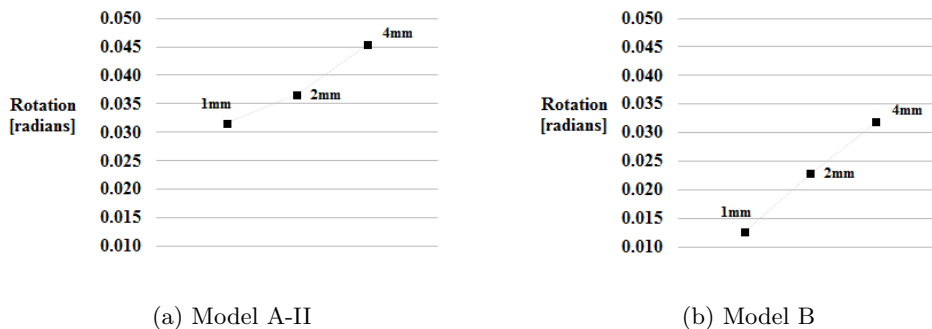
Figure 3.35: Rotation capacity convergence

The plastic strain field of the connection of the two simulations with mesh densities of 1mm are presented on Fig. 3.36 for comparison.

(a) Model A-II   (b) Model B
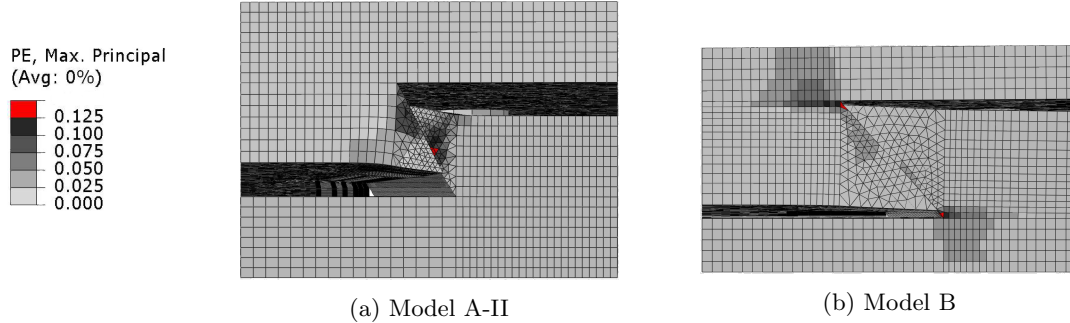
Figure 3.36: ϵ_p field of the connection

Discussion of the results

It is shown in Fig. 3.34 that both models represent their respective behaviours accurately for all three mesh densities. It is also demonstrated that the capture of the critical plastic strain is influenced by the mesh size. On Fig. 3.35 it is noticed that while the rotation capacity of Model A-II shows a convergence towards a stable value, Model B, shows a linear path and seems not to converge; this is attributed to the location of the critical plastic strain. As it may be seen on Fig. 3.36 Model A-II finds its critical plastic strain at mid-height of the dovetail, on the other hand, the critical plastic strain of Model B is located at the root of the dovetail. When the critical strains are located at the root of the dovetail the solution of the current model is not able to converge.

Consequently, the risk of fracture may be detected in this simplified form, if the mesh is sufficiently refined and the critical plastic strain is not located at the roots of the dovetail. If that is not the case, a more developed model is required to predict this type of failure.

Chapter 4

Snap-Fit connection sensitivities

This section studies the influence of different aspects that may affect the performance of the connection with the aim of gaining extra insight on the understanding of the connection. Five aspects are concerned: (1) Frictional influence with and without position pins,(2) the influence of shear forces, (3) the influence of different BC due to the location of the welds, (4) the influence of rounded and fillet corners on the dovetail and (5) the effect of the inclination of the dovetail. The results of each those studies are presented and discussed.

4.1 Frictional sensitivity

When two parts are in contact frictional forces will appear, some parameters are difficult to measure or are unknown. This section studies the influence of (uncertain) parameters that are expected to have a relevant effect on the behaviour of the connection.

The procedure is as follows:

- Step I. Identification of the parameters of study

- Step II. Estimation of the boundaries

- Step III. Analysis of combinations

Step I Identification of the parameters of study

During the experimental cantilever test in section 2.1 an uplift of the male part of the connection is observed. In absence of the position pins, the uplift is produced because the resultant force in the inclined part of the shoulders of the connections has a larger vertical component than the resistant friction force between the parts. Therefore the friction coefficient and the surface of contact play a relevant role in the behaviour of the connection. The following parameters are considered uncertain:

1. *Friction coefficient*
   The friction coefficient between two parts in contact is directly related to the resistant frictional force through a friction law, such as Coulombs' law.

2. *Tolerances of the fitting parts*
   The milling processing of a part such a dovetail produced in the shop can be regarded as

a precision work. However tolerances may always exist in order to achieve a fitting of the parts. Assuming perfectly flat surfaces, tolerances influence the area of contact and therefore the resistant frictional force.

Step II Estimation of the boundaries

The friction coefficient between two parts may be influenced by several factors such as material, surface quality, lubrication or speed of the test. An accurate value or an accurate description of the friction coefficient would require a deep study and precise specific laboratory measurements. Instead, here a range based on literature is adopted. Castelli in [6] provides a list of kinetic and static friction coefficients tested with different lubricants for two hardened steels (see Fig. 4.1).

(Reference letters indicate the lubricant used)

Materials	Static		Sliding	
	Dry	Greasy	Dry	Greasy
Hard steel on hard steel	0.780	0.230 (a)	0.420	0.120(c)
		0.150 (b)		0.108(g)
		0.110 (c)		0.105(h)
		0.110 (d)		0.096(i)
		0.007 (e)		0.084(d)
		0.005 (f)		0.081(b)
				0.080(j)
				0.058(k)
				0.029(l)

Figure 4.1: Coefficient of static and kinetic friction [6]

(a) Atlantic spindle oil; (b) Castor oil; (c) Oleic acid; (d) Lard oil; (e) Palmitic acid; (f) Stearic acid; (g) Turbine oil; (h) Turbine oil plus 1 percent graphite; (i) Turbine oil plus 1 percent stearic acid; (j) Grease (zinc oxide base); (k) Graphite; (l) Stearic acid.

A tolerance control is assumed in this document to give a possible range of variability see Fig. 4.2. The angular tolerance is assumed to be of greater accuracy and therefore is disregarded for matters of simplicity. The depth and width of the male dovetail are controlled through a minus deviation; the depth and width of the female are controlled by a bilateral tolerance. In order to simplify those controls, hereafter the effective vertical distance between the parts will be regarded as vertical tolerance (**Vtol**) and similarly the difference in width as horizontal tolerance (**Htol**) see Fig. 4.3 Note that Htol relates to the complete horizontal tolerance, that is to say that the effective space at each side of the parts is half of Htol because of symmetry see Fig. 4.3.

Note that the tolerances determined here are not intended to provide a detailed tolerance control but rather determine plausible values of tolerances.

Step III Analysis of combinations

The range of variability of the three selected parameters is too wide to investigate all possibilities. Instead a study of the influence of those parameters is undertaken. Fig. 4.4 shows a graphic representation of the size of the problem, the grey spots are the analysis performed to investigate the influence of the parameters, and the black stars represent the best and worst case scenario within this range.

1. Friction coefficient $\mu = 0.005 - 0.230$
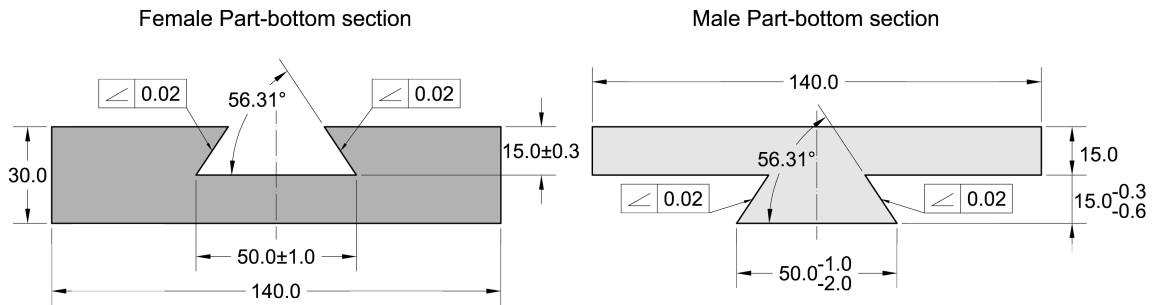
Figure 4.2: Estimation of tolerance control
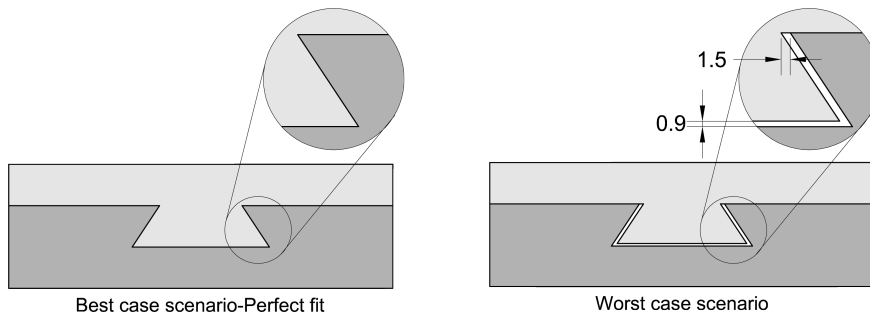
Figure 4.3: Best vs. Worst case scenario

2. Vertical tolerance $Vtol = 0.00 - 1.00\,mm$

3. Horizontal tolerance $Htol = 1.00 - 3.00\,mm$

Results of the simulations

In this section a representative selection of the analysis performed is presented to explain the influence of those parameters. The numerical model used to simulate the selected case scenarios regards to the Model A in a parametric form.

In the following graphs the results of the "Cantilever test A" are included for reference displayed in black, the results of the simulations are printed in different shades of gray. The definition of the simulations describe the characteristics of the simulation i.e. $V50 - H150\ \mu = 0.110$ relates to a simulation with a vertical tolerance of $Vtol = 0.50\,mm$ a horizontal tolerance of $Htol = 1.50\,mm$ ($0.75\,mm$ of effective space) with a friction coefficient of $\mu = 0.110$.

The first graph in Fig. 4.5 shows 9 simulations running linearly from the best case scenario to the worst case scenario of this study.

The second graph in Fig. 4.6 presents 6 simulations where the parameter varied is μ with the following values [0.02,0.03,0.04,0.05,0.06,0.07]. The tolerances of those analysis correspond to a $Vtol = 0.50\,mm$ and $Htol = 0.50\,mm$.

The third graph in Fig. 4.7 shows 4 simulations where the parameter varied is $Htol$ with values of [0.50,1.00,1.50,2.00]. The vertical tolerance and friction coefficient of those analysis correspond to values of $Vtol = 0.25\,mm$ and $\mu = 0.05$.
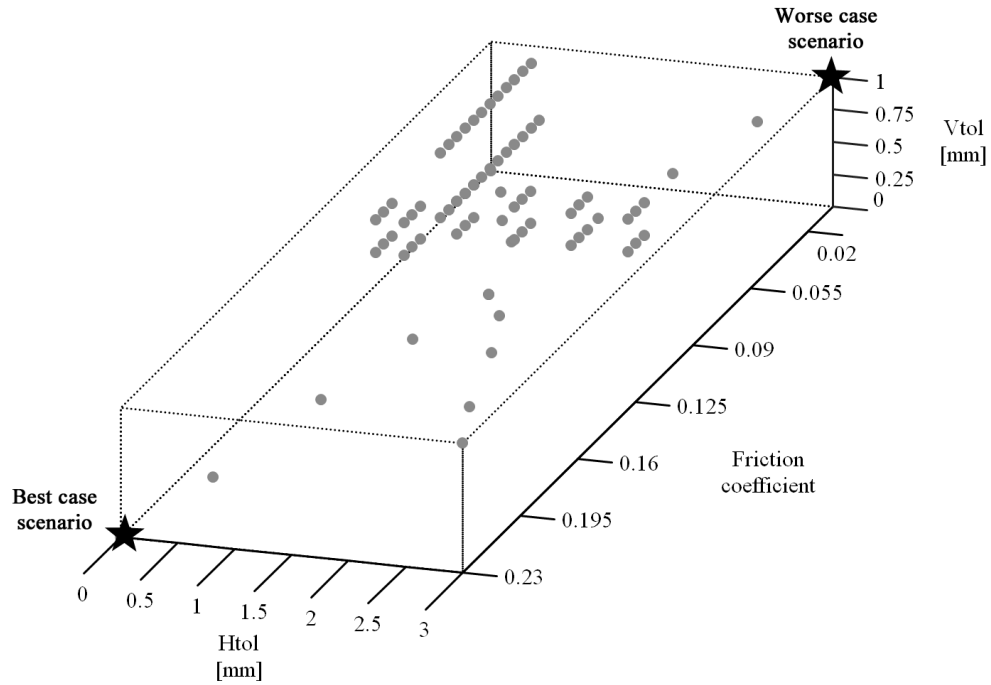
Figure 4.4: 3D representation of the variability of the 3 selected parameters
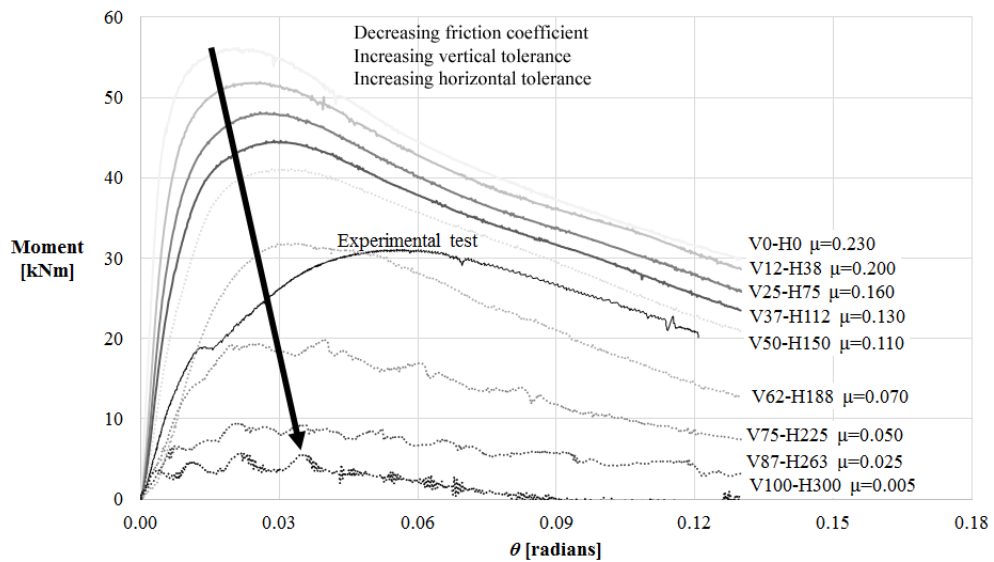
Figure 4.5: Variability of the $M - \theta$ behaviour due to the uncertainity of the unknow factors
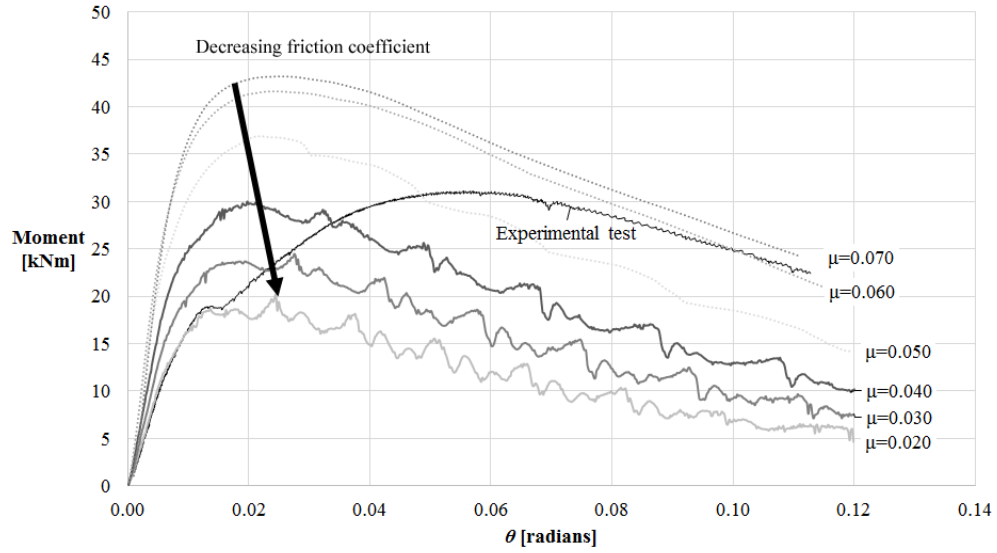
Figure 4.6: Influence of the friction coefficient variability
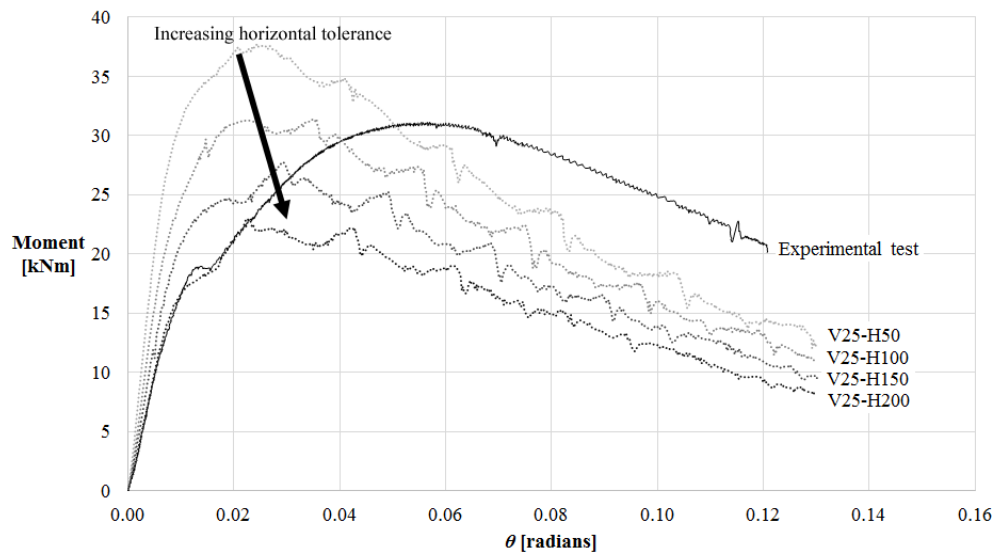
Figure 4.7: Influence of the Horizontal tolerance variability

The fourth graph in Fig. 4.8 presents 3 simulations where the parameter varied is $Vtol$ with values of [0.00,0.50,1.00]. The horizontal tolerance and friction coefficient of those analysis correspond to values of $Htol = 1.00\,mm$ and $\mu = 0.05$.
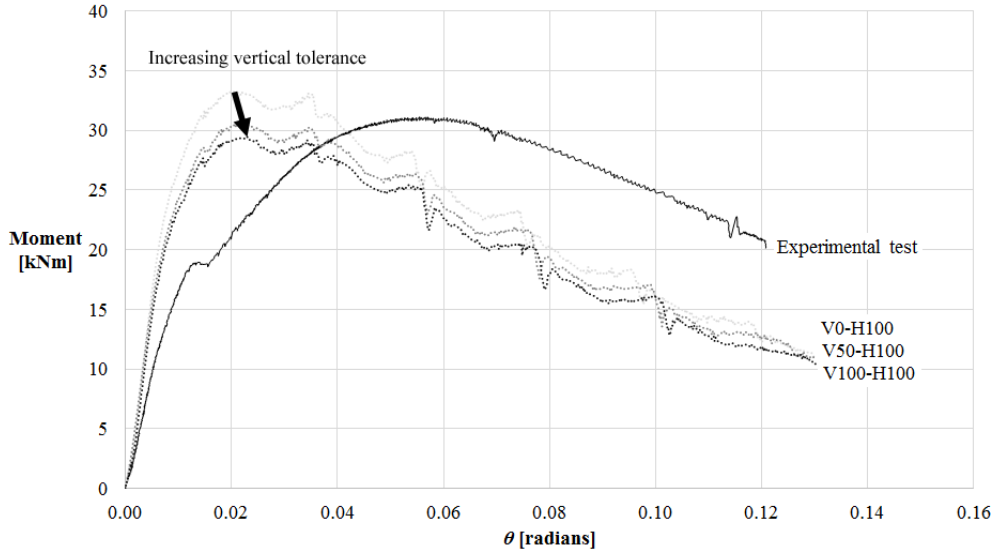
Figure 4.8: Influence of the Vertical tolerance variability

Discussion of the results

As expected both the friction coefficient as well as the tolerances influence the behaviour, stiffness and maximum capacity of the connection.

While increasing the tolerances decrease the stiffness and capacity of the connection, the friction coefficient is inversely related, thus a high friction coefficient increases the stiffness and maximum bending moment.

In Fig. 4.5, is shown the high level of variability of the study, simulations with a combination of little tolerances and high friction coefficients show a stiff connection with large moment capacities, due to the high friction resistance and the complete yielding of the shoulders of the connection. On the other hand, when the tolerances are large and the friction coefficients low, the connection rotates largely by applying small bending moments thus exhibiting uplift of the male part of the connection and not developing the potential plastic resistance of the connection.

The variation of the friction coefficient shown in Fig. 4.6 shows that the coefficient has a larger sensitivity for smaller values than for larger values, this may be explained by the behaviour of this particular connection. When the combination of a low friction coefficient and a large tolerance gap takes place, results in a relatively small friction resistant force, the male part of the connection experiences an uplift and the shoulders of the connection do not yield. Oppositely, when the friction coefficient in combination with the tolerances result in a relatively high friction resistant force, the values have a smaller impact, because there is no alternative possible to the yielding of the shoulders of the connection.

Vertical and Horizontal tolerances are related to the initial contact area of the connection. The greater the tolerance the smaller the contact area and therefore lower the resistant frictional force. It is however worth to note, that the sensitivity of the horizontal tolerance is significantly greater than the vertical tolerance, that is due to the fact that the inclination of the shoulders has been

assumed perfect, thus when adding a horizontal tolerance a vertical gap is introduced intrinsically due to the rotation introduced by the self-weight of the beam.

Frictional sensitivity with position pins

This section similarly to section 4.1 investigates the influence of parameters such as μ, $Htol\ or\ Vtol$ in the overall behaviour of the *Snap-Fit connection* in which now the vertical movement of the male part is restrained by means of position pins. The numerical model used to simulate those case scenarios is the Model A-II.

Results of the simulations

To evaluate whether level of variability decreases an equivalent study as the one performed in the previous section is presented in graph in Fig. 4.9. It shows the $M - \theta$ behaviour of 9 simulations running linearly from the best to the worst case scenario to compare how the variability of the behaviour is affected by the introduction of the position pins, for comparison see the results without position pins displayed in Fig: 4.5 in page 54.
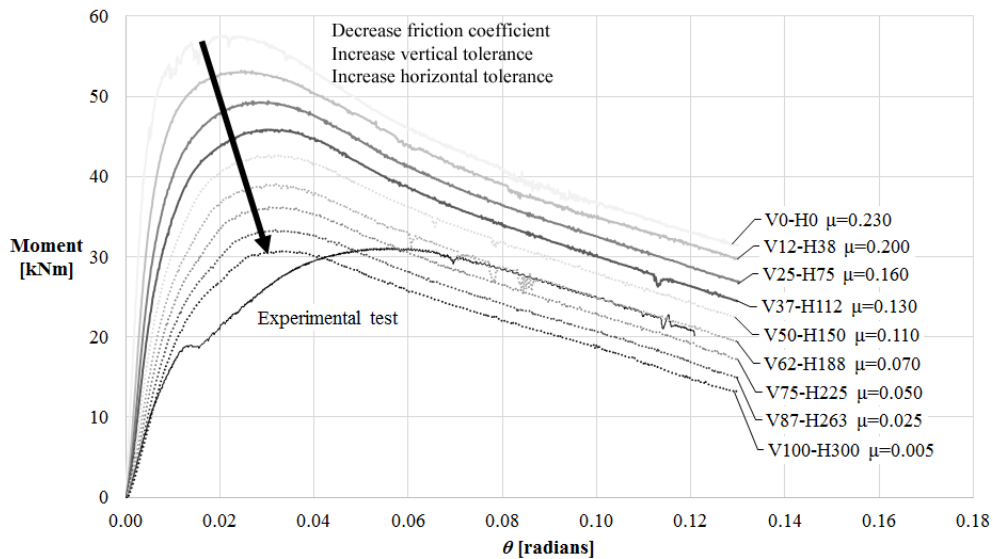
Figure 4.9: Variability of the $M - \theta$ behaviour of the connection with position pins

The second graph in Fig. 4.10 presents 6 simulations in which the friction coefficient is varied with the following values $[0.02, 0.03, 0.04, 0.05, 0.06, 0.07]$. The tolerances of those simulations correspond to a $Vtol = 0.50\,mm$ and a $Htol = 0.50\,mm$. For comparison see the results without position pins displayed in Fig: 4.6 in page 55.

The third graph in Fig. 4.11 shows 4 simulations where the parameter varied is $Htol$ with values of $[0.50,1.00,1.50,2.00]$. The vertical tolerance and friction coefficient of those analysis correspond to values of $Vtol = 0.25\,mm$ and $\mu = 0.05$. For comparison see the results without position pins displayed in Fig: 4.7 in page 55.

The fourth graph in Fig. 4.12 presents 3 simulations where the parameter varied is $Vtol$ with values of $[0.00,0.50,1.00]$. The horizontal tolerance and friction coefficient of those analysis correspond to values of $Htol = 1.00\,mm$ and $\mu = 0.05$. For comparison see the results without position pins displayed in Fig: 4.8 in page 56.
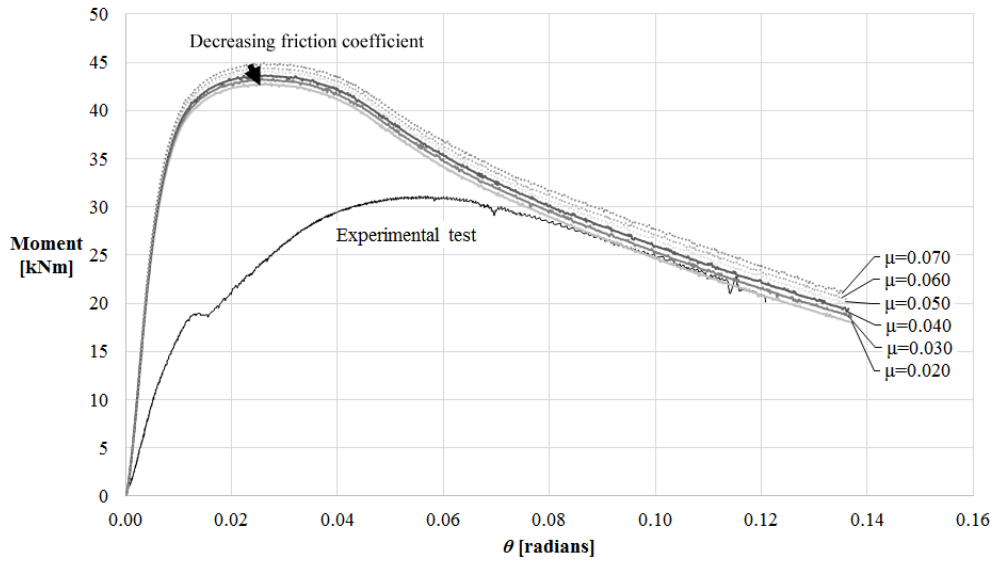
Figure 4.10: Influence of the Friction coefficient variability
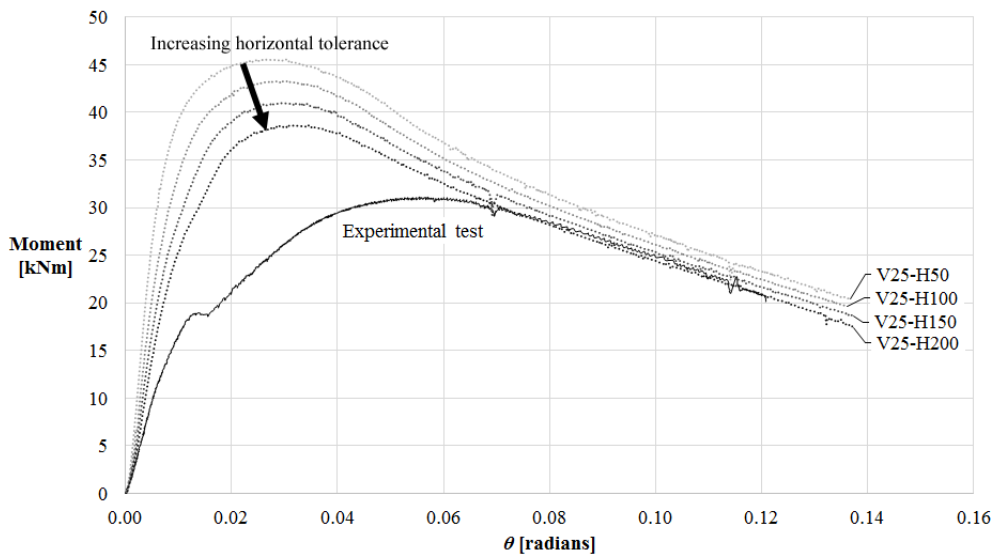
Figure 4.11: Influence of the Horizontal tolerance variability
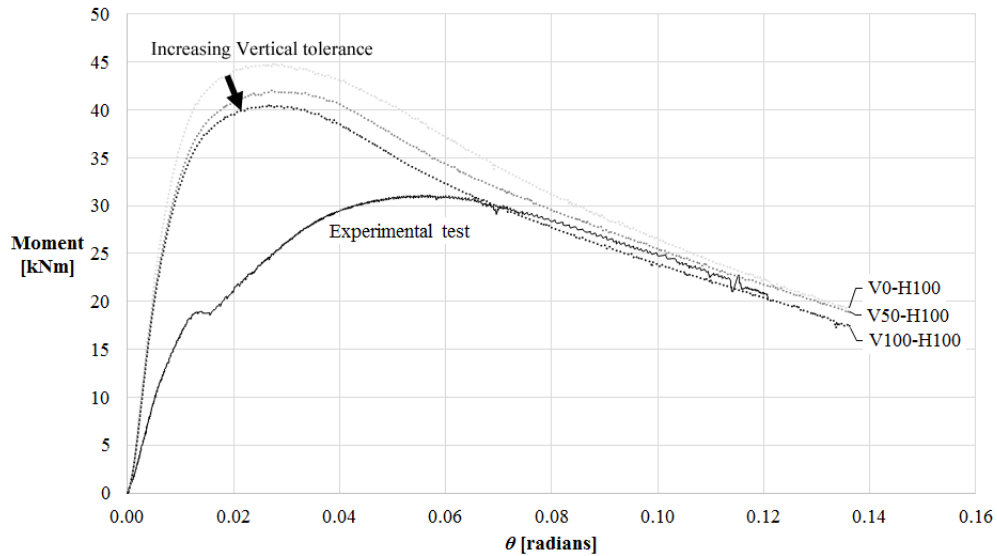
Figure 4.12: Influence of the Vertical tolerance variability

Discussion of the results

In Fig. 4.9 can be seen that the behaviour of the connection with the position pins becomes more stable and reliable, its bending capacity does not rely completely in the frictional behaviour but a low boundary bending capacity is set, achieving in the worst case scenario a bending resistance of about $30\,kNm$.

Fig. 4.10 shows how the friction coefficient loses its relevancy when the connection is restrained. The connection without connection pins in Fig. 4.6 showed a variability range of half of the complete resistance of the connection, while now the resistance for that same range is decreased to about a 5%.

The influence of the horizontal tolerance is considerably reduced, but it remains an issue to consider, the effect of that tolerance on the contact area is now negligible, however this tolerance still affects the amount of material of the shoulder of the connection that can yield, therefore has an effect on the connection; similarly also the effect of the vertical tolerance reduces but remains.

4.2 Shear sensitivity

This section gives and indication of the influence that shear forces have on the overall performance of the *Snap-Fit connection*. The *Snap-Fit connection* transfers shear forces from one part of the connection to the other by contact. This influences the stress field and may affect the behaviour of the connection.

Four simulations are performed with different beam lengths. The variations performed correspond to lengths of a a quarter, a half, an a double of the length of the beam profile used on the "Cantilever test A" (1360mm). Thus varying the lever arm and relation between the applied moment and the applied shear force.

The configuration of the numerical model used to run those simulations relates to the Model A-II with a friction coefficient equal to $\mu = 0.07$.

Fig. 4.13 shows the $M - \theta$ behaviour of the four simulations in different shades of gray. It can be seen that for the range studied here no significant changes on capacity are shown. However this cannot be generalised, only a specific configuration has been tested and the range of M-V studied is limited.
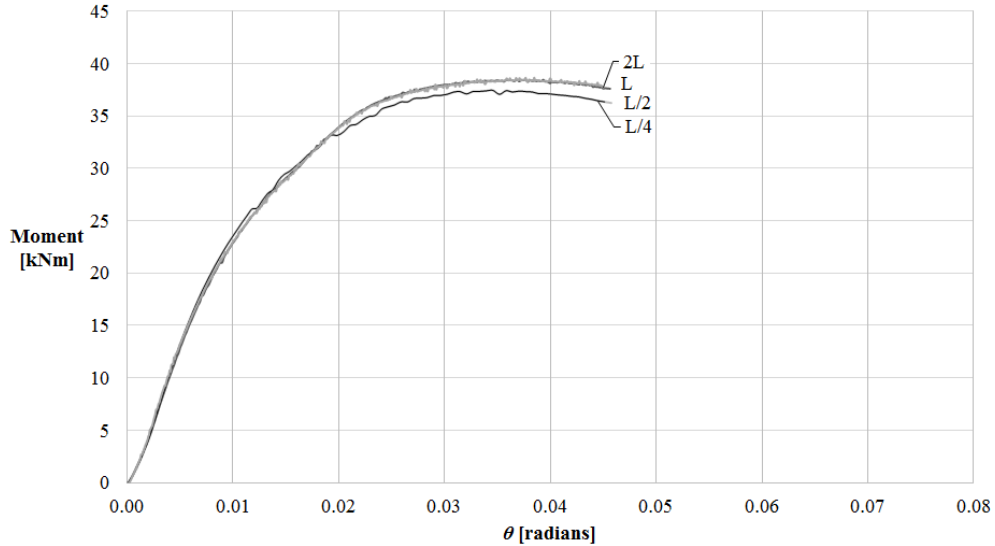
Figure 4.13: $M - \theta$ comparison for different shear levels

4.3 BC sensitivity

This section studies the influence that the position of the welds may have on the overall performance of the *Snap-Fit connection*. Two case studies are considered; The first simulates the BC that the connection would have if connected to a plate or a column, thus the perimeter welds would restrain the DOF contained within the black lines (see Fig. 4.14a). The second case study simulates the BC that would occur in a beam splice connection, thus the beam profile would be welded on its perimeter to the back part of the connection and the restrained DOF would be those contained within the black lines of Fig. 4.14b.

The numerical model used to simulate those two case scenarios corresponds to Model B, with an average mesh of 4mm with a refined mesh of 1mm at the shoulders to capture well the critical plastic strain.

Results of the simulations

Fig. 4.15 shows the $M - \theta$ behaviour of the two simulations in different shades of gray, the limit strain of 0.13 is shown with a black cross indicating risk of fracture.

The second graph in Fig. 4.17a shows the stress field of both simulation at four reference points indicated in Fig. 4.15.

On Fig. 3.18 the tensile plastic strain of both simulations at the stage where the critical strain is reached are compared.

(a) Perimetral welds

(b) Profile welds
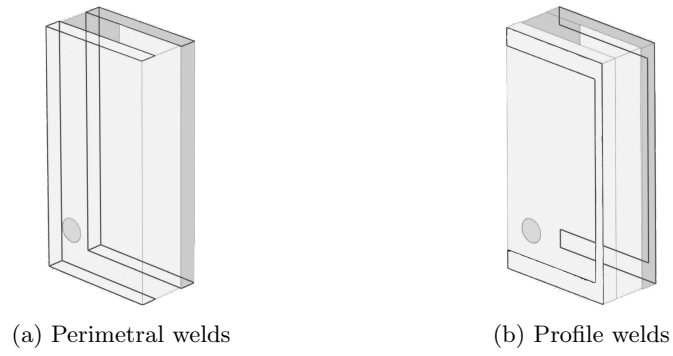
Figure 4.14: BC comparison
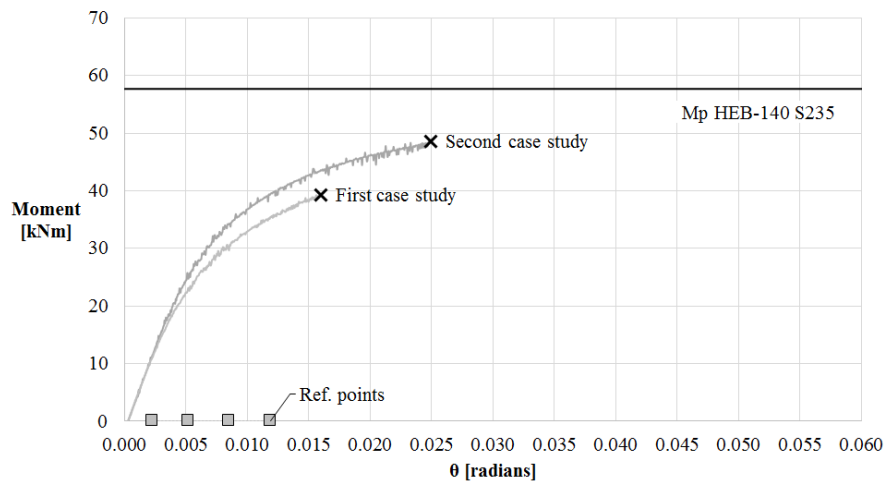
Figure 4.15: $M - \theta$ behaviour comparison of the weld sensibility case studies

(a) Case study 1 ref.1

(b) Case study 2 ref.1

(c) Case study 1 ref.2

(d) Case study 2 ref.2

(e) Case study 1 ref.3

(f) Case study 2 ref.3

(g) Case study 1 ref.4

(h) Case study 2 ref.4

Figure 4.16: Comparison of the σ field of the case studies at the ref.points

(a) Case study 1
(b) Case study 2
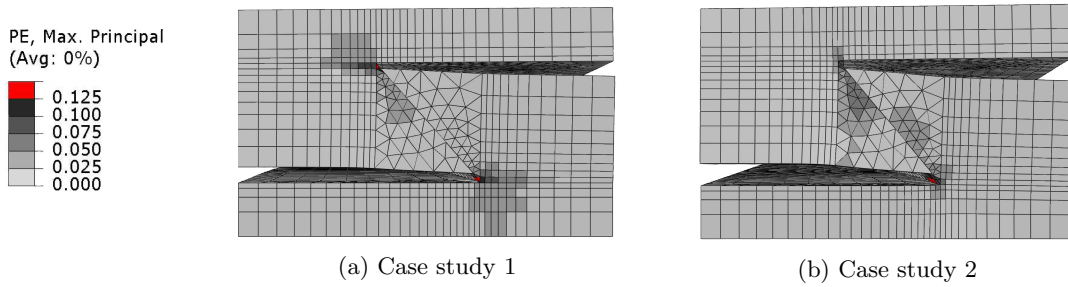
Figure 4.17: ϵ_p field of the case studies

Discussion of the results

From Fig. 4.15 it is visible that the simulation with boundary conditions simulating the splice connection (second case study) shows a higher bending resistance and more rotation capacity. This is explained by the stress field distribution. As it is seen from Fig. 4.16, the first case study, where the BC directly restrain the DOF next to the root of the dovetail, a stress concentration at the top of the dovetail is visualized. On the other hand on the second case scenario the localization of the restrained DOF is on the back part of the connection, the stress field is diffused from that part to the root of the connection, as it can be seen the amount of material stressed is greater and therefore the critical stage may be reached at a later stage.

Fig. 4.17 shows that the root of the dovetail becomes critical in both cases, it may be appreciated that the critical strain in the second case scenario is reached at a larger rotation, however those results must be read very carefully, thus as seen earlier on section 3.5 predicting the risk of failure of a dovetail with a critical spot at its root may be influenced by the size of the mesh of the simulation.

4.4 Round-and-Fillet corners

As shown during the "Cantilever test B" as well as on the validation of Model B on sections 2.2 and 3.3 the sharp root corner of the dovetail concentrates pick stresses, the capacity of the connection is limited as consequence of large strains at this location and the model has difficulties to converge.

This subsection studies the effects of smoothing the sharp corners with round and fillet geometries. On Fig. 4.18 is presented the geometry of the upper part of the connection in comparison with its equivalent with sharp edges, the inner corners are smoothed with a radius of $3\,mm$, and consequently also the exterior corners, to avoid gaps between the parts of the connection.

The design and numerical model used for those simulations are based on the Model B (see section 3.5).
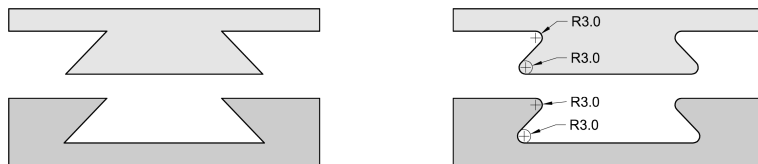
Figure 4.18: Geometry comparison of the Round-and-fillet dovetail

Results of the simulations

The graph in Fig. 4.19 shows a comparison of the $M - \theta$ behaviour of the simulations with a configuration representing the "Cantilever test B" and the equivalent with Round-and-Fillet corners.

A second graph in Fig. 4.20 shows a comparison of the ϵ_p field of both simulations at its critical strain limit. Fig. 4.21 and Fig. 4.22 present a comparison of the convergence of each of the geometries and a comparison of the convergence of the rotation of the simulations respectively.
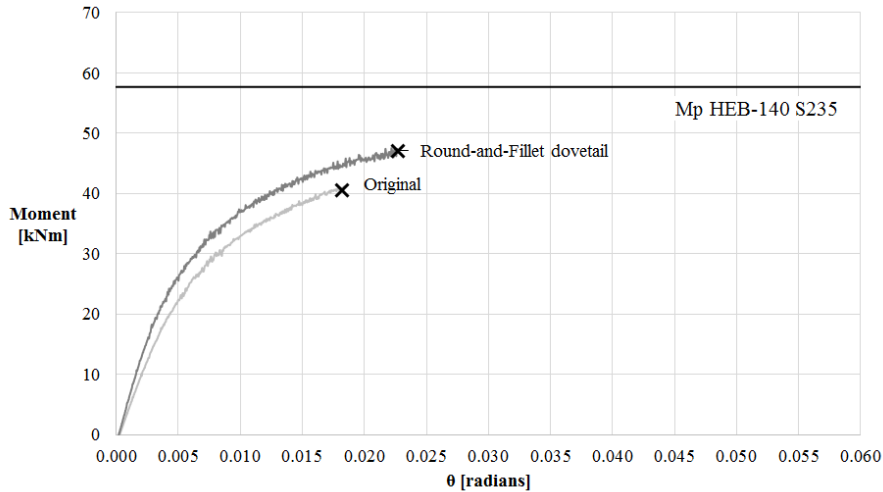
Figure 4.19: $M - \theta$ behaviour comparison

(a) Original
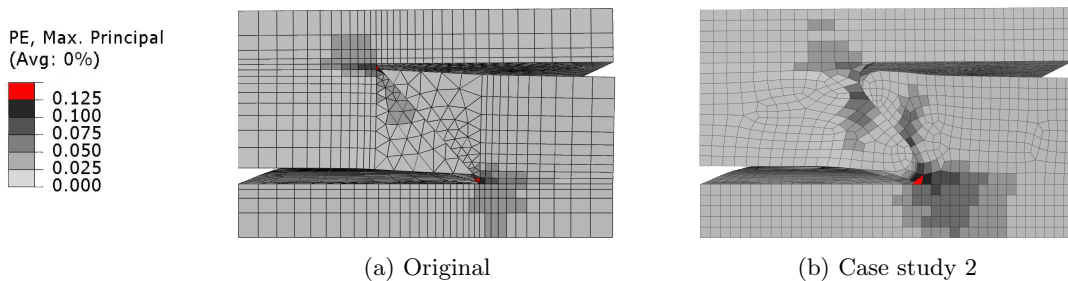
(b) Case study 2

Figure 4.20: ϵ_p field of the case studies

Discussion of the results

It is noticeable from Fig. 4.19 that the stiffness, capacity are slightly increased with respect to the compared model. The change on stiffness is explained by the rounding of the tops of the dovetails, thus is intuitive that the sharp edges are more flexible than those rounded ones. The increase on bending and rotation capacity may be explained by the better stress distribution of a fillet root in comparison to a sharp root. However those results are only indicative, thus as shown in section 3.5, the model is sensitive to the prediction of the critical plastic strain specially when its located at the root of the dovetail.

It is remarkable that the solution of the Model representing the *Round-and-Fillet* connection seems to converge to a stable value as opposed to Model B. This may be explained because of the corner changes, thus smoother fields are better captured by the mathematical solutions.

(a) Model B   (b) Model Round-and-Fillet
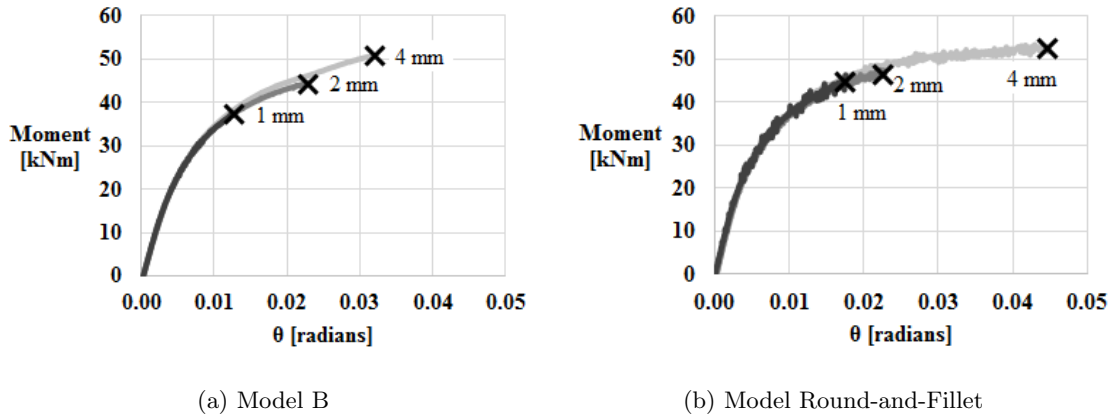
Figure 4.21: $M - \theta$ behaviour comparison

(a) Model B   (b) Model Round-and-Fillet
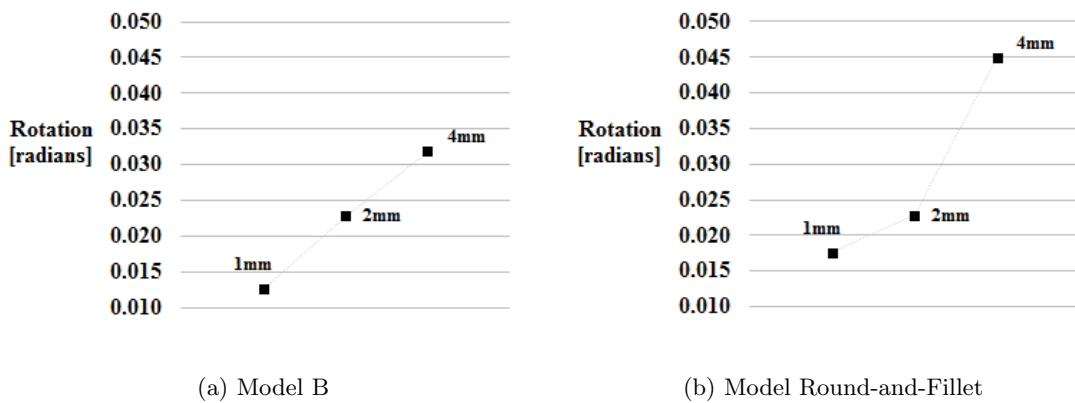
Figure 4.22: Rotation capacity convergence

4.5 Inclination sensitivity

This section studies geometric changes on the *Snap-Fit connection* configuration to reduce or delay the risk of fracture.

According to the criteria established, the risk of fracture is considered to be present when the maximal principal strain equals 13%, which is the lowest strain measured on the tensile tests when fracture occurred (see section 2.4).

It has been shown during the cantilever test B and its numerical validation on sections 2.2 and 3.3, that for a dovetail with an angle of 45 degrees the root of the dovetail becomes critical and risk of fracture appears at a relative early stage. On the other hand, it is intuitive that with a right angle (when the dovetail shape becomes a rectangle) there is no risk of fracture and neither significant moment capacity resistance.

Four intermediate configuration designs within those boundaries are considered. The balance between ductility and moment-capacity is compared and discussed.

The simulations used to study the configuration designs have a refined mesh of 1mm over the contact boundary and the dovetail shoulder to capture accurately changes of strain. The numerical model correspond to an adaptation of Model A-II with a friction coefficient of 0.42 (simulating a dry and clean surface) and the particularity that the horizontal offset of the dovetail is varied (parameter A of Fig 6.1) to the following values $[10.0, 5.0, 2.5$ and 1.0mm$]$ which represent dovetail inclinations of $[56.31°, 71.57°, 80.54°$ and $86.19°]$ (see Fig. 4.23).

(a) Alternative 1   (b) Alternative 2   (c) Alternative 3   (d) Alternative 4
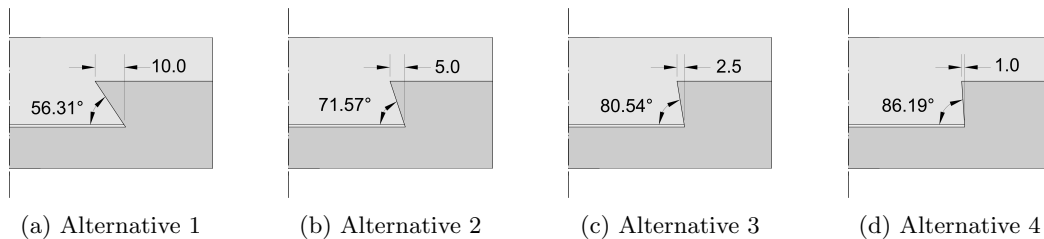
Figure 4.23: Comparison of the geometry of the alternatives

Results of the simulations

The graph on Fig. 4.24 displays the $M - \theta$ behaviour of the four alternative configuration designs in different shades of gray. The risk of fracture at a plastic tensile strain of 13% is shown with a black cross.

Fig. 4.25 presents the tensile plastic strain field of the design alternatives with different inclinations at the stage when risk of fracture is detected. As the legend describes, the strain output field it is not averaged, the elements are colored in different shades of gray for plastic tensile strains ranging from 0 to 0.125, and elements with a plastic tensile strain over 0.130 are displayed in red.

Discussion of the results

It is shown on Fig. 4.24 that increasing the angle of the dovetail, decreases the maximum bending capacity of the connection and increases its rotation capacity.
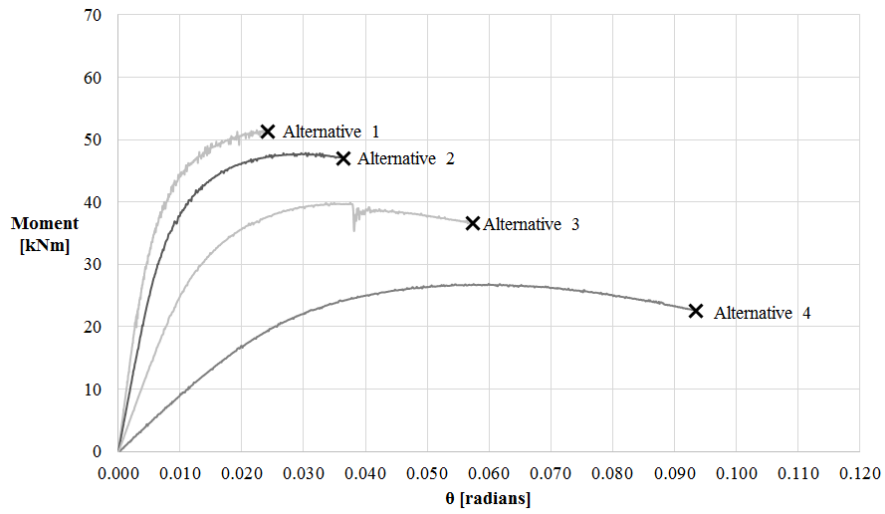
Figure 4.24: $M - \theta$ behaviour comparison

(a) Alternative 1

(b) Alternative 2

(c) Alternative 3

(d) Alternative 4
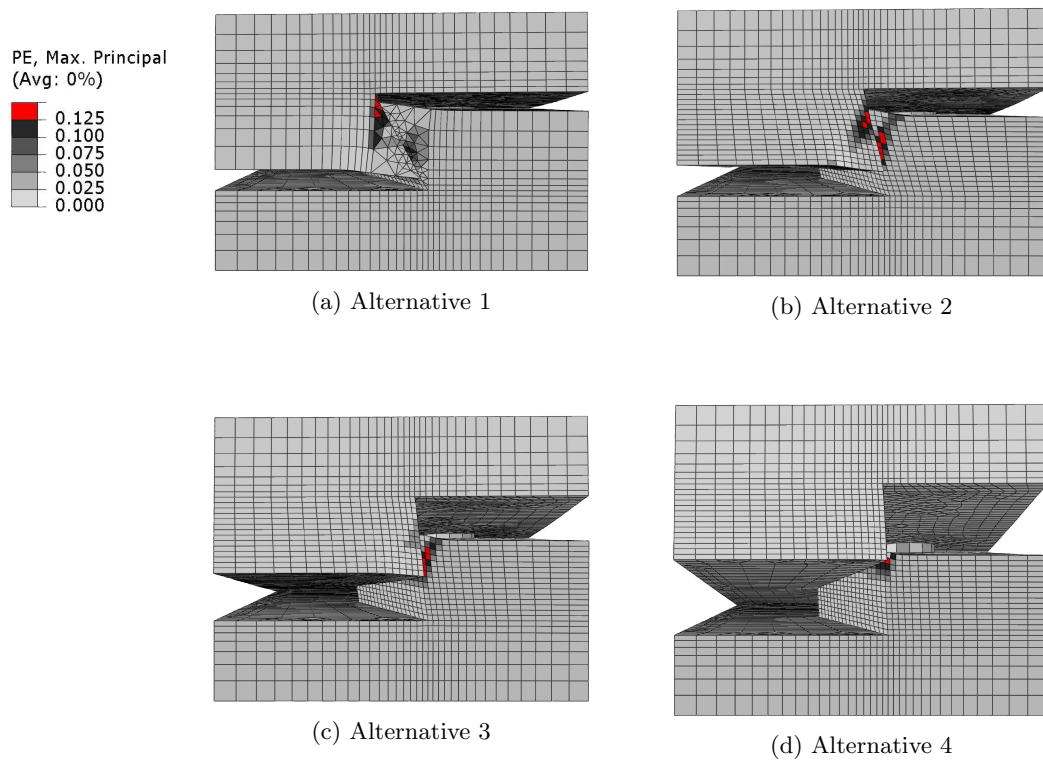
Figure 4.25: Tensile ϵ_p field

It may be noticed from Fig. 4.25 that the critical location where the plastic strain is found changes by altering the inclination of the dovetail, thus by increasing the angle, the location where the critical strain is founded rises from the root of the dovetail towards its top.

It is true that the inclination of the dovetail affects the ductility of the connection. While *Alternative 1* indicates the possibility of fracture at a rotation of 0.242 radians, *Alternative 4* does not show risk of fracture until a rotation of 0.0934. The cost of this ductility is a reduction of the capacity of about 50%; *Alternative 1* shows a $M_{max} = 51.76kNm$ while *Alternative 4* has a $M_{max} = 26.88kNm$.

Even more relevant is the high variability that the behaviour of the connection experiences for high inclinations (*Alternative 3* and *4*). Thus the difference in geometry between *Alternatives 3* and *4* is only 1.5mm of dovetail offset (see Fig. 4.24). This slight geometry change has a great impact both on ductility and resistance. It is because of that effect that such a geometry is not recommended, thus tolerances or manufacturing imperfections may lead to unexpected behaviours.

If greater ductility is required, it is suggested to study other alternatives. For instance the manufacturing of the connection with a more ductile material. As an example, an ordinary structural steel shows a strain on tensile tests of the order of a 30%, according to [9], which hypothetically would allow for larger rotations in comparison with the current design.

Chapter 5

Comparison with a bolted connection

This chapter compares the *Snap-Fit connection* with a bolted connection. The first section gives an overview of different typologies of bolted connections. A second section introduces a comparison between the two connections in terms of maximum capacity and ductility.

5.1   Overview of bolted connections

Four bolted connections that are commonly used on the built environment are presented, see Fig. 5.1. First the physical characteristics of the connections are described, then the $M - \theta$ behaviour of each of them is compared and discussed.

(a) Double web angle

(b) Top and seat angle

(c) End-plate

(d) Extended end-plate
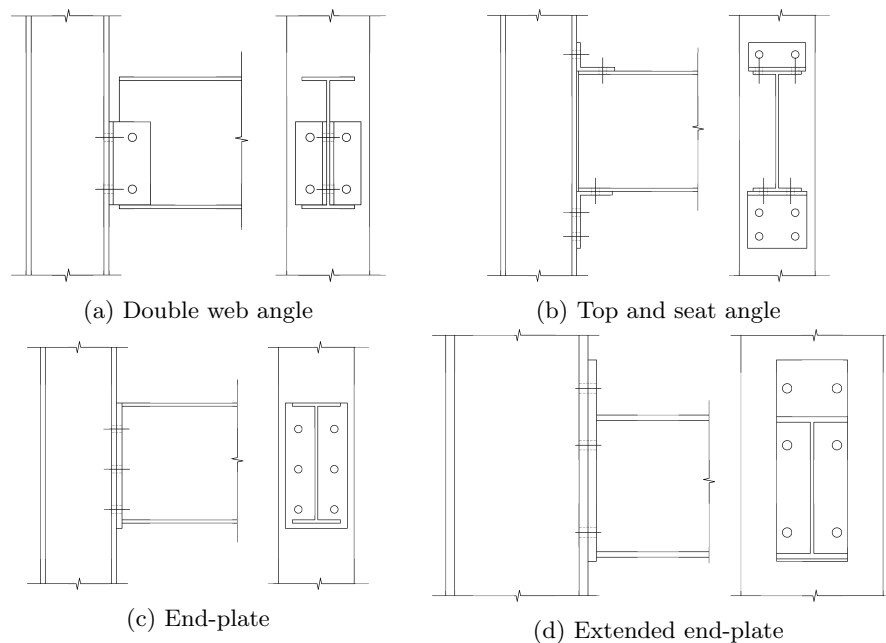
Figure 5.1: Overview of bolted connections

Double web angle connection

A double web angle connection refers to a beam-to-column connection, in which the beam and column profiles are connected by means of two angles that connect the web of the beam with the column. As can be seen in Fig. 5.1a, the connections between beam and web angles and between column and web angle are both bolted in this case.

The results related to this connection were collected by an experimental test carried out by Davison and collected in [8].

Characteristics of the connection:
Angle dimensions: 80x60x8 mm
Angle length: 160 mm
Beam: W 10x15
Column: W 6x16
Fasteners M16 bolts in oversized holes

Top and seat angle connection

A top and seat angle connection refers in this document to a beam-to-column connection, in which the beam and column profiles are joint by means of angles located at the top and bottom of the beam profile. Those angles connect the flanges of the beam profile with the column. In this case, the angles are bolted to both beam and column (see Fig. 5.1b).

The results related to this connection were collected by an experimental test carried out by Davison and collected in [8].

Characteristics of the connection:
Angle length: 120mm
Beam: W 10x15
Column: W 6x16
Fasteners M16 bolts in oversized holes
Seat angle dimensions: 125x75x8 mm
Top angle dimensions: 80x60x8 mm

End-plate

An end-plate connection as its name intuitively indicates, is a connection joint by means of a plate at the end of the profile. In this beam-to-column connection, the plate is welded at the end of the beam profile and the plate is then bolted to the column (see Fig. 5.1c).

The results related to this connection were collected by an experimental test carried out by Davison and collected in [8].

Characteristics of the connection:
Beam: W 10x15
Bolt rows: 3
Column: W 6x16
Fasteners M16 bolts in oversized holes
Plate dimensions: 265x125x12 mm

Extended end-plate

An extended end-plate connection is a variation of an end-plate connection, which differs from the original in that the plate connecting the members can be extended on the tension and/or compression sides to reinforce the connection. Fig. 5.1d shows an example where the extension is done on the tensile side only.

The results related to this connection were collected by an experimental test carried out by Zandonnini and collected in [8].

Characteristics of the connection:
Beam:IPE 300
Bolt rows: 3
Column:-
Fasteners M20 bolts in oversized holes
Plate dimensions: 420x150x18 mm
Plate extension: tension side

Results of the comparison

The graph in Fig. 5.2 shows a comparison of the experimental results of the presented connections. On the vertical axis is displayed a normalized bending moment, this normalization is done assuming that the design of those connections is proportional to the beam cross section, thus the applied bending moment is normalized as a function of the section modulus, such as $\dot{M} = \frac{M}{W_{el}}$. On the horizontal axis the rotation of the complete joint (including the flexibility of all components) is displayed. If failure of any of the components occurred, a black cross is shown, otherwise the $M - \theta$ behaviour ends with a question mark.
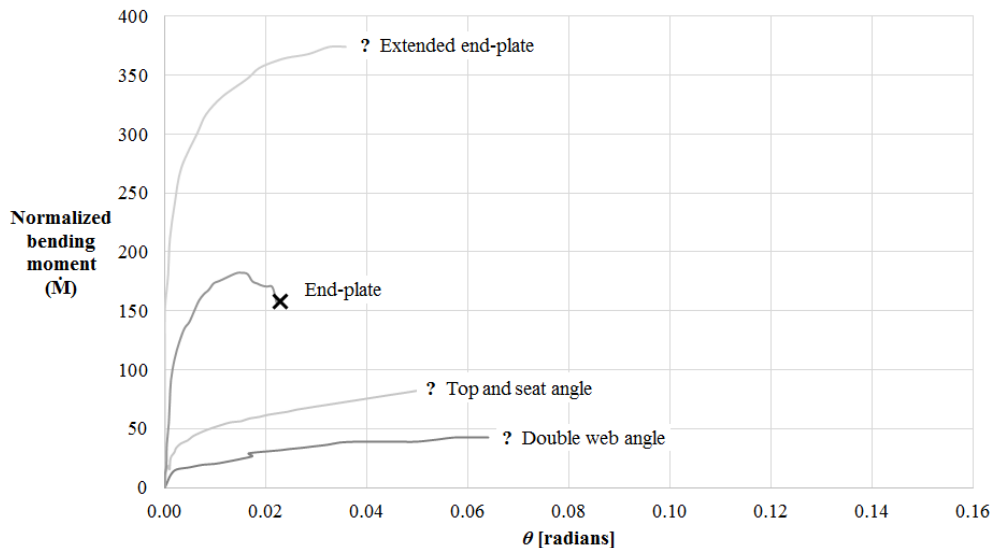
Figure 5.2: $\dot{M} - \theta$ comparison of experimental tests

Discussion of the results

Firstly, it has to be pointed out that the results of Fig. 5.2 have to be read with great care thus, the use of different steel grades or configurations may influence the results.

It may be seen that the different typologies of connections present behaviours that are ususaly classified from rigid to pinned. As is expected, the "pinned" connections (joint with angles) rotate without developing significant moments. On the other hand, rigid and semi-rigid connections develop greater moment resistances. The extended end-plate connection shows the higher moment resistance, and is therefore the chosen reference connection to which the *Snap-Fit connection* is to be compared to.

5.2 Comparison with an extended end-plate

This section compares an extended end-plate and the *Snap-Fit connection*, see Fig. 5.3. The resistance and stiffness of both connections are computed by determining those parameters for each of the components that build up the joint by means of the component method, the minimum of the resistances governs the maximum capacity of the connection and the global rotational stiffness of the connection is estimated according to the mechanical models of Fig. 5.4.

(a) Extended end-plate   (b) *Snap-Fit connection*
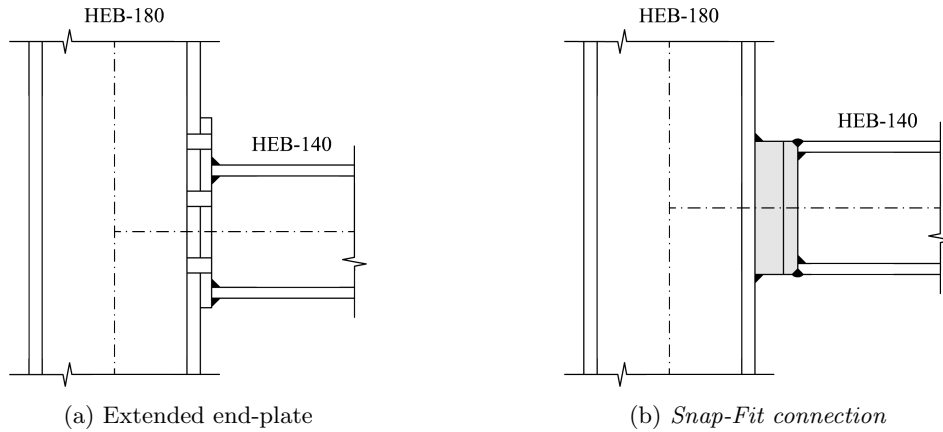
Figure 5.3: Compared connections

(a) Extended end-plate   (b) *Snap-Fit connection*
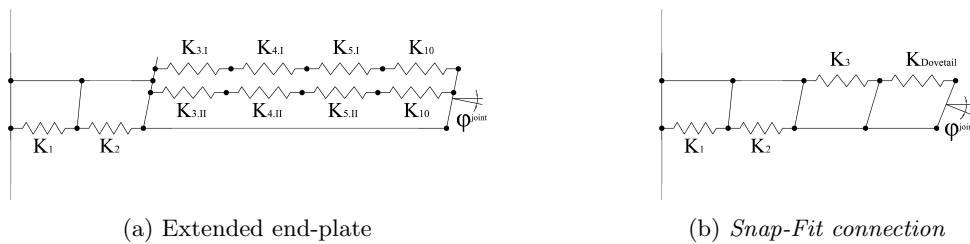
Figure 5.4: Mechanical models

The nomenclature of the translational springs of the mechanical models relate to the basic joint components as described in Table 6.1 of EC3.1-8. Component 1 represents the column web panel in shear; component 2: column web in transverse compression; component 3: column web in transverse tension; component 4: column flange in bending; component 5: end plate in bending and component 10: bolt in tension. The subscripts *I* and *II* refer to the first and second bolt rows respectively. Additionally, $K_{dovetail}$ is added to include the effect of the stiffness of the dovetail in the *Snap-Fit connection*.

The resistances of the components of the extended end-plate are estimated as described on the EC3.1-8. The rotational stiffness is estimated following the same code. Note that not all ele-

ments are included in the mechanical model, thus some elements may limit the resistance of the connection , but do not affect the rotational stiffness due to its relative greater stiffness, e.g. welds.

In relation with the *Snap-Fit connection*, the same procedure is used, the resistance and rotational stiffness of common elements are estimated as determined by EC3. The finite element model Model A-II ,described in section 3 with appropriate BC for this case scenario is used to determine the resistance and rotational stiffness of the *Snap-Fit connection*. This specific component (light shaded in Fig. 5.3b) is referred in this section as "Dovetail" for clarity.

Here an overview of the resistances of the components and its rotational stiffness is presented and the results are discussed. Further detail on the computation of the resistances and stiffness are described in Annex B.1 for the extended end-plate and on Annex B.2 for the *Snap-Fit connection*.

Design resistances of the components of the Extended end-plate:
Tensile loads which can be supported by bolt row I individually

Column flange in bending	$222.37kN$
Column web in tension	$220.45kN$
End-plate in bending	$122.10kN$
	$F_{I.min} = 122.10kN$

Tensile loads which can be supported by bolt row II individually

Beam web in tension	$277.59kN$
Column flange in bending	$222.37kN$
Column web in tension	$220.45kN$
End-plate in bending	$182.00kN$
	$F_{II.min} = 182.00kN$

Tensile loads which can be supported by bolt rows I and II as a group

Column flange in bending	$392.64kN$
Column web in tension	$280.73kN$
	$F_{I.II.min} = 280.73kN$

To ensure equilibrium the compression internal forces are compared with the tensile forces

Beam flange and web in compression	$450.54kN$
Column web in compression	$277.43kN$
Column web panel in shear	$247.15kN$
	$F_{c.min} = 247.15kN$

The resistance of the column web panel in shear limits the maximal load that can be supported, the force in the second bolt row is estimated to ensure equilibrium:

$$F_{II.min.red} = F_{c.min} - F_{I.min} = 125.05kN$$

The design bending resistance of the joint is estimated as follows:

$$\mathbf{M_{j.Rd}} = F_{I.min}\,h_I + F_{II.min.red}\,h_{II} = \mathbf{31.79kNm}$$

Rotational stiffness of the components of the Extended end-plate:

Column web panel in shear	$k_1 = 1312.17 kN/mm$
Column web panel in compression	$k_2 = 1904.67 kN/mm$
Column web in tension bolt row I	$k_{3.I} = 972.97 kN/mm$
Column web in tension bolt row II	$k_{3.II} = 972.97 kN/mm$
Column flange in bending bolt row I	$k_{4.I} = 17235.36 kN/mm$
Column flange in bending bolt row II	$k_{4.II} = 17235.36 kN/mm$
End-plate in bending bolt row I	$k_{5.I} = 3131.11 kN/mm$
End-plate in bending bolt row II	$k_{5.I} = 4031.87 kN/mm$
Bolts in tension	$k_{10} = 1256.00 kN/mm$

Effective stiffness per bolt row (components in series):

$$k_{eff.I} = \frac{1}{\frac{1}{k_{3.I}} + \frac{1}{k_{4.I}} + \frac{1}{k_{5.I}} + \frac{1}{k_{10}}} = 454.27 kN/mm$$

$$k_{eff.II} = \frac{1}{\frac{1}{k_{3.II}} + \frac{1}{k_{4.II}} + \frac{1}{k_{5.II}} + \frac{1}{k_{10}}} = 469.48 kN/mm$$

Equivalent stiffness coefficient related to the tensile part of the joint (components in parallel):

$$z_{eq} = \frac{k_{eff.I}\, h_I^2 + k_{eff.II}\, h_{II}^2}{k_{eff.I}\, h_I + k_{eff.II}\, h_{II}} = 135.51 mm$$

$$k_{eq} = \frac{k_{eff.I}\, h_I + k_{eff.II}\, h_{II}}{z_{eq}} = 876.02 kN/mm$$

Stiffness of the joint:

$$\mathbf{S_{j.ini}} = \frac{z_{eq}^2}{\frac{1}{k_{eq}} + \frac{1}{k_1} + \frac{1}{k_2}} = \mathbf{7441 kNm/rad}$$

$$\mathbf{S_j} = \frac{z_{eq}^2}{\mu\left(\frac{1}{k_{eq}} + \frac{1}{k_1} + \frac{1}{k_2}\right)} \quad \text{with} \quad \mu = \left(\frac{1.5 M_{Ed}}{M_{Rd}}\right)^{2.7}$$

Design resistances of the components of the *Snap-Fit connection*:

Tensile loads which can be supported

Column flange in bending	$90.48 kN$
Column web in tension	$242.56 kN$
Dovetail in bending	$285.41 kN$
Welds in tension	$68.60 kN$
	$F_{I.min} = 68.60 kN$

To ensure equilibrium the compression internal forces are compared with the tensile forces

Beam flange and web in compression	$450.54kN$
Column web in compression	$258.52kN$
Column web panel in shear	$247.15kN$
	$F_{c.min} = 247.15kN$

The resistance of the welds limits the maximal load that can be supported. The design bending resistance of the joint is estimated as follows:

$$\mathbf{M_{j.Rd}} = F_{t.min} \, z_{dovetail} = \mathbf{9.24kNm}$$

Rotational stiffness of the components of the the *Snap-Fit connection*:

Column web panel in shear	$k_1 = 1198.63kN/mm$	
Column web panel in compression	$k_2 = 1693.99kN/mm$	
Column web in tension	$k_3 = 1687.58kN/mm$	
Dovetail in bending	$k_{Dovetail} = f(F_{t.dovetail})$	see Fig. 5.5
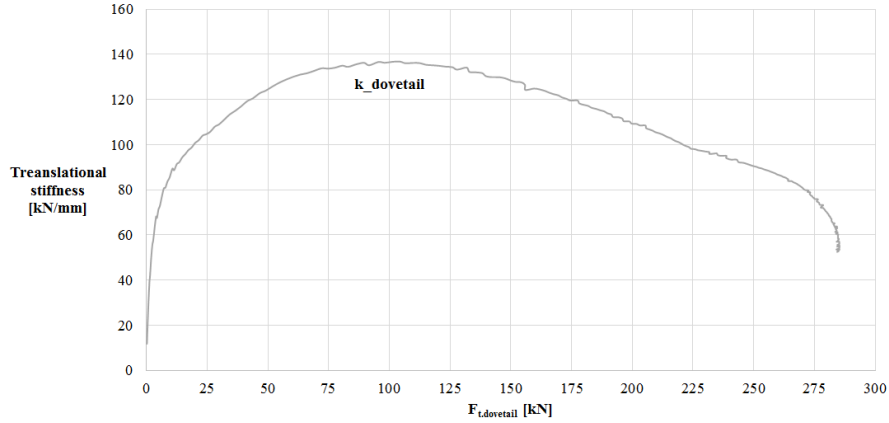
Figure 5.5: Non-linear relation of the $k_{dovetail}$ as a function of the applied tensile force

Stiffness of the joint:
Note, that in this case a failure of the weld may be expected, a brittle failure which will probably show no ductility. In order to represent this behaviour. The stiffeness modification factor μ, which accounts for the ductility on the last third of M_{Rd}. Is not related to the M_{Rd} of the joint determined by the failure of the weld but to the next failure mechanism, in this case, the column flange.

$$\mathbf{S_{j.ini}} = \frac{z_{eq}^2}{\frac{1}{k_1} + \frac{1}{k_2} + \frac{1}{k_3} + \frac{1}{k_{Dovetail}}}$$

$$\mathbf{S_j} = \frac{z_{eq}^2}{\mu \left(\frac{1}{k_1} + \frac{1}{k_2} + \frac{1}{k_3} + \frac{1}{k_{Dovetail}} \right)} \quad \text{with} \quad \mu = \left(\frac{1.5M_{Ed}}{M_{Rd.flange}} \right)^{2.7}$$

$$M_{Rd.flange} = F_{fc.Rd} \left(h_b + \frac{\sqrt{2}a_{fc}}{2} \right) = 13.11kNm$$

Discussion of the results

Fig. 5.6 compares the $M - \theta$ behaviour of the two connections. In dark grey the behaviour of the extended end-plate estimated as described by EC3.1-8. The *Snap-Fit connection* in lighter grey exhibits a brittle behaviour due to the premature failure of the welds between the connection and the flange of the column. As specified by EC3.1-8. The last two thirds of the $M_{j.Rd}$ may be represented by S_j instead of by a $S_{j.ini}$, which means that the last third of the resistance of the connection is assumed that will have a ductile behaviour. However on this case, in which the welds are dominating, the 2/3 of $M_{j.Rd}$ to which refer to develop this ductility have not been referred to the failure load of the welds but to the following failure mechanism if the welds were not to be governing. As consequence it is shown how the connection fails in a brittle manner, thus in accordance with a weld failure.
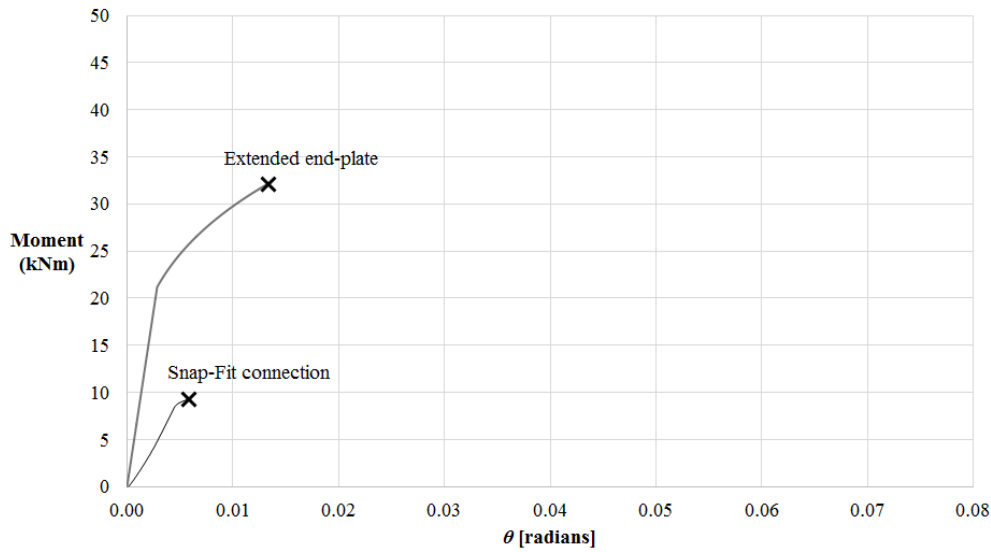
Figure 5.6: M-θAnalytical comparison of the connections

Comparison of the connections with stiffeners

This section presents similarly to section 5.2 a comparison of the two connections, in this case they include horizontal stiffeners in the compression and tension sides, see Fig. 5.7. As consequence the mechanical models of the connections are modified to account for the greater stiffness of the column web (see Fig. 5.8).

Design resistances of the components of the Extended end-plate:
Tensile loads which can be supported by row I individually

Column flange in bending	$207.48 kN$
Colum web in tension	$219.73 kN$
End-plate in bending	$122.10 kN$
	$F_{I.min} = 122.10 kN$

(a) Extended end-plate with stiffeners   (b) *Snap-Fit connection* with stiffeners
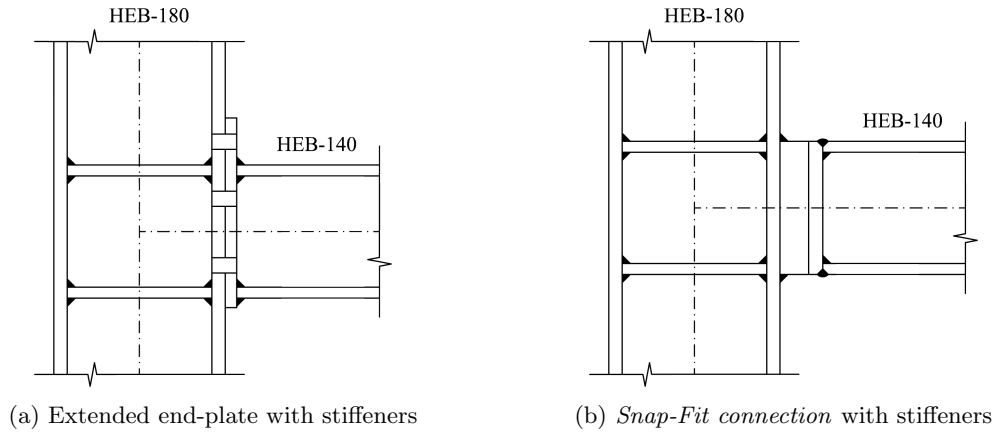
Figure 5.7: Compared connections with stiffeners

(a) Extended end-plate with stiffeners   (b) *Snap-Fit connection* with stiffeners
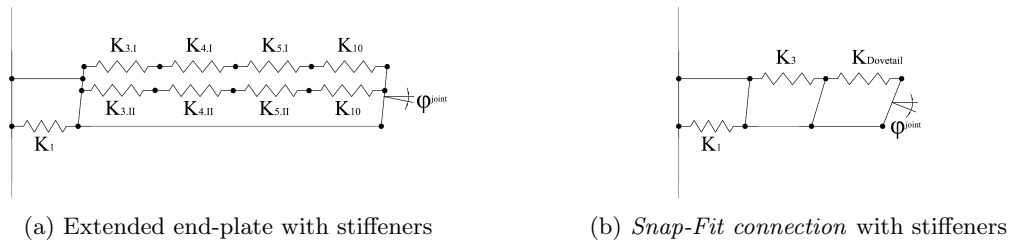
Figure 5.8: Mechanical models with stiffeners

Tensile loads which can be supported by row II individually

Beam web in tension	$277.55kN$
Column flange in bending	$207.48kN$
Colum web in tension	$219.73kN$
End-plate in bending	$182.00kN$

$$F_{II.min} = 182.00kN$$

To ensure equilibrium the compression internal forces are compared with the tensile forces

Beam flange and web in compression	$450.54kN$
Column web in compression	$(Sufficient)$
Column web panel in shear	$300.82kN$

$$F_{c.min} = 300.82kN$$

The resistance of the column web panel in shear limits the maximal load that can be supported, the force in the second bolt row is estimated to ensure equilibrium:

$$F_{II.min.red} = F_{c.min} - F_{I.min} = 178.72kN$$

The design bending resistance of the joint is estimated as follows:

$$\mathbf{M_{j.Rd}} = F_{I.min}\,h_I + F_{II.min.red}\,h_{II} = \mathbf{37.10kNm}$$

Rotational stiffness of the components of the Extended end-plate:

Column web panel in shear	$k_1 = 1312.17 kN/mm$
Column web panel in compression	$k_2 \approx \infty$
Column web in tension bolt row I	$k_{3.I} = 972.97 kN/mm$
Column web in tension bolt row II	$k_{3.II} = 972.97 kN/mm$
Column flange in bending bolt row I	$k_{4.I} = 17235.36 kN/mm$
Column flange in bending bolt row II	$k_{4.II} = 17235.36 kN/mm$
End-plate in bending bolt row I	$k_{5.I} = 3131.11 kN/mm$
End-plate in bending bolt row II	$k_{5.I} = 4031.87 kN/mm$
Bolts in tension	$k_{10} = 1256.00 kN/mm$

Effective stiffness per bolt row (components in series):

$$k_{eff.I} = \frac{1}{\frac{1}{k_{3.I}} + \frac{1}{k_{4.I}} + \frac{1}{k_{5.I}} + \frac{1}{k_{10}}} = 454.27 N/mm$$

$$k_{eff.II} = \frac{1}{\frac{1}{k_{3.II}} + \frac{1}{k_{4.II}} + \frac{1}{k_{5.II}} + \frac{1}{k_{10}}} = 469.48 kN/mm$$

Equivalent stiffness coefficient related to the tensile part of the joint (components in parallel):

$$z_{eq} = \frac{k_{eff.I}\, h_I^2 + k_{eff.II}\, h_{II}^2}{k_{eff.I}\, h_I + k_{eff.II}\, h_{II}} = 135.51 mm$$

$$k_{eq} = \frac{k_{eff.I}\, h_I + k_{eff.II}\, h_{II}}{z_{eq}} = 876.02 kN/mm$$

Stiffness of the joint:

$$\mathbf{S_{j.ini}} = \frac{z_{eq}^2}{\frac{1}{k_{eq}} + \frac{1}{k_1}} = \mathbf{9494 kNm/rad}$$

$$\mathbf{S_j} = \frac{z_{eq}^2}{\mu \left(\frac{1}{k_{eq}} + \frac{1}{k_1} \right)} \quad \text{with} \quad \mu = \left(\frac{1.5 M_{Ed}}{M_{Rd}} \right)^{2.7}$$

Design resistances of the components of the *Snap-Fit connection* with stiffeners:

Tensile loads which can be supported

Column flange in bending	$325.70 kN$
Column web in tension	$242.56 kN$
Dovetail in bending	$285.41 kN$
Welds in tension	$249.46 kN$
	$F_{I.min} = 242.56 kN$

To ensure equilibrium the compression internal forces are compared with the tensile forces

Beam flange and web in compression	$450.54kN$
Column web in compression	$(sufficient)$
Column web panel in shear	$300.82kN$

$$F_{c.min} = 300.82kN$$

The resistance of the Column web in tension limits the maximal load that can be supported. The design bending resistance of the joint is estimated as follows:

$$\mathbf{M_{j.Rd}} = F_{I.min}\, z_{weld} = \mathbf{36.38kNm}$$

$$z_{weld} = h_b + \frac{2\sqrt{2}\,a_{fb}}{2} = 149.90mm$$

Rotational stiffness of the components of the the *Snap-Fit connection*:

Column web panel in shear	$k_1 = 1198.63kN/mm$
Column web panel in compression	$k_2 \approx \infty$
Column web in tension	$k_3 = 1687.58kN/mm$
Dovetail in bending	$k_{Dovetail} = f(F_{t.dovetail})$ see Fig. 5.5

Stiffness of the joint:

$$\mathbf{S_{j.ini}} = \frac{z_{eq}^2}{\frac{1}{k_1} + \frac{1}{k_{Dovetail}}}$$

$$\mathbf{S_j} = \frac{z_{eq}^2}{\mu\left(\frac{1}{k_1} + \frac{1}{k_{Dovetail}}\right)} \quad \text{with} \quad \mu = \left(\frac{1.5M_{Ed}}{M_{Rd}}\right)^{2.7}$$
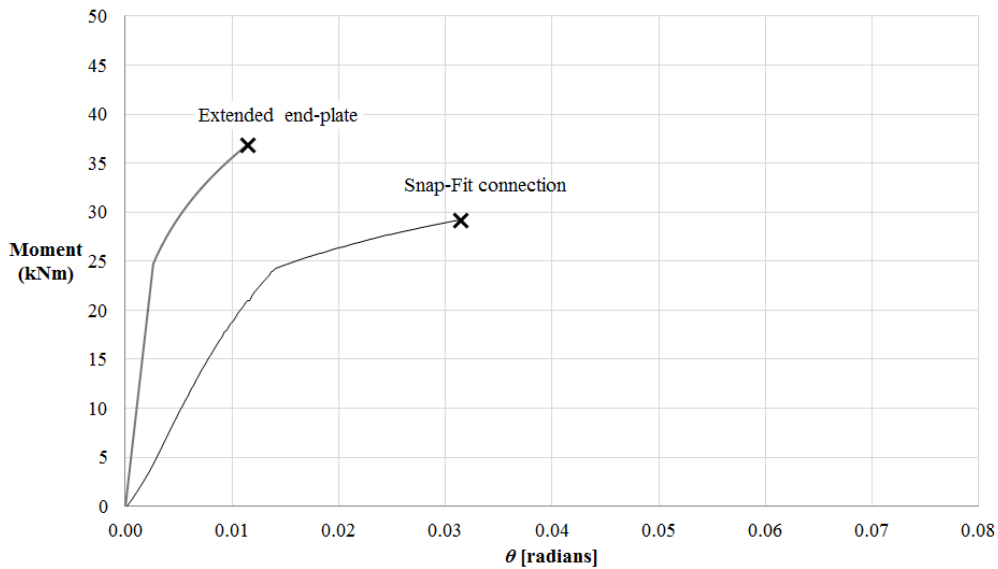
Figure 5.9: M-θ Analytical comparison of the connections with stiffeners

Discussion of the results

It is shown in Fig. 5.9 that rigidizing the flanges of the column affects both the resistance of the welds and the column flanges of connection, thus the resistance of the joint connected with the *Snap-Fit connection* is significantly increased resect to the earlier case.

It may be noted that, both bending resistances are of the same order or magnitude, Extended end-plate has a $M_{max} = 37.10kNm$ and the *Snap-Fit connection* $M_{max} = 36.38kNm$. However on the graph of Fig. 5.9 it may be seen that the *Snap-Fit connection* is limited at a bending resistance of $M = 30kNm$. This may be explained, by the rotation capacity of the connection. From the "rotational stiffness of the components of the *Snap-Fit connection*", may be seen that the stiffness of the "Dovetail" component is relatively lower than the rest of components, thus this component being responsible for that ductility, the rotation of that component has to be limited at a rotation of about 0.3 radians because according to the numerical model of section 3.5 at this stage its critical plastic strain is reached; Meaning that, the lack of more rotation capacity limits the total bending resistance of the joint.

On the other hand, it also appreciated that the introduction of such a component introduces a great amount of ductility on a connection while achieving high bending moments.

Chapter 6

Parametric study

This chapter presents a parametric study of the geometry of the *Snap-Fit connection*. It aims to gain insight on the behaviour of the connection and optimize the performance of the connection by modifying geometric parameters. The procedure is divided on the following tasks:

- Description of the geometrical parameters

- Sensitivity of the parameters

- Combination of parameters

The two latter tasks are simulated with Model A-II (see section 3.5) with a friction coefficient equal to 0.07, simulating a lubricant between the parts and the correspondent parametric adaptations to each of the configurations, the models are meshed with an average mesh size of 4mm due to its good balance between accuracy and computational cost. Despite the fact that the ductility shown by the simulations is questionable. Thus as shown in section 3.5 the prediction of risk of failure with this model may be affected both by the mesh size and the location of the critical plastic strain.

6.1   Description of the geometrical parameters

This section is dedicated to define and describe the parameters that take part in this study. The geometry of the connection can be described with different variables, in this case due to the modelling procedures used to create the computational model seven parameters are used to describe and control the geometry of the connection.

Those parameters are graphically represented in Fig. 6.1. The first parameter **A**, is the vertical offset of the shoulder of the dovetail, which is constant along the height of the connection. The second parameter, **B**, refers to the tapered offset of the dovetail. The third parameter, **C**, is the straight length of the dovetail. The fourth, **D**, is half of the greater width of the dovetail in the non-tapered part. The fifth, **E**, is the base thickness of the connection; note that it is assumed that both female and male parts of the connection are assumed to have equal base thickness. The sixth parameter **F**, refers to the thickness of the dovetail. Finally, **G**, is the total width of the connection.

(a) Female part   (b) Male part
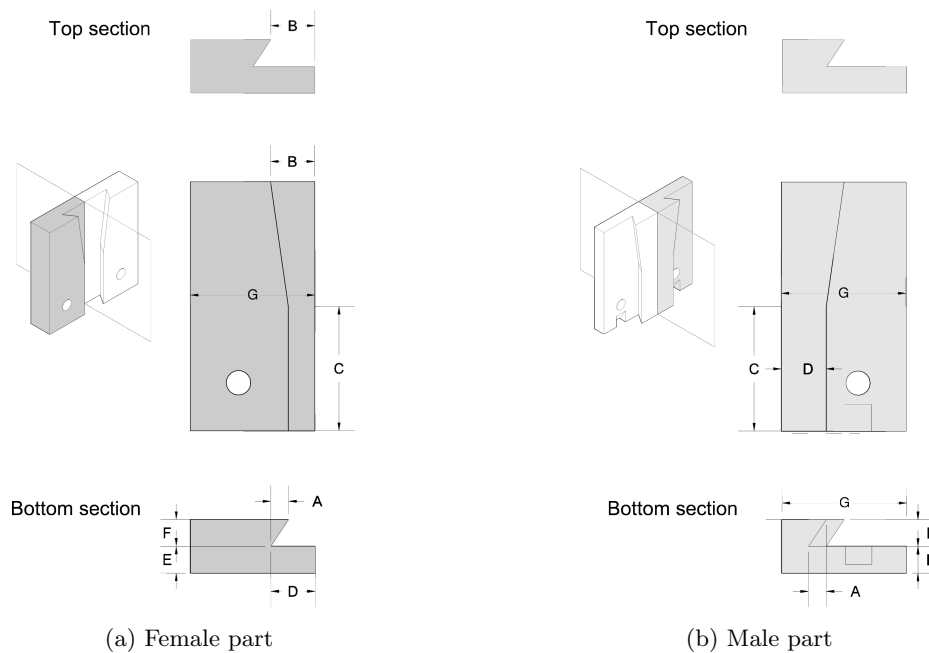
Figure 6.1: Geometrical control parameters

6.2   Sensitivity of the parameters

This section studies the influence of the overall behaviour due to single changes of geometrical parameters. The seven parameters described in the previous sub-section are modified individually as follows:

The first parameter **A** has an original length of $10.0\,mm$, four simulations are performed with values equal to $[5.0, 7.5, 12.5, 15.0]$. In Fig. 6.2 a graphic representation of those changes is presented and in Fig. 6.3 the $M - \theta$ behaviours corresponding to the simulations with changes are displayed in different shades of gray, the parameter corresponding to the original design is highlighted.

The second parameter **B** has an original length of $15\,mm$, variations are performed with values equal to $[5, 10, 15, 20, 25]$. In Fig. 6.4 a graphic representation of those changes is presented and Fig. 6.5 shows the $M - \theta$ behaviour comparison.

The third parameter **C** has an original length of $70\,mm$, which is varied to $[50, 60, 80, 90]$. Fig. 6.6 and Fig. 6.7 present the variations and their effects on the $M - \theta$ behaviour.

Parameter **D** has an original length of $25.0\,mm$, four simulations are performed with values equal to $[20.0, 22.5, 27.5, 30.0]$. In Fig. 6.8 a graphic representation of those changes is presented and in Fig. 6.9 the correspondent behaviour results.

The fifth parameter **E** has an original length of $15.0\,mm$, four simulations are performed with values equal to $[5.0, 7.5, 10.0, 12.5]$. In Fig. 6.10 a graphic representation of those changes is presented and Fig. 6.11 shows the $M - \theta$ behaviour of those variations.

The sixth parameter **F** has an original length of $15.0\,mm$, four simulations are performed with values equal to $[5.0, 7.5, 10.0, 12.5]$. In Fig. 6.12 a graphic representation of those changes is presented and in Fig. 6.13 the $M - \theta$ behaviours are compared.
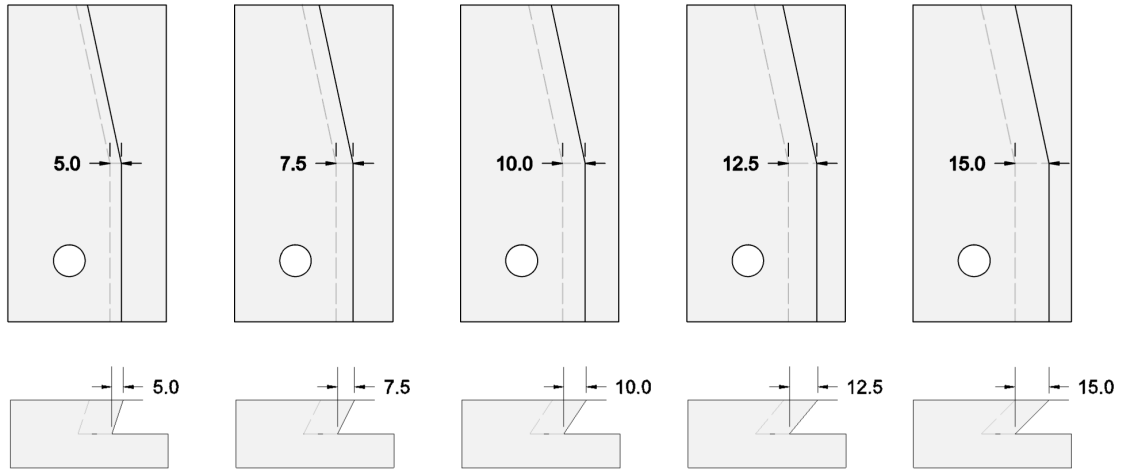
Figure 6.2: Graphic representation of the **A** variability
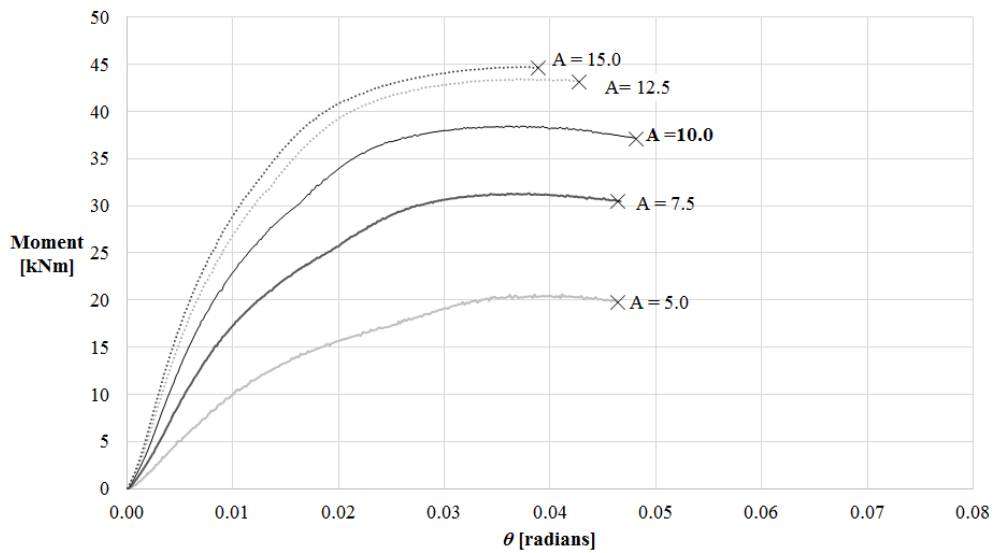
Figure 6.3: $M - \theta$ comparison for **A** variability
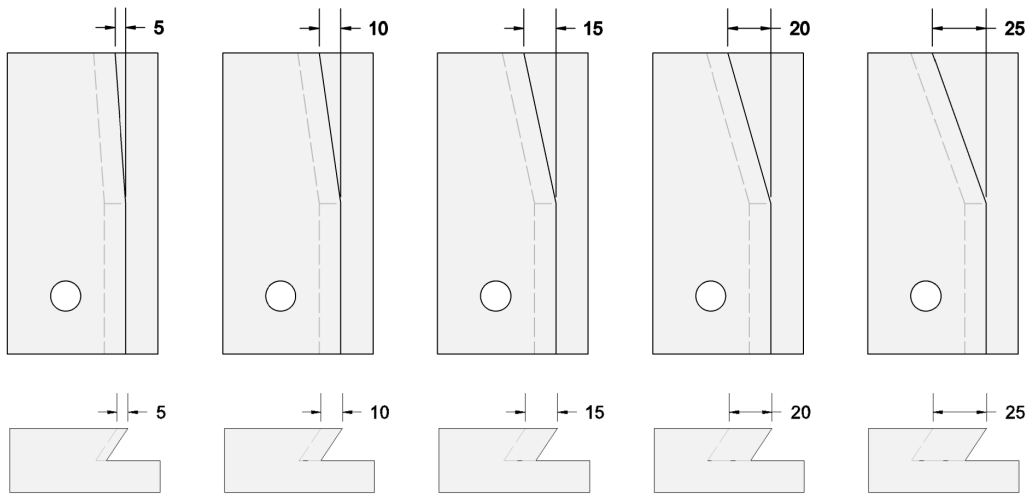
Figure 6.4: Graphic representation of the **B** variability
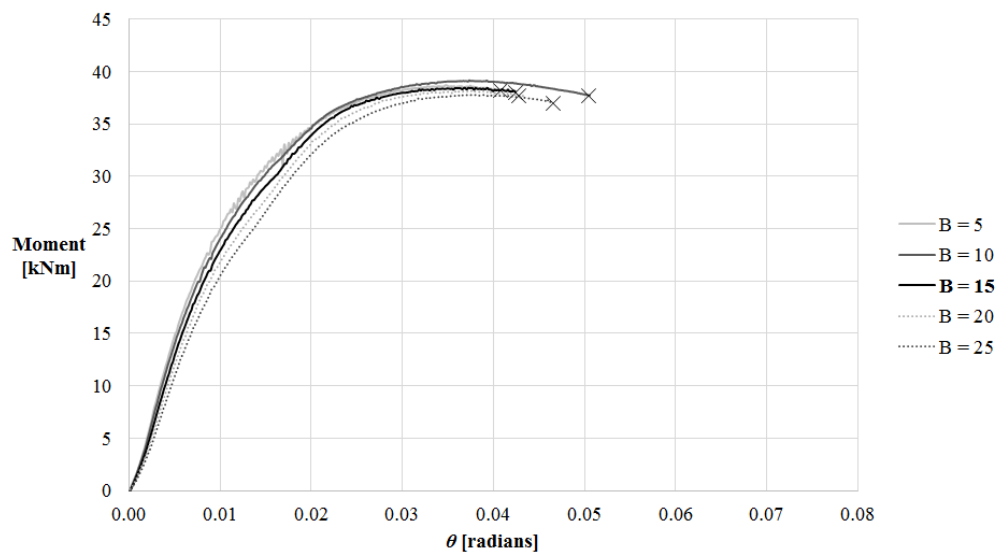
Figure 6.5: $M - \theta$ comparison for **B** variability
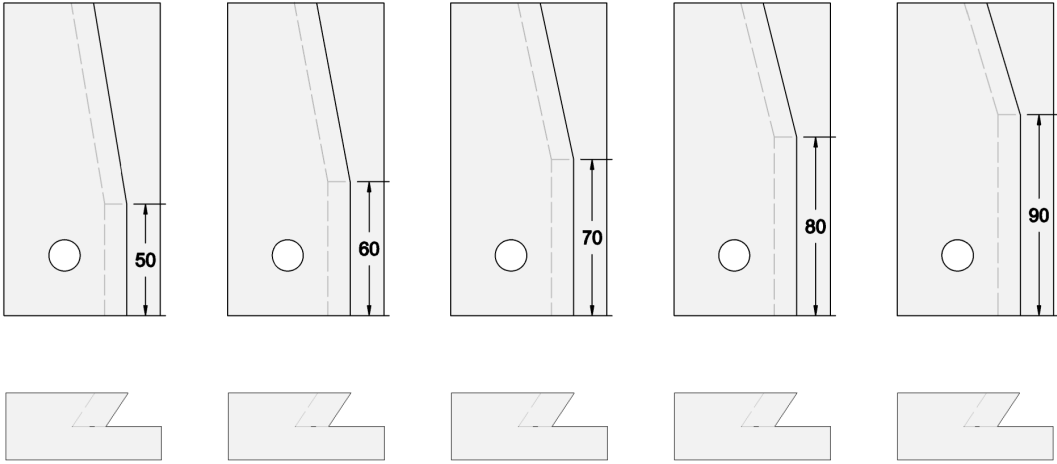
Figure 6.6: Graphic representation of the **C** variability
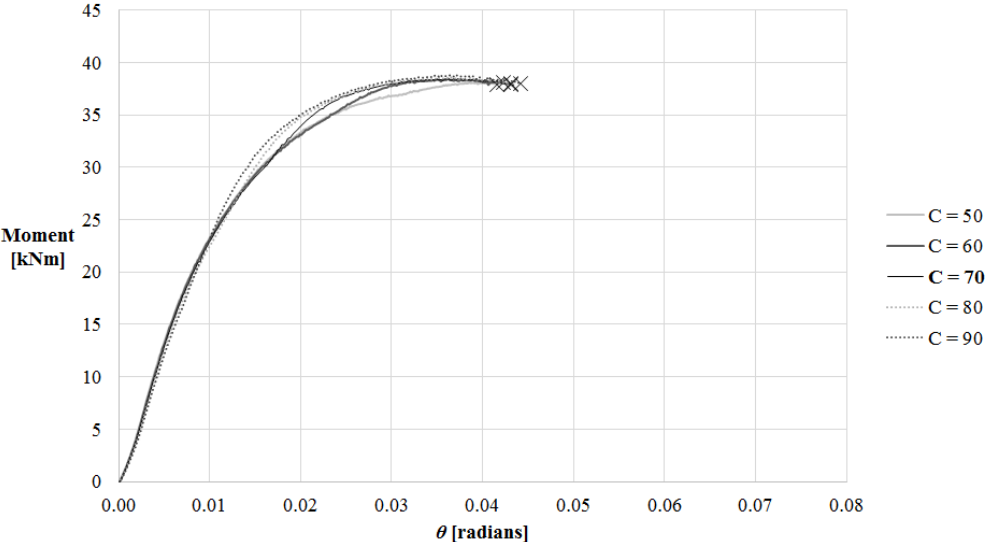
Figure 6.7: $M - \theta$ comparison for **C** variability
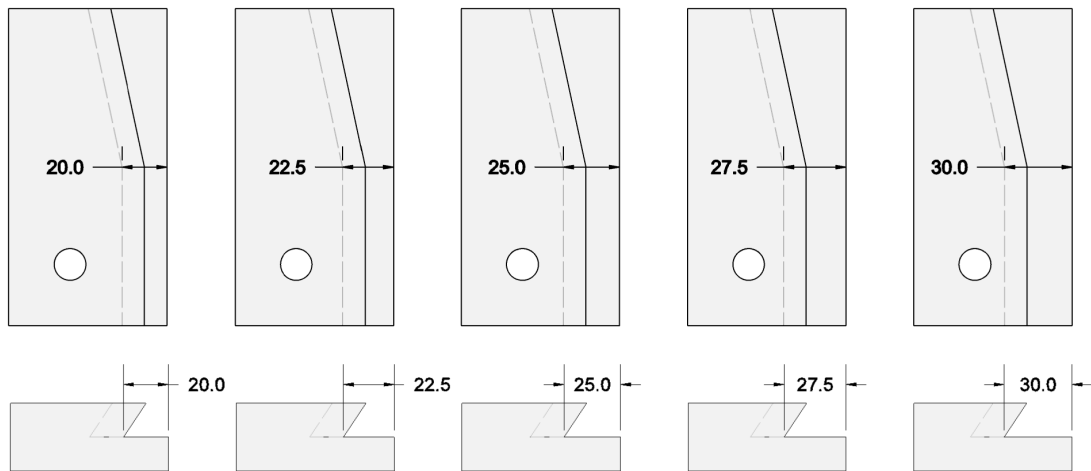
Figure 6.8: Graphic representation of the **D** variability
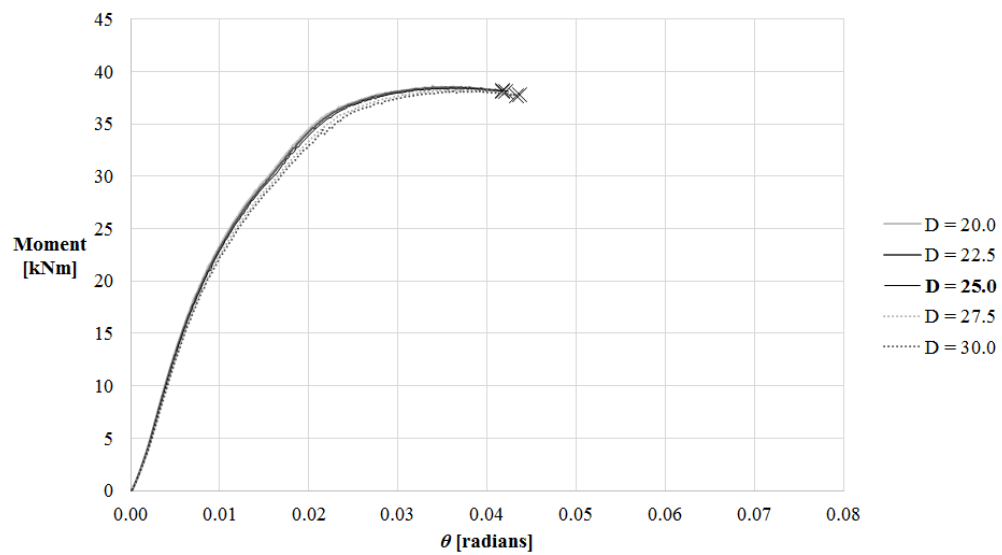
Figure 6.9: $M - \theta$ comparison for **D** variability
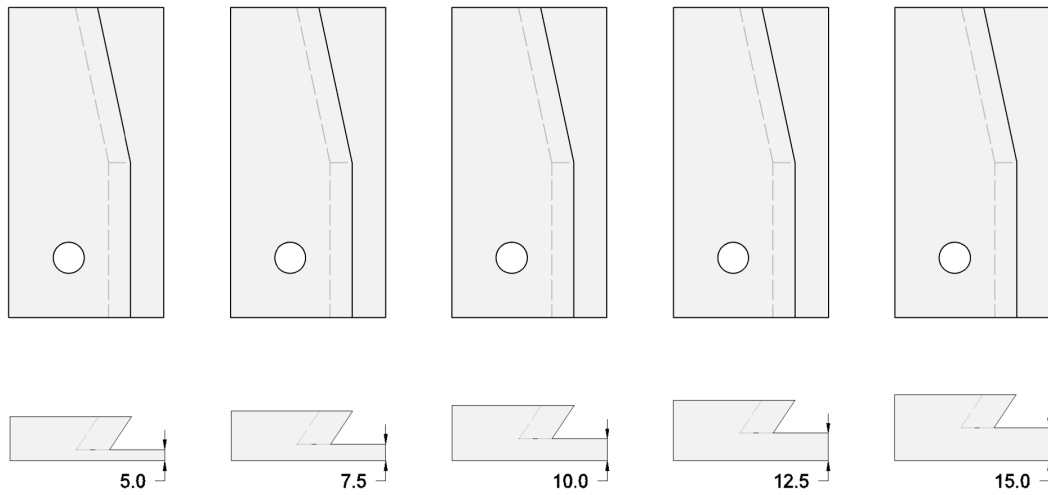
Figure 6.10: Graphic representation of the **E** variability
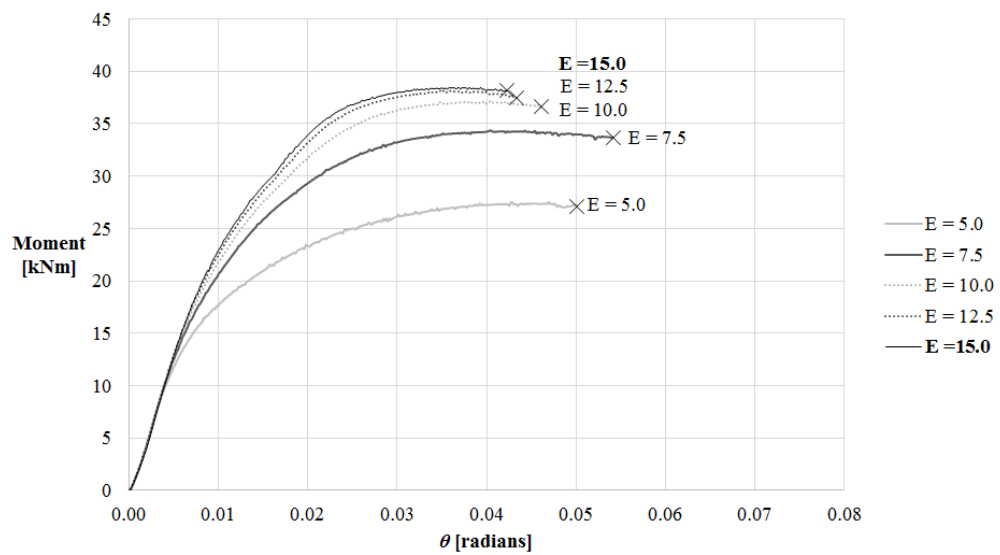
Figure 6.11: $M - \theta$ comparison for **E** variability
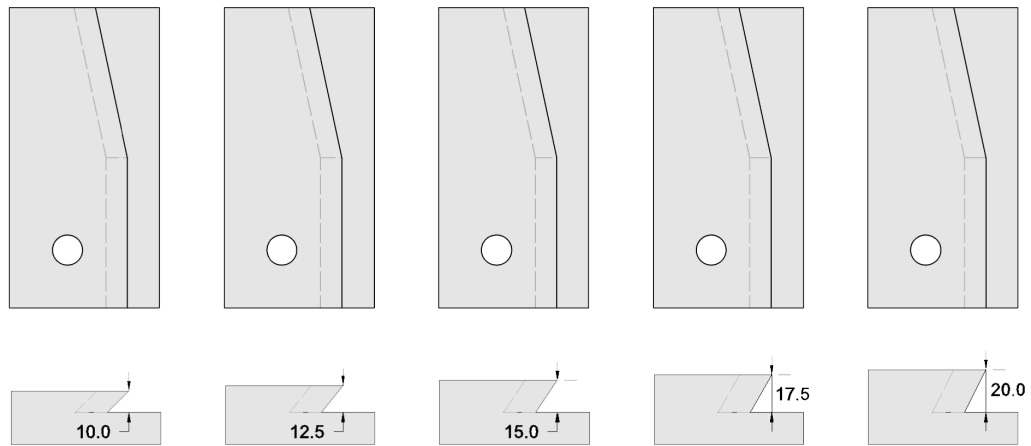
Figure 6.12: Graphic representation of the **F** variability
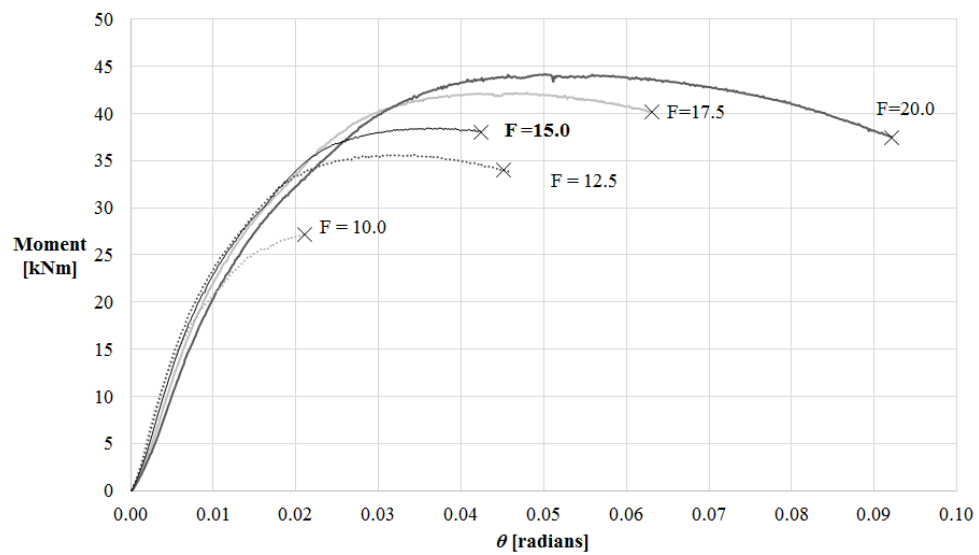
Figure 6.13: $M - \theta$ comparison for **F** variability

The seventh and last parameter **G** has an original length of $70.0\,mm$, four simulations are performed with values equal to $[40.0, 45.0, 50.0, 60.0]$. In Fig. 6.14 a graphic representation of those changes is presented and in Fig. 6.15 a $M - \theta$ behaviour comparison is shown.
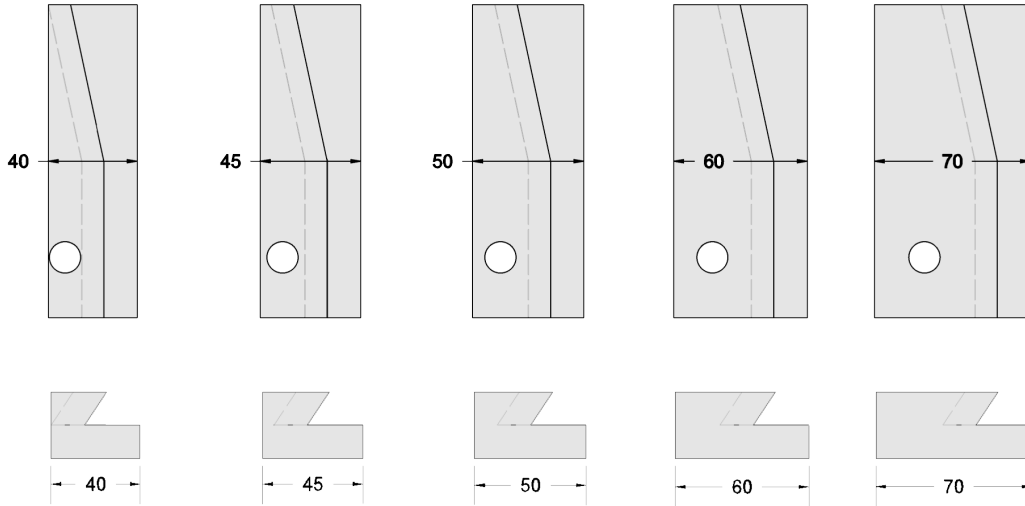
Figure 6.14: Graphic representation of the **G** variability
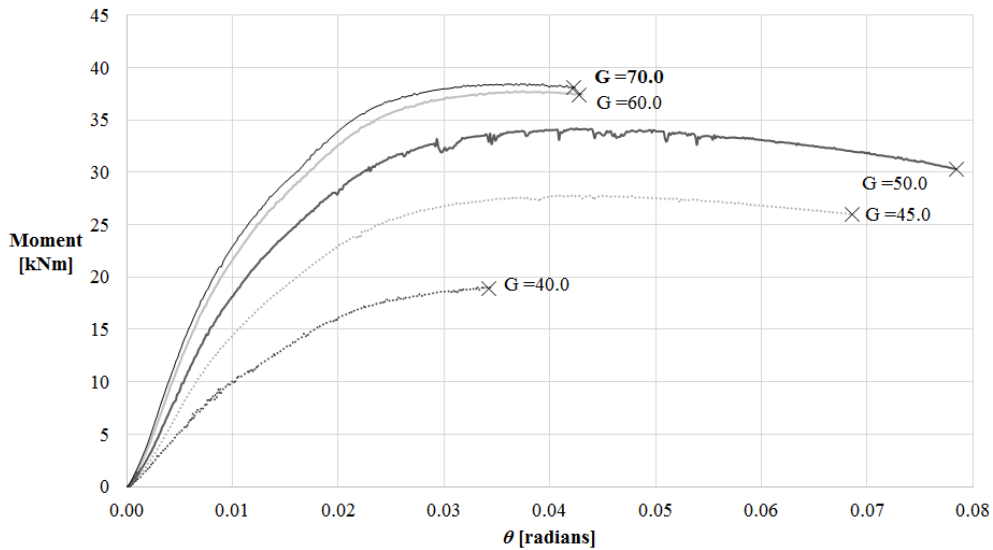
Figure 6.15: $M - \theta$ comparison for **G** variability

Discussion of the results

It may be seen that the individual variability of parameters **B, C** and **D** have no influence on the overall behaviour of the connection when varied within those ranges. This may be explained because non of them affect directly the amount of material that yields. On the other hand parameters **A, E, F** and **G** directly affect the bending capacity of the connection and its ductility.

The first case, parameter **A**, has a direct impact on the maximum bending capacity and stiffness of the connection. With an increase of **A** a related increase of M_{max} and stiffness is observed, thus

the amount of material that is activated is greater. However it is remarkable that the increase of bending capacity from 12.5 to 15.0 is marginal. This may be explained, by the interaction of other geometrical parameters, the relation between the height and length of the shoulder of the dovetail becomes too large; the shoulders are too slender and as consequence the material of the shoulder does not completely yield (see Fig. 6.16).

(a) **A** 12.5 mm (b) **A** 15.0 mm
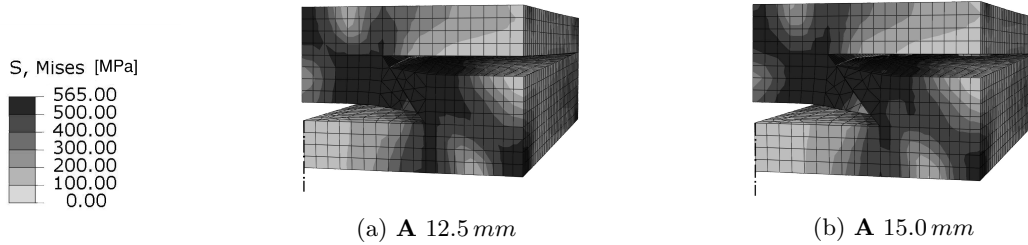
Figure 6.16: Comparison of σ field of parameter **A**

The second parameter of influence, parameter **E**, relates to the base thickness of the connection. It may be seen from Fig. 6.11 that the resistance is not affected when decreasing the value up to 10.0 mm however when the base thickness is thinner becomes critical before the dovetail develops its resistance see Fig. 6.17.

(a) **E** 5.0 mm (b) **E** 7.5 mm (c) **E** 15.0 mm
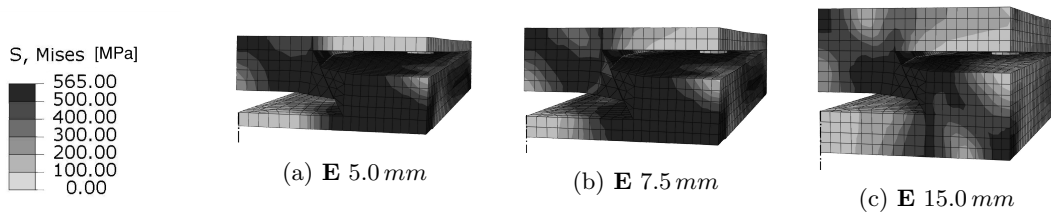
Figure 6.17: Comparison of σ field of parameter **E**

Parameter **F** relates to the thickness of the dovetail, as the parameter **A** remains constant implicitly changes the inclination of the dovetail. Smaller values provide smaller areas of the shoulders of the dovetail and consequently smaller capacities. When **F** is increased, the capacity and the ductility rise. This may be explained by two reasons, firstly, the area able to yield is greater and consequently also its capacity. Secondly, when the height of the dovetail is enlarged, the inclination becomes less pronounced, thus allowing larger rotations (see Fig. 6.18).

(a) **F** 10.0 mm (b) **F** 15.0 mm (c) **F** 20.0 mm
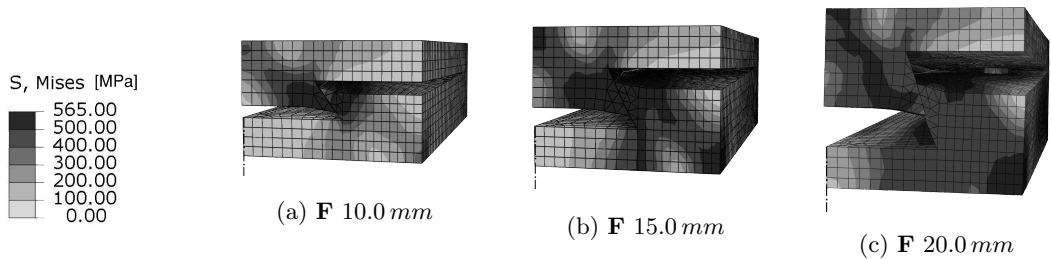
Figure 6.18: Comparison of σ field of parameter **F**

Last parameter, which shows an influence on the behaviour is parameter **G**, related to the complete width of the connection. Fig. 6.15 shows that by reducing **G** the capacity of the connection is decreased and its stiffness is lowered. It is remarkable that within this range some specific widths seem to provide extra ductility. This is explained by the relation between the the widths of the female and male parts and its end distances. When the width of the connection is small such

as in **G**=40, the end distance is determining, when the end distance is large enough such as in **G**=60 this part is not affected and the shoulder of the dovetail is determining, however when the relation between end distance and the shoulder of the dovetail allows for a simultaneous yielding, the connection provides extra ductility (see Fig. 6.19).

S, Mises [MPa]
565.00
500.00
400.00
300.00
200.00
100.00
0.00

(a) **G** $40.0\,mm$ (b) **G** $50.0\,mm$ (c) **G** $60.0\,mm$
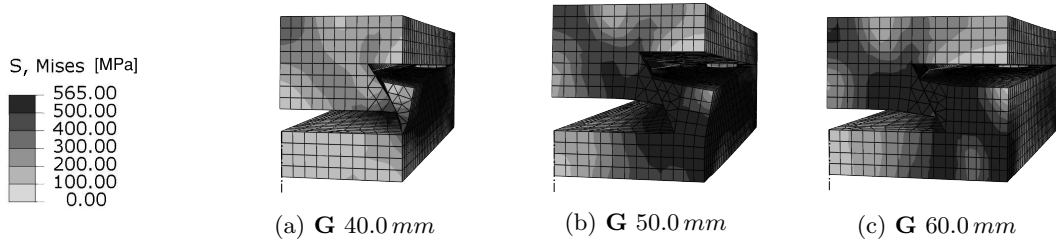
Figure 6.19: Comparison of σ field of parameter **G**

6.3 Combination of parameters

In the previous section the influence of geometrical parameters is studied individually, it has been seen that the effects are a consequence of the combination of geometric parameters. Therefore this section is devoted to study the effects when several parameters are varied simultaneously.

Here only those parameters showing a relevant influence are taken into consideration. Moreover the range of study is limited to a connection of a thickness of $30.0\,mm$. Indirectly parameters **E** and **F** become a function of each other, such that $\mathbf{E} = \mathbf{F} - 30.0\,mm$. The combination of parameters to be studied are based on the results gathered from the previous section.

Parameter **A**, the dovetail vertical offset, is varied to values equal to $[10.0, 15.0, 20.0]$, parameter **F**, thickness of the dovetail, is varied with $[15.0, 17.5, 20.0, 22.5]$ and the width of the connection, **G**, is varied with $[50.0, 60.0, 70.0]$ The combinations are to be performed with the rest of parameters defined as on the original design such as that $\mathbf{B} = 15.0$, $\mathbf{C} = 70.0$ and $\mathbf{D} = 25.0$. The parameters of study are combined with any other parameter varied creating out of each combination a new design. Where every entry of the following matrix represents a design of study. The subscripts of the variables relate to the values in an increasing order, for instance the variability of parameter **A** is expressed as: $_{A1} = 10.0$, $_{A2} = 15.0$ and $_{A3} = 20.0$.

$$[D]_{A,F,G} = \begin{pmatrix} D_{A1,F1,G1} & D_{A1,F2,G1} & D_{A1,F3,G1} & D_{A1,F4,G1} \\ D_{A2,F1,G1} & D_{A2,F2,G1} & D_{A2,F3,G1} & D_{A2,F4,G1} \\ D_{A3,F1,G1} & D_{A3,F2,G1} & D_{A3,F3,G1} & D_{A3,F4,G1} \\ D_{A1,F1,G2} & D_{A1,F2,G2} & D_{A1,F3,G2} & D_{A1,F4,G2} \\ D_{A2,F1,G2} & D_{A2,F2,G2} & D_{A2,F3,G2} & D_{A2,F4,G2} \\ D_{A3,F1,G2} & D_{A3,F2,G2} & D_{A3,F3,G2} & D_{A3,F4,G2} \\ D_{A1,F1,G3} & D_{A1,F2,G3} & D_{A1,F3,G3} & D_{A1,F4,G3} \\ D_{A2,F1,G3} & D_{A2,F2,G3} & D_{A2,F3,G3} & D_{A2,F4,G3} \\ D_{A3,F1,G3} & D_{A3,F2,G3} & D_{A3,F3,G3} & D_{A3,F4,G3} \end{pmatrix}$$

The results of the simulations are presented on nine different $M-\theta$ graphs comparing the behaviour shown by the configurations of each of the rows of matrix $[D]$ with the original design. E.g. the first graph in Fig. 6.20 shows in different shades of gray the simulations related to the fist row of matrix $[D]$ in which parameters **A** and **G** are fixed values of $10.0\,mm$ and $50.0\,mm$ respectively and parameter **F** is varied along all range of study $[15.0, 17.5, 20.0, 22.5]$. The simulations are

stopped when the maximum critical plastic strain of 0.13 is reached, this is only indicative, as shown in section 3.5 the prediction of risk of fracture is sensitive to mesh size and location.

For clarity the legend attached to the graphs relates to the description of those three variables of study, for instance $A10F15.0G50$ relates to the design configuration $(D_{A1,F1,G1})$ in which variable $A = 10.0$, variable $F = 15.0$ and variable $G = 50.0mm$.

Additionally after each $M - \theta$ graph the σ and ϵ_p fields of the connection are displayed at the stage where the critical plastic strain is detected; the upper part of the figures refers to the male part of the connection, and the symmetry plane lies on the left hand side of each figure.
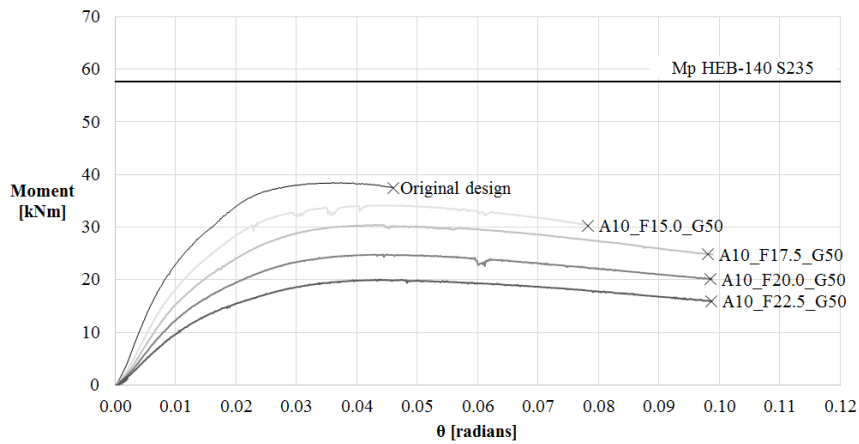
Figure 6.20: $M - \theta$ comparison of parametric optimization designs of row 1 of matrix $[D]$

(a) A10F15G50   (b) A10F17G50   (c) A10F20G50   (d) A10F22G50
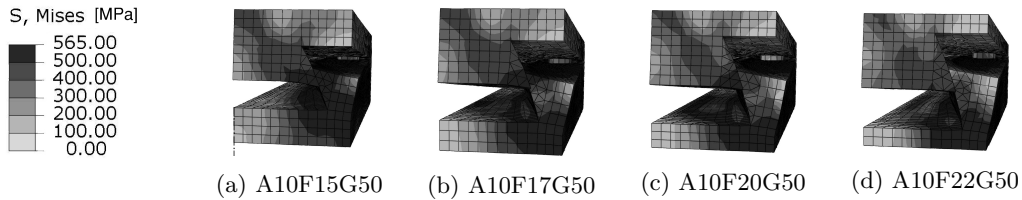
Figure 6.21: Comparison of σ field of parametric optimization designs of row 1 of matrix $[D]$

(a) A10F15G50   (b) A10F17G50   (c) A10F20G50   (d) A10F22G50
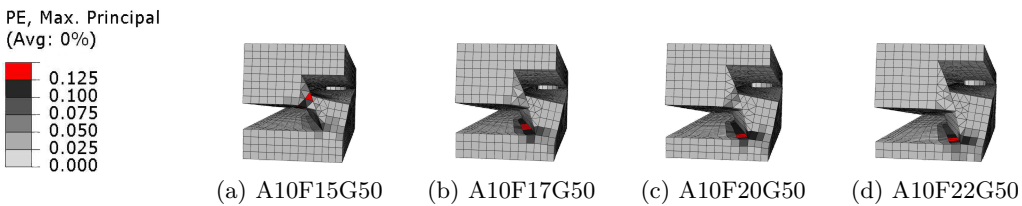
Figure 6.22: Comparison of ϵ_p field of parametric optimization designs of row 1 of matrix $[D]$

Discussion of the results

The designs corresponding to rows 1,4 and 7 of matrix $[D]$ do not show a relevant increase in the overall performance of the connection due to the reduction of variable **A** to 10mm; thus showing its influence on the bending capacity. Designs corresponding to rows 2 and 3, in which the width of the connection (parameter **G**) is decreased to $50\,mm$, also do not exhibit behaviours with higher capacities than the original design; the root distance of the female part of the connection is too small and becomes critical. The designs contained in rows 5 and 6, have a width that is slightly
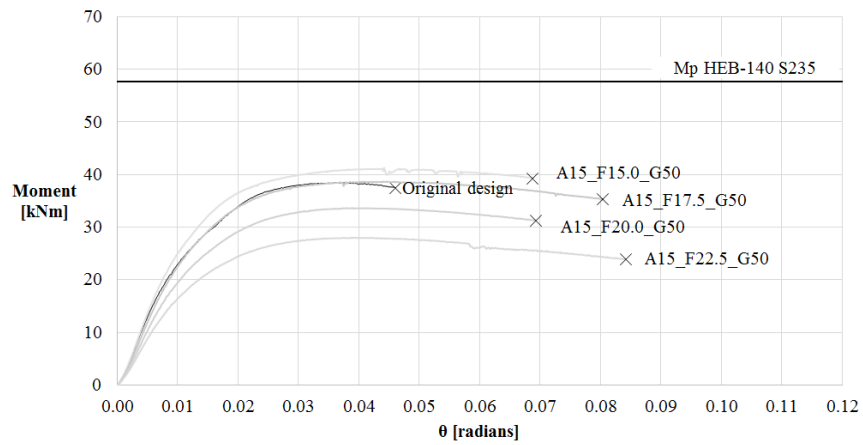
Figure 6.23: $M - \theta$ comparison of parametric optimization designs of row 2 of matrix $[D]$
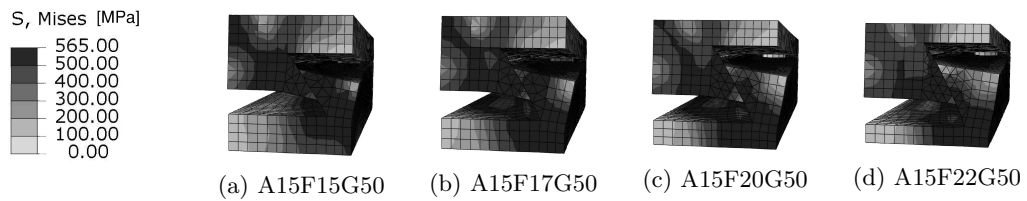
Figure 6.24: Comparison of σ field of parametric optimization designs of row 2 of matrix $[D]$
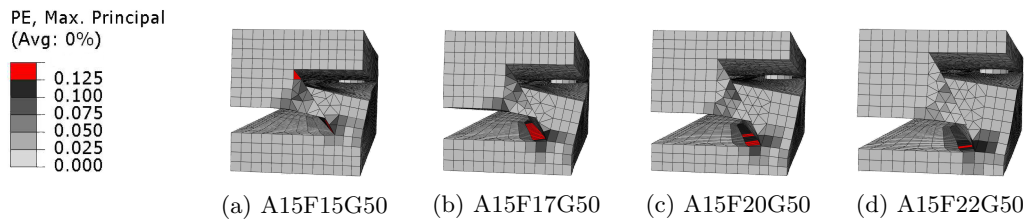
Figure 6.25: Comparison of ϵ_p field of parametric optimization designs of row 2 of matrix $[D]$
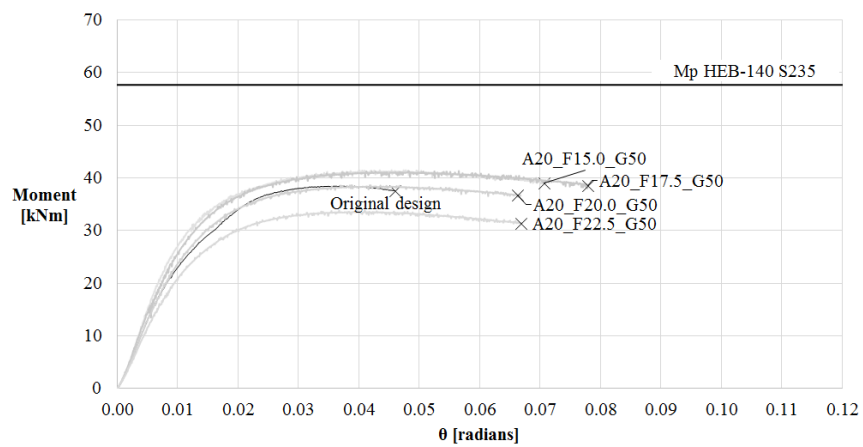
Figure 6.26: $M - \theta$ comparison of parametric optimization designs of row 3 of matrix $[D]$

(a) A20F15G50   (b) A20F17G50   (c) A20F20G50   (d) A20F22G50
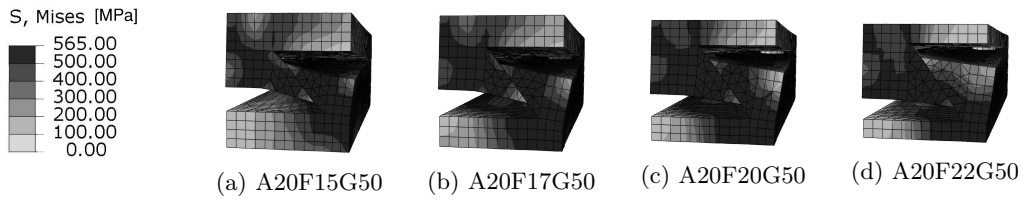
Figure 6.27: Comparison of σ field of parametric optimization designs of row 3 of matrix $[D]$

(a) A20F15G50   (b) A20F17G50   (c) A20F20G50   (d) A20F22G50
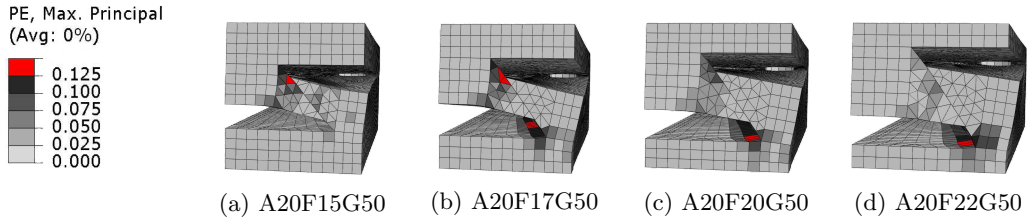
Figure 6.28: Comparison of ϵ_p field of parametric optimization designs of row 3 of matrix $[D]$
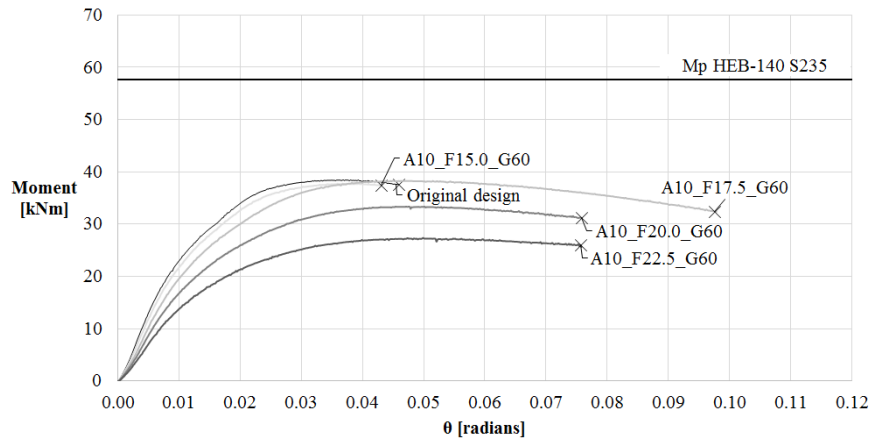
Figure 6.29: $M - \theta$ comparison of parametric optimization designs of row 4 of matrix $[D]$

(a) A10F15G60   (b) A10F17G60   (c) A10F20G60   (d) A10F22G60
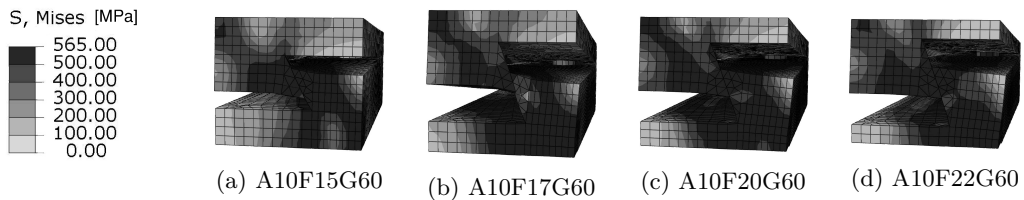
Figure 6.30: Comparison of σ field of parametric optimization designs of row 4 of matrix $[D]$

(a) A10F15G60   (b) A10F17G60   (c) A10F20G60   (d) A10F22G60
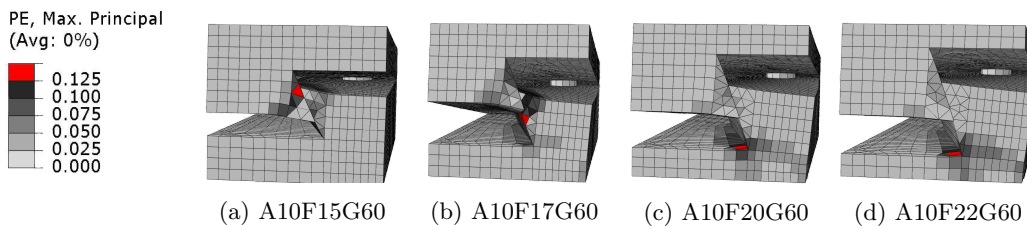
Figure 6.31: Comparison of ϵ_p field of parametric optimization designs of row 4 of matrix $[D]$
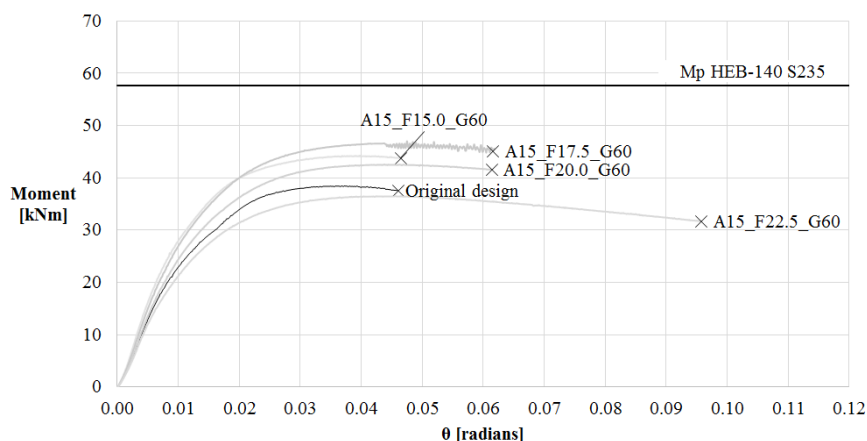
Figure 6.32: $M - \theta$ comparison of parametric optimization designs of row 5 of matrix $[D]$

(a) A15F15G60 (b) A15F17G60 (c) A15F20G60 (d) A15F22G60
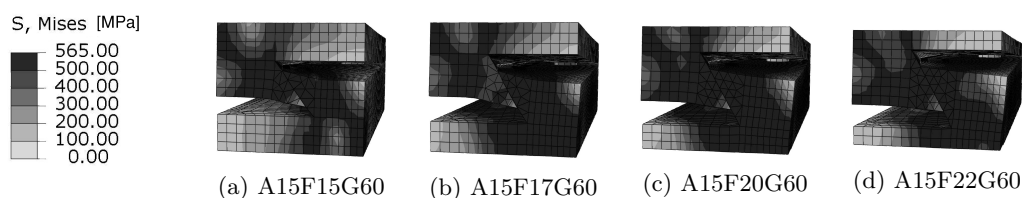
Figure 6.33: Comparison of σ field of parametric optimization designs of row 5 of matrix $[D]$

(a) A15F15G60 (b) A15F17G60 (c) A15F20G60 (d) A15F22G60
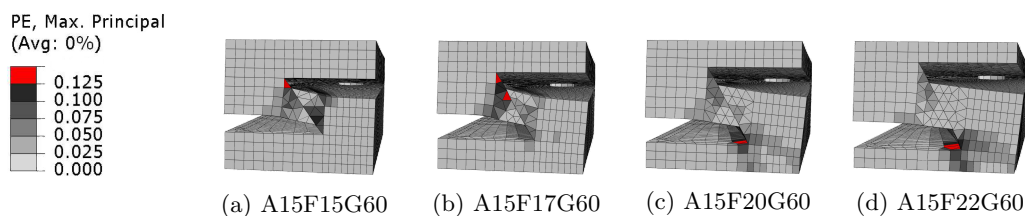
Figure 6.34: Comparison of ϵ_p field of parametric optimization designs of row 5 of matrix $[D]$
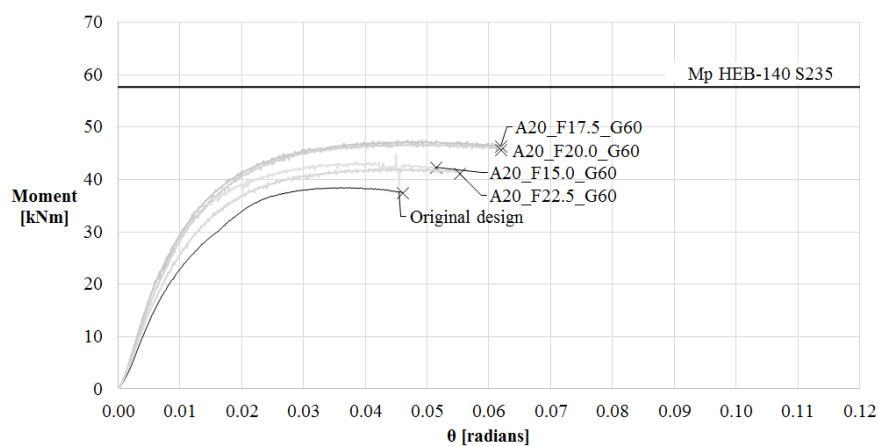
Figure 6.35: $M - \theta$ comparison of parametric optimization designs of row 6 of matrix $[D]$
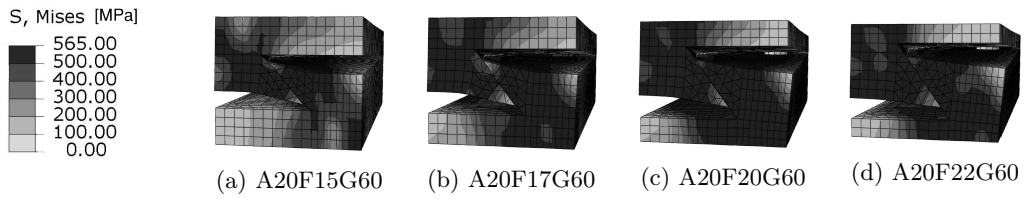
Figure 6.36: Comparison of σ field of parametric optimization designs of row 6 of matrix $[D]$
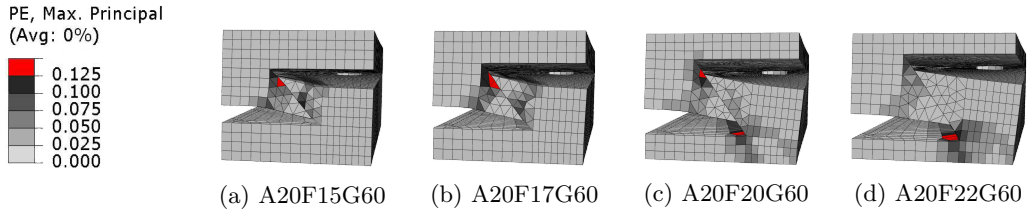
Figure 6.37: Comparison of ϵ_p field of parametric optimization designs of row 6 of matrix $[D]$
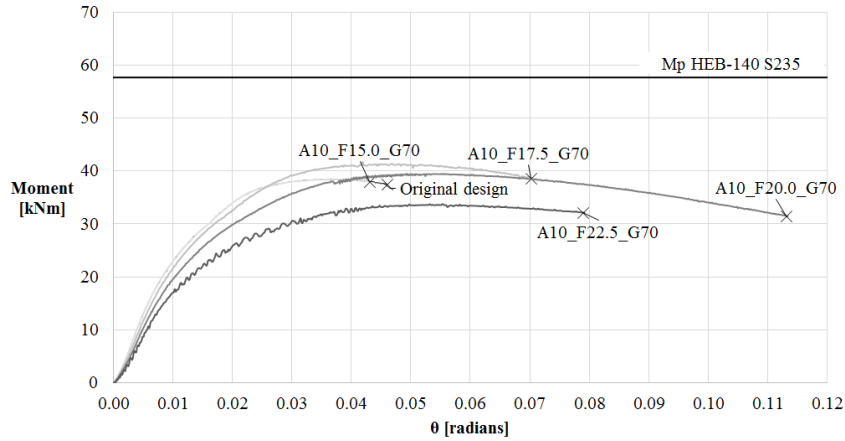
Figure 6.38: $M - \theta$ comparison of parametric optimization designs of row 7 of matrix $[D]$
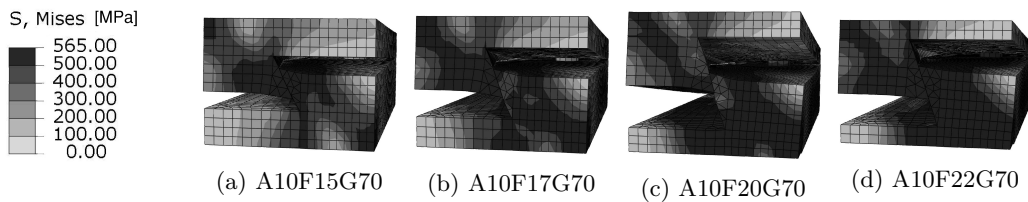
Figure 6.39: Comparison of σ field of parametric optimization designs of row 7 of matrix $[D]$
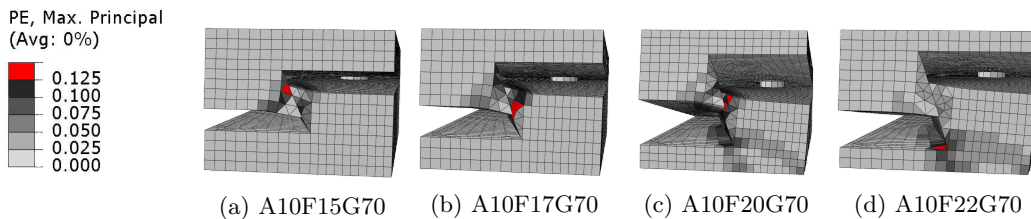
Figure 6.40: Comparison of ϵ_p field of parametric optimization designs of row 7 of matrix $[D]$
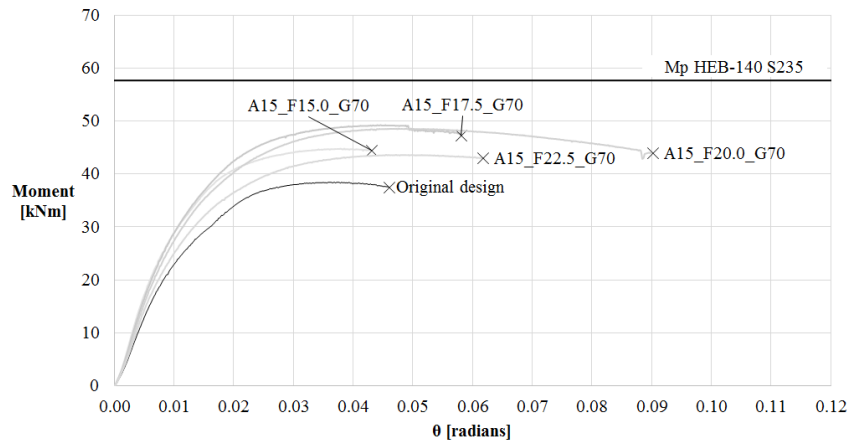
Figure 6.41: $M - \theta$ comparison of parametric optimization designs of row 8 of matrix $[D]$

(a) A15F15G70   (b) A15F17G70   (c) A15F20G70   (d) A15F22G70
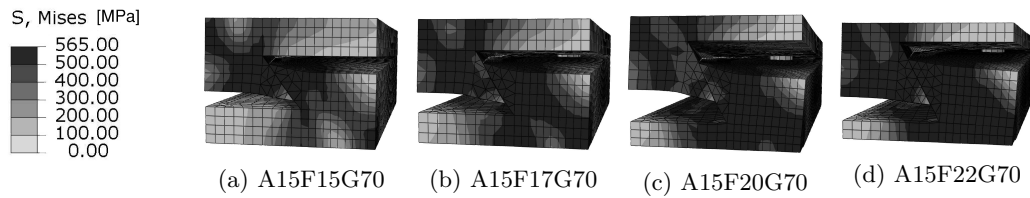
Figure 6.42: Comparison of σ field of parametric optimization designs of row 8 of matrix $[D]$

(a) A15F15G70   (b) A15F17G70   (c) A15F20G70   (d) A15F22G70
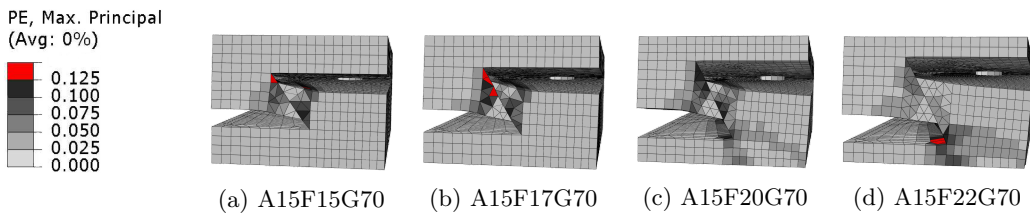
Figure 6.43: Comparison of ϵ_p field of parametric optimization designs of row 8 of matrix $[D]$
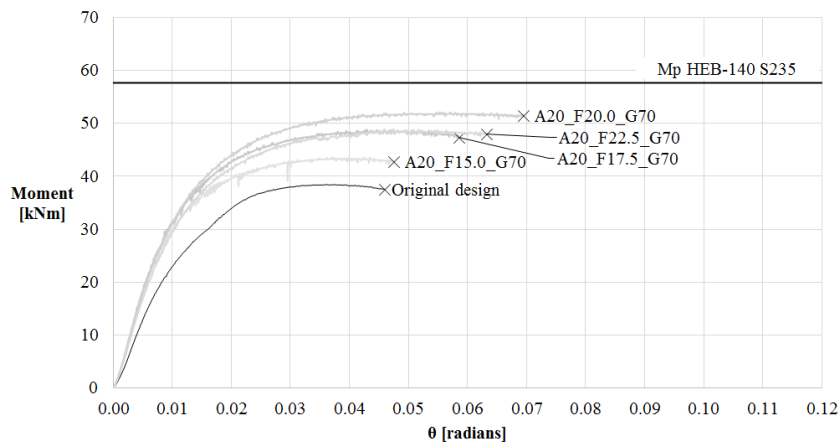
Figure 6.44: $M - \theta$ comparison of parametric optimization designs of row 9 of matrix $[D]$

S, Mises [MPa]

565.00
500.00
400.00
300.00
200.00
100.00
0.00

(a) A20F15G70   (b) A20F17G70   (c) A20F20G70   (d) A20F22G70
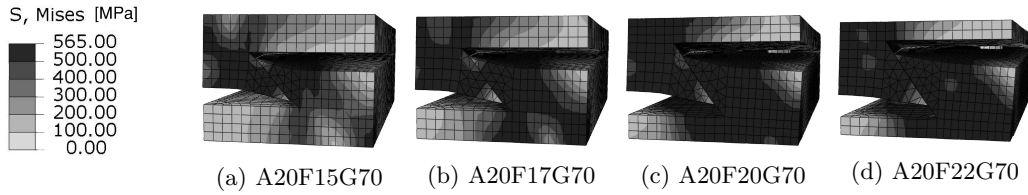
Figure 6.45: Comparison of σ field of parametric optimization designs of row 9 of matrix $[D]$

PE, Max. Principal
(Avg: 0%)

0.125
0.100
0.075
0.050
0.025
0.000

(a) A20F15G70   (b) A20F17G70   (c) A20F20G70   (d) A20F22G70
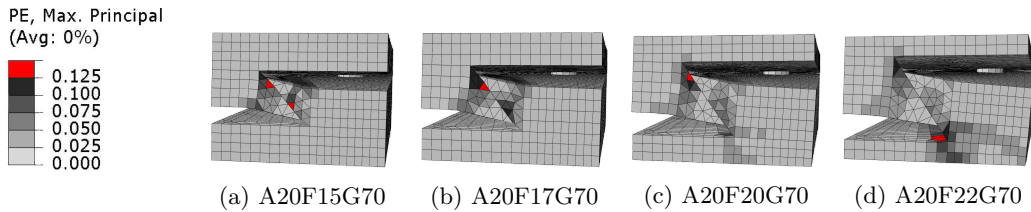
Figure 6.46: Comparison of ϵ_p field of parametric optimization designs of row 9 of matrix $[D]$

narrower than the original $60\,mm$, but thanks to the increase of the two other parameters, the capacities shown by the simulations are of the order of magnitude as the original or in some cases slightly higher. Finally, the designs of rows 8 and 9, where the width of the connection is kept constant and the other two parameters are increased, show bending capacities up to 25% higher.

It is worth to note that the capture of the critical strains on the model is sensitive to mesh size and specially to its location, thus when the critical strain is located at the root of the dovetail, the magnitude of the critical strain is doubtful. As consequence risk of fracture is not well predicted and neither the ductility shown by those simulations. Therefore those simulations are disregarded because their results are unreliable.

Taking into account that the simulations showing the highest capacities on rows 8 and 9 are invalidated, the capacity of the connection by parametric means can be only increased marginally. According to the simulations, the ductility of the connection may be increased by modifying the inclination of the dovetail, such in sample A10F17G70, however to confirm those results the mesh needs to be refined.

Chapter 7

Alternative configuration

This chapter proposes an alternative design configurations by considering design changes other than just parametric variations. The proposed design is described, their results are presented and discussed.

7.1 Double dovetail

The *Double dovetail* connection similarly to the *Snap-Fit connection* develops its resistance by the locking of dovetails, the assembling direction is locked by position pins. The main difference with the original design lies on the number of dovetails. (see Fig. 7.1).

<table>
<tr><td>(a) Female part</td><td>(b) Male part</td></tr>
</table>

Figure 7.1: Double-dovetail design

When introducing two dovetails within the same design area, the amount of material activated by the rotation of the connection is increased, thus allowing to increase the capacity of the connection.

The design presented here is a consequence of the knowledge gathered on chapter 6. The inclination of the dovetails, induce the critical strain to appear within the shoulder of the dovetail such in samples (A10F15G70 or A10F17G70), where the model is able to predict its magnitude; the width of the dovetails is equally divided for the internal dovetails and provides extra material for the outer half dovetails so they do no become critical such in the samples of rows (4,5 and 6 of matrix $[D]$).

Figure 7.2 provides a graphical description of the female part of the *Double dovetail* connection. The male part as shown in Fig. 7.1b has a geometry which fulfils the female part, the backplate of the male part has the same thickness and dimensions as the female.
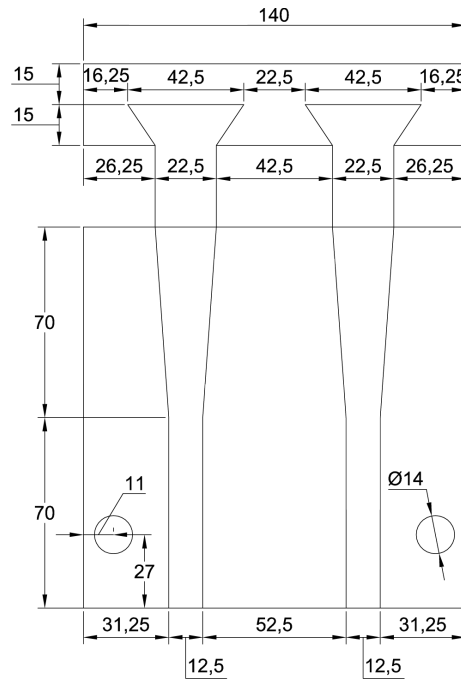
Figure 7.2: Geometry description of the female part of the double-dovetail connection

Double dovetail model

The numerical model used to perform the simulations is a modification of Model A-II with a friction coefficient of 0.07 (see section 3.5), the geometry of the model has been parametrically modified from the python script, the BC, materials and tasks are similar to the ones of the original model. A plane of symmetry at mid-width of the connection allows significant savings on computational time, therefore only half of the connection is modelled.

Due to considerable changes on the geometry and on the stress field a new verification of the mathematical model is performed. Following a similar procedure as on section 3.5, this section investigates the influence of the mesh size by means of a convergence study. It contains 3 simulations of the model of the *Double dovetail* with different mesh densities with average mesh sizes of [8, 4 and 2mm] (see Fig. 7.3)

(a) Mesh 8mm   (b) Mesh 4mm   (c) Mesh 2mm
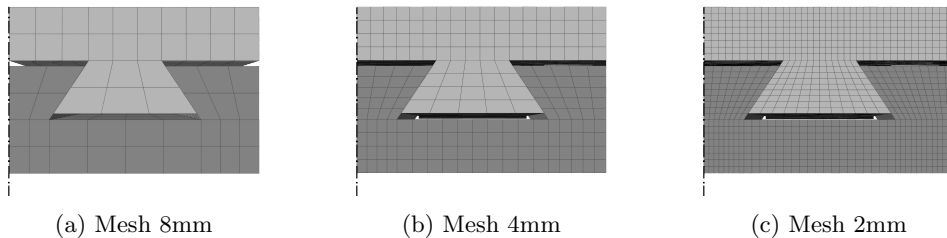
Figure 7.3: Mesh refinement of the convergence study

Results of the simulations

The results of the convergence study are presented in Fig. 7.4 where the $M - \theta$ behaviour of the three simulations are compared. Fig. 7.5 shows a comparison between the maximum capacity and

the relative error shown by the different simulations. For last Fig. 7.6 shows the ϵ_p field of the three simulations at the stage where the critical plastic strain is captured.

A brief study of the inclination of the dovetail is performed to investigate the influence of those changes on the overall behaviour of the connection. Three simulations with a mesh size of $4\,mm$ are compared on Fig. 7.7. Those simulations differ from each other on the amount of vertical offset of the dovetail, the original proposed design has an offset of $10\,mm$, the other two have offsets of $7.50\,mm$ and $12.50\,mm$, which correspond to inclinations of $[50.19°, 56.31°$ and $63.44°]$. On Fig. 7.8 the maximum principal ϵ_p field is displayed at the stage when the critical strain is reached.

Fig. 7.9 shows a comparison of the $M - \theta$ behaviour of the *Double dovetail* with $56.31°$ and the original design of the *Snap-Fit* connection with position pins. The first is displayed in a light grey and the second in a darker grey. For reference only, the plastic moment of a HEB-140 is displayed on the graph.

Similarly to the comparison of section 5.2, the *Double dovetail* connection component is introduced into the component method (described on section 5.2) to represent the global performance of a beam-to-column connection with horizontal stiffeners connected with this connection. Fig. 7.10 shows a comparison of $M - \theta$ behaviour of the joint connected with the *Double dovetail* connection and the common extended end-plate of section 5.2.
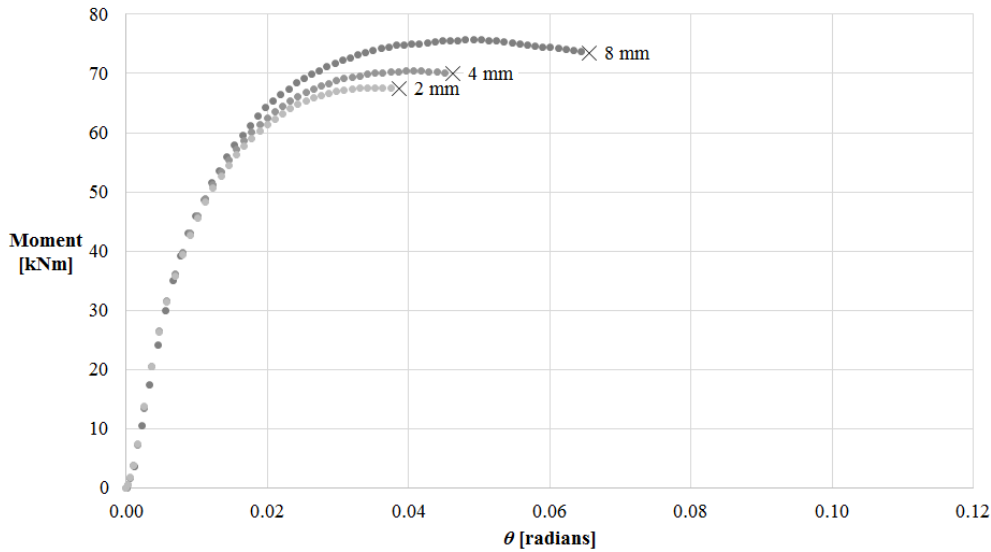
Figure 7.4: $M - \theta$ behaviour comparison of the convergence study

Discussion of the results

It is shown on Fig. 7.4 that the meshes of 4 and 2mm show agreement on terms of stiffness and maximum capacity, the simulation with an average mesh of 8mm, represents the same behaviour on terms of stiffness but an offset on the bending capacity is observed. Fig. 7.5 shows that when refining the size of the mesh, the solution progressively converges. Additionally it may be seen from Fig. 7.6 that the critical plastic strain is located within the dovetail, according to section 3.5 and as Fig. 7.4 shows, the critical principal strain seems to converge as the mesh is refined.

Fig. 7.7 shows that when increasing the amount of offset the capacity of the connection and the stiffness increase, this as shown during the parametric study is due to the amount of material

(a) Maximum moment comparison

(b) Relative error comparison
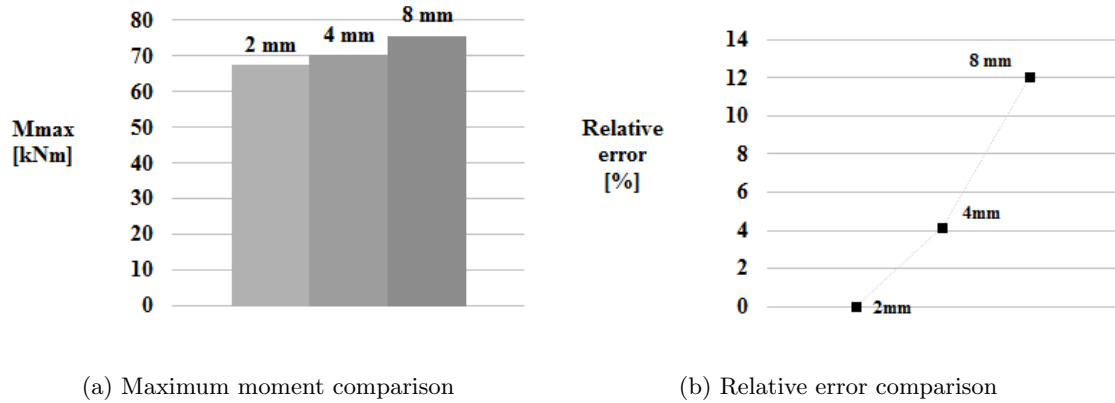
Figure 7.5: Convergence study

(a) Mesh 8mm

(b) Mesh 4mm

(c) Mesh 2mm
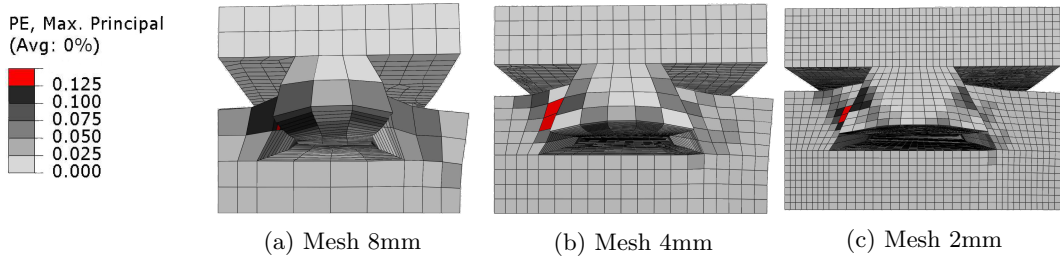
Figure 7.6: Comparison of the ϵ_p of the convergence study
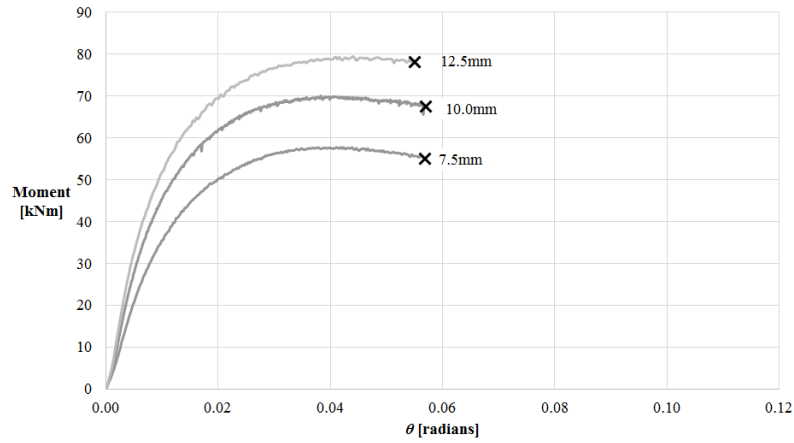
Figure 7.7: $M - \theta$ comparison of the configurations with different offsets

(a) Offset 7.5mm

(b) Offset 10.0mm

(c) Offset 12.5mm
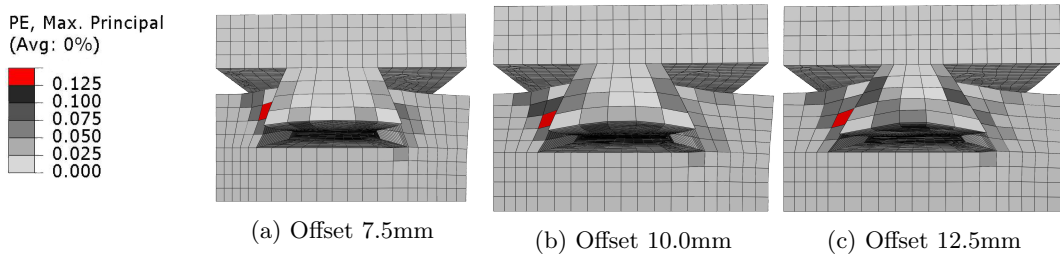
Figure 7.8: Comparison of the ϵ_p of the configurations with different offsets
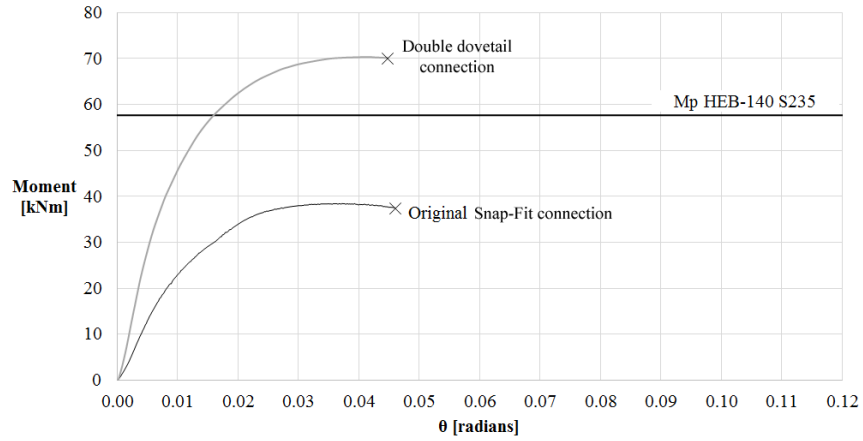
Figure 7.9: $M - \theta$ comparison of the configuration optimization
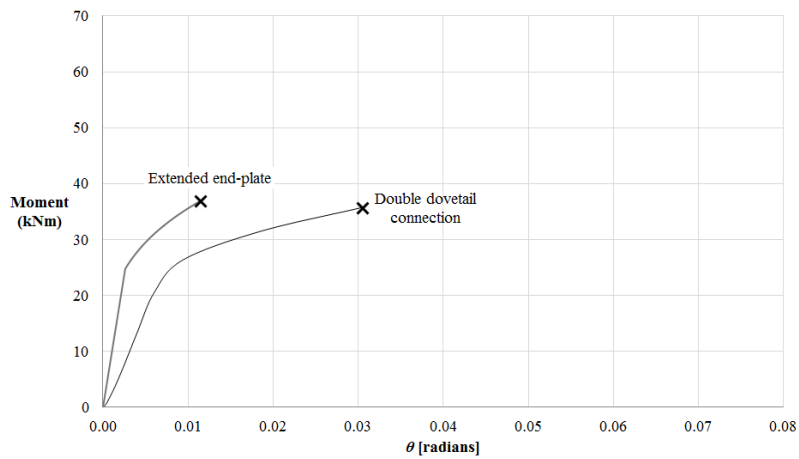
Figure 7.10: M-θ Analytical comparison of the connections

that is activated as result of the rotation. Fig. 7.8 shows that by modifying the inclination of the dovetail the critical plastic strain lowers and rises within the height of the dovetail.

It can be seen from Fig. 7.9 that the stiffness as well as the capacity of the connection are increased with respect to the original design. Those two factors are explained by the new dovetail configuration, the fact that two dovetails are interlocking the system forces to displace more material when the connection rotates, as consequence the connection becomes stiffer and the bending capacity increases roughly 75%.

The comparison of Fig. 7.10, shows that the effective increase of the bending capacity of the global joint performance is only of about 25% in comparison with the original design (see Fig. 5.9), this increase is attributed to the higher stiffness of the *Double-dovetail* rather than to its capacity, it may be seen that the full capacity of the connection is not developed, thus the welds and flanges of the column are still determining the behaviour of the connection (see section 5.2).

Chapter 8

Conclusions

This thesis presents a research of the behaviour of a steel *Snap-Fit connection* for the built environment. Several experimental tests are used for the validation of finite element models. Parametric and sensitivity studies are performed with those numerical models providing a better understanding of the connection. Finally, the results provided by the numerical model are introduced into a mechanical component model which represents the complete joint and allows to compare their global performance.

Sensitivities

The combination of processing tolerances between the fitting parts and the possibility of a lubricant between the surfaces of contact results in a highly unpredictable behaviour. It is shown how those factors govern the bending capacity of the connection when it is not restrained, showing capacities from 50kNm to 5kNm. When introducing a restraining system, such as position pins, this sensitivity is drastically decreased. Therefore the introduction of position pins as structural elements is recommended.

The relation between the M-V on the original design does not seem to play a relevant role on the bending capacity of the connection. Thus variations on the length of the cantilever of the order of a quarter to a double of the original length do not show variations on the $M - \theta$ behaviour. Still to generalize those results a larger study should be undertaken.

The location of the welds on the connection seem to be of influence, the same connection with BC representing a splice or a beam-to-column connection show different resistances. However due to the difficulties of the model to accurately predict the rotation capacity of those connections with their critical strains at their roots, those results are not confirmed.

The Round-and-Fillet corners on the dovetails apparently show benefits on the rotational capacity of the connection, thus the stresses concentrated at the root are better distributed, but again the limitations of the model do not allow to firmly support those conclusions.

The inclination of the dovetail influences the stiffness, bending and rotation capacities of the connection. Dovetails with high inclinations (45°) show critical tensile strains at the roots of the dovetails, when the inclination is decreased (45°- 90° dovetails) the critical location where the tensile strain is found rises towards the top of the dovetail, in those cases the connections show lower bending resistances but become more ductile. It should be highlighted that the resistance of those connections rely mainly on frictional forces, consequently small changes of tolerances or local imperfections may lead to unexpected behaviours.

Optimization

Based on a parametric study of the geometry of the connection, there are two main parameters that directly influence the capacity of the connection; namely: height and inclination of the dovetail. On the other hand it is shown that the interaction between the parameters is intrinsic. 32 combinations are simulated resulting in several designs which show an increase on bending capacity up to 25%. But those designs show their critical strain at the root of the dovetail, where the finite element model has difficulties to accurately predict them.

With the aim of providing an improvement of the performance an alternative design configuration is proposed, a *Double-dovetail* connection. This configuration by interlocking two dovetails activates more material when rotates and consequently provides capacities of the order of 75% higher while the ductility is not diminished.

Global performance

The optimization of a single component of the complete joint does not report benefits in terms of capacity if that is not the determining component. The joint must be reinforced on the weaker parts to be able to optimize its global performance. In agreement with the component model, the original *Snap-Fit connection* with position pins connecting an unreinforced beam-to-column connection would have a 33% of the bending capacity of a comparable extended end-plate and only 50% of its rotation capacity. This is due to a brittle failure of the welds governing the resistance of the joint. On the other hand when the *Snap-Fit connection* is connecting a beam-to-column connection reinforced with horizontal stiffeners, the capacity of the joint reaches almost an 80% of the bending capacity of a comparable extended end-plate and doubles its rotation capacity.

According to the component model, the global performance of the proposed *Double-dovetail* connection in a beam-to-column connection with horizontal reinforcements provides a bending resistance 25% greater than the *Snap-Fit connection*. In comparison with the extended end-plate, the bending capacity is equivalent and the rotation capacity two times larger.

Recommendations for further research

Brittle failure mechanisms such as fracture should preferably be avoided, therefore its accurate prediction is an essential tool. This could be achieved for instance, by developing further the numerical model with the introduction of fracture mechanics.

The deformation capacity of the steel used to manufacture the connection is relatively low due to cold-forming of the product. Manufacturing the connection with other steel types will provide other relations between resistance and ductility, which could be beneficial.

Bibliography

[1] Branko E Gorenc, Ron Tinyou, and Arun A Syam. *Steel designers' handbook*. NewSouth Publishing, Sydney, 8th. edition, 2013.

[2] Snap-fit joints for plastics A design guide. Technical report, Bayer MaterialScience, 2000.

[3] Association Copper Development. CuZn30 datasheet.pdf. Technical report, 1970.

[4] Association Copper Development. CuZn33 datasheet.pdf. Technical report, 1970.

[5] Association Copper Development. CuZn37 datasheet.pdf. Technical report, 1970.

[6] Vittorio Castelli. Mechanics of solids. In *Marks Standard Handbook for Mechanical Engineers*, chapter FRICTION. Mc Graw Hill, 11th edition, 1993.

[7] Dow corning. Molykote Industrial assembly and maintenance. Technical report.

[8] Khairedin M. Abdalla, Wai-Fah Chen, and Norimitsu Kishi. Expanded database of semi-rigid steel connections. Technical report, School of Civil Engineering. Purdue-University, 1994.

[9] John Symonds. Strength of Materials. In *Marks Standard Handbook for Mechanical Engineers*, chapter MECHANICAL PROPERTIES OF MATERIALS. Mc Graw Hill, 11th edition, 1993.

Appendix A

Explicit-dynamic solver

Some of the simulations performed during the course of the thesis are solved with a explicit dynamic solver to overcome the difficulties of convergence of the static solver, e.g. when introducing low friction coefficients.

To assure that the behaviour represented by those simulations represent a truly static analysis two checks are performed. A comparison of the behaviours exhibited by simulations solved with a static and dynamic solvers and an energy balance study.

The first graph shows the results of a $M - \theta$ behaviour of four simulations, two of them are solved with a static procedure (displayed in black) and the other two are solved by means of explicit solver (displayed in gray). It is shown how both responses are in agreement with the results of the static simulations. Additionally, it is shown that the static simulation may fail to converge.
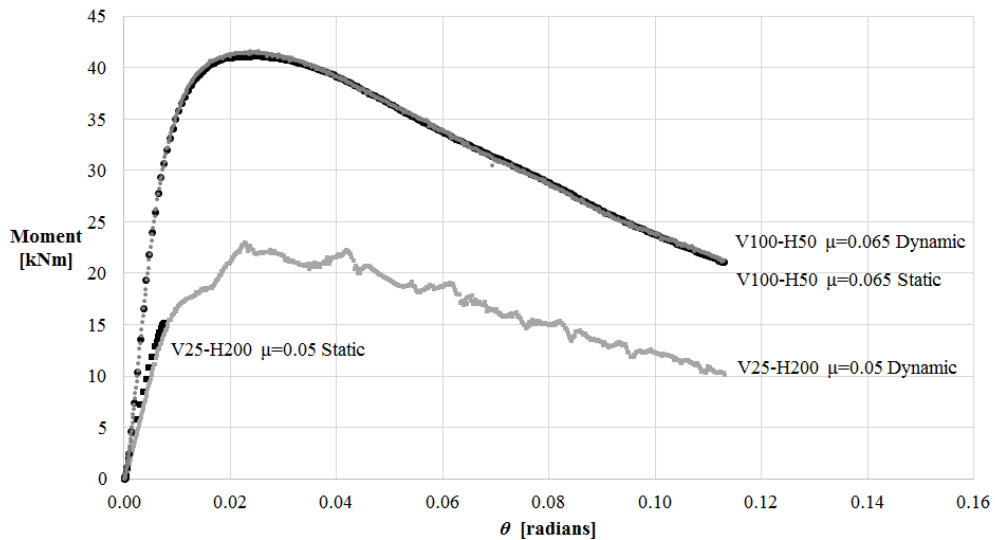
Figure A.1: Comparison of static and dynamic simulation

The second and third graph present an overview of the energy balance of the simulations $V25 - H200\ \mu = 0.05$ and $V100 - H50\ \mu = 0.065$ respectively. The external work is displayed in a discontinuous dotted black line and represents the input energy of the system, the Internal energy, kinetic energy and frictional dissipation are the energies produced as a consequence of that input.

The total Internal energy (displayed in a continuous black line) is the sum of the three grey reaction energies.
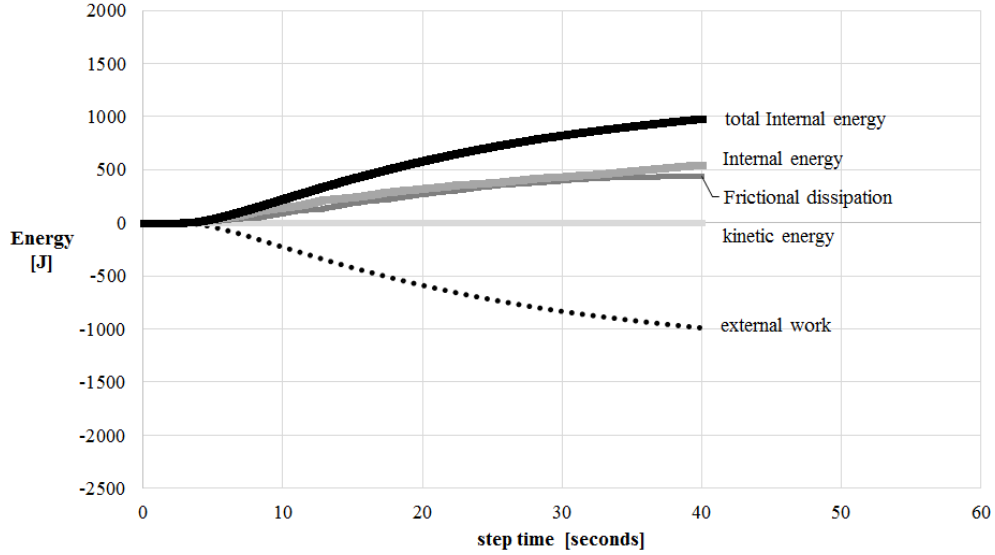
Figure A.2: Energy balance of $V25 - H200\,\mu = 0.05$
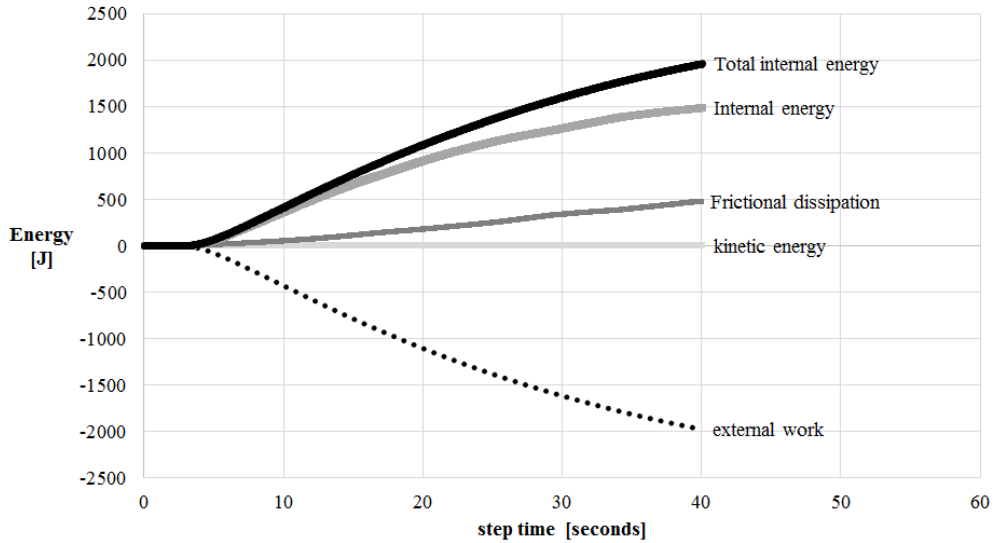
Figure A.3: Energy balance of $V100 - H50\,\mu = 0.065$

It can be seen that the kinetic energy remains 0 in comparison with the other energies thus representing a static behaviour. Additionally it is shown that the external work and total internal energy are opposite and equal in magnitude, thus keeping a constant energy balance 0. It may be pointed out that the second simulation with a connection $V100 - H50\,\mu = 0.065$ shows larger total internal energy and external work than $V25 - H200\,\mu = 0.05$ this is in agreement to the bigger resistance capacity shown in Fig. A.1.

Appendix B

Component method

This section describes the process used to compute the stiffness and moment capacity of the connections used for comparison in section 5. The procedure relates to a analytical analysis of a mechanical model in accordance with the component method described in Eurocode 3 part 1 section 8:Design of Joints. It first computes the critical resistance of the components, the maximum bending capacity is computed by limiting the resistance to each of the components to its maximum resistance according to the force distribution on the connection. Thereafter the stiffness of every of the components on the connection is computed and the stiffness of the connection is assembled according to a mechanical model.

B.1   Extended end-plate

The geometry of the Extended end plate connection and a detail of the end plate are represented in Fig. B.1. The nomenclature of the components relates to the basic joint components as described in Table 6.1 of EC3.1-8. Thus component 1 represents the column web panel in shear, component 2: column web in transverse compression, component 3: column web in transverse tension, component 4: column flange in bending, component 5: end plate in bending, component 7: beam flange and web in compression, component 8: beam web in tension, component 10: bolts in tension and component 19: welds.

Determination of the components individual resistances:

- Component 1. Column web panel in shear:

$$V_{wp.Rd} = \frac{0.9 f_y A_{vc}}{\sqrt{3}\, \gamma_{M0}} = 247.15 kN \qquad\qquad \text{6.2.6.1 (6.7) EC3.1-8}$$

$$F_{wp.Rd} = \frac{V_{wp.Rd}}{\beta} = 247.15 kN$$
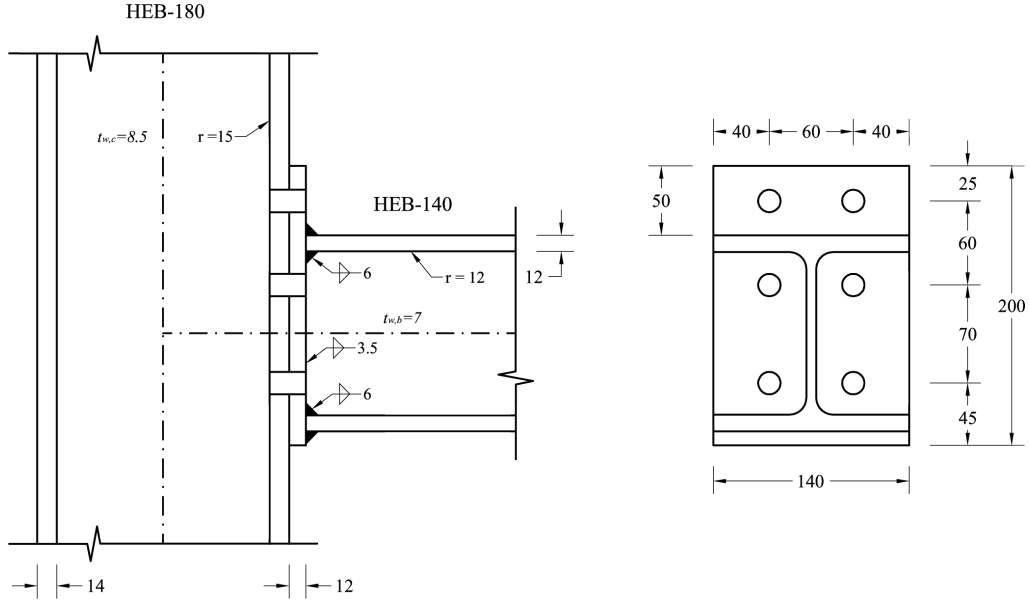
Figure B.1: End-plate connection

- Component 2. Column web in compression:

$$b_{eff.c.wc} = t_{fb} + 2\sqrt{2}a_p + 5(t_{fc} + r_c) + t_p \qquad \text{6.2.6.2 (6.11) EC3.1-8}$$
$$b_{eff.c.wc} = 185.97mm$$
$$\omega = \omega_1 \quad \text{for} \quad \beta = 1.00$$
$$\omega_1 = \frac{1}{\sqrt{1 + 1.3\left(\frac{b_{eff.c.wc}\, t_{wc}}{A_{vc}}\right)^2}} = 0.75$$
$$\bar{\lambda}_p = 0.932\sqrt{\frac{b_{eff.c.wc}\, d_c\, f_y}{E\, t_{wc}^2}} = 0.55 \qquad \text{6.2.6.2 (6.13c) EC3.1-8}$$
$$\rho = \frac{\bar{\lambda}_p - 0.2}{\bar{\lambda}_p^{\,2}} = 1.15$$
$$F_{c.wc.Rd} = \frac{\omega\, k_{wc}\, b_{eff.c.wc}\, t_{wc}\, f_y}{\gamma_{M0}} = 277.43kN \qquad \text{6.2.6.2 (6.9) EC3.1-8}$$
$$\text{but}$$
$$F_{c.wc.Rd} \leq \frac{\omega\, k_{wc}\, \rho\, b_{eff.c.wc}\, t_{wc}\, f_y}{\gamma_{M0}}$$

- Component 3. Column web in tension:

First the individual and the group effective lengths related to the column are computed. The subscripts of the effective lengths describe the yield pattern *cp* (circular pattern) or *nc* (non-circular), the bolt row in tension *I* (firs bolt row), *II* (second bolt row), *gI* (first bolt row as part of a group) and *gII* (second bolt row as part of a group) and finally the element they refer *C* (column) or *P* (end-plate). Fig. B.2 shows the geometry of the column in detail to account for the related T-stubs.
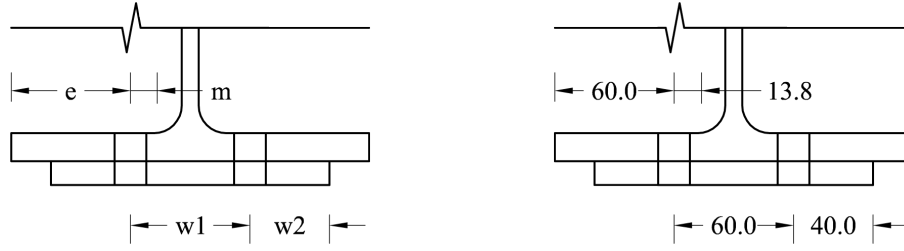
Figure B.2: T-Stub column flange geometrical parameters

Row I. Individual effective length

$$l_{eff.cp.I.C} = 2\pi m = 86.39 mm \qquad \text{Table 6.4 EC3.1-8}$$
$$l_{eff.nc.I.C} = 4m + 1.25e = 130.00 mm \qquad \text{Table 6.4 EC3.1-8}$$

Row I. Effective length as first bolt row of a group

$$l_{eff.cp.gI.C} = \pi m + p = 103.20 mm \qquad \text{Table 6.4 EC3.1-8}$$
$$l_{eff.nc.gI.C} = 2m + 0.625e + 0.5p = 95.00 mm \qquad \text{Table 6.4 EC3.1-8}$$

Row II. Individual effective length

$$l_{eff.cp.II.C} = 2\pi m = 86.39 mm \qquad \text{Table 6.4 EC3.1-8}$$
$$l_{eff.nc.II.C} = 4m + 1.25e = 130.00 mm \qquad \text{Table 6.4 EC3.1-8}$$

Row II. Effective length as last bolt row of a group

$$l_{eff.cp.gII.C} = \pi m + p = 103.20 mm \qquad \text{Table 6.4 EC3.1-8}$$
$$l_{eff.nc.gII.C} = 2m + 0.625e + 0.5p = 95.00 mm \qquad \text{Table 6.4 EC3.1-8}$$

Individual bolt resistances of bolt rows I and II

$$b_{eff.t.wc} = 130.00 mm$$

$$\omega = \frac{1}{\sqrt{1 + 1.3 \left(\frac{b_{eff.t.wc}\, t_{wc}}{A_{vc}} \right)^2}} = 0.85$$

$$F_{t.wc.Rd} = \frac{\omega\, b_{eff.t.wc}\, t_{wc}\, f_y}{\gamma_{M0}} = 220.45 kN \qquad \text{6.2.6.3 (6.15) EC3.1-8}$$

Resistance of the group of bolt rows I and II

$$b_{eff.t.wc.g} = 190.00 mm$$

$$\omega = \frac{1}{\sqrt{1 + 1.3 \left(\frac{b_{eff.t.wc.g}\, t_{wc}}{A_{vc}} \right)^2}} = 0.74$$

$$F_{t.wc.Rd} = \frac{\omega\, b_{eff.t.wc.g}\, t_{wc}\, f_y}{\gamma_{M0}} = 280.73 kN \qquad \text{6.2.6.3 (6.15) EC3.1-8}$$

- Component 4. Column flange in bending:
  Individual bolt resistances of bolt rows I and II. Failure mode 1

$$M_{pl.1.Rd} = \frac{0.25\, l_{eff.1.I.C}\, t_{fc}^2\, f_y}{\gamma_{M0}} = 994.82 kNmm \qquad \text{Table 6.2 EC3.1-8}$$

$$F_{T.1.Rd} = \frac{4\, M_{pl.1.Rd}}{m} = 289.40 kN \qquad \text{Table 6.2 EC3.1-8}$$

Individual bolt resistances of bolt rows I and II. Failure mode 2

$$M_{pl.2.Rd} = \frac{0.25\,l_{eff.2.I.C}\,t_{fc}^2\,f_y}{\gamma_{M0}} = 1496.95kNmm \qquad \text{Table 6.2 EC3.1-8}$$

$$F_{t.Rd} = \frac{0.9\,A_s\,f_{ub}}{\gamma_{M2}} = 113.04kN \qquad \text{Table 3.4 EC3.1-8}$$

$$n = min(e_{min}, 1.25m) = 17.19mm \qquad \text{Table 6.2 EC3.1-8}$$

$$F_{T.2.Rd} = \frac{2\,M_{pl.2.Rd} + 2n\,F_{t.Rd}}{m + n} = 222.37kN \qquad \text{Table 6.2 EC3.1-8}$$

Individual bolt resistances of bolt rows I and II. Failure mode 3

$$F_{T.3.Rd} = 2\,F_{t.Rd} = 226.08kN \qquad \text{Table 6.2 EC3.1-8}$$

Resistances of the group of bolt rows I and II. Failure mode 1

$$M_{pl.1.Rd} = \frac{0.25\,l_{eff.1.g.C}\,t_{fc}^2\,f_y}{\gamma_{M0}} = 2187.85kNmm \qquad \text{Table 6.2 EC3.1-8}$$

$$F_{T.1.Rd} = \frac{4\,M_{pl.1.Rd}}{m} = 636.47kN \qquad \text{Table 6.2 EC3.1-8}$$

Resistances of the group of bolt rows I and II. Failure mode 2

$$M_{pl.2.Rd} = \frac{0.25\,l_{eff.2.g.C}\,t_{fc}^2\,f_y}{\gamma_{M0}} = 2187.85kNmm \qquad \text{Table 6.2 EC3.1-8}$$

$$F_{T.2.Rd} = \frac{2\,M_{pl.2.Rd} + 4n\,F_{t.Rd}}{m + n} = 392.64kN \qquad \text{Table 6.2 EC3.1-8}$$

Resistances of the group of bolt rows I and II. Failure mode 3

$$F_{T.3.Rd} = 4\,F_{t.Rd} = 452.16kN \qquad \text{Table 6.2 EC3.1-8}$$

- Component 5. End-plate in bending:
  First the individual and the group effective lengths related to the end-plate are computed.
  Fig. B.3 shows the geometry of the column in detail to account for the related T-stubs.
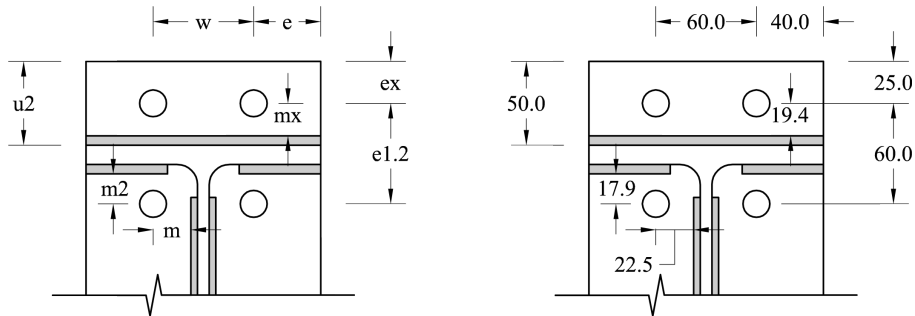
Figure B.3: T-Stub end-plate geometrical parameters

Row I. Individual effective length

$$l_{eff.cp.1.I.P} = 2\pi\, m_x = 121.89mm \qquad\qquad \text{Table 6.6 EC3.1-8}$$

$$l_{eff.cp.2.I.P} = \pi\, m_x + w = 180.95mm \qquad\qquad \text{Table 6.6 EC3.1-8}$$

$$l_{eff.cp.3.I.P} = \pi\, m_x + 2e = 140.95mm \qquad\qquad \text{Table 6.6 EC3.1-8}$$

$$l_{eff.cp.I.P} = 114.43mm$$

$$l_{eff.nc.1.I.P} = 4m_x + 1.25e_x = 108.85mm \qquad\qquad \text{Table 6.6 EC3.1-8}$$

$$l_{eff.nc.2.I.P} = e + 2m_x + 0.625e_x = 94.43mm \qquad\qquad \text{Table 6.6 EC3.1-8}$$

$$l_{eff.nc.3.I.P} = 0.5b_p = 70.0mm \qquad\qquad \text{Table 6.6 EC3.1-8}$$

$$l_{eff.nc.4.I.P} = 0.5w + 2m_x + 0.625e_x = 114.43mm \qquad\qquad \text{Table 6.6 EC3.1-8}$$

$$l_{eff.nc.I.P} = 70.00mm$$

$$l_{eff.1.I.P} = l_{eff.nc.I.P} \quad \text{but} \quad \leq l_{eff.cp.I.P} \qquad\qquad \text{Table 6.6 EC3.1-8}$$

$$l_{eff.2.I.P} = l_{eff.nc.I.P} \qquad\qquad \text{Table 6.6 EC3.1-8}$$

Row II. Individual effective length

$$\lambda_1 = 0.36 \qquad\qquad \text{Figure 6.11 EC3.1-8}$$

$$\lambda_2 = 0.29 \qquad\qquad \text{Figure 6.11 EC3.1-8}$$

$$\alpha = 7.5 \qquad\qquad \text{Figure 6.11 EC3.1-8}$$

$$l_{eff.cp.II.P} = 2\pi\, m = 141.37mm \qquad\qquad \text{Table 6.6 EC3.1-8}$$

$$l_{eff.nc.II.P} = \alpha\, m = 168.75mm \qquad\qquad \text{Table 6.6 EC3.1-8}$$

$$l_{eff.1.II.P} = l_{eff.nc.II.P} \quad \text{but} \quad \leq l_{eff.cp.II.P} \qquad\qquad \text{Table 6.6 EC3.1-8}$$

$$l_{eff.2.II.P} = l_{eff.nc.II.P} \qquad\qquad \text{Table 6.6 EC3.1-8}$$

Individual bolt resistance of bolt rows I. Failure mode 1

$$M_{pl.1.Rd} = \frac{0.25\, l_{eff.1.I.P}\, t_p^2\, f_y}{\gamma_{M0}} = 592.20kNmm \qquad\qquad \text{Table 6.2 EC3.1-8}$$

$$F_{T.1.Rd} = \frac{4\, M_{pl.1.Rd}}{m_x} = 122.10kN \qquad\qquad \text{Table 6.2 EC3.1-8}$$

Individual bolt resistance of bolt rows I. Failure mode 2

$$n_x = min(e_x, 1.25m_x) = 24.25$$

$$M_{pl.2.Rd} = \frac{0.25\, l_{eff.2.I.P}\, t_p^2\, f_y}{\gamma_{M0}} = 592.20kNmm \qquad\qquad \text{Table 6.2 EC3.1-8}$$

$$F_{t.Rd} = \frac{0.9\, A_s\, f_{ub}}{\gamma_{M2}} = 113.04kN \qquad\qquad \text{Table 3.4 EC3.1-8}$$

$$F_{T.2.Rd} = \frac{2\, M_{pl.2.Rd} + 2n_x\, F_{t.Rd}}{m_x + n_x} = 152.73kN \qquad\qquad \text{Table 6.2 EC3.1-8}$$

Individual bolt resistance of bolt rows I. Failure mode 3

$$F_{T.3.Rd} = 2\, F_{t.Rd} = 226.08kN \qquad\qquad \text{Table 6.2 EC3.1-8}$$

Individual bolt resistance of bolt rows II. Failure mode 1

$$M_{pl.1.Rd} = \frac{0.25\, l_{eff.1.II.P}\, t_p^2\, f_y}{\gamma_{M0}} = 1196.00kNmm \qquad\qquad \text{Table 6.2 EC3.1-8}$$

$$F_{T.1.Rd} = \frac{4\, M_{pl.1.Rd}}{m} = 212.62kN \qquad\qquad \text{Table 6.2 EC3.1-8}$$

Individual bolt resistance of bolt rows II. Failure mode 2

$$n = min(e_{min}, 1.25m) = 28.18$$

$$M_{pl.2.Rd} = \frac{0.25 \, l_{eff.2.II.P} \, t_p^2 \, f_y}{\gamma_{M0}} = 1427.63 kNmm \qquad \text{Table 6.2 EC3.1-8}$$

$$F_{t.Rd} = \frac{0.9 \, A_s \, f_{ub}}{\gamma_{M2}} = 113.04 kN \qquad \text{Table 3.4 EC3.1-8}$$

$$F_{T.2.Rd} = \frac{2 \, M_{pl.2.Rd} + 2n \, F_{t.Rd}}{m + n} = 182.00 kN \qquad \text{Table 6.2 EC3.1-8}$$

Individual bolt resistance of bolt rows I. Failure mode 3

$$F_{T.3.Rd} = 2 \, F_{t.Rd} = 226.08 kN \qquad \text{Table 6.2 EC3.1-8}$$

- Component 6. Flange and web of the beam in compression:

$$M_{c.Rd} = W_{b.pl} \, f_{fy} = 56.67 kNm$$

$$F_{c.fb.Rd} = \frac{M_{c.Rd}}{h_b - t_{fb}} = 450.54 kNm \qquad \text{6.2.6.7 (6.21) EC3.1-8}$$

- Component 7. Beam web in tension
  Only bolt row II is considered

$$b_{eff.t.wb} = l_{eff.1.II.P} = 168.75 mm$$

$$F_{t.wb.Rd} = \frac{b_{eff.t.wb} \, t_w \, f_y}{\gamma_{M0}} = 277.59 kN \qquad \text{6.2.6.8 (6.22) EC3.1-8}$$

- Component 19. Welds
  A double fillet weld is considered with a throat thickness sufficient to provide a full strength weld, therefore no resistance check is performed

Assembly of the components:

Loads which can be supported by row I individually

Column flange in bending	$222.37 kN$
Column web in tension	$220.45 kN$
End-plate in bending	$122.10 kN$
	$F_{I.min} = 122.10 kN$

Loads which can be supported by row II individually

Beam web in tension	$277.59 kN$
Column flange in bending	$222.37 kN$
Column web in tension	$220.45 kN$
End-plate in bending	$182.00 kN$
	$F_{II.min} = 182.00 kN$

Loads which can be supported by rows I and II as a group

Column flange in bending	$392.64 kN$
Column web in tension	$280.73 kN$
	$F_{I.II.min} = 280.73 kN$

The maximum tensile force is determined by the minimum of the sum of individual forces of the bolt rows or the loads that support as a group. To ensure equilibrium the compression internal forces are compared with the tensile forces:

Beam flange and web in compression	$450.54kN$
Column web in compression	$277.43kN$
Column web panel in shear	$247.15kN$

$$F_{c.min} = 247.15kN$$

The resistance of the column web panel in shear limits the maximal load that can be supported, therefore the maximum tensile forces that the bolt rows can support is reduced as follows:

$$F_{II.min.red} = F_{c.min} - F_{I.min} = 125.05kN$$

The design bending resistance of the joint is estimated as follows:

$$\mathbf{M_{j.Rd}} = F_{I.min}\,h_I + F_{II.min.red}\,h_{II} = \mathbf{31.79kNm}$$

Determination of the rotational stiffness:

Column web panel in shear:

$$z = \frac{F_{I.min}\,h_I + F_{II.min.red}\,h_{II}}{h_I + h_{II}} = 123.09mm$$

$$k_1 = \frac{0.38\,A_{vc}\,E}{\beta\,z} = 1312.17kN/mm \qquad \text{adapted Table 6.11 EC3.1-8}$$

Column web panel in compression:

$$k_2 = \frac{0.7\,b_{eff.c.wc}\,t_{wc}\,E}{d_c} = 1904.67kN/mm \qquad \text{adapted Table 6.11 EC3.1-8}$$

Column web in tension:

$$k_{3.I} = \frac{0.7\,l_{eff.nc.gI.C}\,t_{wc}\,E}{d_c} = 972.97kN/mm \qquad \text{adapted Table 6.11 EC3.1-8}$$

$$k_{3.II} = \frac{0.7\,l_{eff.nc.gII.C}\,t_{wc}\,E}{d_c} = 972.97kN/mm \qquad \text{adapted Table 6.11 EC3.1-8}$$

Column flange in bending:

$$k_{4.I} = \frac{0.9\,l_{eff.nc.gI.C}\,t_{fc}^3\,E}{m^3} = 17235.36kN/mm \qquad \text{adapted Table 6.11 EC3.1-8}$$

$$k_{4.II} = \frac{0.9\,l_{eff.nc.gII.C}\,t_{fc}^3\,E}{m^3} = 17235.36kN/mm \qquad \text{adapted Table 6.11 EC3.1-8}$$

End-plate in bending:

$$k_{5.I} = \frac{0.9\,l_{eff.1.I.P}\,t_p^3\,E}{m_x^3} = 3131.11kN/mm \qquad \text{adapted Table 6.11 EC3.1-8}$$

$$k_{5.II} = \frac{0.9\,l_{eff.1.II.P}\,t_p^3\,E}{m^3} = 4031.87kN/mm \qquad \text{adapted Table 6.11 EC3.1-8}$$

Bolts in tension:

$$k_{10} = \frac{1.6\,A_s\,E}{L_b} = 1256.00 kN/mm \qquad \text{adapted Table 6.11 EC3.1-8}$$

Effective stiffness per bolt row:

$$k_{eff.I} = \frac{1}{\frac{1}{k_{3.I}} + \frac{1}{k_{4.I}} + \frac{1}{k_{5.I}} + \frac{1}{k_{10}}} = 454.27 kN/mm \qquad \text{adapted 6.3.3.1 (6.30) EC3.1-8}$$

$$k_{eff.II} = \frac{1}{\frac{1}{k_{3.II}} + \frac{1}{k_{4.II}} + \frac{1}{k_{5.II}} + \frac{1}{k_{10}}} = 469.48 kN/mm \qquad \text{adapted 6.3.3.1 (6.30) EC3.1-8}$$

Equivalent stiffness coefficient related to the tensile part of the joint:

$$z_{eq} = \frac{k_{eff.I}\,h_I^2 + k_{eff.II}\,h_{II}^2}{k_{eff.I}\,h_I + k_{eff.II}\,h_{II}} = 135.51 mm \qquad \text{6.3.3.1 (6.31) EC3.1-8}$$

$$k_{eq} = \frac{k_{eff.I}\,h_I + k_{eff.II}\,h_{II}}{z_{eq}} = 876.02 kN/mm \qquad \text{adapted 6.3.3.1 (6.29) EC3.1-8}$$

According to 6.3.3.1(6.27) EC3.1-8, the stiffness of the joint on the first two thirds of $M_{j.Rd}$ may be estimated with $S_{j.ini}$, for the last third the stiffness may be computed with S_j:

$$\mathbf{S_{j.ini}} = \frac{z_{eq}^2}{\frac{1}{k_{eq}} + \frac{1}{k_1} + \frac{1}{k_2}} = \mathbf{7441 kNm/rad} \qquad \text{adapted 6.3.3.1 (6.27) EC3.1-8}$$

$$\mathbf{S_j} = \frac{z_{eq}^2}{\mu\left(\frac{1}{k_{eq}} + \frac{1}{k_1} + \frac{1}{k_2}\right)} \qquad \text{adapted 6.3.3.1 (6.27) EC3.1-8}$$

$$\mu = \left(1.5\frac{M_{j.Ed}}{M_{j.Rd}}\right)^{2.7} \qquad \text{6.3.3.1 (6.28b) EC3.1-8}$$

B.2 Snap-Fit connection

The geometry of the *Snap-Fit connection* is represented in Fig. B.4, the connection used for comparison relates to the original design of the *Snap-Fit connection* with position pins. For further detail on the geometry of the connection refer to chapter 3. The nomenclature used on the determination of individual resistances and rotational stiffness of the components is the same as on the previous example, the stiffness of the *Snap-Fit connection* is introduced through a translational spring $k_{Dovetail}$ into the mechanical model.

Determination of the components individual resistances:

- Component 1. Column web panel in shear:

$$V_{wp.Rd} = \frac{0.9 f_y\,A_{vc}}{\sqrt{3}\,\gamma_{M0}} = 247.15 kN \qquad \text{6.2.6.1 (6.7) EC3.1-8}$$

$$F_{wp.Rd} = \frac{V_{wp.Rd}}{\beta} = 247.15 kN$$
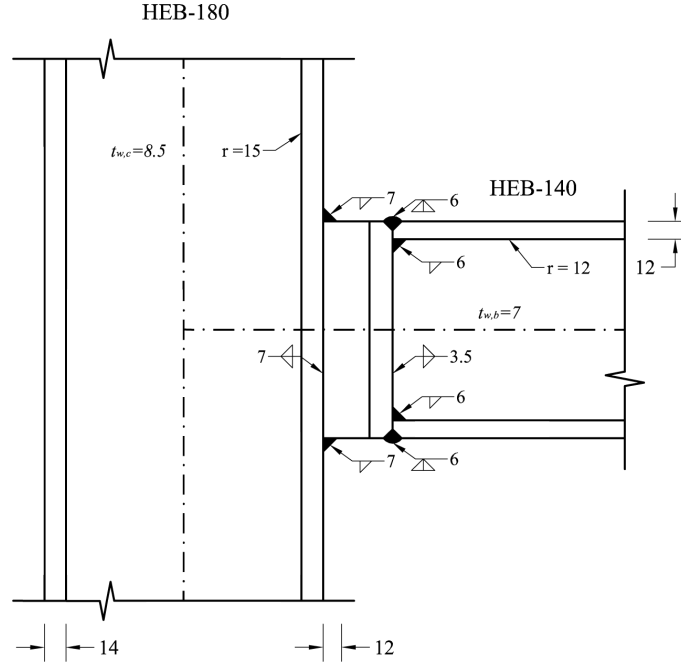
Figure B.4: *Snap-Fit connection*

- Component 2. Column web in compression:
  Assuming that the center of rotation of the *Snap-Fit connection* is located at its bottom. The commpresion zone due to the rotation of the connection is found at its lowest material fiber. According to Saint Venant, a stress perturbation will dissipate approximately at a distance equal to the depth. Therefore it is assumed that the widht of influence due to this stress concentration at the interface between the *Snap-Fit connection* and the column is equal to the thickness of the *Snap-Fit connection* backplate.

$$b_{eff.c.dovetail} = 10.0mm$$

$$b_{eff.c.wc} = b_{eff.c.dovetail} + \sqrt{2}a_{fc} + 5(t_{fc} + r_c) \qquad \text{adapted 6.2.6.2 (6.11) EC3.1-8}$$

$$b_{eff.c.wc} = 164.9mm$$

$$\omega = \omega_1 \quad \text{for} \quad \beta = 1.00$$

$$\omega_1 = \frac{1}{\sqrt{1 + 1.3 \left(\frac{b_{eff.c.wc}\, t_{wc}}{A_{vc}} \right)^2}} = 0.78$$

$$\bar{\lambda}_p = 0.932 \sqrt{\frac{b_{eff.c.wc}\, d_c\, f_y}{E\, t_{wc}^2}} = 0.52 \qquad \text{6.2.6.2 (6.13c) EC3.1-8}$$

$$\rho = \frac{\bar{\lambda}_p - 0.2}{\bar{\lambda}_p^{\,2}} = 1.18$$

$$F_{c.wc.Rd} = \frac{\omega\, k_{wc}\, b_{eff.c.wc}\, t_{wc}\, f_y}{\gamma_{M0}} = 258.52kN \qquad \text{6.2.6.2 (6.9) EC3.1-8}$$

but

$$F_{c.wc.Rd} \leq \frac{\omega\, k_{wc}\, \rho\, b_{eff.c.wc}\, t_{wc}\, f_y}{\gamma_{M0}}$$

- Component 3. Column web in tension:

$$b_{eff.t.wc} = \sqrt{2}a_{fc} + 5(t_{fc} + r_c) \qquad \text{adapted 6.2.6.3 (6.16) EC3.1-8}$$
$$b_{eff.t.wc} = 154.90mm$$
$$F_{t.wc.Rd} = \frac{\omega \, b_{eff.t.wc} \, t_{wc} \, f_y}{\gamma_{M0}} = 242.56kN \qquad \text{6.2.6.3 (6.15) EC3.1-8}$$

- Component 4. Column flange in bending:

The effective width that is assumed to be transferring the tensile forces to the flange of the beam is directly related to the stiffness of the flange. In this case the stiffer part of the column flange is assumed to transfer the tensile forces. This part is conservatively defined as the thickness of the web plus the two root radius. The thickness that transfers the tensile stress it is assumed to be equal to the thickness of the weld between the *Snap-Fit connection* and the column.

$$b_{eff.dovetail} = t_w + 2s = 38.5mm$$
$$t_{eff} = \sqrt{2}a_{fc} = 10mm$$
$$F_{fc.Rd} = \frac{b_{eff.b.fc} \, t_{fb} \, f_y}{\gamma_{M0}} = 90.48kN \qquad \text{6.2.6.4.3 (6.20) EC3.1-8}$$

- Component 6. Flange and web of the beam in compression:

$$M_{c.Rd} = W_{b.pl} \, f_{fy} = 56.67kNm$$
$$F_{c.fb.Rd} = \frac{M_{c.Rd}}{h_b - t_{fb}} = 450.54kN \qquad \text{6.2.6.7 (6.21) EC3.1-8}$$

- Component 19. Welds
  The assumed force distribution relates to a plastic approach in which the top and bottom welds resist the applied moment and the welds along the height of the connection resist the shear. Their resistance is computed according to the directional method described in EC3-1.8. The stress distribution between the column and the female part of the Dovetail takes into account the flexibility of the column flange and the stress distribution within the female dovetail.

$$b_{eff.w.fc} = b_{eff.b.fc} = 38.5mm$$
$$\sigma_\perp = \tau_\perp = \frac{\sigma_{weld}}{\sqrt{2}}$$
$$\frac{f_u}{\beta_w \, \gamma_{M2}} = \sqrt{\left(\frac{\sigma_{weld}}{\sqrt{2}}\right)^2 + 3\left(\frac{\sigma_{weld}}{\sqrt{2}}\right)^2}$$
$$\sigma_{weld} = 254.55N/mm^2$$
$$F_{t.weld} = a_{fc} \, b_{eff.w.fc} \, \sigma_{weld} = 68.60kN$$

- Component Dovetail. Dovetail in bending:
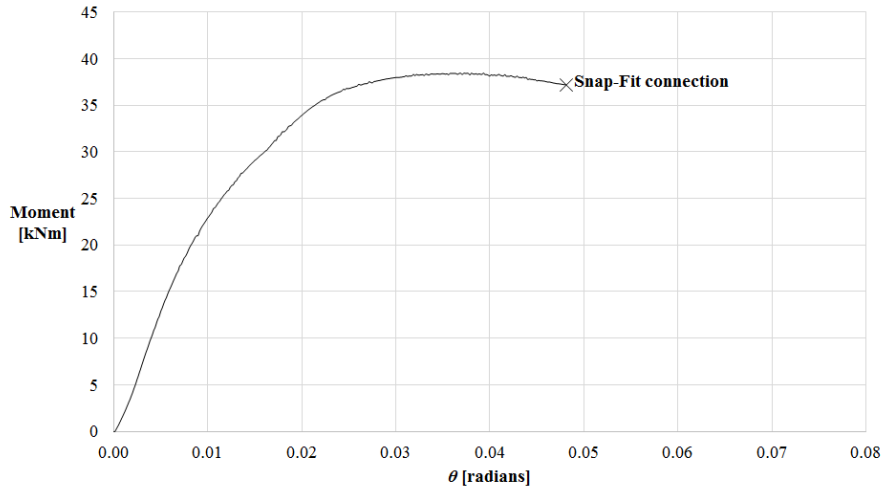
Figure B.5: M-θ behaviour of original *Snap-Fit connection* design with position pins

$$Mmax = 38.46kNm \qquad \text{Fig. B.5}$$

$$z_{dovetail} = h_{dovetail} - \frac{b_{eff.c.dovetail}}{2} = 134.75mm$$

$$F_{dovetail.Rd} = \frac{M_{max}}{z_{dovetail}} = 285.41kN$$

Assembly of the components:

Tensile loads which can be supported

Column flange in bending	$90.48kN$
Column web in tension	$242.56kN$
Dovetail in bending	$285.41kN$
Welds in tension	$68.60kN$

$$F_{I.min} = 68.60kN$$

To ensure equilibrium the compression internal forces are compared with the tensile forces:

Beam flange and web in compression	$450.54kN$
Column web in compression	$258.52kN$
Column web panel in shear	$247.15kN$

$$F_{c.min} = 247.15kN$$

The design bending resistance of the joint is estimated as follows:

$$\mathbf{M_{j.Rd}} = F_{I.min} \, z_{dovetail} = \mathbf{9.24kNm}$$

Determination of the rotational stiffness:

Column web panel in shear:

$$k_1 = \frac{0.38\, A_{vc}\, E}{\beta\, z_{dovetail}} = 1198.63 kN/mm \qquad \text{adapted Table 6.11 EC3.1-8}$$

Column web panel in compression:

$$k_2 = \frac{0.7\, b_{eff.c.wc}\, t_{wc}\, E}{d_c} = 1693.99 kN/mm \qquad \text{adapted Table 6.11 EC3.1-8}$$

Column web in tension:

$$k_3 = \frac{0.7\, b_{eff.t.wc}\, t_{wc}\, E}{d_c} = 1687.58 kN/mm \qquad \text{adapted Table 6.11 EC3.1-8}$$

Dovetail in bending:
the rotational stiffness is transformed into a translational spring:

$$k_{dovetail} = \frac{M_{Ed}}{2 h_{dovetail}\, z_{dovetail} \sin \frac{\theta}{2}} \qquad \text{with M and } \theta \text{ from Fig. B.5}$$

Stiffness of the joint:
Note, that in this case a failure of the weld may be expected, a brittle failure which will probably show no ductility. In order to represent this behaviour. The stiffeness modification factor μ, which accounts for the ductility on the last third of M_{Rd}. Is not related to the M_{Rd} of the joint determined by the failure of the weld but that would be determining by the next failure, in this case, the column of the flange.

$$\mathbf{S_{j.ini}} = \frac{z_{dovetail}^2}{\frac{1}{k_1} + \frac{1}{k_2} + \frac{1}{k_3} + \frac{1}{k_{dovetail}}} \qquad \text{adapted 6.3.3.1 (6.27) EC3.1-8}$$

$$\mathbf{S_j} = \frac{z_{eq}^2}{\mu \left(\frac{1}{k_1} + \frac{1}{k_2} + \frac{1}{k_3} + \frac{1}{k_{Dovetail}} \right)} \qquad \text{adapted 6.3.3.1 (6.27) EC3.1-8}$$

$$\mu = \left(\frac{1.5 M_{Ed}}{M_{Rd.flange}} \right)^{2.7}$$

$$M_{Rd.flange} = F_{fc.Rd} \left(h_b + \frac{\sqrt{2} a_{fc}}{2} \right) = 13.11 kNm$$

B.3 Extended end plate with stiffeners

This section similarly to Annex section B.1 describes the procedure followed to determine the resistances and stiffness of the components of an extended end plate, in this section only will be included those components that resulted influenced from the introduction of the stiffeners. The geometry of the connection and a detail of the end-plate is shown in Fig. B.6.

Determination of the components individual resistances:
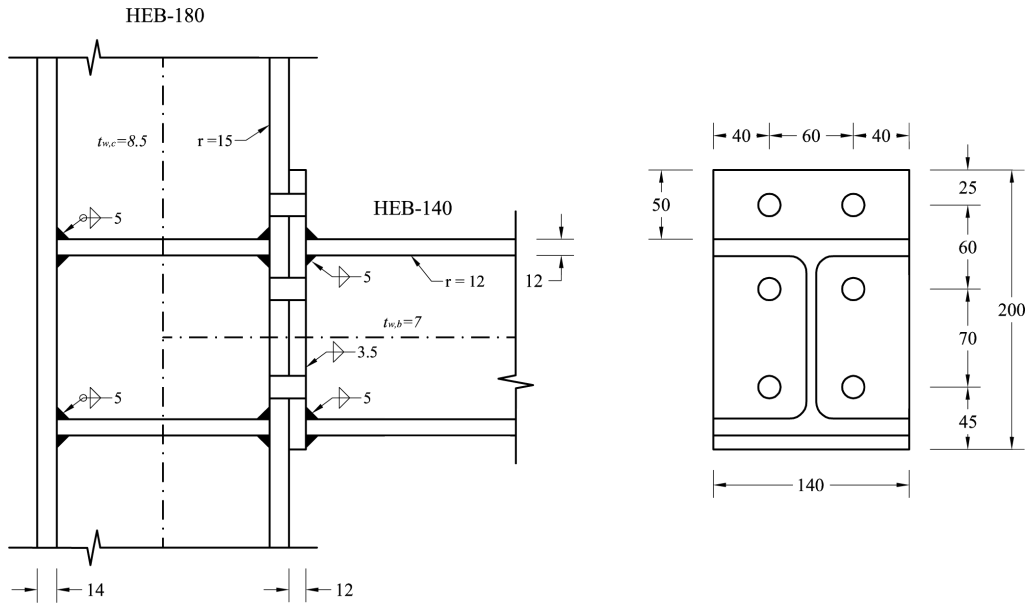
Figure B.6: End-plate connection with stiffeners

- Component 1. Column web panel in shear with stiffeners:

$$l_{eff.fc} = b_c = 180.00mm$$

$$l_{eff.st} = 2w_s - 2r_c = 142.00mm$$

$$M_{pl.fc.Rd} = \frac{0.25l_{eff.fc}\, t_{fc}^2\, f_y}{\gamma_{M0}} = 2072.70kNmm$$

$$M_{pl.st.Rd} = \frac{0.25l_{eff.st}\, t_{fc}^2\, f_y}{\gamma_{M0}} = 1201.32kNmm$$

$$V_{wp.add.Rd} = \frac{4M_{pl.fc.Rd}}{d_s} = 67.95kN \qquad\qquad \text{6.2.6.1 (6.8) EC3.1-8}$$

$$\text{but}\quad V_{wp.add.Rd} \leq \frac{2M_{pl.fc.Rd} + 2M_{pl.st.Rd}}{d_s} = 53.67kN \qquad\qquad \text{6.2.6.1 (6.8) EC3.1-8}$$

$$V_{wp.Rd} = \frac{0.9f_y\, A_{vc}}{\sqrt{3}\,\gamma_{M0}} + V_{wp.add.Rd} = 300.82kN \qquad\qquad \text{6.2.6.1 (6.7) EC3.1-8}$$

$$F_{wp.Rd} = \frac{V_{wp.Rd}}{\beta} = 300.82kN$$

- Component 2. Column web in compression with stiffeners:
  The resistance check is omitted because all of the following conditions are met:

  – The stiffeners are at least of the same steel grade than the beam profile

  – the thickness of the stiffener is at least the same than the flange of the profile

  – the stiffener in compression side is aligned with the beam flange.

- Component 3. Column web in tension with stiffeners:
  According to 6.2.6.3 (3) EC3.1-8 The effective width for a bolted connection is taken equal to the representative effective length of the equivalent T-stub of the column flange. Individual

bolt resistance of bolt rows I and II

$$l_{eff.t.wc} = 110.00mm$$

$$F_{t.wc.Rd} = \frac{l_{eff.t.wc}\, t_{wc}\, f_y}{\gamma_{M0}} = 219.73$$

- Component 4. Column flange in bending with stiffeners:
  Due to the introduction of the stiffeners, the flange of the column will not show yield patterns of group of bolts. Fig. B.7 shows the geometry of the column in detail to account for the related T-stubs.
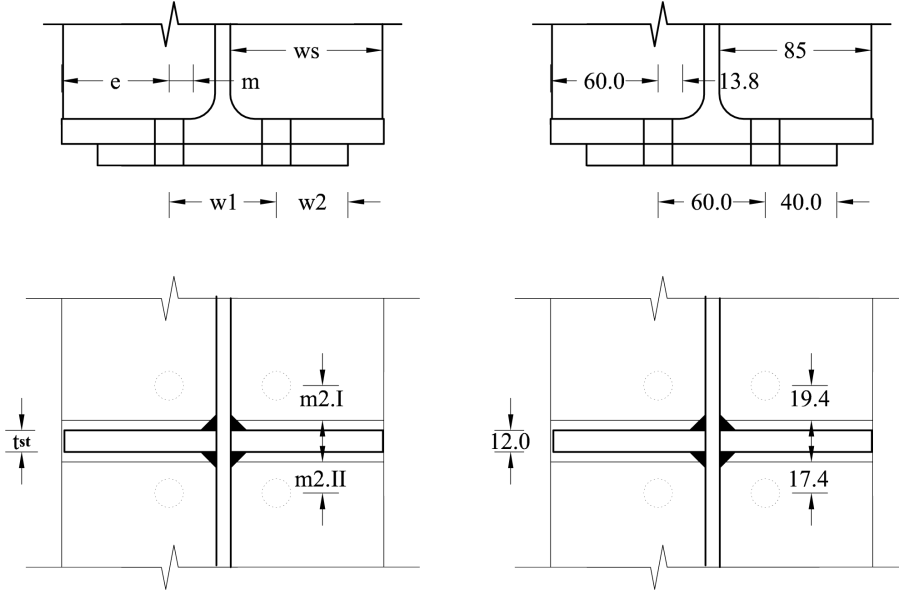
Figure B.7: T-Stub column flange with stiffeners geometrical parameters

Row I. Individual effective length

$$l_{eff.cp.I.C} = 2\pi m = 86.39mm \hspace{3cm} \text{Table 6.5 EC3.1-8}$$

$$\lambda_1 = \frac{m}{m+e} = 0.19 \hspace{3cm} \text{Figure 6.11 EC3.1-8}$$

$$\lambda_2 = \frac{m_2}{m+e} = 0.26 \hspace{3cm} \text{Figure 6.11 EC3.1-8}$$

$$\alpha = f(\lambda_1, \lambda_2) = 8 \hspace{3cm} \text{Figure 6.11 EC3.1-8}$$

$$l_{eff.nc.I.C} = \alpha\, m = 110.00mm \hspace{3cm} \text{Table 6.5 EC3.1-8}$$

Row II. Individual effective length

$$l_{eff.cp.II.C} = 2\pi m = 86.39mm \hspace{3cm} \text{Table 6.5 EC3.1-8}$$

$$\lambda_1 = \frac{m}{m+e} = 0.19 \hspace{3cm} \text{Figure 6.11 EC3.1-8}$$

$$\lambda_2 = \frac{m_2}{m+e} = 0.24 \hspace{3cm} \text{Figure 6.11 EC3.1-8}$$

$$\alpha = f(\lambda_1, \lambda_2) = 8 \hspace{3cm} \text{Figure 6.11 EC3.1-8}$$

$$l_{eff.nc.II.C} = \alpha\, m = 110.000mm \hspace{3cm} \text{Table 6.5 EC3.1-8}$$

Individual bolt resistances of bolt rows I. Failure mode 1

$$M_{pl.1.Rd} = \frac{0.25\, l_{eff.1.I.C}\, t_{fc}^2\, f_y}{\gamma_{M0}} = 1012.85 kNmm \qquad \text{Table 6.2 EC3.1-8}$$

$$F_{T.1.Rd} = \frac{4\, M_{pl.1.Rd}}{m} = 289.40 kN \qquad \text{Table 6.2 EC3.1-8}$$

Individual bolt resistances of bolt rows I. Failure mode 2

$$M_{pl.2.Rd} = \frac{0.25\, l_{eff.2.I.C}\, t_{fc}^2\, f_y}{\gamma_{M0}} = 1266.65 kNmm \qquad \text{Table 6.2 EC3.1-8}$$

$$F_{t.Rd} = \frac{0.9\, A_s\, f_{ub}}{\gamma_{M2}} = 113.04 kN \qquad \text{Table 3.4 EC3.1-8}$$

$$n = min(e_{min}, 1.25m) = 17.18 mm \qquad \text{Table 6.2 EC3.1-8}$$

$$F_{T.2.Rd} = \frac{2\, M_{pl.2.Rd} + 2n\, F_{t.Rd}}{m + n} = 207.48 kN \qquad \text{Table 6.2 EC3.1-8}$$

Individual bolt resistances of bolt rows I. Failure mode 3

$$F_{T.3.Rd} = 2\, F_{t.Rd} = 226.08 kN \qquad \text{Table 6.2 EC3.1-8}$$

Individual bolt resistances of bolt rows II. Failure mode 1

$$M_{pl.1.Rd} = \frac{0.25\, l_{eff.1.II.C}\, t_{fc}^2\, f_y}{\gamma_{M0}} = 1012.85 kNmm \qquad \text{Table 6.2 EC3.1-8}$$

$$F_{T.1.Rd} = \frac{4\, M_{pl.1.Rd}}{m} = 289.40 kN \qquad \text{Table 6.2 EC3.1-8}$$

Individual bolt resistances of bolt rows II. Failure mode 2

$$M_{pl.2.Rd} = \frac{0.25\, l_{eff.2.II.C}\, t_{fc}^2\, f_y}{\gamma_{M0}} = 1289.68 kNmm \qquad \text{Table 6.2 EC3.1-8}$$

$$F_{t.Rd} = \frac{0.9\, A_s\, f_{ub}}{\gamma_{M2}} = 113.04 kN \qquad \text{Table 3.4 EC3.1-8}$$

$$n = min(e_{min}, 1.25m) = 17.50 mm \qquad \text{Table 6.2 EC3.1-8}$$

$$F_{T.2.Rd} = \frac{2\, M_{pl.2.Rd} + 2n\, F_{t.Rd}}{m + n} = 207.48 kN \qquad \text{Table 6.2 EC3.1-8}$$

Individual bolt resistances of bolt rows II. Failure mode 3

$$F_{T.3.Rd} = 2\, F_{t.Rd} = 226.08 kN \qquad \text{Table 6.2 EC3.1-8}$$

- Rest of components:
  The rest of components remains unaltered with the introduction of the transversal stiffeners.

  Assembly of the components:

Tensile loads which can be supported by row I individually

Column flange in bending	$207.48 kN$
Column web in tension	$219.73 kN$
End-plate in bending	$122.10 kN$
	$F_{I.min} = 122.10 kN$

Tensile loads which can be supported by row II individually

Beam web in tension	$277.59kN$
Column flange in bending	$207.48kN$
Column web in tension	$219.73kN$
End-plate in bending	$182.00kN$
	$F_{II.min} = 182.00kN$

The maximum tensile force is determined by the minimum of the sum of individual forces of the bolt rows or the loads that support as a group. To ensure equilibrium the compression internal forces are compared with the tensile forces:

Beam flange and web in compression	$450.54kN$
Column web in compression	$(sufficient)$
Column web panel in shear	$300.82kN$
	$F_{c.min} = 300.82kN$

The resistance of the column web panel in shear limits the maximal load that can be supported, therefore the maximum tensile forces that the bolt rows can support is reduced as follows:

$$F_{II.min.red} = F_{c.min} - F_{I.min} = 178.72kN$$

The design bending resistance of the joint is estimated as follows:

$$\mathbf{M_{j.Rd}} = F_{I.min}\, h_I + F_{II.min.red}\, h_{II} = \mathbf{37.10kNm}$$

Determination of the rotational stiffness:
The individual rotational stiffness not included in this section are assumed that remain constant with respect to the example without stiffeners

Column web panel in compression:
The stiffness of the web panel in compression is assumed infinite with the introduction of stiffeners.

According to 6.3.3.1(6.27) EC3.1-8, the stiffness of the joint on the first two thirds of $M_{j.Rd}$ may be estimated with $S_{j.ini}$, for the last third the stiffness may be computed with S_j:

$$\mathbf{S_{j.ini}} = \frac{z_{eq}^2}{\frac{1}{k_{eq}} + \frac{1}{k_1}} = \mathbf{9494kNm/rad} \qquad \text{adapted 6.3.3.1 (6.27) EC3.1-8}$$

$$\mathbf{S_j} = \frac{z_{eq}^2}{\mu\left(\frac{1}{k_{eq}} + \frac{1}{k_1}\right)} \qquad \text{adapted 6.3.3.1 (6.27) EC3.1-8}$$

$$\mu = \left(1.5\frac{M_{j.Ed}}{M_{j.Rd}}\right)^{2.7} \qquad \text{6.3.3.1 (6.28b) EC3.1-8}$$

B.4 Snap-Fit connection with stiffeners

This section similarly to Annex section B.2 describes the procedure followed to determine the resistances and stiffness of the components of the *Snap-Fit connection*, in this section only will be included those components that resulted influenced from the introduction of the stiffeners. The geometry of the connection is shown in Fig. B.8.
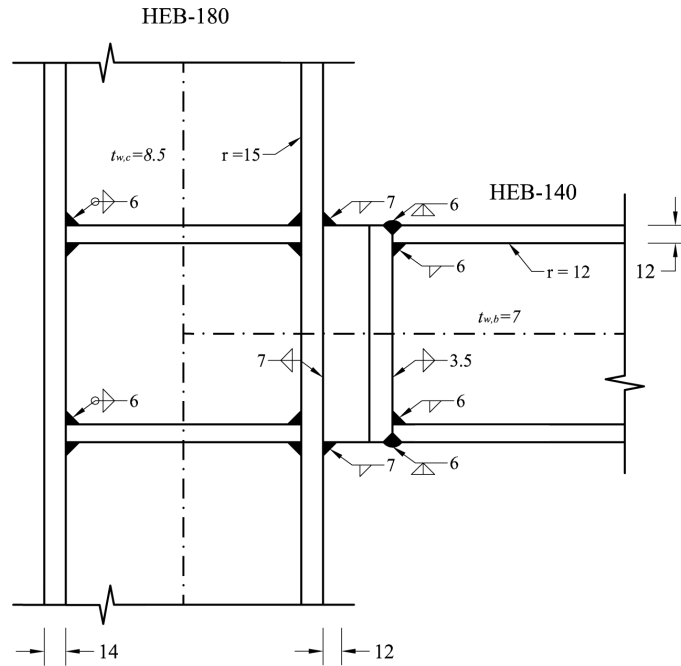
Figure B.8: *Snap-Fit connection* with stiffeners

- Component 1. Column web panel in shear:
  Similarly to section B.3 the resistance of this component is increased with the introduction of stiffeners.

- Component 2. Column web in compression:
  Similarly to section B.3 the resistance with the introduction of stiffeners is considered sufficient.

- Component 4. Column flange in bending:
  With the introduction of horizontal stiffeners, the flange of the column becomes stiffer, and therefore the complete width of the flange it is assumed to be able to transfer tensile stresses.

$$b_{eff} = 140mm$$

$$F_{fc.Rd} = \frac{b_{eff} \sqrt{2} \, a_{fc} \, f_y}{\gamma_{M0}} = 325.70kN \qquad \text{adapted 6.2.6.4.3 (6.20) EC3.1-8}$$

- Component 19. Welds

As a consequence of the stiffening effect of the flange of the column, also the welds attached to that region become effective along its width.

$$b_{eff.w.fc} = b_{eff.b.fc} = 140mm$$

$$\sigma_\perp = \tau_\perp = \frac{\sigma_{weld}}{\sqrt{2}}$$

$$\frac{f_u}{\beta_w\,\gamma_{M2}} = \sqrt{\left(\frac{\sigma_{weld}}{\sqrt{2}}\right)^2 + 3\left(\frac{\sigma_{weld}}{\sqrt{2}}\right)^2}$$

$$\sigma_{weld} = 254.55 N/mm^2$$

$$F_{t.weld} = a_{fc}\,b_{eff.w.fc}\,\sigma_{weld} = 249.46kN$$

Assembly of the components:

Tensile loads which can be supported

Column flange in bending	$325.70kN$
Column web in tension	$242.56kN$
Dovetail in bending	$285.41kN$
Welds in tension	$249.46kN$

$$F_{I.min} = 242.56kN$$

To ensure equilibrium the compression internal forces are compared with the tensile forces:

Beam flange and web in compression	$450.54kN$
Column web in compression	$(sufficient)$
Column web panel in shear	$300.82kN$

$$F_{c.min} = 300.82kN$$

The design bending resistance of the joint is estimated as follows:

$$\mathbf{M_{j.Rd}} = F_{I.min}\,z_{weld} = \mathbf{36.38kNm}$$

$$z_{weld} = h_b + \frac{2\sqrt{2}\,a_{fb}}{2} = 149.90mm$$

Determination of the rotational stiffness:

Apart from the stiffness of the component 2 (Column web in compression) which is now assumed to be infinite, the rest of the rotation stiffness remain unaltered.

According to 6.3.3.1(6.27) EC3.1-8, the stiffness of the joint on the first two thirds of $M_{j.Rd}$ may be estimated with $S_{j.ini}$, for the last third the stiffness may be computed with S_j:

$$\mathbf{S_{j.ini}} = \frac{z_{dovetail}^2}{\frac{1}{k_1} + \frac{1}{k_2} + \frac{1}{k_3} + \frac{1}{k_{dovetail}}} \qquad \text{adapted 6.3.3.1 (6.27) EC3.1-8}$$

$$\mathbf{S_j} = \frac{z_{eq}^2}{\mu\left(\frac{1}{k_1} + \frac{1}{k_2} + \frac{1}{k_3} + \frac{1}{k_{Dovetail}}\right)} \qquad \text{adapted 6.3.3.1 (6.27) EC3.1-8}$$

$$\mu = \left(\frac{1.5M_{Ed}}{M_{Rd}}\right)^{2.7}$$

Appendix C

Verification analytical calculations

This appendix contains the verification of the analytical computations of the extended end-plate with and without stiffeners.

The software used for verification is CoP (The Connection Program) version 1.8.1

C.1   Extended end-plate

Fig. C.1 shows a comparison of the results obtained with the analytical component method of Appendix B.1 and the results of CoP. Both relations show the same behaviour in global terms. Slight differences on the stiffness of the connection of an order of a 9% are visible, those are attributed to the stiffness estimation method.

Below there is a pdf file attached which relates to the output file given by the software for the calculation of the extended end-plate *without* stiffeners. The file contains first the geometrical and material properties, thereafter the resistance and stiffness of the components are computed and finally the components are assembled and a global resistance and stiffness is provided.

Figure C.1: M-θ comparison of the extended end-plate

Design of joints

1 General

Project name   Extended end-plate connection

Project number

Comment   Verification of the analytical calculation of the extended end-plate without stiffeners used for comparison in chapter "Comparison with a bolted connection" of the report.

Client name

Client address

Company

Company address

Designer

Calculation in accordance with   CEN EN 1993-1-8

Note: In the following calculations references to the Eurocodes are given. If the relevant part of Eurocode is not specified reference is made to EN 1993-1-8.

1.1 Safety factors

Safety factor	γ_{M0}	=	1
Safety factor	γ_{M1}	=	1
Safety factor	γ_{M2}	=	1.25
Safety factor	γ_{M5}	=	1
Safety factor	γ_{s}	=	1.15
Safety factor	γ_{c}	=	1.5

2 Joint configuration

Name: Single sided beam-to-column joint configuration (1)

Comment:

Configuration: Single sided beam-to-column joint configuration

Connection type: End plate connection (moment resistant)

Position number:

Position name:

Braced structure: No

Ratio Kb/Kc greater or equal 0.1:   Yes

Global design procedure: Elastic

CoP2 Professional 1.8.1   Eindhoven University of Technology
© 2016 Feldmann + Weynand GmbH

2.1 Joint 1

2.1.1 Joint geometry

2.1.1.1 Supporting member profile

Name		HE 180 B, S235
Section height	h =	180 mm
Section width	b =	180 mm
Flange thickness	t_f =	14 mm
Web thickness	t_w =	8.5 mm
Radius	r =	15 mm
Yield strength of flange	$f_{y,f}$ =	235 N/mm²
Ultimate strength of flange	$f_{u,f}$ =	360 N/mm²
Yield strength of web	$f_{y,w}$ =	235 N/mm²
Ultimate strength of web	$f_{u,w}$ =	360 N/mm²
Web height	d =	122 mm
Profile area	A =	6525 mm²
Profile shear area	A_{vz} =	2024 mm²

Figure 1: Supporting member profile

2.1.1.2 Beam profile

Name		HE 140 B, S235
Section height	h =	140 mm
Section width	b =	140 mm
Flange thickness	t_f =	12 mm
Web thickness	t_w =	7 mm
Radius	r =	12 mm
Yield strength of flange	$f_{y,f}$ =	235 N/mm²
Ultimate strength of flange	$f_{u,f}$ =	360 N/mm²
Yield strength of web	$f_{y,w}$ =	235 N/mm²
Ultimate strength of web	$f_{u,w}$ =	360 N/mm²

Web height	d	=	92 mm
Profile area	A	=	4296 mm²
Profile shear area	A_{vz}	=	1308 mm²

HE 140 B

Figure 2: *Beam profile*

2.1.1.3 End plate

End plate height	h	=	200 mm
End plate width	b	=	140 mm
End plate thickness	t_{cp}	=	12 mm
Yield stress of end plate	f_y	=	235 N/mm²

2.1.1.4 Bolt pattern

2.1.1.4.1 Bolt properties

Caption		M16, 10.9	
Diameter	d	=	16 mm
Hole diameter	d_0	=	18 mm
Shank area	A_s	=	157 mm²
Bolt head height	k_b	=	10 mm
Nut height	m_n	=	14.8 mm
Washer thickness	h_w	=	4 mm
Yield strength	f_{yb}	=	900 N/mm²
Ultimate strength	f_{ub}	=	1000 N/mm²

2.1.1.4.2 Bolt positions

No. of rows	n_1	=	3
Pitch between bolt rows	p_{11}	=	60 mm
Pitch between bolt rows	p_{12}	=	70 mm
No. of columns	n_2	=	2
Pitch between bolt columns	p_{21}	=	60 mm
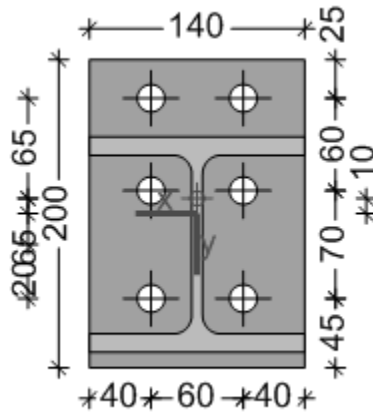
Figure 3: *End plate*

2.1.1.5 Welds

Flange weld size	a_f	=	5 mm
Web weld size	a_w	=	3.5 mm

2.1.1.6 General

Alternative T stub method   No

2.1.2 Loading on joint

Table 1: *Loading*

No.	Name	V [kN]	M [kNm]	N [kN]
1	Default loadcase	0	0	0

2.1.3 Joint properties

Remark: Member checks according to EN 1993-1-1 are not part of this calculation note.

2.1.3.1 Positive moment

2.1.3.1.1 Components

2.1.3.1.1.1 Beam flange and web in compression (1)

Section class for My	Class	=	1
Plastic section modulus	$W_{pl,y}$	=	$2.454 \cdot 10^5$ mm³
Elastic section modulus	$W_{el,y}$	=	$2.156 \cdot 10^5$ mm³

Effective section modulus	$W_{eff,y}$	=	$2.156 \cdot 10^5$ mm³	EN 1993-1-5 4.3(4)
Moment capacity of beam flanges	$M_{c,Rd}$	=	57.68 kNm	
Beam flange resistance	F_{Rd}	=	**450.6 kN**	**6.2.6.7 (6.21)**
Stiffness coefficient	k_7	=	**+∞ m**	

2.1.3.1.1.2 Column web in shear (Loadcase 1: Default loadcase)

Column web height	d	=	122 mm	
Column web thickness	t_w	=	8.5 mm	
Epsilon	ε	=	1	EN 1993-1-1 Tbl. 5.2
Check of column web slenderness EN 1993-1-8 6.2.6.1 (1)	$d / t_w ≤ 69ε$			
Normal force in column	N_c	=	0 kN	
Load transformation parameter	β	=	1	5.3 (9) (5.4a/b)
Internal lever arm	z_s	=	126.1 mm	
Height of web panel in shear	z	=	126.1 mm	
Column profile shear area	$A_{vz,c}$	=	2024 mm²	EN 1993-1-1 6.2.6 (3)
Shear resistance of web	$V_{wp,Rd}$	=	247.2 kN	6.2.6.1 (2) (6.7)
Shear resistance	F_{Rd}	=	**247.2 kN**	
	$F_{Rd}/β$	=	247.2 kN	
Stiffness coefficient	$k_{1,a}$	=	0.006099 m	6.3.2 (1) Tbl. 6.11
Stiffness coefficient	k_1	=	**0.006099 m**	

2.1.3.1.1.3 Column web in compression (Loadcase 1: Default loadcase)

Load transformation parameter	β	=	1	
Max. longit. compressive stress due to axial force and bending in column	$σ_{com,a}$	=	0 N/mm²	
Loaded length	L_0	=	41.07 mm	
Total column shear area	$A_{vz,tot}$	=	2024 mm²	
Column profile web height	$d_{w,c}$	=	122 mm	
Effective width	$b_{eff,c,wc}$	=	186.1 mm	6.2.6.2(1) (6.10-6.12)
Plate slenderness	$λ_p$	=	0.5526	6.2.6.2(1) (6.13c)
Reduction factor for plate buckling	ρ	=	1	6.2.6.2(1)
Factor	$ω_1$	=	0.7467	6.2.6.2 Tbl. 6.3
Factor	$ω_2$	=	0.4894	6.2.6.2 Tbl. 6.3
Reduction factor for interaction with shear	ω	=	0.7467	6.2.6.2 Tbl. 6.3
Reduction factor for compression in column	$k_{wc,a}$	=	1	6.2.6.2(2)
Crushing resistance of web	$F_{a,c,wc,cr,Rd}$	=	277.5 kN	6.2.6.2(1) (6.9)
Buckling resistance of Web	$F_{a,c,wc,bu,Rd}$	=	277.5 kN	6.2.6.2(1) (6.9)
Resistance	F_{Rd}	=	**277.5 kN**	
Web thickness	t_w	=	8.5 mm	
Web height	$d_{w,c}$	=	122 mm	
Effective width	$b_{eff,c}$	=	186.1 mm	6.2.6.2(1) (6.10-6.12)
Stiffness of column web	$k_{a,wc,c}$	=	0.009075 m	Tbl. 6.11 (EN1994-1-1 A.2.2.2)
Stiffness coefficient	k_2	=	**0.009075 m**	

2.1.3.1.1.4 Bolts in tension

Shear area of bolt	A_s	= 157 mm²	
Factor	k_2	= 0.9	3.6.1 Tbl. 3.4
Tension resistance (per bolt)	$F_{t,Rd}$	**= 113 kN**	**3.6.1 Tbl. 3.4**
Bolt elongation length	L_b	= 42.4 mm	
Stiffness per bolt row	k_{10}	**= 0.005925 m**	

2.1.3.1.1.5 Bolt row 1:

2.1.3.1.1.5.1 Column flange in bending

Effective length in mode 1	$L_{eff,1}$	= 86.39 mm	
Effective length in mode 2	$L_{eff,2}$	= 130 mm	
Edge distance	n	= 17.19 mm	EN1993-1-8 Tbl. 6.2
Design tension resistance of t-stub in mode 1	$F_{T,1,Rd}$	= 289.4 kN	EN1993-1-8 Tbl. 6.2
Design tension resistance of t-stub in mode 2	$F_{T,2,Rd}$	= 222.4 kN	EN1993-1-8 Tbl. 6.2
Design tension resistance of t-stub in mode 3	$F_{T,3,Rd}$	= 226.1 kN	EN1993-1-8 Tbl. 6.2
Resistance	F_{Rd}	**= 222.4 kN**	**6.2.4 Tbl. 6.2**
Stiffness coefficient	k_4	**= 0.08207 m**	**6.3.2 Tbl. 6.11**

2.1.3.1.1.5.2 Column web in tension (Loadcase 1: Default loadcase)

Effective width	$b_{eff,t,wc}$	= 130 mm	6.2.6.3 (2) (6.16)
Column profile shear area	$A_{vz,c}$	= 2024 mm²	6.2.6 (3)
Total column shear area	$A_{vz,tot}$	= 2024 mm²	
Factor	ω_1	= 0.849	6.2.6 Tbl. 6.3
Factor	ω_2	= 0.6263	6.2.6 Tbl. 6.3
Reduction factor for shear interaction	ω	= 0.849	6.2.6 Tbl. 6.3
Tension resistance of web	$F_{a,t,wc,Rd}$	= 220.5 kN	6.2.6.3 (1) (6.15)
Resistance	F_{Rd}	**= 220.5 kN**	
Stiffness coefficient	k_3	**= 0.004213 m**	**6.3.2 Tbl. 6.11**

2.1.3.1.1.5.3 End plate in bending

Effective length in mode 1	$L_{eff,1}$	= 70 mm	
Effective length in mode 2	$L_{eff,2}$	= 70 mm	
Edge distance	n	= 24.18 mm	EN1993-1-8 Tbl. 6.2
Design tension resistance of t-stub in mode 1	$F_{T,1,Rd}$	= 122.5 kN	EN1993-1-8 Tbl. 6.2
Design tension resistance of t-stub in mode 2	$F_{T,2,Rd}$	= 152.8 kN	EN1993-1-8 Tbl. 6.2
Design tension resistance of t-stub in mode 3	$F_{T,3,Rd}$	= 226.1 kN	EN1993-1-8 Tbl. 6.2
Resistance	F_{Rd}	**= 122.5 kN**	**6.2.4 Tbl. 6.2**
Stiffness coefficient	k_5	**= 0.01504 m**	**6.3.2 Tbl. 6.11**

2.1.3.1.1.6 Bolt row 2:

2.1.3.1.1.6.1 Column flange in bending

Effective length in mode 1	$L_{eff,1}$	= 86.39 mm	
Effective length in mode 2	$L_{eff,2}$	= 130 mm	
Edge distance	n	= 17.19 mm	EN1993-1-8 Tbl. 6.2
Design tension resistance of t-stub in mode 1	$F_{T,1,Rd}$	= 289.4 kN	EN1993-1-8 Tbl. 6.2
Design tension resistance of t-stub in mode 2	$F_{T,2,Rd}$	= 222.4 kN	EN1993-1-8 Tbl. 6.2

Design tension resistance of t-stub in mode 3	$F_{T,3,Rd}$	=	226.1 kN	EN1993-1-8 Tbl. 6.2
Resistance	$\mathbf{F_{Rd}}$	**=**	**222.4 kN**	**6.2.4 Tbl. 6.2**
Stiffness coefficient	$\mathbf{k_4}$	**=**	**0.06175 m**	**6.3.2 Tbl. 6.11**

2.1.3.1.1.6.2 Column flange in bending / Group 1 to 2

Effective length in mode 1	$L_{eff,1}$	=	190 mm	
Effective length in mode 2	$L_{eff,2}$	=	190 mm	
Edge distance	n	=	17.19 mm	EN1993-1-8 Tbl. 6.2
Design tension resistance of t-stub in mode 1	$F_{T,1,Rd}$	=	636.5 kN	EN1993-1-8 Tbl. 6.2
Design tension resistance of t-stub in mode 2	$F_{T,2,Rd}$	=	392.6 kN	EN1993-1-8 Tbl. 6.2
Design tension resistance of t-stub in mode 3	$F_{T,3,Rd}$	=	452.2 kN	EN1993-1-8 Tbl. 6.2

2.1.3.1.1.6.3 Column web in tension (Loadcase 1: Default loadcase)

Effective width	$b_{eff,t,wc}$	=	130 mm	6.2.6.3 (2) (6.16)
Column profile shear area	$A_{vz,c}$	=	2024 mm²	6.2.6 (3)
Total column shear area	$A_{vz,tot}$	=	2024 mm²	
Factor	ω_1	=	0.849	6.2.6 Tbl. 6.3
Factor	ω_2	=	0.6263	6.2.6 Tbl. 6.3
Reduction factor for shear interaction	ω	=	0.849	6.2.6 Tbl. 6.3
Tension resistance of web	$F_{a,t,wc,Rd}$	=	220.5 kN	6.2.6.3 (1) (6.15)
Resistance	$\mathbf{F_{Rd}}$	**=**	**220.5 kN**	
Stiffness coefficient	$\mathbf{k_3}$	**=**	**0.00317 m**	**6.3.2 Tbl. 6.11**

2.1.3.1.1.6.4 Column web in tension (Loadcase 1: Default loadcase) / Group 1 to 2

Effective width	$b_{eff,t,wc}$	=	190 mm	6.2.6.3 (2) (6.16)
Column profile shear area	$A_{vz,c}$	=	2024 mm²	6.2.6 (3)
Total column shear area	$A_{vz,tot}$	=	2024 mm²	
Factor	ω_1	=	0.7397	6.2.6 Tbl. 6.3
Factor	ω_2	=	0.4817	6.2.6 Tbl. 6.3
Reduction factor for shear interaction	ω	=	0.7397	6.2.6 Tbl. 6.3
Tension resistance of web	$F_{a,t,wc,Rd}$	=	280.7 kN	6.2.6.3 (1) (6.15)
Resistance	$\mathbf{F_{Rd}}$	**=**	**280.7 kN**	

2.1.3.1.1.6.5 End plate in bending

Effective length in mode 1	$L_{eff,1}$	=	141.6 mm	
Effective length in mode 2	$L_{eff,2}$	=	169.5 mm	
Edge distance	n	=	28.18 mm	EN1993-1-8 Tbl. 6.2
Design tension resistance of t-stub in mode 1	$F_{T,1,Rd}$	=	212.6 kN	EN1993-1-8 Tbl. 6.2
Design tension resistance of t-stub in mode 2	$F_{T,2,Rd}$	=	182.1 kN	EN1993-1-8 Tbl. 6.2
Design tension resistance of t-stub in mode 3	$F_{T,3,Rd}$	=	226.1 kN	EN1993-1-8 Tbl. 6.2
Resistance	$\mathbf{F_{Rd}}$	**=**	**182.1 kN**	**6.2.4 Tbl. 6.2**
Stiffness coefficient	$\mathbf{k_5}$	**=**	**0.01825 m**	**6.3.2 Tbl. 6.11**

2.1.3.1.1.6.6 Beam web in tension

Resistance	$\mathbf{F_{Rd}}$	**=**	**278.8 kN**	**6.2.6.8**

2.1.3.1.1.7 Bolt row 3:

2.1.3.1.1.7.1 Column flange in bending

Effective length in mode 1	$L_{eff,1}$	= 86.39 mm	
Effective length in mode 2	$L_{eff,2}$	= 130 mm	
Edge distance	n	= 17.19 mm	EN1993-1-8 Tbl. 6.2
Design tension resistance of t-stub in mode 1	$F_{T,1,Rd}$	= 289.4 kN	EN1993-1-8 Tbl. 6.2
Design tension resistance of t-stub in mode 2	$F_{T,2,Rd}$	= 222.4 kN	EN1993-1-8 Tbl. 6.2
Design tension resistance of t-stub in mode 3	$F_{T,3,Rd}$	= 226.1 kN	EN1993-1-8 Tbl. 6.2
Resistance	F_{Rd}	= **222.4 kN**	**6.2.4 Tbl. 6.2**
Stiffness coefficient	k_4	= **0.08207 m**	**6.3.2 Tbl. 6.11**

2.1.3.1.1.7.2 Column flange in bending / Group 2 to 3

Effective length in mode 1	$L_{eff,1}$	= 200 mm	
Effective length in mode 2	$L_{eff,2}$	= 200 mm	
Edge distance	n	= 17.19 mm	EN1993-1-8 Tbl. 6.2
Design tension resistance of t-stub in mode 1	$F_{T,1,Rd}$	= 670 kN	EN1993-1-8 Tbl. 6.2
Design tension resistance of t-stub in mode 2	$F_{T,2,Rd}$	= 400.1 kN	EN1993-1-8 Tbl. 6.2
Design tension resistance of t-stub in mode 3	$F_{T,3,Rd}$	= 452.2 kN	EN1993-1-8 Tbl. 6.2

2.1.3.1.1.7.3 Column flange in bending / Group 1 to 3

Effective length in mode 1	$L_{eff,1}$	= 260 mm	
Effective length in mode 2	$L_{eff,2}$	= 260 mm	
Edge distance	n	= 17.19 mm	EN1993-1-8 Tbl. 6.2
Design tension resistance of t-stub in mode 1	$F_{T,1,Rd}$	= 871 kN	EN1993-1-8 Tbl. 6.2
Design tension resistance of t-stub in mode 2	$F_{T,2,Rd}$	= 570.3 kN	EN1993-1-8 Tbl. 6.2
Design tension resistance of t-stub in mode 3	$F_{T,3,Rd}$	= 678.2 kN	EN1993-1-8 Tbl. 6.2

2.1.3.1.1.7.4 Column web in tension (Loadcase 1: Default loadcase)

Effective width	$b_{eff,t,wc}$	= 130 mm	6.2.3 (2) (6.16)
Column profile shear area	$A_{vz,c}$	= 2024 mm²	6.2.6 (3)
Total column shear area	$A_{vz,tot}$	= 2024 mm²	
Factor	ω_1	= 0.849	6.2.6 Tbl. 6.3
Factor	ω_2	= 0.6263	6.2.6 Tbl. 6.3
Reduction factor for shear interaction	ω	= 0.849	6.2.6 Tbl. 6.3
Tension resistance of web	$F_{a,t,wc,Rd}$	= 220.5 kN	6.2.3 (1) (6.15)
Resistance	F_{Rd}	= **220.5 kN**	
Stiffness coefficient	k_3	= **0.004213 m**	**6.3.2 Tbl. 6.11**

2.1.3.1.1.7.5 Column web in tension (Loadcase 1: Default loadcase) / Group 2 to 3

Effective width	$b_{eff,t,wc}$	= 200 mm	6.2.3 (2) (6.16)
Column profile shear area	$A_{vz,c}$	= 2024 mm²	6.2.6 (3)
Total column shear area	$A_{vz,tot}$	= 2024 mm²	
Factor	ω_1	= 0.7223	6.2.6 Tbl. 6.3
Factor	ω_2	= 0.4628	6.2.6 Tbl. 6.3
Reduction factor for shear interaction	ω	= 0.7223	6.2.6 Tbl. 6.3
Tension resistance of web	$F_{a,t,wc,Rd}$	= 288.5 kN	6.2.3 (1) (6.15)
Resistance	F_{Rd}	= **288.5 kN**	

CoP2 Professional 1.8.1
© 2016 Feldmann + Weynand GmbH

Eindhoven University of Technology

2.1.3.1.1.7.6 Column web in tension (Loadcase 1: Default loadcase) / Group 1 to 3

Effective width	$b_{eff,t,wc}$	= 260 mm	6.2.6.3 (2) (6.16)
Column profile shear area	$A_{vz,c}$	= 2024 mm²	6.2.6 (3)
Total column shear area	$A_{vz,tot}$	= 2024 mm²	
Factor	ω_1	= 0.6263	6.2.6 Tbl. 6.3
Factor	ω_2	= 0.3727	6.2.6 Tbl. 6.3
Reduction factor for shear interaction	ω	= 0.6263	6.2.6 Tbl. 6.3
Tension resistance of web	$F_{a,t,wc,Rd}$	= 325.2 kN	6.2.6.3 (1) (6.15)
Resistance	$\mathbf{F_{Rd}}$	**= 325.2 kN**	

2.1.3.1.1.7.7 End plate in bending

Effective length in mode 1	$L_{eff,1}$	= 141.6 mm	
Effective length in mode 2	$L_{eff,2}$	= 169.5 mm	
Edge distance	n	= 28.18 mm	EN1993-1-8 Tbl. 6.2
Design tension resistance of t-stub in mode 1	$F_{T,1,Rd}$	= 212.6 kN	EN1993-1-8 Tbl. 6.2
Design tension resistance of t-stub in mode 2	$F_{T,2,Rd}$	= 182.1 kN	EN1993-1-8 Tbl. 6.2
Design tension resistance of t-stub in mode 3	$F_{T,3,Rd}$	= 226.1 kN	EN1993-1-8 Tbl. 6.2
Resistance	$\mathbf{F_{Rd}}$	**= 182.1 kN**	**6.2.4 Tbl. 6.2**
Stiffness coefficient	$\mathbf{k_5}$	**= 0.01825 m**	**6.3.2 Tbl. 6.11**

2.1.3.1.1.7.8 End plate in bending / Group 2 to 3

Effective length in mode 1	$L_{eff,1}$	= 268.8 mm	
Effective length in mode 2	$L_{eff,2}$	= 268.8 mm	
Edge distance	n	= 28.18 mm	EN1993-1-8 Tbl. 6.2
Design tension resistance of t-stub in mode 1	$F_{T,1,Rd}$	= 403.6 kN	EN1993-1-8 Tbl. 6.2
Design tension resistance of t-stub in mode 2	$F_{T,2,Rd}$	= 340.9 kN	EN1993-1-8 Tbl. 6.2
Design tension resistance of t-stub in mode 3	$F_{T,3,Rd}$	= 452.2 kN	EN1993-1-8 Tbl. 6.2
Resistance	$\mathbf{F_{Rd}}$	**= 340.9 kN**	

2.1.3.1.1.7.9 Beam web in tension

Resistance	$\mathbf{F_{Rd}}$	**= 278.8 kN**	**6.2.6.8**

2.1.3.1.1.7.10 Beam web in tension / Group 2 to 3

Resistance	$\mathbf{F_{Rd}}$	**= 442.2 kN**	**6.2.6.8**

2.1.3.1.2 Moment resistance / stiffness

2.1.3.1.2.1 Loadcase 1 (Default loadcase)

Table 2: Component assembly for hogging moment

Compression	Beam flange in compression	$F_{BFC,Rd}$	450.6 kN	k_7	$+\infty$ mm
	Column web in shear	$F_{CWS,Rd}$	247.2 kN	k_1	6.099 mm
	Column web in compression	$F_{CWC,Rd}$	277.5 kN	k_2	9.075 mm
	Compression resistance	$F_{c,Rd}$	247.2 kN		
Bolts	Bolts in tension	$F_{t,Rd}$	113 kN	k_{10}	5.925 mm
				$k_{10,ext}$	5.925 mm
Bolt row 1	End plate in bending	$F_{EPB,1,Rd}$	122.5 kN	k_5	15.04 mm
	Column web in tension	$F_{CWT,1,Rd}$	220.5 kN	k_3	4.213 mm
	Column flange in bending	$F_{CFB,1,Rd}$	222.4 kN	k_4	82.07 mm
	Tension resistance	$F_{t,1,Rd}$	122.5 kN		
	Lever arm	z_1	159 mm		
Bolt row 2	End plate in bending	$F_{EPB,2,Rd}$	182.1 kN	k_5	18.25 mm
	Beam web in tension	$F_{BWT,2,Rd}$	278.8 kN	k_8	$+\infty$ mm
	Column web in tension	$F_{CWT,2,Rd}$	220.5 kN	k_3	3.17 mm
	Column flange in bending	$F_{CFB,2,Rd}$	222.4 kN	k_4	61.75 mm
	Tension resistance	$F_{t,2,Rd}$	124.7 kN		
	Lever arm	z_2	99 mm		
Bolt row 3	End plate in bending	$F_{EPB,3,Rd}$	182.1 kN	k_5	18.25 mm
	Beam web in tension	$F_{BWT,3,Rd}$	278.8 kN	k_8	$+\infty$ mm
	Column web in tension	$F_{CWT,3,Rd}$	220.5 kN	k_3	4.213 mm
	Column flange in bending	$F_{CFB,3,Rd}$	222.4 kN	k_4	82.07 mm
	Tension resistance	$F_{t,3,Rd}$	0 kN		
	Lever arm	z_3	29 mm		

Plastic moment resistance	$M_{pl,Rd}$	= **31.82 kNm**
Elastic moment resistance	$M_{el,Rd}$	= **21.21 kNm**
Initial rotational stiffness	$S_{j,ini}$	= **117.4 kNm/°**
Rotational stiffness	S_j	= **58.72 kNm/°**

2.1.3.1.3 Shear components

2.1.3.1.3.1 Bolts in shear (Loadcase 1: Default loadcase)

Factor	α_v	= 0.6	3.6.1 Tbl. 3.4
Shear resistance per shear plane	$F_{v,Rd}$	= 96.51 kN	3.6.1 Tbl. 3.4
Shear resistance of bolt row 1	$F_{v,1,Rd}$	= 118.3 kN	
Shear resistance of bolt row 2	$F_{v,2,Rd}$	= 117 kN	
Shear resistance of bolt row 3	$F_{v,3,Rd}$	= 193 kN	

2.1.3.1.3.2 End plate in bearing

2.1.3.1.3.2.1 Bolt row 1:

Factor	α_d	=	0.463	3.6.1 Tbl. 3.4
Factor	α_b	=	0.463	3.6.1 Tbl. 3.4
Factor	k_1	=	2.5	3.6.1 Tbl. 3.4
Bearing resistance	$F_{b,Rd}$	=	64 kN	3.6.1 Tbl. 3.4
Resistance	$F_{b,Rd}$	=	128 kN	

2.1.3.1.3.2.2 Bolt row 2:

Factor	α_d	=	0.8611	3.6.1 Tbl. 3.4
Factor	α_b	=	0.8611	3.6.1 Tbl. 3.4
Factor	k_1	=	2.5	3.6.1 Tbl. 3.4
Bearing resistance	$F_{b,Rd}$	=	119 kN	3.6.1 Tbl. 3.4
Resistance	$F_{b,Rd}$	=	238.1 kN	

2.1.3.1.3.2.3 Bolt row 3:

Factor	α_d	=	1.046	3.6.1 Tbl. 3.4
Factor	α_b	=	1	3.6.1 Tbl. 3.4
Factor	k_1	=	2.5	3.6.1 Tbl. 3.4
Bearing resistance	$F_{b,Rd}$	=	138.2 kN	3.6.1 Tbl. 3.4
Resistance	$F_{b,Rd}$	=	276.5 kN	

2.1.3.1.3.3 Column flange in bearing

2.1.3.1.3.3.1 Bolt row 1:

Factor	α_d	=	$+\infty$	3.6.1 Tbl. 3.4
Factor	α_b	=	1	3.6.1 Tbl. 3.4
Factor	k_1	=	2.5	3.6.1 Tbl. 3.4
Bearing resistance	$F_{b,Rd}$	=	161.3 kN	3.6.1 Tbl. 3.4
Resistance	$F_{b,Rd}$	=	322.6 kN	

2.1.3.1.3.3.2 Bolt row 2:

Factor	α_d	=	0.8611	3.6.1 Tbl. 3.4
Factor	α_b	=	0.8611	3.6.1 Tbl. 3.4
Factor	k_1	=	2.5	3.6.1 Tbl. 3.4
Bearing resistance	$F_{b,Rd}$	=	138.9 kN	3.6.1 Tbl. 3.4
Resistance	$F_{b,Rd}$	=	277.8 kN	

2.1.3.1.3.3.3 Bolt row 3:

Factor	α_d	=	1.046	3.6.1 Tbl. 3.4
Factor	α_b	=	1	3.6.1 Tbl. 3.4
Factor	k_1	=	2.5	3.6.1 Tbl. 3.4
Bearing resistance	$F_{b,Rd}$	=	161.3 kN	3.6.1 Tbl. 3.4
Resistance	$F_{b,Rd}$	=	322.6 kN	

2.1.3.1.3.4 End plate in block tearing

Net area in tension	$A_{nt,1}$	=	504 mm²	3.10.2 (2)
Net area in shear	$A_{nv,1}$	=	384 mm²	3.10.2 (2)

Resistance of shape 1	$V_{eff,Rd,1}$ =	197.3 kN	3.10.2 (2) (3.9/3.10)
Net area in tension	$A_{nt,2}$ =	744 mm²	3.10.2 (2)
Net area in shear	$A_{nv,2}$ =	384 mm²	3.10.2 (2)
Resistance of shape 2	$V_{eff,Rd,2}$ =	266.4 kN	3.10.2 (2) (3.9/3.10)
Net area in tension	$A_{nt,3}$ =	1248 mm²	3.10.2 (2)
Net area in shear	$A_{nv,3}$ =	0 mm²	3.10.2 (2)
Resistance of shape 3	$V_{eff,Rd,3}$ =	359.4 kN	3.10.2 (2) (3.9/3.10)

2.1.3.1.3.5 Beam web in shear

Shear area	A_v =	1308 mm²	
Resistance	$V_{Rd,7}$ =	88.71 kN	EN 1993-1-1 6.2.6 (2)

(6.18)

(Remark: resistance is limited to 50% of the shear resistance of the beam {0} to avoid reduction of moment due to interaction with shear.)

2.1.3.1.3.6 Web weld in shear

Weld size	a_w =	3.5 mm	
Length of web weld	L_w =	184 mm	
Resistance	$V_{Rd,weld}$ =	133.9 kN	4.5.3.2

2.1.3.1.4 Shear downwards

Resistance	V_{Rd} =	88.71 kN	

Table 3: Component assembly for shear downwards(LC 1)

Bolt row 1	$V_{Rd,1}$	118.3 kN
Bolt row 2	$V_{Rd,2}$	117 kN
Bolt row 3	$V_{Rd,3}$	193 kN
Total	$V_{Rd,1-3}$	428.3 kN
Beam web in shear	$V_{Rd,BWS}$	88.71 kN
Web weld in shear	$V_{Rd,weld}$	133.9 kN
Shear resistance	V_{Rd}	88.71 kN

2.1.4 Joint checks

2.1.4.1 Moment

Table 4: Moment check

LC	M_{Ed}	M_{Rd}	Utilization factor	Design check
1	0 kNm	31.82 kNm	0	OK

2.1.4.2 Shear

Table 5: Shear check

LC	V_{Ed}	V_{Rd}	Utilization factor	Design check
1	0 kN	88.71 kN	0	OK

2.1.4.3 M-N interaction

Check if interaction between N and M has to be considered (see 6.2.7.1 (2))

Table 6: M-N interaction check

LC	N_{Ed}	5% $N_{pl,Rd,beam}$	
1	0 kN	50.47 kN	Not required

Interaction check M-N is not required.

2.1.4.4 Further checks

2.1.4.4.1 Column web panel in shear

Table 7: Column web panel in shear check

LC	$V_{wp,Ed}$	$V_{wp,Rd}$	Utilization factor	Design check
1	0 kN	247.2 kN	0	OK

2.1.4.4.2 Check of welds

Table 8: Welds of beam 1

LC	a_f	$a_{f,req}$	Design check	a_w	$a_{w,req}$	Design check
1	5 mm	3.899 mm	OK	3.5 mm	3 mm	OK

2.1.5 Classification

2.1.5.1 Stiffness classification

Factor	k_b	= 25	EN1993-1-8 5.2.2.5
Span of beam	L_b	= 5 m	
Stiffness boundary for rigid joints	$S_{j,Lim1}$	= 276.6 kNm/°	EN1993-1-8 5.2.2.5
Stiffness boundary for pinned joints	$S_{j,Lim2}$	= 5.532 kNm/°	EN1993-1-8 5.2.2.5

Table 9: Stiffness classification

LC	Initial rotational stiffness $S_{j,ini}$	Classification
1	117.4 kNm/°	Semi-rigid

2.1.5.2 Strength classification

Relevant moment $\qquad$ $M_{relevant}$ = 57.68 kNm $\quad$ EN1993-1-8 5.2.3.3

Table 10: Strength classification

LC	Moment resistance $M_{j,Rd}$	Classification
1	31.82 kNm	Partial-strength

3 References

[1] CEN: Eurocode 3: Design of steel structures - Part 1-1: General rules and rules for buildings, EN 1993-1-1:2005 + AC:2009, December 2010

[2] CEN: Eurocode 3: Design of steel structures - Part 1-8: Design of joints, EN 1993-1-8:2005 + AC:2009, December 2010

[3] CEN: Eurocode 4: Design of composite steel and concrete structures - Part 1-1: General rules and rules for buildings, EN 1994-1-1:2004, December 2004

[4] Steel and composite building frames: sway response under conventional loading and developmet of membrane effects in beams further to an exceptional action, Jean-Francois Demonceau, PhD thesis, University of Liege, Belgium, 2008

[5] European recommendations for the design of simple joints in steel structures, ECCS Technical commitee 10 Structural connections, ECCS No. 126, 2009

C.2   Extended end-plate with stiffeners

Fig. C.2 shows a comparison of the results obtained with the analytical component method of Appendix B.3 and the results of CoP. Both relations show the same behaviour in global terms. Slight differences on the stiffness of both connections are visible, those differences are of a magnitude of 7% and are attributed to different stiffness estimation methods.

Below there is a pdf file attached which relates to the output file given by the software for the calculation of the extended end-plate *without* stiffeners. The file contains first the geometrical and material properties, thereafter the resistance and stiffness of the components are computed and finally the components are assembled and a global resistance and stiffness is provided.

Figure C.2: M-θ comparison of the extended end-plate with stiffeners

Design of joints

1 General

Project name	Optimization of a Snap-Fit connection
Project number	-
Comment	Verification of the analytical calculation of the extended end-plate with

stiffeners used for comparison in chapter "Comparison with a bolted connection" of the report.

Client name	-
Client address	-
Company	-
Company address	-
Designer	
Calculation in accordance with	CEN EN 1993-1-8

Note: In the following calculations references to the Eurocodes are given. If the relevant part of Eurocode is not specified reference is made to EN 1993-1-8.

1.1 Safety factors

Safety factor	γ_{M0}	=	1
Safety factor	γ_{M1}	=	1
Safety factor	γ_{M2}	=	1.25
Safety factor	γ_{M5}	=	1
Safety factor	γ_{s}	=	1.15
Safety factor	γ_{c}	=	1.5

2 Joint configuration

Name:	Single sided beam-to-column joint configuration (1)
Comment:	
Configuration:	Single sided beam-to-column joint configuration
Connection type:	End plate connection (moment resistant)
Position number:	
Position name:	
Braced structure:	No
Ratio Kb/Kc greater or equal 0.1:	Yes
Global design procedure:	Elastic

2.1 Joint 1

2.1.1 Joint geometry

2.1.1.1 Supporting member profile

Name			HE 180 B, S235
Section height	h	=	180 mm
Section width	b	=	180 mm
Flange thickness	t_f	=	14 mm
Web thickness	t_w	=	8.5 mm
Radius	r	=	15 mm
Yield strength of flange	$f_{y,f}$	=	235 N/mm²
Ultimate strength of flange	$f_{u,f}$	=	360 N/mm²
Yield strength of web	$f_{y,w}$	=	235 N/mm²
Ultimate strength of web	$f_{u,w}$	=	360 N/mm²
Web height	d	=	122 mm
Profile area	A	=	6525 mm²
Profile shear area	A_{vz}	=	2024 mm²

Figure 1: Supporting member profile

2.1.1.2 Stiffeners

Top stiffener			Yes
Bottom stiffener			Yes
Diagonal stiffener			No
Stiffener thickness	t_s	=	12 mm
Stiffener width	b_s	=	85 mm
Stiffener flange weld	a_f	=	6 mm
Stiffener web weld	a_w	=	6 mm
Stiffener yield stress	$f_{y,st}$	=	235 N/mm²
Stiffener ultimate strength	$f_{u,st}$	=	360 N/mm²

2.1.1.3 Beam profile

Name			HE 140 B, S235
Section height	h	=	140 mm
Section width	b	=	140 mm
Flange thickness	t_f	=	12 mm
Web thickness	t_w	=	7 mm
Radius	r	=	12 mm
Yield strength of flange	$f_{y,f}$	=	235 N/mm²
Ultimate strength of flange	$f_{u,f}$	=	360 N/mm²
Yield strength of web	$f_{y,w}$	=	235 N/mm²
Ultimate strength of web	$f_{u,w}$	=	360 N/mm²
Web height	d	=	92 mm
Profile area	A	=	4296 mm²
Profile shear area	A_{vz}	=	1308 mm²

Figure 2: Beam profile

2.1.1.4 End plate

End plate height	h	=	200 mm
End plate width	b	=	140 mm
End plate thickness	t_{cp}	=	12 mm
Yield stress of end plate	f_y	=	235 N/mm²

2.1.1.5 Bolt pattern

2.1.1.5.1 Bolt properties

Caption			M16, 10.9
Diameter	d	=	16 mm
Hole diameter	d_0	=	18 mm
Shank area	A_s	=	157 mm²
Bolt head height	k_b	=	10 mm
Nut height	m_n	=	14.8 mm
Washer thickness	h_w	=	4 mm

Yield strength	f_{yb}	=	900 N/mm²
Ultimate strength	f_{ub}	=	1000 N/mm²

2.1.1.5.2 Bolt positions

No. of rows	n_1	=	3
Pitch between bolt rows	p_{11}	=	60 mm
Pitch between bolt rows	p_{12}	=	70 mm
No. of columns	n_2	=	2
Pitch between bolt columns	p_{21}	=	60 mm
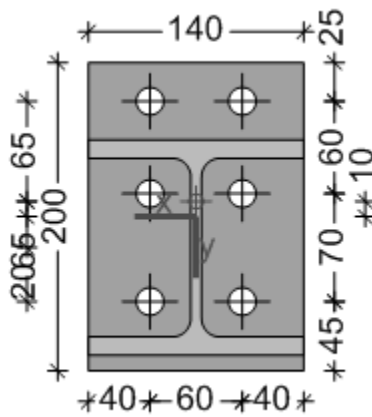
***Figure 3:** End plate*

2.1.1.6 Welds

Flange weld size	a_f	=	5 mm
Web weld size	a_w	=	3.5 mm

2.1.1.7 General

Alternative T stub method		No

2.1.2 Loading on joint

***Table 1:** Loading*

No.	Name	V [kN]	M [kNm]	N [kN]
1	Default loadcase	0	0	0

2.1.3 Joint properties

Remark: Member checks according to EN 1993-1-1 are not part of this calculation note.

2.1.3.1 Positive moment

2.1.3.1.1 Components

2.1.3.1.1.1 Beam flange and web in compression (1)

Section class for My	Class	=	1	
Plastic section modulus	$W_{pl,y}$	=	$2.454 \cdot 10^5$ mm³	
Elastic section modulus	$W_{el,y}$	=	$2.156 \cdot 10^5$ mm³	
Effective section modulus	$W_{eff,y}$	=	$2.156 \cdot 10^5$ mm³	EN 1993-1-5 4.3(4)
Moment capacity of beam flanges	$M_{c,Rd}$	=	57.68 kNm	
Beam flange resistance	F_{Rd}	=	**450.6 kN**	**6.2.6.7 (6.21)**
Stiffness coefficient	k_7	=	**+∞ m**	

2.1.3.1.1.2 Column web in shear (Loadcase 1: Default loadcase)

Column web height	d	=	122 mm	
Column web thickness	t_w	=	8.5 mm	
Epsilon	ε	=	1	EN 1993-1-1 Tbl. 5.2
Check of column web slenderness EN 1993-1-8 6.2.6.1 (1)	$d / t_w \leq 69\varepsilon$			
Normal force in column	N_c	=	0 kN	
Load transformation parameter	β	=	1	5.3 (9) (5.4a/b)
Internal lever arm	z_s	=	124.7 mm	
Height of web panel in shear	z	=	124.7 mm	
Column profile shear area	$A_{vz,c}$	=	2024 mm²	EN 1993-1-1 6.2.6 (3)
Shear resistance of web	$V_{wp,Rd}$	=	247.2 kN	6.2.6.1 (2) (6.7)

2.1.3.1.1.3 Top/bottom stiffeners

Moment resistance of column flange	$M_{pl,fc,Rd}$	=	2.073 kNm	6.2.6.1 (4)
Moment resistance of stiffeners	$M_{pl,st,Rd}$	=	1.184 kNm	6.2.6.1 (4)
Distance of horizontal stiffeners	d_{st}	=	128 mm	
Shear resistance of stiffeners	$V_{wp,add,Rd}$	=	50.89 kN	6.2.6.1 (4) (6.8)
Shear resistance	F_{Rd}	=	**298.1 kN**	
	F_{Rd}/β	=	298.1 kN	
Stiffness coefficient	$k_{1,a}$	=	0.006168 m	6.3.2 (1) Tbl. 6.11
Stiffness coefficient	k_1	=	**0.006168 m**	

2.1.3.1.1.4 Column web in compression (Loadcase 1: Default loadcase)

Load transformation parameter	β	=	1	
Max. longit. compressive stress due to axial force and bending in column	$\sigma_{com,a}$	=	0 N/mm²	
Loaded length	L_0	=	41.07 mm	
Total column shear area	$A_{vz,tot}$	=	2024 mm²	
Column profile web height	$d_{w,c}$	=	122 mm	
Effective width	$b_{eff,c,wc}$	=	186.1 mm	6.2.6.2(1) (6.10-6.12)
Plate slenderness	λ_p	=	0.5526	6.2.6.2(1) (6.13c)
Reduction factor for plate buckling	ρ	=	1	6.2.6.2(1)

Factor	ω_1	=	0.7467	6.2.6.2 Tbl. 6.3
Factor	ω_2	=	0.4894	6.2.6.2 Tbl. 6.3
Reduction factor for interaction with shear	ω	=	0.7467	6.2.6.2 Tbl. 6.3
Reduction factor for compression in column	$k_{wc,a}$	=	1	6.2.6.2(2)
Crushing resistance of web	$F_{a,c,wc,cr,Rd}$	=	277.5 kN	6.2.6.2(1) (6.9)
Buckling resistance of Web	$F_{a,c,wc,bu,Rd}$	=	277.5 kN	6.2.6.2(1) (6.9)

2.1.3.1.1.4.1 Requirements for stiffeners

Stiffener width	b_{st}	=	85 mm	
Stiffener thickness	t_{st}	=	12 mm	
Stiffener yield stress	$f_{y,st}$	=	235 N/mm²	
Stiffener weld size	$a_{w,st}$	=	6 mm	
Beam width	b_b	=	140 mm	
Beam yield stress	$f_{y,b}$	=	235 N/mm²	
Beam flange thickness	t_{st}	=	12 mm	
Stiffener class 3 check	$(b_{st}-\sqrt{2}*a_w)/t_{st} \le 14*\sqrt{(235/f_{y,st})}$			

Stiffener yield stress check $\qquad\qquad\qquad\qquad f_{y,st} \ge f_{y,b}$
ENV 1993-1-1 J.3.5.2 / J.3.3.2

Stiffener thickness check $\qquad\qquad\qquad\qquad t_{st} \ge t_{f,b}$
ENV 1993-1-1 J.3.5.2 / J.3.3.2

Stiffener width check $\qquad\qquad\qquad\qquad b_{st} \ge (b_b-t_{w,c})/2$

Resistance	F_{Rd}	=	**+∞ kN**	
Web thickness	t_w	=	8.5 mm	
Web height	$d_{w,c}$	=	122 mm	
Effective width	$b_{eff,c}$	=	186.1 mm	6.2.6.2(1) (6.10-6.12)
Stiffness of column web A.2.2.2)	$k_{a,wc,c}$	=	0.009075 m	Tbl. 6.11 (EN1994-1-1
Stiffness coefficient	k_2	=	**+∞ m**	

2.1.3.1.1.5 Bolts in tension

Shear area of bolt	A_s	=	157 mm²	
Factor	k_2	=	0.9	3.6.1 Tbl. 3.4
Tension resistance (per bolt)	$F_{t,Rd}$	=	**113 kN**	**3.6.1 Tbl. 3.4**
Bolt elongation length	L_b	=	42.4 mm	
Stiffness per bolt row	k_{10}	=	**0.005925 m**	

2.1.3.1.1.6 Bolt row 1:

2.1.3.1.1.6.1 Column flange in bending

Effective length in mode 1	$L_{eff,1}$	=	86.39 mm	
Effective length in mode 2	$L_{eff,2}$	=	124.3 mm	
Edge distance	n	=	17.19 mm	EN1993-1-8 Tbl. 6.2
Design tension resistance of t-stub in mode 1	$F_{T,1,Rd}$	=	289.4 kN	EN1993-1-8 Tbl. 6.2
Design tension resistance of t-stub in mode 2	$F_{T,2,Rd}$	=	218.2 kN	EN1993-1-8 Tbl. 6.2

Design tension resistance of t-stub in mode 3	$F_{T,3,Rd}$	=	226.1 kN	EN1993-1-8 Tbl. 6.2
Resistance	F_{Rd}	**=**	**218.2 kN**	**6.2.4 Tbl. 6.2**
Stiffness coefficient	k_4	**=**	**0.08207 m**	**6.3.2 Tbl. 6.11**

2.1.3.1.1.6.2 Column web in tension (Loadcase 1: Default loadcase)

Effective width	$b_{eff,t,wc}$	=	124.3 mm	6.2.6.3 (2) (6.16)
Column profile shear area	$A_{vz,c}$	=	2024 mm²	6.2.6 (3)
Total column shear area	$A_{vz,tot}$	=	2024 mm²	
Factor	ω_1	=	0.8593	6.2.6 Tbl. 6.3
Factor	ω_2	=	0.6431	6.2.6 Tbl. 6.3
Reduction factor for shear interaction	ω	=	0.8593	6.2.6 Tbl. 6.3
Tension resistance of web	$F_{a,t,wc,Rd}$	=	213.4 kN	6.2.6.3 (1) (6.15)
Resistance	F_{Rd}	**=**	**213.4 kN**	
Stiffness coefficient	k_3	**=**	**0.004213 m**	**6.3.2 Tbl. 6.11**

2.1.3.1.1.6.3 End plate in bending

Effective length in mode 1	$L_{eff,1}$	=	70 mm	
Effective length in mode 2	$L_{eff,2}$	=	70 mm	
Edge distance	n	=	24.18 mm	EN1993-1-8 Tbl. 6.2
Design tension resistance of t-stub in mode 1	$F_{T,1,Rd}$	=	122.5 kN	EN1993-1-8 Tbl. 6.2
Design tension resistance of t-stub in mode 2	$F_{T,2,Rd}$	=	152.8 kN	EN1993-1-8 Tbl. 6.2
Design tension resistance of t-stub in mode 3	$F_{T,3,Rd}$	=	226.1 kN	EN1993-1-8 Tbl. 6.2
Resistance	F_{Rd}	**=**	**122.5 kN**	**6.2.4 Tbl. 6.2**
Stiffness coefficient	k_5	**=**	**0.01504 m**	**6.3.2 Tbl. 6.11**

2.1.3.1.1.7 Bolt row 2:

2.1.3.1.1.7.1 Column flange in bending

Effective length in mode 1	$L_{eff,1}$	=	86.39 mm	
Effective length in mode 2	$L_{eff,2}$	=	125.5 mm	
Edge distance	n	=	17.19 mm	EN1993-1-8 Tbl. 6.2
Design tension resistance of t-stub in mode 1	$F_{T,1,Rd}$	=	289.4 kN	EN1993-1-8 Tbl. 6.2
Design tension resistance of t-stub in mode 2	$F_{T,2,Rd}$	=	219 kN	EN1993-1-8 Tbl. 6.2
Design tension resistance of t-stub in mode 3	$F_{T,3,Rd}$	=	226.1 kN	EN1993-1-8 Tbl. 6.2
Resistance	F_{Rd}	**=**	**219 kN**	**6.2.4 Tbl. 6.2**
Stiffness coefficient	k_4	**=**	**0.08207 m**	**6.3.2 Tbl. 6.11**

2.1.3.1.1.7.2 Column web in tension (Loadcase 1: Default loadcase)

Effective width	$b_{eff,t,wc}$	=	125.5 mm	6.2.6.3 (2) (6.16)
Column profile shear area	$A_{vz,c}$	=	2024 mm²	6.2.6 (3)
Total column shear area	$A_{vz,tot}$	=	2024 mm²	
Factor	ω_1	=	0.8572	6.2.6 Tbl. 6.3
Factor	ω_2	=	0.6397	6.2.6 Tbl. 6.3
Reduction factor for shear interaction	ω	=	0.8572	6.2.6 Tbl. 6.3
Tension resistance of web	$F_{a,t,wc,Rd}$	=	214.9 kN	6.2.6.3 (1) (6.15)
Resistance	F_{Rd}	**=**	**214.9 kN**	
Stiffness coefficient	k_3	**=**	**0.004213 m**	**6.3.2 Tbl. 6.11**

2.1.3.1.1.7.3 End plate in bending

Effective length in mode 1	$L_{eff,1}$	=	141.6 mm	
Effective length in mode 2	$L_{eff,2}$	=	169.5 mm	
Edge distance	n	=	28.18 mm	EN1993-1-8 Tbl. 6.2
Design tension resistance of t-stub in mode 1	$F_{T,1,Rd}$	=	212.6 kN	EN1993-1-8 Tbl. 6.2
Design tension resistance of t-stub in mode 2	$F_{T,2,Rd}$	=	182.1 kN	EN1993-1-8 Tbl. 6.2
Design tension resistance of t-stub in mode 3	$F_{T,3,Rd}$	=	226.1 kN	EN1993-1-8 Tbl. 6.2
Resistance	F_{Rd}	=	**182.1 kN**	**6.2.4 Tbl. 6.2**
Stiffness coefficient	k_5	=	**0.01825 m**	**6.3.2 Tbl. 6.11**

2.1.3.1.1.7.4 Beam web in tension

Resistance	F_{Rd}	=	**278.8 kN**	**6.2.6.8**

2.1.3.1.1.8 Bolt row 3:

2.1.3.1.1.8.1 Column flange in bending

Effective length in mode 1	$L_{eff,1}$	=	86.39 mm	
Effective length in mode 2	$L_{eff,2}$	=	125.5 mm	
Edge distance	n	=	17.19 mm	EN1993-1-8 Tbl. 6.2
Design tension resistance of t-stub in mode 1	$F_{T,1,Rd}$	=	289.4 kN	EN1993-1-8 Tbl. 6.2
Design tension resistance of t-stub in mode 2	$F_{T,2,Rd}$	=	219 kN	EN1993-1-8 Tbl. 6.2
Design tension resistance of t-stub in mode 3	$F_{T,3,Rd}$	=	226.1 kN	EN1993-1-8 Tbl. 6.2
Resistance	F_{Rd}	=	**219 kN**	**6.2.4 Tbl. 6.2**
Stiffness coefficient	k_4	=	**0.08207 m**	**6.3.2 Tbl. 6.11**

2.1.3.1.1.8.2 Column flange in bending / Group 2 to 3

Effective length in mode 1	$L_{eff,1}$	=	191 mm	
Effective length in mode 2	$L_{eff,2}$	=	191 mm	
Edge distance	n	=	17.19 mm	EN1993-1-8 Tbl. 6.2
Design tension resistance of t-stub in mode 1	$F_{T,1,Rd}$	=	639.8 kN	EN1993-1-8 Tbl. 6.2
Design tension resistance of t-stub in mode 2	$F_{T,2,Rd}$	=	393.4 kN	EN1993-1-8 Tbl. 6.2
Design tension resistance of t-stub in mode 3	$F_{T,3,Rd}$	=	452.2 kN	EN1993-1-8 Tbl. 6.2

2.1.3.1.1.8.3 Column web in tension (Loadcase 1: Default loadcase)

Effective width	$b_{eff,t,wc}$	=	125.5 mm	6.2.6.3 (2) (6.16)
Column profile shear area	$A_{vz,c}$	=	2024 mm²	6.2.6 (3)
Total column shear area	$A_{vz,tot}$	=	2024 mm²	
Factor	ω_1	=	0.8572	6.2.6 Tbl. 6.3
Factor	ω_2	=	0.6397	6.2.6 Tbl. 6.3
Reduction factor for shear interaction	ω	=	0.8572	6.2.6 Tbl. 6.3
Tension resistance of web	$F_{a,t,wc,Rd}$	=	214.9 kN	6.2.6.3 (1) (6.15)
Resistance	F_{Rd}	=	**214.9 kN**	
Stiffness coefficient	k_3	=	**0.004213 m**	**6.3.2 Tbl. 6.11**

2.1.3.1.1.8.4 Column web in tension (Loadcase 1: Default loadcase) / Group 2 to 3

Effective width	$b_{eff,t,wc}$	=	191 mm	6.2.6.3 (2) (6.16)
Column profile shear area	$A_{vz,c}$	=	2024 mm²	6.2.6 (3)
Total column shear area	$A_{vz,tot}$	=	2024 mm²	
Factor	ω_1	=	0.738	6.2.6 Tbl. 6.3

Factor	ω_2	=	0.4798	6.2.6 Tbl. 6.3
Reduction factor for shear interaction	ω	=	0.738	6.2.6 Tbl. 6.3
Tension resistance of web	$F_{a,t,wc,Rd}$	=	281.5 kN	6.2.6.3 (1) (6.15)
Resistance	$\mathbf{F_{Rd}}$	=	**281.5 kN**	

2.1.3.1.1.8.5 End plate in bending

Effective length in mode 1	$L_{eff,1}$	=	141.6 mm	
Effective length in mode 2	$L_{eff,2}$	=	169.5 mm	
Edge distance	n	=	28.18 mm	EN1993-1-8 Tbl. 6.2
Design tension resistance of t-stub in mode 1	$F_{T,1,Rd}$	=	212.6 kN	EN1993-1-8 Tbl. 6.2
Design tension resistance of t-stub in mode 2	$F_{T,2,Rd}$	=	182.1 kN	EN1993-1-8 Tbl. 6.2
Design tension resistance of t-stub in mode 3	$F_{T,3,Rd}$	=	226.1 kN	EN1993-1-8 Tbl. 6.2
Resistance	$\mathbf{F_{Rd}}$	=	**182.1 kN**	**6.2.4 Tbl. 6.2**
Stiffness coefficient	$\mathbf{k_5}$	=	**0.01825 m**	**6.3.2 Tbl. 6.11**

2.1.3.1.1.8.6 End plate in bending / Group 2 to 3

Effective length in mode 1	$L_{eff,1}$	=	268.8 mm	
Effective length in mode 2	$L_{eff,2}$	=	268.8 mm	
Edge distance	n	=	28.18 mm	EN1993-1-8 Tbl. 6.2
Design tension resistance of t-stub in mode 1	$F_{T,1,Rd}$	=	403.6 kN	EN1993-1-8 Tbl. 6.2
Design tension resistance of t-stub in mode 2	$F_{T,2,Rd}$	=	340.9 kN	EN1993-1-8 Tbl. 6.2
Design tension resistance of t-stub in mode 3	$F_{T,3,Rd}$	=	452.2 kN	EN1993-1-8 Tbl. 6.2
Resistance	$\mathbf{F_{Rd}}$	=	**340.9 kN**	

2.1.3.1.1.8.7 Beam web in tension

Resistance	$\mathbf{F_{Rd}}$	=	**278.8 kN**	**6.2.6.8**

2.1.3.1.1.8.8 Beam web in tension / Group 2 to 3

Resistance	$\mathbf{F_{Rd}}$	=	**442.2 kN**	**6.2.6.8**

2.1.3.1.2 Moment resistance / stiffness

2.1.3.1.2.1 Loadcase 1 (Default loadcase)

Table 2: *Component assembly for hogging moment*

Compression	Beam flange in compression	$F_{BFC,Rd}$	450.6 kN	k_7	+∞ mm	
	Column web in shear	$F_{CWS,Rd}$	298.1 kN	k_1	6.168 mm	
	Column web in compression	$F_{CWC,Rd}$	+∞ kN	k_2	+∞ mm	
	Compression resistance	$F_{c,Rd}$	298.1 kN			
Bolts	Bolts in tension	$F_{t,Rd}$	113 kN	k_{10}	5.925 mm	
				$k_{10,ext}$	5.925 mm	
Bolt row 1	End plate in bending	$F_{EPB,1,Rd}$	122.5 kN	k_5	15.04 mm	
	Column web in tension	$F_{CWT,1,Rd}$	213.4 kN	k_3	4.213 mm	
	Column flange in bending	$F_{CFB,1,Rd}$	218.2 kN	k_4	82.07 mm	
	Tension resistance	$F_{t,1,Rd}$	122.5 kN			
	Lever arm	z_1	159 mm			
Bolt row 2	End plate in bending	$F_{EPB,2,Rd}$	182.1 kN	k_5	18.25 mm	
	Beam web in tension	$F_{BWT,2,Rd}$	278.8 kN	k_8	+∞ mm	
	Column web in tension	$F_{CWT,2,Rd}$	214.9 kN	k_3	4.213 mm	
	Column flange in bending	$F_{CFB,2,Rd}$	219 kN	k_4	82.07 mm	
	Tension resistance	$F_{t,2,Rd}$	175.6 kN			
	Lever arm	z_2	99 mm			
Bolt row 3	End plate in bending	$F_{EPB,3,Rd}$	182.1 kN	k_5	18.25 mm	
	Beam web in tension	$F_{BWT,3,Rd}$	278.8 kN	k_8	+∞ mm	
	Column web in tension	$F_{CWT,3,Rd}$	214.9 kN	k_3	4.213 mm	
	Column flange in bending	$F_{CFB,3,Rd}$	219 kN	k_4	82.07 mm	
	Tension resistance	$F_{t,3,Rd}$	0 kN			
	Lever arm	z_3	29 mm			

Plastic moment resistance $\quad\quad$ $M_{pl,Rd}$ $\quad$ = 36.86 kNm

Elastic moment resistance $\quad\quad$ $M_{el,Rd}$ $\quad$ = 24.57 kNm

Initial rotational stiffness $\quad\quad$ $S_{j,ini}$ $\quad$ = 153.9 kNm/°

Rotational stiffness $\quad\quad$ S_j $\quad$ = 76.93 kNm/°

2.1.3.1.3 Shear components

2.1.3.1.3.1 Bolts in shear (Loadcase 1: Default loadcase)

Factor	α_v	=	0.6	3.6.1 Tbl. 3.4
Shear resistance per shear plane	$F_{v,Rd}$	=	96.51 kN	3.6.1 Tbl. 3.4
Shear resistance of bolt row 1	$F_{v,1,Rd}$	=	118.3 kN	
Shear resistance of bolt row 2	$F_{v,2,Rd}$	=	85.93 kN	
Shear resistance of bolt row 3	$F_{v,3,Rd}$	=	193 kN	

2.1.3.1.3.2 End plate in bearing

2.1.3.1.3.2.1 Bolt row 1:

Factor	α_d	=	0.463	3.6.1 Tbl. 3.4
Factor	α_b	=	0.463	3.6.1 Tbl. 3.4
Factor	k_1	=	2.5	3.6.1 Tbl. 3.4
Bearing resistance	$F_{b,Rd}$	=	64 kN	3.6.1 Tbl. 3.4
Resistance	$F_{b,Rd}$	=	128 kN	

2.1.3.1.3.2.2 Bolt row 2:

Factor	α_d	=	0.8611	3.6.1 Tbl. 3.4
Factor	α_b	=	0.8611	3.6.1 Tbl. 3.4
Factor	k_1	=	2.5	3.6.1 Tbl. 3.4
Bearing resistance	$F_{b,Rd}$	=	119 kN	3.6.1 Tbl. 3.4
Resistance	$F_{b,Rd}$	=	238.1 kN	

2.1.3.1.3.2.3 Bolt row 3:

Factor	α_d	=	1.046	3.6.1 Tbl. 3.4
Factor	α_b	=	1	3.6.1 Tbl. 3.4
Factor	k_1	=	2.5	3.6.1 Tbl. 3.4
Bearing resistance	$F_{b,Rd}$	=	138.2 kN	3.6.1 Tbl. 3.4
Resistance	$F_{b,Rd}$	=	276.5 kN	

2.1.3.1.3.3 Column flange in bearing

2.1.3.1.3.3.1 Bolt row 1:

Factor	α_d	=	$+\infty$	3.6.1 Tbl. 3.4
Factor	α_b	=	1	3.6.1 Tbl. 3.4
Factor	k_1	=	2.5	3.6.1 Tbl. 3.4
Bearing resistance	$F_{b,Rd}$	=	161.3 kN	3.6.1 Tbl. 3.4
Resistance	$F_{b,Rd}$	=	322.6 kN	

2.1.3.1.3.3.2 Bolt row 2:

Factor	α_d	=	0.8611	3.6.1 Tbl. 3.4
Factor	α_b	=	0.8611	3.6.1 Tbl. 3.4
Factor	k_1	=	2.5	3.6.1 Tbl. 3.4
Bearing resistance	$F_{b,Rd}$	=	138.9 kN	3.6.1 Tbl. 3.4
Resistance	$F_{b,Rd}$	=	277.8 kN	

2.1.3.1.3.3.3 Bolt row 3:

Factor	α_d	=	1.046	3.6.1 Tbl. 3.4
Factor	α_b	=	1	3.6.1 Tbl. 3.4
Factor	k_1	=	2.5	3.6.1 Tbl. 3.4
Bearing resistance	$F_{b,Rd}$	=	161.3 kN	3.6.1 Tbl. 3.4
Resistance	$F_{b,Rd}$	=	322.6 kN	

2.1.3.1.3.4 End plate in block tearing

Net area in tension	$A_{nt,1}$	=	504 mm²	3.10.2 (2)
Net area in shear	$A_{nv,1}$	=	384 mm²	3.10.2 (2)

Resistance of shape 1	$V_{eff,Rd,1}$	=	197.3 kN	3.10.2 (2) (3.9/3.10)
Net area in tension	$A_{nt,2}$	=	744 mm²	3.10.2 (2)
Net area in shear	$A_{nv,2}$	=	384 mm²	3.10.2 (2)
Resistance of shape 2	$V_{eff,Rd,2}$	=	266.4 kN	3.10.2 (2) (3.9/3.10)
Net area in tension	$A_{nt,3}$	=	1248 mm²	3.10.2 (2)
Net area in shear	$A_{nv,3}$	=	0 mm²	3.10.2 (2)
Resistance of shape 3	$V_{eff,Rd,3}$	=	359.4 kN	3.10.2 (2) (3.9/3.10)

2.1.3.1.3.5 Beam web in shear

Shear area	A_v	=	1308 mm²	
Resistance	$V_{Rd,7}$	=	88.71 kN	EN 1993-1-1 6.2.6 (2) (6.18)

(Remark: resistance is limited to 50% of the shear resistance of the beam {0} to avoid reduction of moment due to interaction with shear.)

2.1.3.1.3.6 Web weld in shear

Weld size	a_w	=	3.5 mm	
Length of web weld	L_w	=	184 mm	
Resistance	$V_{Rd,weld}$	=	133.9 kN	4.5.3.2

2.1.3.1.4 Shear downwards

Resistance	V_{Rd}	=	88.71 kN

Table 3: *Component assembly for shear downwards(LC 1)*

Bolt row 1	$V_{Rd,1}$	118.3 kN
Bolt row 2	$V_{Rd,2}$	85.93 kN
Bolt row 3	$V_{Rd,3}$	193 kN
Total	$V_{Rd,1-3}$	397.3 kN
Beam web in shear	$V_{Rd,BWS}$	88.71 kN
Web weld in shear	$V_{Rd,weld}$	133.9 kN
Shear resistance	V_{Rd}	88.71 kN

2.1.4 Joint checks

2.1.4.1 Moment

Table 4: *Moment check*

LC	M_{Ed}	M_{Rd}	Utilization factor	Design check
1	0 kNm	36.86 kNm	0	OK

2.1.4.2 Shear

Table 5: *Shear check*

LC	V_{Ed}	V_{Rd}	Utilization factor	Design check
1	0 kN	88.71 kN	0	OK

2.1.4.3 M-N interaction

Check if interaction between N and M has to be considered (see 6.2.7.1 (2))

Table 6: M-N interaction check

LC	N_{Ed}	5% $N_{pl,Rd,beam}$	
1	0 kN	50.47 kN	Not required

Interaction check M-N is not required.

2.1.4.4 Further checks

2.1.4.4.1 Column web panel in shear

Table 7: Column web panel in shear check

LC	$V_{wp,Ed}$	$V_{wp,Rd}$	Utilization factor	Design check
1	0 kN	298.1 kN	0	OK

2.1.4.4.2 Check of welds

Table 8: Welds of beam 1

LC	a_f	$a_{f,req}$	Design check	a_w	$a_{w,req}$	Design check
1	5 mm	4.702 mm	OK	3.5 mm	3 mm	OK

2.1.5 Classification

2.1.5.1 Stiffness classification

Factor	k_b	= 25	EN1993-1-8 5.2.2.5
Span of beam	L_b	= 5 m	
Stiffness boundary for rigid joints	$S_{j,Lim1}$	= 276.6 kNm/°	EN1993-1-8 5.2.2.5
Stiffness boundary for pinned joints	$S_{j,Lim2}$	= 5.532 kNm/°	EN1993-1-8 5.2.2.5

Table 9: Stiffness classification

LC	Initial rotational stiffness $S_{j,ini}$	Classification
1	153.9 kNm/°	Semi-rigid

2.1.5.2 Strength classification

Relevant moment	$M_{relevant}$	= 57.68 kNm	EN1993-1-8 5.2.3.3

Table 10: Strength classification

LC	Moment resistance $M_{j,Rd}$	Classification
1	36.86 kNm	Partial-strength

3 References

[1] CEN: Eurocode 3: Design of steel structures - Part 1-1: General rules and rules for buildings, EN 1993-1-1:2005 + AC:2009, December 2010

[2] CEN: Eurocode 3: Design of steel structures - Part 1-8: Design of joints, EN 1993-1-8:2005 + AC:2009, December 2010

[3] CEN: Eurocode 4: Design of composite steel and concrete structures - Part 1-1: General rules and rules for buildings, EN 1994-1-1:2004, December 2004

[4] Steel and composite building frames: sway response under conventional loading and developmet of membrane effects in beams further to an exceptional action, Jean-Francois Demonceau, PhD thesis, University of Liege, Belgium, 2008

[5] European recommendations for the design of simple joints in steel structures, ECCS Technical commitee 10 Structural connections, ECCS No. 126, 2009